SAPIENZA
UNIVERSITÀ DI ROMA

Doctoral Course in Aeronautical and Space Technology
XXVIII Cycle

Department of Mechanical and Aerospace Engineering

Sapienza University of Rome

Doctoral Dissertation by

GIOVANNA GARGIULO

on

SUPERCRITICAL REACTIVE FLOW MODELING IN LRE THRUST CHAMBERS

Advisor: Prof. M. Valorani

Assistant Advisor: Dr. P.P.Ciottoli

ABSTRACT

This CFD study is devoted to the characterization and the analysis of the flow field and heat loads evaluation in oxygen/methane liquid rocket engines. Thanks to CFD we obtain a compromise between details and experimental cost and it is possible a full scale engine analysis as support to the engine design phase. Our work is focused on the heat flux evaluation, hot gas and on flame structure in a thrust chamber. The importance of flame position leads to a study of mesh refinement of post tip. As consequence, a small recirculation zone near the post tip is identified and is studied to guarantee a stable flame also in term of position in the chamber. Also three large recirculation zones of hot gases are located in the combustion chamber and their presence assures, near the walls and the plate, the presence of high heat fluxes. We considered the usage of EOSs and a preliminary analysis was realised before the CFD simulations. Simple test cases are simulated and used to identify the best numerical strategy employ. Finally, we reproduced a simulation of the DEMO a regenerative cooled chamber LOX/methane, obtaining by combustion process simulation the heat flux at the chamber and nozzle walls.

And therefore as a stranger give it welcome. There are more things in heaven and earth, Horatio, Than are dreamt of in your philosophy.

Hamlet, Act I, Scene 5

Polonius - [...] What do you read, my lord?
Hamlet - Words, words, words.

Hamlet, Act II, Scene 2

And thus thy fall hath left a kind of blot To mark the full-fraught man and best endued With some suspicion. I will weep for thee, For this revolt of thine methinks is like Another fall of man.

Henry V, Act II, Scene 2

ACKNOWLEDGEMENTS

This work has been made possible thanks to the support of many, each I want to address individually in the following.

The Italian Center for Aerospace (CIRA) provided a significant part of the financial support within the HyProb Project sponsored by the Italian Ministry of University and Research and the Italian Space Agency (ASI). CIRA also kindly provided us with unlimited and free access to their HPC facilities in Capua.

I ought to thank Metacomp Technologies Inc. for the continued technical support and for the very favorable license arrangement they provided for the making of this work. Namely, I express my deepest gratitude to prof. S. Chakravarthy, and Mr. J. Chakravarthy, Dr. S. Palaniswamy, and Dr. R. Oberoi.

The Cineca HPC Center provided us access to their HPC facilities through the grant No.HP10CRKE5U.

I want to thank my internal reviewers profs. F. Nasuti and F. Creta for their careful reading of my thesis draft and their criticisms and suggestions to improve the quality of the draft.

I thank prof. F. Creta for his support during the making of the axisymmetric analyses and the initial phase of the 3D calculations.

I thank prof. F. Nasuti, Dr. M.Pizzarelli for sharing their tools on real gas EOS with me, and for the instructive discussions on the subject.

I thank Dr. B. Betti for pointing to me a number of very relevant journal articles about heat loads in LRE thrust chambers.

Thanks also to master's candidate U. Palmieri that collaborated with me implementing some tools for post-processing analysis.

Last but not least, I express my heartfelt gratitude to Dr. P. P. Ciottoli for his continuos technical support during the whole duration of this work.

In closing, I thank my advisor Professor M. Valorani for his guidance, support, and patience.

One final thought to my family, my mother who is my strength and my aunt who is my supporter. My sister often in my thoughts.

Rome, October, 2016

CONTENTS

NOMENCLATURE

A	EOS's coefficient
a	Reduced Helmholtz Free Energy
a_{ij}	Pure Fluid Parameters. Cross parameters obtained from a set of combining rules
B	EOS's coefficient
b_{ij}	Pure Fluid Parameters. Cross parameters obtained from a set of combining rules
c_{ij}	Pure Fluid Parameters. Cross parameters obtained from a set of combining rules
c	Speed of Sound
c_p	Specific Heat at Constant Pressure
c_v	Specific Heat at Constant Volume
D	Injector Diameter
E	Mixture Ratio
e	Internal Energy
H	Enthalpy
J	Momentum Flux Ratio
k_{ij}	Interaction Parameter
k	Boltzmann Constant (R/N_a)
m	Slope of $\alpha^{1/2}$ against $T^{1/2}$
$\dot{m}$	Massflow
N_A	Avogrado Number
P	Pressure
$\dot{Q}$	Heat flux
R	Gas Constant
$r_{1/2}$	Radial Location of Half-Maximum Value of a Parameter

$\mathfrak{R}$	Universal Gas Constant
s	Entropy
T	Temperature
u	Axial Velocity
V	Volume
v	Specific Volume
x_i	Mole Fraction of Species
x/D	Non Dimensional Length
Y_i	Mass Fraction of Species
Z	Compressibility Factor

ACRONYMS

BWR	Benedict-Webb-Rubin
BWRS	Benedict-Webb-Rubin-Starling
CH_4	methane
CSP	Correspondent State Principle
DEMO	Demonstrator
DTF	Thickened Flame Model
ECSP	Extended Correspondent State Principle
EOS	Equations of State
GERG	Groupe Europèen de Recherches Gaziéres
H_2	hydrogen
I_{sp}	Specific Impulse
LES	Large Eddy Simulation
LOX	Liquid oxygen
LRE	Liquid Rocket Engine
N_2	nitrogen
NIST	National Institute Standards Technologies

Oh Ohnesorge Number

PR Peng-Robinson

PVT Pressure-Volume-Temperature

RANS Reynolds Averaged Navier Stokes Equations

Re Reynolds Number

RK Redlich-Kwong

SRK Soave-Redlich-Kwong

SRM Solid Rocket Motor

SSBB Sub Scale Bread Board

SSME Space Shuttle Main Engine

URANS Unsteady Reynolds Averaged Navier Stokes Equations

VDW Van der Waals

VLE Volume-Liquid-Equilibrium

We Weber Number

GREEK SYMBOLS

α_{EOS} Scaling Factor in Cubic EOS

α Constant Value in cubic EOS

β Constant Value in cubic EOS

β_{ij} Interaction Parameter

γ Constant Value in cubic EOS

δ_{ij} Interaction Parameter

ω Acentric Factor

ρ Density

σ Surface tension

ϕ Equivalence ratio

μ dynamic viscosity

SUBSCRIPTS

a	ambient
c	Critical Value
mix	Mixing
pb	pseudo-boiling
r	Reduced Value

SUPERSCRIPTS

L	Liquid
Sat	Saturation Value
V	Vapor

LIST OF FIGURES

LIST OF TABLES

1

INTRODUCTION

Contents

Liquid rocket engines (LRE) have been conseived in the 20th century (Goddard, 1926). LREs are employed as first stage, booster, and upper stage engines in launchers, space propulsion, attitude control on spacecrafts and satellites. LREs provide quick restart, ready reuse, and thrust variation on command. A LRE is formed by three main subsystems: propellant tanks, feed system and thrust chamber. The tanks store the propellants, the feed system ensures that the propellants stored in the tanks are delivered at the required pressure to the combustion chamber, and the thrust chamber that is the assembly composed by injectors, combustion chamber and nozzle (Fig. 1.0.1), generates thrust. All thrust chamber components have to stand the high temperatures (above 3000 K) and heat fluxes (from 10 to 100 MW/m^2) produced by combustion and its main function is to generate thrust by converting the propellant chemical energy into kinetic energy of the combustion products.

The propellant chemical energy is efficiently converted into thrust thanks to a series of processes that take place in the combustion chamber, which involve liquid propellant injection, atomisation, vaporisation, mixing, and combustion so as to obtain hot combustion products, which are eventually accelerated and ejected at high velocity through the nozzle.

Since its early design, there has been a continuous trend to raise the chamber pressure to increase the engine performance and decrease the engine weight. The value of specific impulse increases with increasing chamber pressure. A higher chamber pressure allows a higher nozzle area ratio without flow separation at sea level, and an increase of performance (Sutton [101]). Higher chamber pressures

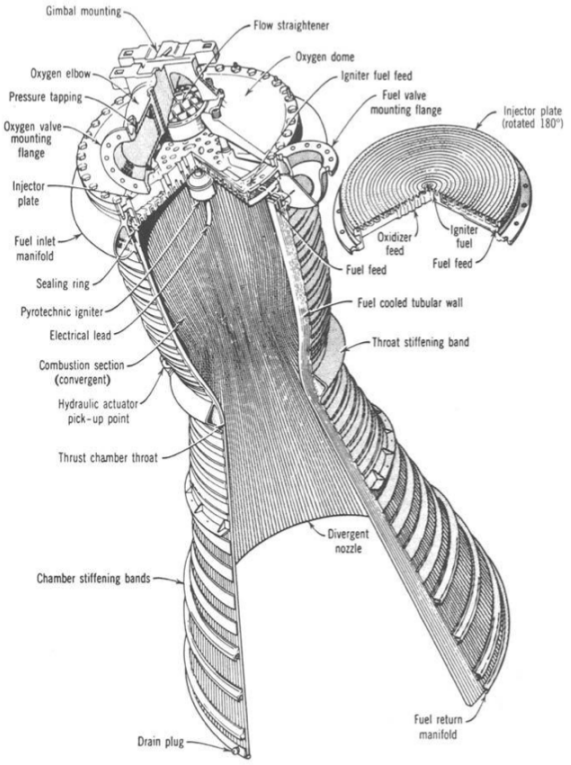

Figure 1.0.1: Thrust chamber; reprinted from Sutton [101]

allow the thrust chamber to be smaller, but there are some disadvantages for what concerns the chamber heat loads that approximately increase as the chamber pressure at the 0.8-th power, consequently the thrust chamber cooling becomes more difficult and the amount of gas flow to drive the turbines increases (Huang [35]). Usually, to attain high pressures in chamber that lead to high engine specific impulse, a suitable design choice is that to select chamber pressure above the critical pressure of the propellants or higher, combined with cryogenic temperatures in the feed system. These design choices imply that the propellants will most likely not behave like pure gases

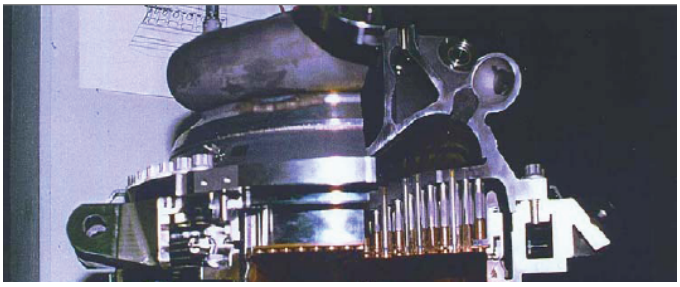

Figure 1.0.2: Injection manifold of thrust chamber.

or pure liquids but rather like real gas "fluids". Rocket engines have been the first thermal engines working under supercritical conditions (temperature and pressure values above the critical point). The usage of cryogenic propellants in LRE at pressures that exceed the thermodynamic critical point of the propellants provides high efficiency and performance for a variety of launch vehicle applications: combustion chambers of rocket engines, jet engines of aircraft, such as gas turbines, diesel piston engines and aeronautical turbines. The high pressure in the combustion chamber and critical work conditions (the liquid fuel may be injected, with a subcritical injection temperature, in an environment, the chamber, where the pressure is above the critical pressure of the fuel) increase the efficiency and thus reduce the CO_2 emissions and in order to limit NOx production the development of special designs of combustion chambers (LPP: Lean-Premix-Prevaporize or RQL: Rich-Quench-Lean) is an efficient help.
A proper LRE design under these operative conditions (cryogenic propellants at pressures that exceed the thermodynamic critical point of the propellants) can be achieved only if the modelling tools account for all the physic of the main phenomena that govern the fluid injection and mixing in various transcritical and supercritical environments.
To lower the cost of access to space the next generation of launchers will employed propellants cheaper to be producted and to supplied have been considered for liquid hydrocarbons/oxygen combinations, whose performance in term of ideal specific vacuum impulse vs propellants mixture ratio (O/F) is shown in Figure 1.0.3 for different propellant combinations. The most common combinations of propellants are oxygen/hydrogen (O2/H2), oxygen/methane (O2/CH4) and oxygen/kerosene (O2/RP-1). The first two options involve cryogenic propellants, that are propellants that are in liquid state at temperatures much lower than the standard temperature, while the third option involves a cryogenic oxidant and a storable fuel, that is a fuel that can be store at standard conditions of pressure and temperature.

The choice of propellants depends not only on the propellants performance but also on the following requirements:

- Liquefaction temperature
- High propellant density
- Capability to absorb heat
- Vapor pressure
- Cheaper handling effort.
- Simple safety precautions and low toxicity

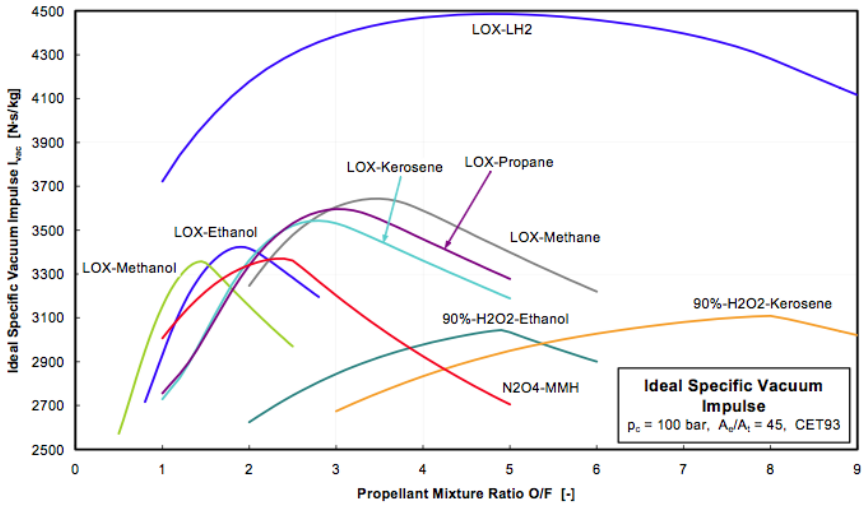

Figure 1.0.3: Ideal specific vacuum impulse VS propellant mixtures. Reprinted from Haidn [30]

In comparison with storable propellants combinations and with other oxygen/hydrocarbons combinations, the combination of oxygen/hydrogen provides a better performance. The LOX/hydrogen engines have been developed for a variety of launch systems, including the Space Shuttle Main Engine (SSME) and the Ariane 5 Vulcain engine. For these engines the pressure in the chamber exceeds 100 atm, which is significantly higher than the thermodynamic critical pressure of both propellants. Another combination that provide a good performance is the oxygen/methane.

In comparison with hydrogen, methane exhibits four main advantages:

- Methane has higher density which implies smaller and lighter tanks.
- Methane is less cryogenic than hydrogen (its liquefaction temperature is higher than the one of hydrogen);
- Methane is a safer fluid than hydrogen because the risk of an explosion is lower.
- Methane has a warmer liquid temperature than hydrogen and lower flammability limit.

These four features have an impact on production, operational and management costs, and for those reasons methane is an interesting alternative to hydrogen, even though the oxygen/methane combination

yields lower specific impulse. There are also other aspect for preferring methane among all hydrocarbons. For instance, methane yields less soot and coke deposition in the thrust chamber and inside the cooling channels and a higher coking temperature. In addition, the combination oxygen/methane is cleaner than other storable propellants which, in general, are toxic and need specific safety procedures for their handling during on ground and on board operations. Indeed, methane and more in general hydrocarbons are referred to as 'green propellants'. This is one of the aspects that make methane well suited for reusable engines.
Because of its interesting performance, many international research programs involve oxygen/methane propellant combination. The Future Launcher Preparatory Program (FLPP), supported by ESA, the ASI's LYRA Program for the evolution of the Vega launcher, the HYPROB Program, includes basic research and system and technology demonstrators of oxygen/methane liquid rocket engine. In USA in the last dacades, oxygen/methane propellant combination has been considered for low-cost small launchers and lunar or Mars missions (Space X project), considering that a possible future mission to Mars which has an atmosphere rich in CO_2, methane could be produced in-situ, thing that should allows a reduction of the mission cost. In Japan, JAXA is considering oxygen/methane to achieve diversity and flexibility for the next generation of space propulsion systems. In Germany, industries and research centers were involved in efforts to investigate key-enabling hydrocarbon technologies focusing on engine combustion devices.

1.1 LITERATURE REVIEW

The studies in field of reacting flows at high pressure in actual rocket engines are two different type: experimental and numerical. In following subsections we introduce the main research groups employed in experimental studies §1.1.1 and numerical §1.1.2, defining the main issues (Reactive flow at subcritical pressure and flame structure, cold and hot flow at subcritical, supercritical and transcritical pressure and mixing, LOX/hydrogen and LOX/methane and real fluids) pertaining to the propellants injected at high pressure.

1.1.1 *Experimental studies*

Experimental data are an essential requisite for CFD validation. However, producing experimental data is a long and costly process due to the difficulties to setup a laboratory reproducing realistic liquid

rocket engine conditions. The principal group leaders active in experimental investigations and some topics of our interest that have been investigated in the last years are:

- The group led by R.Santoro at Pennsylvania State University, mostly addressed to GOX-GH2 combustion;
- The group led by W.Mayer at DLR. Their efforts range from the visualization of supercritical mixing and combustion (also in collaboration with the Japanese Space Agency) to the acquisition of quantitative data for both mixing and burning under supercritical conditions.
- The group led by S.Candel at Ecole Centrale de Paris, which mostly focuses on supercritical combustion and especially on the stabilization mechanisms of the flame: how it is anchored, influence of the injector geometry and control of combustion instabilities.
- The group led by C.Segal at University of Florida, who recently investigated H2/Air and H2/LOX combustion in high pressure combustion chambers, in order to provide data for CFD validation.

Tables 1 and 2 offer an overview of the range of conditions investigated until today.

Reference	Dimensions (mm)	Recess	Chamber size	Chamber shape	Propellants	Measurements
Ferraro et al. (1996, 2002)	2.26-3.76-5.03	2.54	4.13	Round sq.	LOX/GH2	PDPA
Woodward et al. (2006)	4.39-5.16-6.32	No	8.07	Round sq.	LOX/GH2	HSPh, BL, Sh
Smith et al. (2002)	4.00-4.32-6.5	No	7.69	Round	LOX/GH2	CARS, OH Ch, Sh
Smith et al. (2002)	4.00-4.32-5.8	No	8.62	Round	LOX/GH2	CARS, OH Ch, Sh
Smith et al. (2004)	N/A	No	N/A	Round	LOX/GH2	OH Ch, Sh, BL, HSPh, H_2O Ch
Candel et al. (1998)	5.00-5.60-12.2	No	4.1	Square	LOX/GH2	BL, LLS, CARS, PLIF, OH^* Ch
Thomas & Zurbach (2001)	5.00-5.60-10.0	No	5	Square	LOX/GH2	
Singla et al. (2006)	5.00-5.60-10.0	No	5	Square	LOX/GH2	Sp, OH^* Ch, OH PLIF
Habiballah et al. (2006)	5.00-5.60-10.0	No	5	Square	LOX/GH2	HSPh, Sh, BL, CARS, PDA
Ivancic & Mayer (2002), Mayer et al. (2001)	4.00-4.60-6.50	No	7.69	Round	LOX/GH2	Sh, OH Ch, H2O Ch

Table 1: Review of coaxial injector hot-fire investigations. Reprinted from Cutrone [19].

Reactive flow at subcritical pressure: flame structure

The first experimental studies of flame patterns for rocket conditions were at subcritical pressures, with coaxial injectors fed with H2/LOx. The pioneering experimental works, "*Herding et al. 1996, Snyder et al. 1997, Herding et al. 1998*" (Ruiz [92]), determined some features of cryogenic propellant combustion. One of the most important features that has been discovered is the anchoring of the flame on the injector rim, independently of propellants operating conditions (H_2/O_2).

Reference	Pcc (MP)	Subcritical Injection Temperature (K)	Momentum ratio (MR)	Velocity ratio (VR)	$Re_o x$	We	mdoto
Ferraro et al. (1996, 2002)	22-55	N/A	2.54	10.4-30.1	$8\ 10^5$	$1\ 10^5$-110^6	0.113 for MR = 4.25
Woodward et al. (2006)	5.17	N/A	22	70	N/A	N/A	0.2118 for MR = 4.67
Woodward et al. (2006)	5.17	N/A	50	107	N/A	N/A	0.139 for MR=3.065
Woodward et al. (2006)	6.55	N/A	50	95	N/A	N/A	0.139 for MR=2.744
Smith et al. (2002)	5.94	Yes (115.5)	3.8	12.1	N/A	Supercritical	0.29 for MR=4.83
Smith et al. (2002)	6.31	Yes (95.7)	1.73	11.5	N/A	Supercritical	0.30 for MR=3.75
Smith et al. (2004)	5.2-6.0	Yes (110-130)	0.2-20	6-70	N/A	Supercritical	N/A
Smith et al. (2004)	4.9-5.1	Yes (110-130)	0.09-12	3-40	N/A	N/A	N/A
Smith et al. (2004)	3.9-4.1	Yes (110-130)	0.08-12	3-35	N/A	N/A	N/A
Candel et al. (1998)	1.0	(89)	14.5	138	N/A	$2.82\ 10^4$	0.05 for MR=2.11
Candel et al. (1998)	1.0	(89)	6.55	92.8	N/A	$1.26\ 10^4$	0.05 for MR=3.16
Thomas & Zurbach (2001)	6.0	(83)	4.48	30.7	$1.04\ 10^5$	Supercritical	0.105 for MR=2.5
Singla et al. (2006)	3.6	Yes (80)	0.645	15.3	N/A	N/A	0.065 for MR=8.66
Singla et al. (2006)	6.3	Yes (80)	8.91	45	N/A	Supercritical	0.092 for MR=1.84
Habiballah et al. (2006)	6.0	Yes (83)	16.1	58.9	N/A	Supercritical	0.100 for MR=1.33
Ivancic & Mayer (2002), Mayer et al. (2001)	6.0	Yes (127)	1.88	12.4	N/A	Supercritical	0.30 for MR=5

Table 2: Review of LOX/GH2 coaxial injector hot-fire investigations. Flow conditions. Reprinted from Cutrone [19].

They used advanced optical diagnostics, $OH^\star$ (a suitable flame indicator since it is an intermediate species), together with Planar Laser Induced Fluorescence (PLIF): the $OH^\star$ technique, use the physical principle that the flame emits light that is composed of wavelengths representative of the local gas composition and the PLIF technique, a laser sheet excites an intermediate species (OH for instance) that emits light to relax towards unexcited state. Herding in "*Herding et al. 1998*" (Ruiz [92]) used the Abel transform, a technique that was first use to retrieve a cut through a time-averaged $OH^\star$ signal, with the assumption of axi-symmetry. The Abel transform was used in experimental studies of high-pressure reacting flows and monitors the effects of operating conditions and geometry of injectors on the flame pattern (Juniper et al. [40] and Singla et al. [96]).

Cold flow at subcritical, supercritical and transcritical pressure: injection and mixing

The study of atomization characteristics of jets inside LREs at subcritical and supercritical conditions can be realized using an alternative species for the study of the characteristics of atomization, e.i. an inert specie (nitrogen) that bears similar characteristics to oxygen (Oschwald et al. [78]). Chehroudi et al. ([13], [10]) studied the injection of liquid nitrogen initially at a subcritical temperature into an environment at a fixed supercritical temperature and at various pressures ranging from sub to supercritical values. The jet exhibits two behaviours: liquid-jet like and gas-jet like, depending on the values of surface tension and heat of vaporization. At subcritical pressures, comparison of shadowgraph measurements show that the jets appear like a liquid spray. As pressure is increased beyond the injected fluid critical pressure, the jet structure changes and the cryogenic jet has the appearance of turbulent gaseous jets. Raman scattering measurements of the density have been used to confirm the earlier shad-

owgraph measurements. A good agreement is realized between the growth rate measurements derived from the Raman measurements at twice the FWHM distance and growth rate derived from the shadowgraph measurements. At subcritical conditions, the joint action of aerodynamic forces and surface tension, determine the formation of ligaments and droplets at the surface of liquid jets. The droplets are a consequence of the competition between inertia forces and surface tension, which promotes disturbances growth (Ghafourian et al.[24]). At supercritical conditions, surface tension vanishes and droplets are do not exhibited on the surface of jets. Instead, in a transcritical injection it can be observed a diffusive interface between dense and light fluid. Chehroudi and Talley [12] tested the influence of waves on the jet at sub and supercritical conditions when the inertial forces increase. At the lowest chamber pressure tested (at subcritical conditions), the jet is influenced by the waves and acoustic field but at a supercritical chamber pressure the effects of the acoustic field on the jet becomes imperceptible. Mayer et al. [62] carried out several testing conditions considered pressures different pressure conditions from 4 to 6 MPa with two velocities and injection temperatures. He observed that the mixing was conditioned to the large-scale vortices within the shear-layer and he measured the length scales quantitatively based itself on the flashlight photography and high-speed cinematography. The numerical results were in agreement with density, length scales and jet spreading angles obtained from Raman and shadowgraph images quantitatively, but they do not an agreement with the angles obtained from FWHM, also multiplying the FWHM values by a factor of 2, do not prove to be very accurate when applied to the numerical results.

Reactive flow at subcritical, supercritical and transcritical pressure: flame structure

Mayer and Tamura [61] employed liquid oxygen and gaseous hydrogen in the experiments at subcritical pressure to study injection, ignition and steady-state combustion. They focused their activities on spray atomization: the cold-flow exhibits a spray atomization behavior at subcritical pressures, whereas a turbulent mixing behavior of a gas-gas type it would result at supercritical pressure and the reactive flow shows a flame always attached instantaneously to the LOX post. The researchers demonstrated that the LOX post do not improve the atomization but is decisive for the stability of the combustion process. Another important work on high-pressure combustion was conducted by Mayer et al. [59]. This work has highlighted the effect of pressure on the atomization and mixing of cryogenic propellants. The flow visualization was achieved by shadowgraph

imaging. The flame appears always attached instantaneously to the LOX post after ignition this suggested that a well-mixed flame with strong radiation was anchored in an intensive recirculation zone. A LOX post wake flame and its interaction with the H_2/O_2 shear-layer were clearly observed. Mayer et al. [63] showed and analyzed the flow and flame transients during engine ignition. They exhibited the effect of heat flux and surrounding temperature on mixing behavior near and above the critical pressure. Under cold-flow conditions, very fine liquid oxygen droplets are visible, which are accelerated by aerodynamic forces from the fast flowing hydrogen. After ignition, only ligaments were visible. They also measured and evaluated the absolute flame propagation speed. Ivancic and Mayer [37] measured, experimentally and numerically, the length and time scales of turbulent reacting flow for a coaxial injector. It was verified by numerical investigation that the Kolmogorov length scale increase downstream. The length scales are related to the structures present within the reactive shear-layer. The interaction mechanism between turbulence and chemistry in the reactive shear-layer were analyzed measuring of the time scales of turbulent mixing and combustion processes. From the comparison of the speed of the mixing process with the speed of the chemistry, one can deduce the turbulent combustion regime at a local position. Candel et al. [9] performed cryogenic combustion experiments at high pressures on the Mascotte facility for gas-liquid momentum flux ratio with a large range of value. They used Optical Emission Spectroscopic (OES) technique to examine the LOX jet and the flame and the mean flame structure is extracted by taking the Abel transformation of average emission images. Their results indicated that the rate of combustion is vaporization-limited when the pressure is below the critical pressure and is mixing-limited when the pressure is above the critical pressure denoting the importance of mixing for rocket combustion chambers designed.

Singla et al. [96] investigated high pressure combustion of LOX and methane for two cases: subcritical LOX injection and supercritical methane injection, and transcritical LOX/methane injection. In the case where both reactants are initially transcritical a double flame front appears in the doubly transcritical injection situation and the experimental results confirmed two regions of emission where light radiation originates from $OH^\star$ and $CH^\star$ radicals. Two reaction layers exist.

The pioneering experimental work on the flame stabilization was Kendrick (Kendrick et al. [44]). They modeled scale experiments where a single jet-flame formed by a coaxial injector was fed by LOX and gaseous hydrogen (GH2) analyzing by imaging the light emitted by OH radicals: the resulting image was treated by numerical tomog-

raphy (based on the Abel transform). The modifications in the near flame structure due to the LOX tube recess were analysed, and one of these showed that the flame is stabilized inside the injector when the LOX tube is recessed. Consequently the flame expansion angle is augmented, the thickness of the flame brush and the size of the volume where reaction takes place is enhanced. The hot gases production implies the hydrogen stream acceleration and an increased of momentum flux ratio J.

LOX/hydrogen and LOX/methane

Although LOX/hydrogen rocket engines have been operated relatively safely for the past several years, the processes that control combustion are still not well understood. The propellant combination LOX/hydrogen has been investigated by several research groups, but only few experimental data are available for the combination LOX/methane at high-pressure conditions. Lux et al. [57] realized the first experimental investigations with an application of optical diagnostics of LOX/methane combustion at elevated pressures. These investigations have been performed using an additional methane fluid system implemented at the European Research and Test Facility P8.

Yang et al. [121] comparing the LOX/hydrogen and LOX/methane, observed significant differences of the sprays and flames caused by Weber number and momentum flux ratio. For hot fire tests LOX/methane showed shorter liquid oxygen core length, more discernible droplets, and larger spray dispersion at similar injection Weber (influences secondary atomization and flame angles) and J numbers (governs the primary breakup and determines the liquid core length). When LOX/methane flames are anchored, exhibit a similar flame angles as anchored LOX/hydrogen flames. The authors deducted that at identical injection conditions of Weber number and momentum flux ratio, the flame stabilization mechanisms may be different for different fuels and might be different the injector designs. In a following analysis Yang et al. [122] observed: the dependence of intact core length for LOX/methane sprays to scale with J^n and the dependence of the intact core length from the LOX post thickness. These differences could be explained by an effect of the We-number. In addiction the LOX/hydrogen flames have always been found attached to the injector whereas rather all LOX/methane flames where detached, at similar injection conditions. Lux et Haidn [56] observed for LOX/methane and LOX/hydrogen of both high-pressure cold flow experiments and LOX/hydrogen combustion have shown significant disparities in the atomization processes at sub, near, and supercritical injection conditions (Mayer and Smith [60]). They detected, by an optically accessible subscale combustion chamber, OH and CH

emission in the near injector region. In similar operating conditions the flame emission spectra of methane are very similar to those from high pressure LOX/hydrogen combustion studies. Using the Abel transform it can show a reacting shear-layer between the LOX and the gaseous methane, which continuously grows with increasing distance from the injector face. The authors showed that near injector flame anchoring and the flame emission further downstream are similar to the characteristics for LOX/hydrogen and LOX/methane. With the operating conditions presented, the reacting shear layer of the LOX/methane flame seems to be slightly thicker than in comparable LOX/hydrogen flames.

More experimentally data are necessary for the validation of numerical tools.

1.1.2 *Numerical studies*

In the last decades several authors developed numerical methodologies to model the mixing and reactive flow at high pressure in supercritcal and transcritical conditions. The main research groups active in numerical investigations of high pressure (supercritical) cryogenic combustion and the main topics debated are the following:

- The group led by S. Candel, at Laboratoire EM2C, CNRS and Ecole Centrale Paris. This group uses LES code (AVBP) adapted to supercritical fluids through the implementation of real gas equations of state. Attention is devoted to the crossing of critical conditions where extremely non-linear thermodynamics exists which may cause severe and unwanted pressure oscillations. The group uses a relatively simple subgrid turbulent combustion model which uses the flamelet approach, i.e. a convolution of a flame structure with a presumed pdf established locally on the basis of transported pdf moments of the mixture faction. The flame structure used is that emerging from the simple Burke-Schumann limit of 'mixed is burnt'. See e.g. [94].

- The group led by X. Petit, G. Ribert, at CORIA Lab. They developed a new version of the SiTCom solver called SiTCom-B (Simulation of Turbulent Combustion with Billions of points) which is mainly designed to perform DNS and highly resolved LES. It is a finite-volume code that solves the unsteady compressible reacting Navier-Stokes equations system on Cartesian meshes. A fourth-order central difference schemes plus artificial dissipation term of the second and fourth order, Runge-Kutta time-discretization (third and fourth orders), full multispecies formulation, realistic thermodynamic (CHEMKIN), realistic transport

properties, complex chemistry, tabulated chemistry, ideal or real gas EoS, NSCBC and immersed boundary method. SiTCom-B does not use any preconditioning scheme and WENO method.

- The group formed by V. Yang and J. Oefelein. Although the two authors work independently they have closely collaborated in the past. They both adopt a similar approach (LES based), which uses an implicit formulation with a dual-time step scheme and a generalized all-Mach-number preconditioning methodology. Their code is a robust computational scheme which can effectively handle the numerical stiffness caused by rapid flow property variations and wide disparities of the characteristic time and length scales involved in cryogenic reacting flows. This group has used various combustion models although some results have been achieved without modeling (i.e. laminar combustion). See e.g. [130, 71]

- Other groups have tackled the complex problem of simulating supercritical reacting flows. One example is the work by Kim et al. [48], where a URANS approach is coupled with real-fluid equations of state and real-fluid thermophysical and transport models. Interaction of combustion and turbulence is approached via flamelet libraries aptly modified to take real-fluid effects into account.

Cold flow at supercritical and transcritical pressure: injection, mixing and combustion

Modeling high-pressure mixing and combustion processes in liquid rocket engines, involves a variety of challenges: closure problems and several problems caused by the introduction of thermodynamic non idealities and transport anomalies. Oefelein and Yang [73] approached the problems focusing on model performance and accuracy requirements, Lagrangian-Eulerian treatments of transcritical spray dynamics, and pure Eulerian treatments of transcritical and supercritical mixing and combustion processes. The results presented an highlighted effect of pressure on near-critical mixing and combustion processes. Also an effect of the density gradient was exhibited and a diminished mass diffusion rates that accompany the liquid-like behavior of near-critical fluids, was demonstrated. The resolved-scale chemical source terms have been approximated neglecting the effects of *sgs* fluctuations and using resolved field quantities only; this implies an assumption that valid only for cases in which reactions are slow relative to the time scales associated with the decay of the species fluctuations. Bellan [5], Miller et al. [66] and Yang [123] were among the first researchers that modeled and approached numerically the mixing layer and the combustion of supercritical fluid.

Miller et al. [66] and Okong'o et al. [76] studied the turbulent mixing phenomenon at supercritical conditions by means of a DNS of heptane/nitrogen and hydrogen/oxygen non-reacting mixing layers.

The supercritical temporal mixing layers were examined and the researchers identified a secondary mechanism (the primary one started the initial density stratification) that could hinder transition to turbulence. A very sharp local density gradients inducing an additional stratification were identified. These high density gradients may suppress transition since density interfaces and seem to hinder entrainment and transfer of energy from large to small scale eddies. The suppression is amplified by the effect of mixture non-ideality which reduces molecular mixing. A different roles of the two forms of thermal diffusion factors was underlined: one promotes density gradients, shear and vorticity, and the other promotes diffusional mixing. Meng and Yang [64] proposed an unified thermodynamic model that may cover from compressed liquid to dilute gas. They used a modified SKR equation of state and a preconditioned system of conservation equations. Their model showed the results in good agreement with the experimental data (droplet lifetime) for the case n-heptane droplet vaporization in quiescent nitrogen environments. Their numerical scheme has demonstrated its ability to capture the droplet dynamics and flow evolution.

Zong and Yang [129] developed a model that use the primitive variables pressure-temperature, in order to avoid the iterative procedure that determined the fluid temperature from the specific enthalpy. They analysed a near-field flow and they studied the flame dynamics of an LOX/methane shear-coaxial injector. Their studies established a treatment of real-fluid thermodynamics based on a preconditioning scheme and derived the numerical properties from fundamental thermodynamics theories using on the concepts of partial-mass and partial-density properties.

DNS studies constituted databases that were used to determine the validity of closure terms for Large Eddy Simulation (LES). In addition Zong and Yang [130], used a LES with a direct closure model for the turbulent combustion. Zong et al. [126] conducted an analysis to investigate the combustion of LOX and methane in the vicinity of a splitter plate under supercritical conditions.

The formulation is based on a large-eddy-simulation technique and three different models of turbulence-chemistry interactions were implemented considering the comparison among the flame and turbulence length and time scale. The authors used a laminar flamelet approach that accommodates a detailed LOX/methane reaction mechanism using the flamelet approach. In this way they simulated the LOX/methane flame in order to remain the turbulent time-scale at

least one order of magnitude greater than the chemical time-scale because the combustion zone is thinner than the turbulent eddies.

Okong'o and Bellan [75] conducted a temporal stability analysis for conservation equations describing a temporal mixing layer at all pressures, including supercritical ones. Their DNS used a conservation equations modified. The difference in the conservation equations was that in addition to Fick and Fourier transport coefficients, there is an other transport coefficient, the thermal diffusion factor, which couples molar and heat fluxes. The coupling occurs through the Soret term in the species equations and the Dufour term in the energy equation.

Oefelein [71] used LES and DNS in order to characterize the multicomponent diffusion processes in the flame zone of a shear-coaxial injector. Results indicated a real-gas effects in the colder mixing regions and relatively small cross-diffusion ones (Dufour and Soret effects) associated with the mass and energy transports in high shear regions just downstream of the liquid oxygen post. The ordinary diffusion terms dominates in the vicinity of the LOX/hydrogen interface. Oefelein underlined that preferential diffusion effects are important in flame zone and the local thermophysical interactions produce a strong counter-recirculating zone of hot fuel-rich products in the vicinity of the injector tip: this zone provides the primary flame-holding mechanism.

Zong and Yang [130] underlined the injector flow field characteristics by the evolution of the three mixing layers caused by the edges of the two concentric tubes of the injector. A diffusion-dominated flame is anchored in the wake of the LOX post and propagates downstream along the boundary of the oxygen stream because of the oxygen stream has a strong inertia whereas the methane stream exhibits a light density. As a consequence of the strong inertia of the oxygen stream and light density of methane, a diffusion dominated flame is anchored in the wake of the LOX post and propagates downstream along the boundary of the oxygen stream.

RANS simulations of the cryogenic round jet experiments were also conducted in Cutrone [19], Kim et al. ([46],[45], [47]), and were able to qualitatively reproduce the mean density profiles from the experiment.

LOX/hydrogen and LOX/methane

Oefelein [71] relied on LES and DNS the ordinary diffusion terms that dominate in the vicinity of the LOX-H2 interface. Zong et al. [126] conducted an analysis to investigate the combustion of LOX and methane in the vicinity of a splitter plate under supercritical conditions and used a laminar flamelet approach.

Several numerical studies (Zong and Yang [130]) about shear coaxial injection and combustion of LOX/hydrogen underlined that a strong recirculating flow acts as a hot-product pool providing the energy to ignite incoming propellants. In LOX/methane combustion case, unlike LOX/hydrogen combustion case, the LOX/methane flame is anchored between two counter-rotating wake recirculation zones contrary to the flame of LOX/hydrogen that is anchored very close to the LOX jet boundary due to the high diffusivity of hydrogen and the strong inertia of the LOX jet. Candel et al. [94] realized a simulation of transcritical combustion. This is carried out using a LES (Large Eddy Simulation) approach and by taking into account the special behavior of fluids injected at high pressure (above critical) but below critical temperature. The combustion model was an infinitely fast combustion. The model calculated a transcritical liquid oxygen/supercritical methane flame. The authors would see if structures of LOX/hydrogen flames are suitably retrieved and if geometrical effects like those of a recess of the LOX injection post are recovered.

Ribert et al. [91] and Pons [86] showed for LOx/GH2 and LOx/GCH4 that the heat release rate per unit flame surface increases with the square root of strain rate and pressure, while the extinction strain rate evolves quasi-linearly with pressure, in addition it was shown that the transcritical flame structure is very similar to a supercritical flame structure. In particular, Ribert et al. [91] analysed undiluted Oxigen/hydrogen flames, considering over a broad range of pressures at both sub-critical and supercritical conditions and studying a laminar counterflow diffusion flames that has been developed for general fluids by a model that incorporates fundamental thermodynamics and transport theories. Ponset al. [86] investigated on effects of pressure on the structure and heat release rate of non-premixed strained flames. They studied the limit solutions of fast chemistry that indicate the consumption and showed that the heat release rates vary like the square root of pressure, with little influence of finite-rate chemistry effects.

Real fluids

The experiments of Baron Charles Cagniard de la Tour (1822) was the first where it is possible that above a certain temperature T_c and pressure P_c, the discontinuity between gaseous and liquid phases disappears.

Harstad et al. [33] proposed a procedure that allows for the use of computational efficient EOS calculations for high pressure gas-turbine and rocket engines. The form was based on the PR EOS and was used for all substances, this determined that conventional mixing rules are readily applied to all the set of components.

Bellan and Okong'o ([74], [75]) were the first that studied the numerical problem considering the effects on equations and boundary conditions of real fluids taking into account the governing equations account for departures from the perfect gas equation of state, for mixture non-ideality and for thermal diffusion effects. They used the boundary conditions based on characteristic wave analysis derived for multicomponent flows in case of real gas equations of state. Ruiz [92] and Schmitt [95] used the PR EOS to model the real gas. Two modifications on the standard low pressure Navier-Stokes equations, essentials in description of supercritical fluid dynamics, were accomplished. One modification is about the EOS, considering the real effects and a second modification is about the transport models for mass and heat transfers. It is important that these models (EOS and transport) are made consistent through the appropriate thermodynamic relations.
Giovangigli et al. ([25], [26]) derived a detailed flame model for a high pressure, from macroscopic and molecular theories, showing that the corresponding entropy production was non negative and considering the SRK EOS. Giovangigli et al. also underlined the rules of non idealities in the EOS and in the transport fluxes that have a influence on the cold zone of the flame. The non idealities in the chemical production rates may also strongly influence flame structures at very high pressures. Also Terashima and Koshi [104] used a SRK EOS to take into consideration the real effect of gases. The researches observed that a fully conservative (FC) formulation of the governing equations leads to spurious numerical oscillations because of the peculiarity of supercritical flows (complicated forms of the equation of state), even with single species flows. Then they decided to use a method with a pressure evolution equations. In this way they tried to obtain a pressure equilibrium and the consistent numerical diffusion terms for the velocity equilibrium at the fluid interfaces. The numerical work consisted in one-dimensional advection problem and a two-dimensional problem. However, the poor energy conservation property is exhibited. Mayer [59] studied the mixing process in cold-flow injection tests under representative conditions (real-gas effects at supercritical pressures and high Weber and Reynolds numbers) oxygen (LOX) and hydrogen were simulated by liquid nitrogen LN2, and hydrogen or helium, respectively.

Meng and Yang [64] analysis was based on a modified SRK EOS to derive all of the thermodynamic properties for the numerical scheme. They tried to develop a rule of general fluid thermodynamics to treat fluid flows over the entire range of their thermodynamic states (from compressed liquids to dilute gases) using for the numerical resolution of problem a preconditioning scheme.

Petite et al. [82] with the SiT-ComB code include the possibility to reproduce a real-gas configurations such as injection of supercritical fluid. In their study (Petite et al. [82]) used SRK and PR EOS with appropriated thermodynamics relations and validated against NIST data and simulation of Mayer et al.

Flame stabilization

One of the first numerical works focused on the stabilization point of a cryogenic LOx/GH2 flame was ones by Oefelein and Yang[73]. Their work demonstrated the dominating effect of the density gradient and the diminishing mass diffusion rates that accompany the liquid-like behavior of near-critical fluids and highlight the effect of pressure on near-critical mixing and combustion processes. After few years also Juniper et al. [40], Zong and Yang [130] investigated on the stabilization of the flame tip at the injector rim. Zong and Yang [130] studied a near-field region of a coaxial injector fed in with transcritical LOx/GCH4. The large-scale vortices emerging from the outer rim of the LOX post facilitate the mixing between the incoming methane stream and hot products. The effects of the momentum-flux ratio of the two streams are also examined. A higher momentum methane stream enhances mixing and shortens the potential cores of both the LOX and methane jets.

1.2 THESIS SCOPE AND METHODOLOGICAL APPROACH

The aim of this Thesis is focused on understanding of combustion physics in combustion chamber and the evaluation of the heat loads on the chamber walls and on the plate by employment of the Computational Fluid Dynamic (CFD). To ensure an accurate prediction of heat fluxes and flame position, the simulations have been designed so as to replicate the extreme operative conditions that participate in combustion chamber at high pressure and high temperature. CFD has the potential to improve the historical rocket injector design process by evaluating the sensitivity of performance, the details of the injector geometry and the key operational parameters. The choice of CFD implies a tests reduction, the design optimization and consequently a costs reduction but the current CFD production capability must be improved, we still need of more experimental data for numerical tools validation.

To pursue our intents (evaluation of the heat loads on the chamber walls) we define the key points and the quantities of our interest linked to them:

- Density, volumes, compressibility variables, temperature and velocity trends, and properties (density and velocity) in the axial

and radial direction: EOSs, high density gradients and a possible two-phase flow problem.

- Temperature, pressure and HCO mass fraction variables: evaluation of flame length and evaluation of combustion efficiency.
- Heat flux evaluation ($\dot{Q}$) and y^+: wall mesh refinement
- Flame anchoring and spread angle: analysis post tip refinement

To understand the physical processes in a combustion chamber and evaluate the heat loads, we **start** from our analysis of a simple model made of a nitrogen jet in nitrogen environment using a model in 3 dimensions. We use this way to understand and to define some critical issues about the numerical approach. We verify the possible limits of our model or/and software and compare the best numerical method that we can use. The **second step** increases the problem complexity: we inject the propellants LOX/methane in an nitrogen environment and after we study the flow and flame behaviour using the numerical method tested in the previous simulations. An **intermediate step** is the 2D axi-symmetric model when we reproduce a reactive flow in a combustion chamber mono-injector and study the mesh resolution at wall in order to evaluate the heat flux. The **last step**, the fourth, is the reproduction of a circular sector (60^o) of a combustion chamber together the previous step that is a part of HYPROB project.
The project conditions and the experimental models (a Sub Scale Bread Board (SSBB) with a single injector, and a DEMOnstrator (DEMO) engine with multiple injectors) used for the CFD simulations in this work, have been provided by C.I.R.A, that sponsored a part of this Thesis project, and by "Agenzia Spaziale Italiana" (A.S.I), in the effort of at developing a national expertise in liquid propulsion employing methane as fuel of choice (LOX/CH_4). The operative conditions of both the SSBB and the DEMO configurations involved a supercritical environment in combustion chamber with methane injected in supercritical state and oxygen injected in transcritical state. A delicate phase is the oxygen transition from transcritical to supercritical state, which occurs in the chamber when the temperature in the chamber exceeds the critical value for oxygen. Other difficulties emerge when the oxygen moves from the transcritical to subcritical regime. In fact, oxygen in the subcritical regime should be modeled as a two-phase flow but in this way the complexity of the flow solver is considerably increased[1]. The simulations on the DEMO configuration have

1 It was later decided to artificially circumvent this problem by preventing the flow to access two-phase regions. This approach allows the numerical integration to proceed, but it is not a correct modeling of the actual flow conditions.

been carried out on a 3D wedge 60^o-wide, which include three injectors. Both SSBB and DEMO configurations are equipped with a convergent-divergent nozzle.

The Thesis can be divided in **four parts** and it is organised as follows:

In **Chapter 2** we present an overview of the main phenomenological aspects of subcritical, transcritical, supercritical fluids, and cryogenic jet flames.

Chapter 3 introduces the concepts of ideal gas and real fluid. Section §3.1 defines the thermodynamic properties of the fluids. In sections §3.2 and §3.3 are explained, respectively, the concepts of Equations of State for an ideal gas pure fluid or mixture and the EOS for several kinds of cubic Equations of State (Van der Waals, Peng-Robinson and Soave-Redlich-Kwong) and non-cubic EOS (as GERG equation). In sections §3.3.1 and §3.3.2 we provide the definitions of Compressibility factor and Departure and Residual function. Subsection §3.3.5 defines the real fluid mixture for the three cubic Equations of State and in §3.3.6 the GERG equation is discussed.

Chapter 5 discusses the physical processes of injection and how to improve the design of flow injectors. Section §5.1 illustrates the main physical processes of injection. The performance of a single injector with or without recess is illustrated in section §5.2.

Chapter 4 summarises the flow equation model and the chemistry model: together with the methodology to generate t he computational mesh using a Conformal Mapping approach.

Chapter 6 *(first part)* we discusse our numerical analyses. The chapter is divided in three sections: (i) results for two simple cases taken by Schmitt et al. [95] and are discussed in section §6.2; (ii) section §6.4 illustrates the results obtained for a reactive flow test case; (iii) section §6.4.5 reports simulation of the reactive flow in a combustion chamber with nozzle.

Chapter 7 *(second, third and fourth parts)* presents an overview of the CFD runs realised on the SSBB and DEMO. Sections §7.2.1, § 7.2.2, §7.2.3 *(second part)* report the two-dimensional URANS runs of the Subscale Breadboard SSBB Assembly. Section §7.3 *(fourth part)* reports the 3-dimensional URANS runs of the DEMO assembly. In addition, the latter section, includes a 2-dimensional high resolution LES simulation *(third part)* of the injector area which specifically addresses the study of the flame anchoring mechanism.

In the section §7.3.2 , we present an extended study the CFD simulation of the 3-dimensional DEMO assembly, for which full azimuthal anchoring of the diffusive flames was artificially achieved for each injector, and section §7.5, which describes the second part of new in-house mesh generation tool tailored to producing a discretisation of

the volume customized for a generic multi-injector combustion chamber.

Chapter 8 summarises the main conclusions drawn from all the CFD analyses and some of the lessons learnt from the simulation campaigns.

The thesis includes a supplementary material organised in appendices as follows: Appendix §A illustrates the meaning of Pseudo-Boiling temperature; Appendices §B and §C.2.2 describe the correspondent state principle to derive thermodynamic and transport properties of mixtures; Appendix §D describes the thickened flame model used by Poinsot (Poinsot et al. [53]) and adopted in CFD++.

A list of relevant references is included at the end of this thesis.

All the simulation runs carried in this work have been performed using Metacomp CFD++[2].

All the post-processing of the databases generated by CFD++ has been performed using TECPLOT[3].

The calculations involving the real gas EoS and the mesh generator have been carried out using Mathematica[4].

2 ©Metacomp Technologies, Inc. All Rights Reserved
3 ©Tecplot, Inc. All Rights Reserved
4 ©Wolfram Mathematica, Inc. All Rights Reserved

2

AN OVERVIEW OF SUPERCRITICAL REACTIVE FLOWS

Contents

OBJECTIVES OF CHAPTER

This Chapter reviews the main features of a real fluid jet in supercitical, transcritical and subcritical state. The flame jet structure is influenced by the injection conditions of the environment and of the fluid. In addition, the definitions of the principal parameters and nondimensional numbers used to characterise a fluid are presented.

2.1 MAIN PARAMETERS IN FLOW INJECTORS

The main parameters that characterise the co-axial injection of two streams of propellants (fuel (f) and oxidizer (o)) are:

- Stoichiometric mixture ratio, E_stoic:

$$E_{stoic} = \left(\frac{Y_f}{Y_o}\right)_{stoic} = \frac{\nu_f W_f}{\nu_o W_o} \tag{2.1.1}$$

  where W_f and W_o are the molecular weights of fuel and oxidizer, respectively, Y_f and Y_o are the mass fractions of fuel and oxidizer, respectively, ν_o and ν_f are the stoichiometric coefficients corresponding to fuel and oxidizer in a single step global

reaction:
$\nu_o F + \nu_f O \longrightarrow$ Products

- Mixture ratio, E, is the ratio of the mass flux of fuel and oxidizer injected in a combustion chamber:

$$E = \left(\frac{Y_f}{Y_o}\right) = \frac{\dot{m}_f}{\dot{m}_o} \tag{2.1.2}$$

In premixed gases, that are created by mixing a fuel stream (first stream) with an oxidizer stream (second stream), we have: a total mass flow rate of first stream, a fuel mass fraction and a total mass flow rate, an oxidizer mass fraction. Both streams can also contain other gases. After two streams are mixed at the combustor inlet, fuel (oxidizer) mass fractions is given by the ratio between the total mass flow rate in first stream (total mass flow rate in second stream) and the sum of total mass flow rate of first steam and total mass flow rate of second steam. We obtain the fuel mass fraction in the same way. At the end we have 2.1.2

- Equivalence ratio, ϕ:

$$\phi = sE = s\frac{\dot{m}_f}{\dot{m}_o} \tag{2.1.3}$$

with $s = \dfrac{1}{E_{stoic}}$.

When the mixture is stoichiometric, $\phi = 1$. When $\phi < 1$ the mixture is called lean and the oxidizer is in excess compared to fuel, if $\phi > 1$ the mixture is called rich and the fuel is in excess compared to oxidizer.

- Momentum flux ratio, J, is the ratio of the injected momentum flux of oxidizer and fuel inside a combustion chamber:

$$J = \frac{(\rho v^2)_f}{(\rho v^2)_o} \tag{2.1.4}$$

- Reynolds number (Re):

$$Re = \frac{\rho U_r d}{\mu} \tag{2.1.5}$$

- Damköhler number (Da):

$$Da = \frac{t_{flow}}{t_{chem}} \tag{2.1.6}$$

where t_{flow} is the flow time and the t_{chem} is chemical time

- Weber Numbers (We), and Ohnesorge Numbers (Oh):

$$We = \frac{\rho_a U_r^2 d_0}{\sigma}, \quad Oh = \frac{\mu_l}{\sqrt{\rho_a \sigma d_0}}, \tag{2.1.7}$$

where:

  - ρ_a =ambient density
  - U_r = jet ambient relative velocity
  - σ = surface tension
  - d_0 = jet diameter

The Oh number can be written as:

$$Oh = \frac{\sqrt{We}}{Re} \tag{2.1.8}$$

Ohnesorge developed identified different regimes of jet breakup by use of dimensional analysis (Ghafourian et al. [24]). The non dimensional numbers of Ohnesorge, Reynolds, Re, and Weber, We, identify different regimes of jet breakup, and have the following physical meanings: the Reynolds number represents the ratio of inertial to viscous forces, the Weber number represents the ratio of inertial to surface tensional forces, the Ohnesorge number, links viscous to inertial and surface tension force; the ratio of the square root of the We number and Re number tends to infinity when surface tension go to zero.

- Reduced temperature, T_r, and pressure, P_r:
the normalization of the temperature T and pressure P by the corresponding critical values, T_c and P_c, defines the reduced temperature and pressure:

$$T_r = \frac{T}{T_c} \quad and \quad P_r = \frac{P}{P_c} \tag{2.1.9}$$

- To compare the flow properties, ρ, T, u (density, temperature and velocity), in the radial direction we use dimensionless variables (see Mayer [62]). Non dimensional density, $\rho^\star$, non dimensional temperature $T^\star$ and non dimensional velocity $u^\star$, are introduced using the following expressions:

$$\rho^\star = (\rho - \rho_\infty)/(\rho_c - \rho_\infty) \tag{2.1.10}$$

where the subscript "c" define the centerline value at specified axial location and the subscript "∞" is for the chamber property away from the jet (Mayer [62]).

$$T^{\star} = (T\infty - T)/(T_{\infty} - T_c) \tag{2.1.11}$$

$$u^{\star} = u/u_c \tag{2.1.12}$$

By definitions "$\star$", non dimensional density, temperature and velocity take values among smaller or equal one: the profiles are 1.0 at the centerline and zero outside the jet itself.

- To compare the flow properties in the axial direction, we use a different non-dimensionalization, so that the density, the temperature and the velocity are called: ρ^{+}, T^{+} and u^{+}:

$$\rho^{+} = (\rho - \rho_{\infty})/(\rho_{inj} - \rho_{\infty}) \tag{2.1.13}$$

where the subscript "inj" define the centerline value at the injector and the subscript "∞" is for the chamber property away from the jet (Mayer [62]). By definitions "+", non dimensional density, temperature and velocity take values among smaller or equal one: the profiles are 1.0 at the injection and near zero far away from injection: in this case the injection values are more important than local centerline values.

$$T^{+} = (T\infty - T)/(T_{\infty} - T_{inj}) \tag{2.1.14}$$

$$u^{+} = u/u_{inj} \tag{2.1.15}$$

2.2 SUBCRITICAL, TRANSCRITICAL, AND SUPERCRITICAL FLUIDS

In this Section, we define the injection regimes of subcritical, transcritical, and supercritical fluids. The injected liquid, at higher pressures, may find itself near critical values (transcritical regime) or above critical values (supercritical regime): a fluid injected at supercritical pressure and at subcritical temperature is in **transcritical conditions**, a fluid injected at supercritical pressure and at supercritical tempera-

ture is in **supercritical condition**. The critical pressures and temperatures for different substances that have been considered in this thesis are listed in Tab. 3 .

Critical Values					
Substances	N_2	He	CH_4	O_2	H_2
Pressure (MPa)	3.4	0.23	4.6	5.04	1.28
Temperature (K)	126.2	5.2	190.6	154.6	32.94

Table 3: Critical properties.

2.2.1 *Supercritical fluids*

The supercritical regime is the locus of fluids states whose temperature and pressure both exceeds their critical values. In the supercritical regime, the interactions between gas particles become more important with a possible formation of small short-lived clusters of particles, due to cooperative interactions. With higher pressures, a change of phase or phase transition occurs in which the gas becomes a liquid. The macroscopic manifestation of a gas-to-liquid phase transition is a discontinuous change in the volume. At the microscopic level, the interparticle interactions cause the gas particles to condense. Further compression leads to the formation of locally ordered structures that resemble a solid substance. As the compression continues, a liquid-to-solid phase transition occurs. Such a transition is accompanied by a discontinuous change in the density, although the change is not as dramatic as in the gas-to-liquid case. A typical phase diagram for a single component substance is shown in fig.2.2.1. In the phase diagram, the lines separating different phases are called coexistence curves: the melting curve (L2) between the liquid and solid phases, the sublimation curve (L1) between the solid and gas phases, and the boiling curve (L3) between the liquid and gas phases. The point at which all three curves meet is called "triple point". Where a constant temperature is assumed, the specific value of the temperature determines whether or not a gas to liquid phase transition can occur. If the temperature is too high, then the system cannot exists as a liquid at any pressure. The temperature at which a gas-liquid phase transition just starts is called the critical temperature, denoted as T_c.
Consider an isothermal line of the equation of state for a simple fluid, as shown in Fig. 2.2.2. For temperatures above T_c (critical temperature), a phase transition cannot occur, and the isothermal line is continuous. In the phase diagram, the region to the right of the critical point is known as the supercritical fluid region where the system

exhibits both gas-like and liquid-like properties. For temperatures below T_c, one observes a discontinuous change in the volume, signifying the transition from gas to liquid.

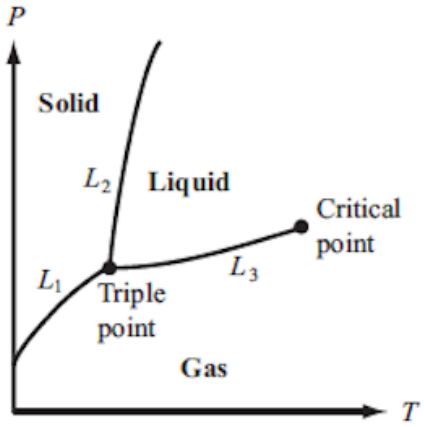

Figure 2.2.1: Phase diagram PT with triple and critical point. Reprinted from Tuckerman [110].

When a phase transition is characterized by a discontinuous change in an associated thermodynamic observable, the transition is referred to as a first-order phase transition. In Fig. 2.2.2, there is one point labeled C at which the phase transition is characterized by a continuous volume change. This point, which is an inflection point along the isothermal line, corresponds to the critical point on the phase diagram. The isothermal line that contains the point C is called the critical isothermal line. At this point, the phase transition that occurs is called second-order phase transition (Tuckerman [110]). A two-component system could have lines of second-order phase transitions, called critical lines; C is a point of zero curvature, meaning that $\frac{\partial P}{\partial \rho}$ and $\frac{\partial^2 P}{\partial \rho^2}$ both vanish at C.

2.2.2 *Transcritical fluids*

The transcritical regime is the locus of fluid states are at a temperature which is lower than the critical value and a pressure which exceeds the critical pressure. The transcritical regime is partitioned in two regions by the pseudo-boiling line. A fluid crossing the *pseudo-boiling* temperature is characterized by a change of thermophysical quantities (such as density or diffusion coefficients) that vary from liquid-like (for $T < T_{pb}$) to gas-like (for $T > T_{pb}$) values. Fig. 2.2.3 shows the transcritical range, where the pressure exceeds the critical pressure of oxygen ($P > P_{c_{O_2}} = 5.04$ MPa) and the temperature of the

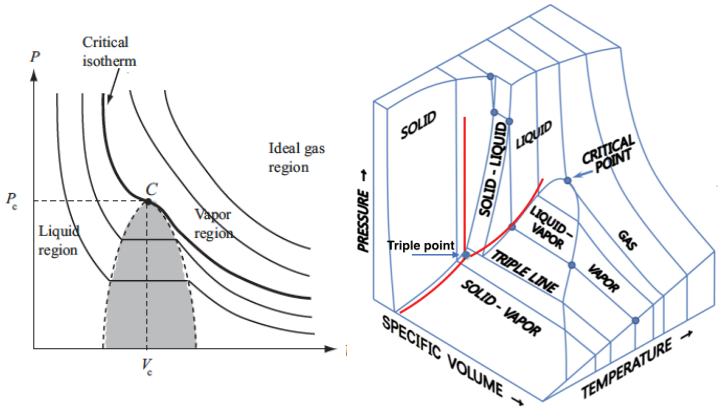

Figure 2.2.2: Phase diagram PV. Left: Equation of State of a simple, one-component fluid. C denote an inflection point. Reprinted from Tuckerman [110].

injected liquid oxygen is below its critical value ($T < T_{c_{O_2}} = 154$ K). The *'pseudo-boiling line'*, Oschwald et al. [79], can be defined as the locus at which the specific heat attains a maximum being the flow at a supercritical pressure. Because of the increase in specific heat experienced across the *'pseudo-boiling'* line, heat addition to jets injected at an initial temperature below the *'pseudo-boiling'* temperature mostly results in a volumetric change with a little increase in temperature, i.e., a *'pseudo-boiling process'*. We address the reader to Appendix A for further details on the pseudo-boiling temperature and related matter.

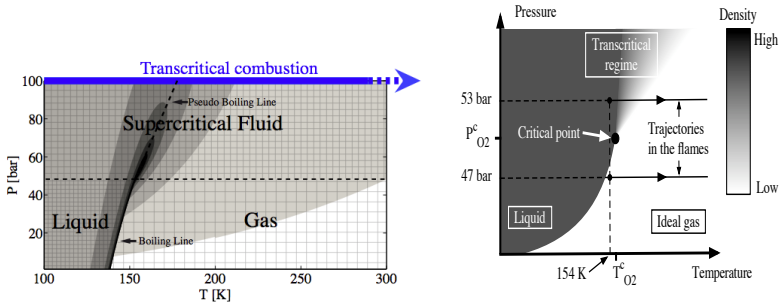

Figure 2.2.3: Phase diagram PT with pseudo boiling line. Left: reprinted from Ruiz [92]. Right: reprinted from Dahms et al. [20]

2.2.3 *Subcritical fluids*

The subcritical regime is the locus of fluid states where the thermophysical variables, in particular pressure and temperature, are below the critical point of a particular substance. At subcritical pressure, the

jet entering the chamber undergoes an atomization process characterized by the development of ligaments that detach from the jet surface, forming spherical droplets, which subsequently break up and vaporize.

2.3 SUBCRITICAL, TRANSCRITICAL, AND SUPERCRITICAL CRYOGENIC JETS

We illustrate qualitatively the subcritical, transcritical and supercritical jets referring to Mayer et Smith [60], Chehroudi et al. [13] that analyzed the flow characteristics of jets injected from subcritical to supercritical conditions (Figures 2.3.2, 2.3.4 and 2.3.5).

(a) Characteristics of subcritical injection

Chehroudi et al. [13] investigates a jet injected in an environment at subcritical and at supercritical pressure, using a high pressure chamber.

In subcritical conditions, the breakup and atomization of a liquid jet occur At lower subcritical chamber pressures, the jet features a *'liquid-like'* behavior characterized by the development of instabilities at the liquid/gas interface. The instabilities at the interface are amplified to form ligaments, which eventually break into droplets surrounding the jet. The creation of droplets is a consequence of the competition between inertia forces and surface tension, which promotes the growth of disturbances (Ghafourian et al.[24]) that play an important role in the atomization process.

Cold flow studies carried out by Mayer et al. [63] involved a jet of liquid nitrogen (LN2) injected in a nitrogen gaseous environment at different pressures and velocities (figures 2.3.1). At subcritical conditions, the jet flow exhibits a wavy surface, with droplets detachment. For enough high pressure and high relative velocities, a lower surface tension cause smaller jet surface structures and droplets, Mayer et Smith [60]. The breakup length describes the intact portion of jet and defines the **jet stability**, Ghafourian et al. [24]. Ghafourian considers that the intact portion of the jet terminates at the **jet breakup length**. He noted that by keeping all other parameters constant, the variation of the breakup length with jet velocity can be used to define various breakup regimes. Reitz and Bracco [88] show that for increasing jet velocities, the jet surface begins to break upstream the rupture of the jet core. This observation suggested to define two new charecteristc lengths: the first length related to the intact portion of the jet

surface (L_1), and the second related to the intact portion of the jet core (L_2). Furthermore, Reitz and Bracco [88], considering th Oh's number constant and Re's number increasing, identified the following breakup regimes:

- Rayleigh jet breakup ($L_1 = L_2$)
- First wind-induced breakup ($L_1 = L_2$)
- Second wind-induced breakup ($L_1 < L_2$)
- Atomization breakup ($L_1 \approx 0$ and $L_2 \neq 0$)

In the *Rayleigh jet breakup* regime, the surface tension force is the main responsible for breakup: the droplets are pinched off from the end of the jet with a diameter comparable to that of the jet. In this regime the relative jet velocity are small and the jet breakup length increases to increase the relative jet velocity (the relative jet velocity and the jet breakup length are proportional)
In the *First wind-induced breakup* regime, the aerodynamic forces also take part and the droplets that are pinched off the end of the jet are larger than those in the previous regime. In this regime the relative jet velocity are high and the jet breakup length decreases to increase the relative jet velocity.
In the *Second wind-induced breakup* regime, the droplets are produced by the unstable growth of short wavelength surface waves; in this case the droplets are smaller than the nozzle diameter.
In the *Atomization breakup* regime, the jet surface appears to break immediately at the nozzle exit and droplets are very small.
For of these considerations, Ghafourian et al. [24] proposed to classify the jet breakup in: "the low velocity breakup" and in "high velocity breakup". The low velocity breakup covers the range where surface tension is the dominant breakup mechanism and the high velocity covers the rest.
At high subcritical chamber pressures, the jet surface exhibits irregularities that amplify downstream, which can break up into irregularly shaped small entities at the jet surface.
When the pressure increases in the chamber, many small droplets on the jet surface are produced only in a narrow region below the critical pressure of the injected fluid.

The experiments by Mayer et al. [62] for even higher chamber pressures exhibited a sudden change in the jet appearance so that the flow resembles the one obtained by a turbulent gas jet injection.

(b) Characteristics of transcritical injection

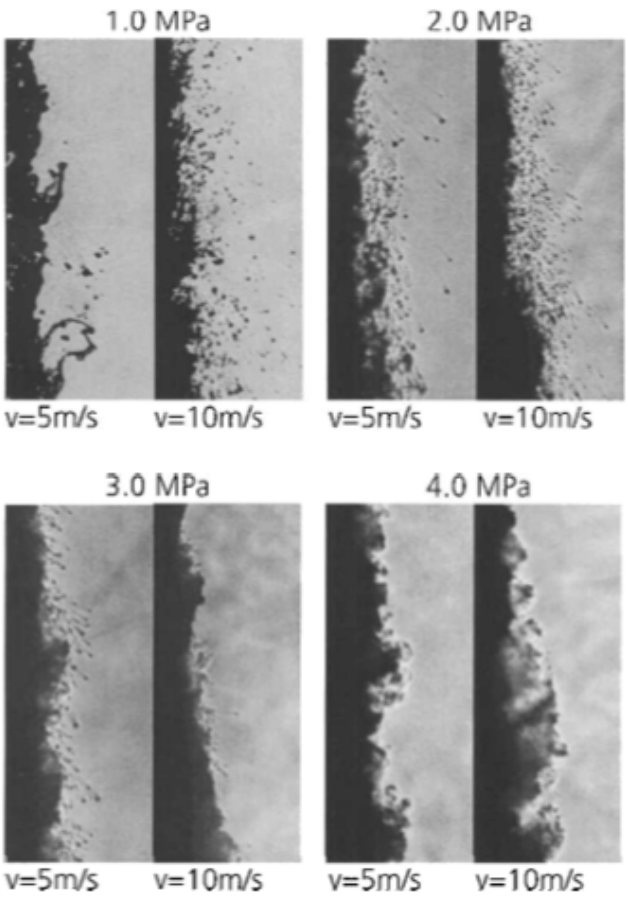

Figure 2.3.1: Nitrogen jet in gaseous nitrogen environment. Reprinted from Mayer et al. [62]

For a pure substance at its critical state in thermodynamic equilibrium conditions the distinction between liquid and gas phase at and above the critical point disappears, and for this reason we refer to the substance at this condition as *'fluids'* (Chehroudi [13]). When the chamber pressure and temperature approaches critical conditions the surface tension and enthalpy of vaporization become vanishingly small, so that the interface separating the liquid and gas phases in the jet disappears .
The fluid properties show liquid-like densities, gas-like diffusivities, and pressure dependent solubilities (Ierardo [36]).

Other investigators, Ierardo [36], Zong and Yang [127], and Dahms and Oefelein [20], point out the substitution of droplet formation and evaporation with mixing and mass transfer from thread-like structures that evolve from the liquid core and diffuse rapidly within the shear layer.

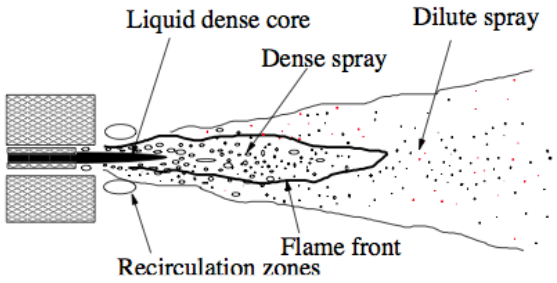

Figure 2.3.2: Subcritical injection. Reprinted from Oefelein [73]

The transcritical state analysis reveals that the two-phase interface breaks down not necessarily because of the vanishing surface tension forces, but because of the thickening interfaces at high subcritical temperatures coupled with an inherent reduction of the mean free molecular path. At a certain point, the combination of reduced surface tension, the thicker interface, and reduced mean free molecular path drive the system into the continuum length scale regime. When this occurs the transport processes dominate across the interfacial region. This leads to a continuous phase transition from compressed liquid to supercritical mixture states (Dahms and Oefelein [20]). Ruiz [92] points out that in transcritical injection a diffuse interface between dense and light fluid develops, where waves or comb-like structures can form. Fig. 2.3.3 shows the vorticity field superimposed on the high-density region. In case of H_2/O_2 mixtures, the emergence of low-speed oxygen fingers inside the high-speed hydrogen stream enhances shear-induced instability and creates small vortices. These small vortices increase the exchange surface between reactants, stretch the material interface and also feed large vortices through merging, which maintain the growth of the oxygen fingers. These finger-like structures are visually similar to experimental observations of transcritical mixing of coaxial jets. In the absence of surface tension, the finger-like structures do not form droplets and therefore are further broken down by turbulence.

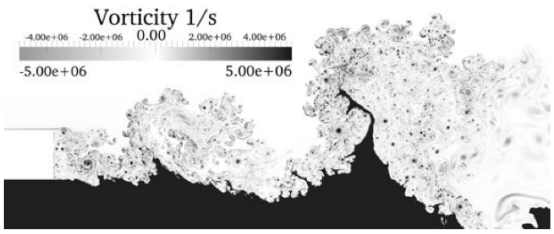

Figure 2.3.3: Transcritical injection. Reprinted from Ruiz [92].

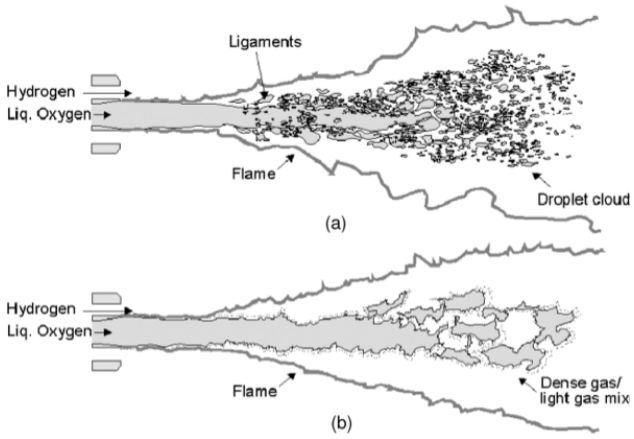

Figure 2.3.4: Subcritical and transcritical injection. Reprinted from Candel et al. [9].

(c) Characteristics of supercritical injection

When chamber pressures approach or exceed the critical pressure, the jet injected in transcritical conditions increases the interface fluid temperature above the saturation or critical temperature of the local mixture. The intermolecular forces diminish and the diffusion processes dominate prior to atomization and jets vaporize, forming a continuous fluid in the presence of exceedingly large gradients, Fig. 2.3.5.Any further increase of pressure in chamber cause a decrease of length and thickness of *dark core* and the jet appears more and more similar to a gaseous turbulent gas jet injected into a gaseous environment.
At pressure and temperature slightly higher that critical values, there are drastic changes of the interface structure: in these conditions, droplets do not form, but Chehroudi observes [13] the development of *thread or finger-like* entities, a behavior later noted by Ruiz [92], when we are in presence of transcritical conditions. These threads or finger-like entities start from the jet and seemingly dissolved at a spectrum of distance from the *'dark core'*, similarly to what occurs in a mixing layer with local non uniformities of density.

2.4 SUBCRITICAL, TRANSCRITICAL, AND SUPERCRITICAL JET FLAMES

We now briefly review the main flow phenomena, which occur when the injected substances are reactants that burn forming jet flames. We will discuss separately the three regimes of supercritical, transcritical and subcritical jet flames.

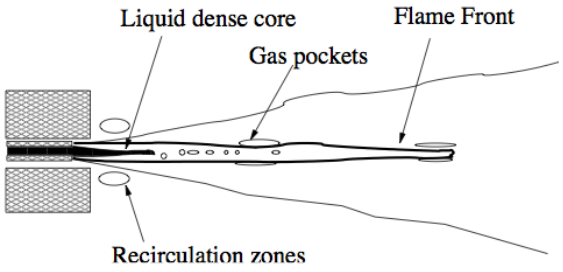

Figure 2.3.5: Supercritical injection. Reprinted from Oefelein and Yang [73]

(a) Subcritical regime:
A subcritical jet flame is stabilized (lifted) somewhat downstream the injector face in a manner consistent with the combustion mechanisms exhibited by local droplet clusters. The vaporization time is the slowest characteristic time (mixing time), and thus it is the controlling flame process as pointed out by Singla [96] (Fig. 2.4.1).

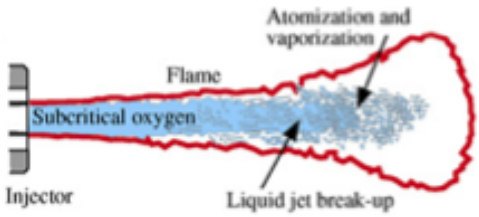

Figure 2.4.1: Subcritical flame. Reprinted from Singla et al. [96].

(b) Transcritical regime:
About the critical point, there occurs volumetric changes that play an important role in the flame structure (Singla [96]). The transcritical fluid behaves like a gas but with a highly nonuniform distribution of density and large gradient in shear layer. In the central core region where the temperature is lower than critical, the density is very high. In the outer layer where the temperature is increased and is higher than critical value, the density is low and promotes the formation of small scale vortical structures. Under these conditions, mass transfer processes between the dense and light regions depend on the turbulent rate of energy transfer from the outer to the inner layers. Thus, at pressures above critical, mixing becomes the slowest and therefore most influential process (Singla [96]) Fig. 2.4.2.

(c) Supercritical regime:
Supercritical flames are dominated by turbulent gas-like mixing. In Yang et al. [73] and Candel [9], the flames location depend on

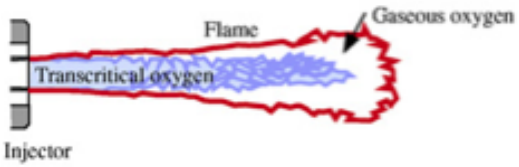

Figure 2.4.2: Transcritical flame. Reprinted from Singla et al. [96].

chamber conditions. With diminishing intermolecular forces, the diffusion process is a more efficient mixing process than atomization, which results in a flame stabilized in the annular post that separates the two propellants.

CONCLUSIONS

We have defined the state of a fluid as: super-trans or subcriticritical. The fluid is in a real physical state like the gaseous, liquid or solid states. In particular, the **supercritical state** of a fluid is such that for a pressure increase at a temperature higher than the critical, the fluid does not liquify. The **transcritical state** is defined as a state where the fluid pressure has a value higher than the critical and the temperature value is lower than the critical. In this state, we have a change of thermophisical properties, density, and diffusion, change from a liquid-like ($T < T_{pb}$) to a gas-like ($T > T_{pb}$). At the end, we have the **subcritical state**. The properties of this state, pressure and temperature, are lower than the critical values. In this state we can have a fluid in a gaseous phase, liquid or both phases. Injection case in **subcritical conditions** (subcritical ambient) is characterised by the development of filaments. When the instabilisation is present, we have the detachment of droplets from the filaments. When the pressure and temperature increase towards the critical conditions, we cross a region where the fluid is at **transcritical conditions**. In these conditions the surface tension and the enthalpy of vaporization vanish and the fluid behaves like a dense liquid-like jet. In **supercritical conditions**, the jet behaves gas-like and the separation between liquid and gas disappears. The intermolecular forces decrease and the diffusion process dominates. When the pressure increases, the dark core reduces his length. At the end, three kind of flames are observed in the subcritical, transcritical and supercritical conditions. In the **subcritical case**, the flame is stabilised downstream the injector. In this regime the jet first is disrupted, next it atomizes and eventually vaporizes. In **transcritical case**, the fluid behaves like a gas, but with a non uniform density distribution especially in the shear layer. In the regimes

of low density, outside the jet, the formation of vortical structures at small scale and a transport of mass, between the area with higher density and lower density, is promoted. In the **supercritical case**, the flames are dominated by turbulence process and by mixing process a gas-like. In this case, the mixing due to the diffusion process is more efficient than the realizeding the atomization process.

3

IDEAL GASES AND REAL FLUIDS

Contents

OBJECTIVES OF CHAPTER

In this chapter, we present the equations of state for an ideal gas and for a real fluid. In particular, we will discuss the cubic equations of (Van der Waals) VDW, PR (Peng-Robinson) and (Redlich-Kwong-Soave) RKS and we will show the GERG (Groupe Europèen de Recherches Gaziéres) non cubic equation. For every kind of EOS we report a valid form for a pure species and for a mixture of species. The definition of the thermodynamic properties of a real fluid follows, and we will present the definitions of a few useful quantity (departure function, residual function and compressibility factor), that we will meet in our study.

3.1 THERMODYNAMIC PROPERTIES OF REAL FLUIDS: CALORIC EOS AND ENTROPY

Aim of this section is to derive the proper thermodynamic state variables, such as the internal energy, specific heats, speed of sound and entropy and of an ideal or real fluid, which have the general definitions as follow: a caloric EOS

$$e(\rho, T) = e_{ref}(T) + \int_{\rho_{ref}}^{\rho} \left[\frac{p}{\rho^2} - \frac{T}{\rho^2} \left(\frac{\partial p}{\partial T} \right)_\rho \right]_T d\rho \tag{3.1.1}$$

$$c_v(\rho, T) = c_{p,ref}(T) - R - \int_{\rho_{ref}}^{\rho} \left[\frac{T}{\rho^2} \left(\frac{\partial^2 p}{\partial T^2} \right)_\rho \right]_T d\rho \tag{3.1.2}$$

$$c_p(\rho, T) = c_v(\rho, T) + \frac{T}{\rho^2} \frac{\left(\frac{\partial p}{\partial T} \right)_\rho^2}{\left(\frac{\partial p}{\partial \rho} \right)_T} \tag{3.1.3}$$

$$c(\rho, T) = \sqrt{\frac{c_p}{c_v} \left(\frac{\partial p}{\partial \rho} \right)_T} \tag{3.1.4}$$

Entropy definition

$$s(\rho, T) = s_{ref} - \int_{\rho_{ref}}^{\rho} \left[\frac{1}{\rho^2} \left(\frac{\partial p}{\partial T} \right)_\rho \right]_T d\rho \tag{3.1.5}$$

where $c_{p,ref}(T)$ is the perfect gas specific heat at constant pressure (in specific EOS can be modelled from Younglove et al. [124]), which is a function of temperature only, and T_{ref}, p_{ref}, $e_{ref} = e_{ref}(T)$, $c_{p,ref}(T) = c_{p,ref}(T)$ and $s_{ref} = s_{ref}(T, \rho_{ref})$ are the perfect gas reference variables (generally: $T_{ref} = 298.15$ K and $p_{ref} = 1.01325$ bar).

3.2 IDEAL GAS EQUATIONS OF STATE

3.2.1 *EOS of a pure species*

The ***thermal EOS*** of state of the ideal gas model in terms of extensive volume (V) and number of moles (n) the pressure can be written:

$$p = \frac{n\Re T}{V} \tag{3.2.1}$$

or in term of density:

$$P = \rho R T \tag{3.2.2}$$

R is the gas constant for one species. Note that R=$\Re/W$ and $\Re$ is the universal gas constant ($\Re$ = 8.31434 J/K/mol), W is the species's molar weight. When a gas is thermally perfect and calorically perfect this gas is also known as an *ideal gas*, where for a thermally perfect gas, the specific internal energy "e" is only a function of the temperature e(T), and for a calorically perfect gas the specific heat at constant volume and pressure are constants and not function of the temperature (if the specific heat capacity changes with temperature, the gas is said to be calorically imperfect).
The ideal gas model was empirically developed by Boyle, Gay-Lussac, and Charles. This model is valid for gases in the limits of low pressures and high temperatures and it is in agreement with the behaviour of most gases at atmospheric pressure. The ideal gas relation assumes that the gas consists of molecules that are infinitesimally hard spheres, occupy a negligible volume and exert forces on each other only through collisions without potential energy interactions between molecules. In case of non ideal gases several kind of equations of state are possible and a scheme of some generic EOS is illustrated in figure 3.3.5
The dependence of c_p with temperature can be modeled with polynomials interpolating experimental data that represent the behaviour of the selected substance in a given temperature range. We can use the thermodynamic data (old NASA Polynomials that has been used for 25 years) for polynomial fitting for specific heat, enthalpy and entropy with different ranges of validity. The ***caloric EOS*** are for specific heat and enthalpy:

$$\frac{c_p}{R} = +a_1 + a_2 T + a_3 T^2 + a_4 T^3 + a_5 T^4 \tag{3.2.3}$$

$$\frac{h}{RT} = a_1 + a_{2,i}\frac{T}{2} + a_3\frac{T^2}{2} + a_4\frac{T^3}{3} + a_5\frac{T^4}{4} + \frac{a_6}{T} \tag{3.2.4}$$

and entropy equation are:

$$\frac{s}{R} = a_1 \ln T + a_2 T + a_3\frac{T^2}{2} + a_4\frac{T^3}{3} + a_5\frac{T^4}{4} + a_7 \tag{3.2.5}$$

3.2.2 *EOS of gas mixtures*

In a mixture formed by N species *Dalton's law* is the rule used for perfect gases. The ***thermal EOS*** for the i-th species can be written in according to the perfect gas law as:

$$p_i = \rho_i R_i T \qquad\qquad i = 1,...,N \tag{3.2.6}$$

where p_i is the partial pressure of i-th species, ρ_i is the partial density of the i-th species, R_i is the gas constant of the i-th species and W_i is the molar weight of the i-th species. Note that $R_i = \Re/W_i$, T is the temperature, and N the number of species in the mixture.
The perfect gas law is the EOS sufficient to correlate pressure, temperature and density but a description of the thermodynamic state is given by a caloric equation of state which allows to correlate enthalpy, internal energy, Helmholtz free energy and Gibbs free energy to other the two independent thermodynamic variables.

$$\rho = \sum_{i=1}^{N} \rho_i Y_i \tag{3.2.7}$$

with Y_i = mass fraction

$$\sum_{i=1}^{N} \rho_i R_i T = T\rho \sum_{i=1}^{N} Y_i R_i \tag{3.2.8}$$

$$p = \sum_{i=1}^{N} p_i = \rho RT \tag{3.2.9}$$

It is possible to get a ***caloric EOS*** providing an expression (NASA standard polynomials from Gordon and McBride [27] and [28]) for the specific heat at constant pressure, c_p, recalling the previous defini-

tions of the thermally perfect gas (value of constant pressure specific heat cannot be considered like a constant), and the calorically perfect gas, the expression of mixture constant pressure specific heat is an average of the contribution of each species, weighted with its molar fraction x_i, as the perfect gas mixture theory:

$$\frac{c_p}{R} = \sum_{i=1}^{N} x_i \frac{c_{p,i}}{R_i} = \sum_{i=1}^{N} x_i (a_{1,i} T^{-2} + a_{2,i} T^{-1} + \\ + a_{3,i} + a_{4,i} T + a_{5,i} T^2 + a_{6,i} T^3 + a_{7,i} T^4) \tag{3.2.10}$$

where $x_i = \frac{W}{W_i} Y_i$, W_i atomic weight of i-th species, and mean molecular weight W ($W = \sum_i^N X_i W_i$).

Enthalpy and entropy at the reference pressure are therefore expressed as:

$$\frac{h}{RT} = \sum_{i=1}^{N} x_i (-a_{1,i} T^{-2} + a_{2,i} T^{-1} \ln T + \\ + a_{3,i} + a_{4,i} \frac{T}{2} + a_{5,i} \frac{T^2}{2} + a_{6,i} \frac{T^3}{3} + a_{7,i} \frac{T^4}{4} + \frac{a_{8,i}}{T}) \tag{3.2.11}$$

$$\frac{s^0}{R} = \sum_{i=1}^{N} x_i (-a_{1,i} \frac{T^{-2}}{2} - a_{2,i} T^{-1} + a_{3,i} \ln T + \\ + a_{4,i} T + a_{5,i} \frac{T^2}{2} + a_{6,i} \frac{T^3}{3} + a_{7,i} \frac{T^4}{4} + a_{9,i}) \tag{3.2.12}$$

The mixture entropy can be written according to:

$$\frac{s}{R} = \frac{s^0}{R} - \ln p - \sum_{i=1}^{N} x_i \ln x_i \tag{3.2.13}$$

3.3 REAL FLUID EQUATIONS OF STATE

3.3.1 *Compressibility factor*

The *compressibility factor* Z describes the transition gap between an ideal gas and a real fluid. The compressibility factor is defined as (in mass units):

$$Z = \frac{p}{\rho R T} \tag{3.3.1}$$

By definition, the Z factor for an ideal gas takes the unit value. A departure from the ideal gas behaviour implies that "Z" is different from the unity. The Z factor can be larger the one ($Z > 1$):

- $Z > 1$
- $Z < 1$

when the molecules can influence each other because of their repulsion forces enlarge the real volume more than the ideal one. Else Z factor can be lower the one ($Z < 1$) when the molecules can influence each other because their attractive forces reduce the real volume more than the ideal one.

From Z definition, and with reference to the definitions of reduced temperature, T_r, and pressure, P_r, we introduce the *specific volume* defined as the reciprocal of the density. Moran and Shapiro [69] consider that for correlation purposes, the *pseudo reduced specific volume* has been found to be preferable to the *reduced specific volume* $\frac{v}{v_c}$ where v_c is the critical specific volume. The result is that the *reduced specific volume* (3.3.2) could not be correlated directly with the specific and critical volume like the reduced pressure and temperature and $V_r \neq \frac{V}{V_c}$. Differently, it is well correlated with the critical pressure and temperature:

$$V'_r = \frac{V P_c}{R T_c} \tag{3.3.2}$$

3.3.2 *Departure and residual function*

The departure function and residual function are useful in real fluids to achieve the thermodynamic properties of the fluids (enthalpy, entropy and the heat constants relations). A coincise description can be found in Smith et al. [97] and Reid et al. [85]. Departure and residual function describe two different approaches to the same concept:

both terms involve the differences between the properties of a substance its hypothetical ideal gas state and in its real state: Van Ness and Abbott in [117], defines the **residual function** as: the real part is subtracted from ideal part of the property of interest (ideal-real), in terms of independent variables temperature and pressure (figure 3.3.1). Sandler, chooses the same variables for the **departure function** (real-ideal) but he prefer to subtract the ideal part from real part of property analyses. A different definition of the term **departure function** and **residual function** is presented by Poling et al. [85]. In this case the **departure function** is the difference between the ideal part and real part (ideal-real) where the property is a function of temperature and pressure. Differently, the **residual function** is the subtraction of ideal part from real part but the property considered is a function of temperature and volume, figure 3.3.1. For Reid [85], the motivations of a different definition are due to a different approach in the choice of the variable, P(T) or V(T), at which the ideal gas property value is compared to the real fluid property value. Indeed, EOS models are based on T and V as the independent variables because that is the only way in which the multiple values of V at phase equilibrium can be obtained; the Virial equation is an exception.

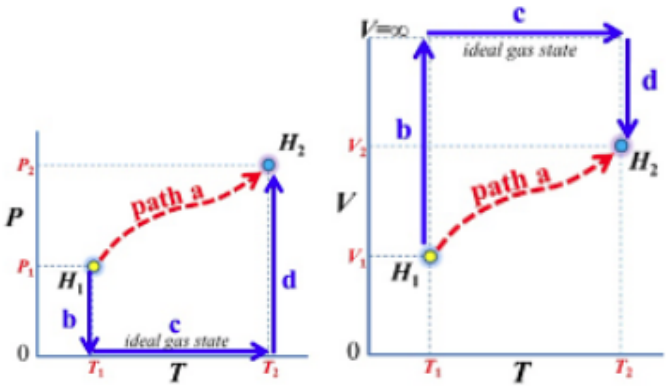

Figure 3.3.1: Two different paths to calculate a change in thermodynamic state variables (for instance, entalpy). The paths consider an ideal gas state. Left: the path is attained at zero pressure. Right: the path is attained at infinite volume. (Reprinted from Smith et al. [97]).

3.3.3 *EOS of a pure species*

In the literature review we found that, for the real fluid, two main approaches for ***thermal EOS*** are proposed:

- EOS based on the corresponding states theory: historically this was the most widely used approach.

- EOS for the Helmholtz free energy with a departure function.

A thorough review on EOS, from Van der Waals (VDW) to the most recent studies, can be found in Valderrama [113].

The finite volume occupied by the molecules was not considered in the ideal gas models earlier than VDW. How Valderrama reminds us, the VDW's idea was to include the volume of the molecules as suggested by Bernoulli. The volume V was replaced by (V - b), where b represents the volume occupied by the molecules and is named by Dupre *covolume*. In his doctoral thesis '***The Continuity of the Liquid and Gaseous States***', VDW proposed a simple and generalized EOS:

$$(P + \frac{a}{V^2})(V - b) = R(1 + \alpha t) \tag{3.3.3}$$

or

$$P = \underbrace{\frac{RT}{V - b}}_{P_R} - \underbrace{\frac{a}{V^2}}_{P_A} \tag{3.3.4}$$

It results that the pressure is the sum of two terms, as we can observe in equation 3.3.4 and in figure 3.3.5: a *repulsion pressure* P_R and an *attraction pressure* P_A. The repulsion pressure was expressed by the VDW hard sphere equation and is a function of the molar volume and the constant *b* (*multiple of the molecular volume*). This constant is related to the size of the hard spheres, in the attraction term "*a*" can be regarded as a measure of the intermolecular attraction force (*specific attraction*). It is possible obtain expressions for a and b at the critical point in terms of critical properties. While *b* is usually treated as temperature independent, *a* is constant only in VDW's equation. In VDW's equation, P is the external pressure, V is the molar volume, *b*, *multiple of the molecular volume* or *covolume* represents the volume occuped by molecules, *a* is *specific attraction* and R is a constant related to the kinetic energy of the molecules. The parameters, *a* and *b* are called **constants of equation of state**, and they were calculated using PVT data and can be related to critical properties applying the condition of continuity of the critical isotherm at the critical point. In this way, the constants are related to the critical pressure and temperature, P_c and T_c, respectively, and give a constant value for the critical compressibility factor Z_c that we will define in section §3.3.1

The discovery of the existence of the critical point by Andrews, helped VDW to formulate a theory that accounts for the behaviour of fluids above and below the critical point. In this way VDW unified the experimental knowledge on fluid properties in a single equation, that

considers the deviations from the ideal gas and also predicted the existence of a critical point. The idea developed by VDW on the separation of repulsion forces caused by molecular size from cohesive forces, caused by molecular attraction, are the basis of several theories concerning the prediction of fluid properties and of computer simulations based on statistical mechanics. After VDW, Clausius recognized that the attractive term should be temperature-dependent and modified the volume dependency of the attractive term. He proposed:

$$P = \frac{RT}{V-b} - \frac{a/T}{(V+c)^2} \tag{3.3.5}$$

An other change of VDW equation was realized by Redlich and Kwong (RK). They defined the correct representations at low density and at high density and proposed the following equation:

$$P = \frac{RT}{V-b} - \frac{a_c\,\alpha(T)}{V(V+b)} \tag{3.3.6}$$

$$\begin{aligned} &\alpha(T) = \frac{a}{T^{0.5}}, \quad a_c = \frac{\Omega_a R^2 T_c^{2.5}}{P_c} \\ &b = \frac{\Omega_b R T_c}{P_c}, \quad \Omega_b = 0.0867, \quad \Omega_a = 0.4278 \end{aligned} \tag{3.3.7}$$

Although this equation did not has a strong theoretical background and in the paper there wasn't any application to liquid, there were good results for many gaseous systems as cited in Valderrama [113]. Later we can find several changes to improve the equations of state of the VDW and RK. The modifications considered the behaviour of different fluids at the same reduced pressure and reduced temperature by introducing Pitzer's acentric factor ω, into the attractive term. For example Soave proposed a new improved version of this idea (acentric factor ω) and redefined the T_r and ω function. The new equation modified by Soave became one of the most popular EOS in the hydrocarbon industry. The Soave-Redlich-Kwong (SRK) equation turns out to be a relative simple equation compared with the more complicated BWR and the further BWRS equation, modified by Starling, that gives us accurate results in equilibrium ratios in VLE calculations. It can be summarized as follows:

$$P = \frac{RT}{V-b} - \frac{a_c\,\alpha(T_r,\omega)}{V(V+b)} \tag{3.3.8}$$

$$a_c = \frac{0.42747 R T_c^{2.5}}{P_c}, \quad b = \frac{0.08664 R T_c}{P_c}$$

$$\alpha(T_r, \omega) = [1 + m(1 - {T_r}^{0.5})]^2 \tag{3.3.9}$$

$$m = 0.480 + 1.574\omega - 0.176\omega^2$$

But the most popular of all modifications was the one proposed by Peng and Robinson (PR). PR improved Soave's equation by modifing the $\alpha(T_r,\omega)$ function and the volume dependency of the attractive term. These changes allowed them to obtain better results for liquid volumes and better representations of vapor-liquid equilibrium (VLE) for many mixtures. In their work [81] Peng and Robinson noted the failure of equations of RK and SRK to generate satisfactory density values for the liquid even though the calculated vapor densities are generally acceptable. The PR equation is:

$$P = \frac{RT}{V - b} - \frac{a_c \alpha(T_r, \omega)}{V(V + b) + (V - b)} \tag{3.3.10}$$

$$a_c = \frac{0.45724 R T_c^{2.5}}{P_c}, \quad b = \frac{0.07780 R T_c}{P_c}$$

$$\alpha(T_r, \omega) = [1 + m(1 - {T_r}^{0.5})]^2 \tag{3.3.11}$$

$$m = 0.37464 - 1.54226\omega - 0.26992\omega^2$$

In spite that SRK and the PR equations are the most popular cubic equations used in simulations. The improvement of EOS follows three way:

- The $\alpha(T_r)$ modifications in the SRK and PR equations that have focused on looking for more *accurate predictions of vapor pressure and vapor-liquid equilibrium* (VLE).
- The modifications of the volume dependence of the attractive pressure term that rises, the so-called *volume-translation* concept.
- The use of a third substance-dependent parameter the so-called group of *three-parameter equations of state*.

Modifications of the temperature-dependent function $\alpha(T_r)$ in the attractive term of the equations have been proposed to improve corre-

lations and predictions of vapor pressure for polar fluids. For example the Soave's term:

$$\alpha(T_r) = 1 + (1 - T_r)\left(m + \frac{n}{T_r}\right) \tag{3.3.12}$$

with m and n available for 500 substance. In conclusion, two-parameter cubic EOS can be adjusted to give good representations of PVT properties of pure polar fluids by modifying the temperature functionality of the attractive term.

The volume-translation concept proposes a volume correction in the SRK equation of state, which improves volume predictions without changing the VLE conditions. The method consists of using a corrected volume $V^{\star} = V + t$, where t is a small component dependent on molar volume correction factor. For the VDW equation the following expression is obtained:

$$P = \frac{RT}{V + t - b} - \frac{a}{(V + t)^2} \tag{3.3.13}$$

Other works on translated equations developed a volume-translated Peng-Robinson (VTPR) equation. The VTPR equation is comparable to other EOS in VLE calculations with various mixing rules, but it yields better predictions for the molar volumes of liquid mixtures.

The ***Three-Parameter Equations of State*** proposes that the fixed value of z_c should be replaced by a substance-dependent adjustable critical parameter, to overcome the drawbacks of VDW type equations provoked by the critical compressibility factor z_c. This approach has been mainly applied by introducing a third parameter into the equation of state. Patel and Teja reworked the equation previously proposed by Heyen and obtained:

$$P = \frac{RT}{V - b} - \frac{a_c\,\alpha(T)}{V(V + b) + c(V - b)} \tag{3.3.14}$$

The constants a_c, b, and c are determined as functions of two substance-dependent parameters, η_c and F. Valderrama generalized this equation using the acentric factor (ω) and the critical compressibility factor (z_c) as generalized parameters. We compare the ideal equation, VDW, PR, and SRK equations with National Institute Standards Technique (NIST) data and in figures 3.3.2 and 3.3.3 are showed, for oxygen, a comparison among volumes and densities graphics, respectively vs pressure and temperature. As verified by Ribert and coworkers [90], comparing the EOS of VDW, SRK and PR with the

NIST data the VDW EOS was not able to yield a good estimation of density in the low-temperature zone. Oefelein [72] has shown comparing by experiments that both equations SRK and PR, used in conjunction with the corresponding states principle, can give accurate results over the range of pressures, temperatures, and for mixture states. The SRK EOS is more suitable when the reduced temperature is less than one and in general follows NIST data over the entire range of temperature how also has showed by Petit et al. [82]. PR coefficients, on the other hand, are more suitable when the reduced temperature is greater than one.

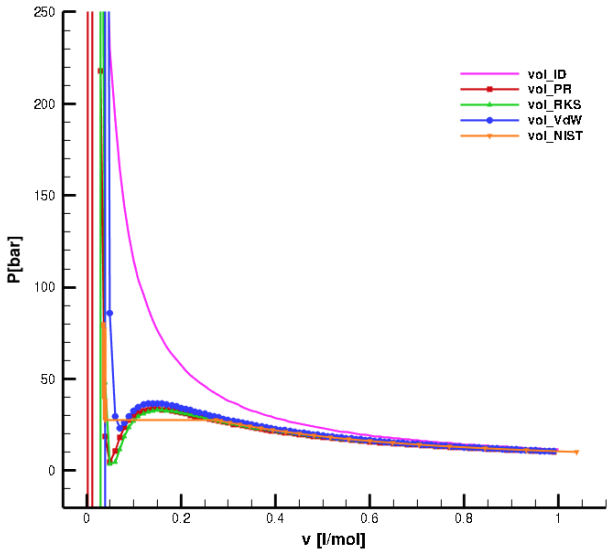

Figure 3.3.2: Volume vs Pressure. Comparison among oxygen diagrams achieved from cubic EOSs and NIST at 140 K. – denotes the ideal gas EOS; ■symbol denotes the PR equation; ▲ symbol denotes the SRK equation; ● symbol denotes the VDW equation; ▼ symbol denotes the NIST data.

In particular, the figure 3.3.3 represent the trends that are shown by Ribert et al. [90].

The errors among the several cubic equations are illustrated in figure 3.3.4. The best fit among the cubic equations is between the SRK and NIST.

Figure 3.3.5 shows a flow chart that illustrates the classification of equations of state.

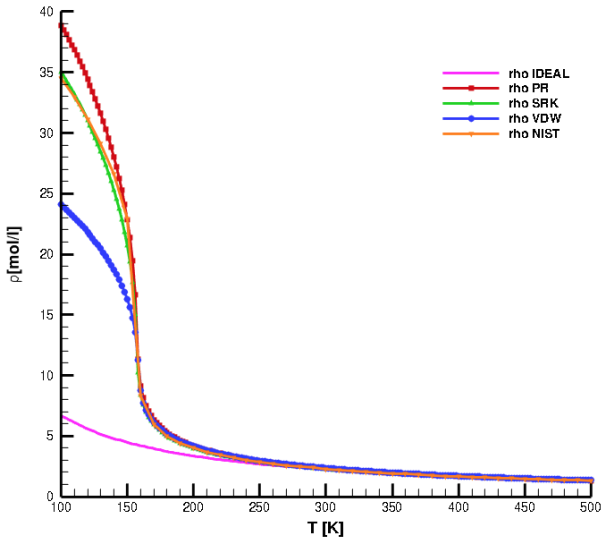

Figure 3.3.3: Comparison among oxygen's density diagram achieved from cubic EOSs and NIST at 55 bar. — symbol denotes the ideal gas EOS; ■ symbol denotes the PR equation; ▲ symbol denotes the SRK equation; ● symbol denotes the VDW equation; ▼symbol denotes the NIST data.

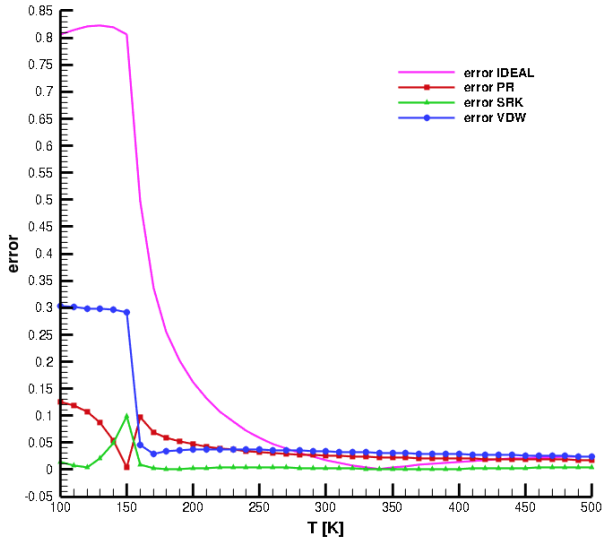

Figure 3.3.4: Comparison among oxygen's density relative errors achieved from cubic EOSs and NIST at 55 bar. – symbol denotes the ideal gas EOS; ■ symbol denotes the PR equation; ▲ symbol denotes the SRK equation; ● symbol denotes the VDW equation.

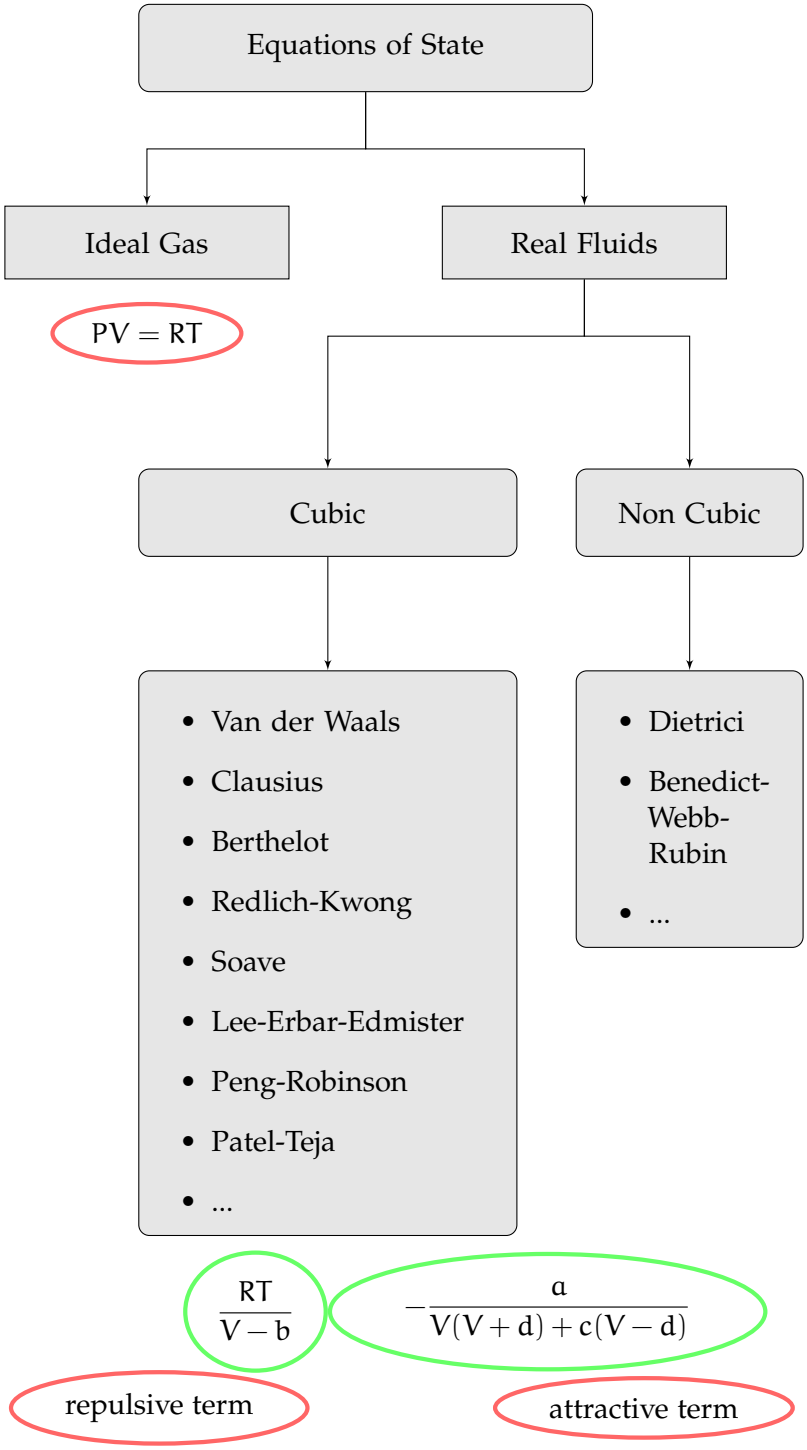

Figure 3.3.5: Different kinds of EOSs.

Summarising, a simple generic cubic equation, is given by VDW:

$$P = \frac{RT}{V-b} - P_{att}(T,V), \quad P_{att}(T,V) = \frac{a}{V(V+d)+c(V-d)} \tag{3.3.15}$$

Here, *a*,*b*, *c*, and *d* can be constants or functions of temperature and some fluid properties (acentric factor, critical compressibility factor, normal boiling point, etc.). These parameters cannot be chosen arbitrarily, as certain theoretical and empirical restrictions must be imposed. There are several reasons for popularity of cubic equations but also several disadvantages that Valderrama [113], summarized in a table that is shown in figure 3.3.6

Table 1. Advantages and Disadvantages of van der Waals Cubic EoS

	advantages		disadvantages
a	third degree in volume, which makes calculations relatively simple to perform	a	actual *PVT* data tend to follow a fourth-degree equation instead of a cubic equation
b	present correct limiting behavior: as $V \rightarrow b$, $P \rightarrow \infty$ in all van der Waals type equations	b	both the repulsive and attractive terms are inaccurate, as shown by molecular simulations
c	known inaccuracies of both the repulsive and attractive terms are canceled when the EoS are used to calculate fluid properties, in particular VLE	c	cubic equations cannot represent all properties of a fluid in all different ranges of *P* and *T*
d	for most applications, cubic EoS can be tuned to give accurate values for any volumetric or thermodynamic property	d	temperature dependency of the force constant *a* is not well established; co-volume *b* seems to be density-dependent, but the dependence is unknown
e	extension to mixtures is relatively easy using mixing and combining rules of any complexity	e	because interactions between unlike molecules are unknown, most mixing and combining rules are empirical, and interaction parameters are usually required
f	cubic equations are suitable for the application of modern mixing rules that include Gibbs free energy models or concentration-dependent parameters	f	in applications to complex mixtures, several interaction parameters might be required, even with the use of modern mixing rules

Figure 3.3.6: Advantages and disadvantages of Van der Waals's equation. Reprinted from Valderrama [113].

A good equation that unifies the SRK EOS and PR EOS is proposed by Cismondi and Mollerup [17]. They develop a three-parameter SRK-PR EOS, an equation that combining the vantages of SRK and PR. This equation was used by Kim [45] when analysed the best results for kerosene/LOX combustion.The three-parameters Cismondi's equation is:

$$P = \frac{\rho RT}{W - b\rho} - \frac{\rho^2 a\alpha(T,\omega)}{(W + \delta_1 b\rho) + (W + \delta_2 b\rho)} \tag{3.3.16}$$

where:

$$\begin{aligned} \delta_1 &= d_1 + d_2(d_3 - 1.168Z_c)^{d_4} + d_5(d_3 - 1.168Z_c)^{d_6}, \\ \delta_2 &= \frac{1-\delta_1}{1+\delta_1} \end{aligned} \tag{3.3.17}$$

Furthermore, $\delta_1 = 1$ gives us SRK and $\delta_1 = 1 + \sqrt{2}$ give us PR.

Another compact shape to write the cubic equation of VDW, PR and SRK is:

$$P = \frac{RT}{v - b} - \frac{a\alpha(T,\omega)}{(v^2 + ubv + wb^2)} \tag{3.3.18}$$

The cubic EOS coefficients in the equation 3.3.16 are showed in table 4

EOS	u	w	$b\frac{P_c}{RT_c}$	$a\frac{P_c}{{RT_c}^2}$	$\alpha(T,\omega)$
VDW	0	0	0.125	0.421875	1
RK	1	0	0.08664	0.42748	$\frac{1}{T^{0.5}}$
SRK	1	0	0.08664	0.42748	$f_{SKR}(\omega, T_c)$
PR	2	-1	0.07780	0.42748	$f_{PR}(\omega, T_c)$
SRK-PR	$\delta_1+\delta_2$	$\delta_1\delta_2$	$\frac{1}{3y+d-1}$	$\frac{3y^2+3dy+d^2+d-1}{(3y+d-1)^2}$	$\left(\frac{3}{2+T/T_c}\right)^k$

Table 4: Cubic EOSs from Petit et al. [82].

Other EOSs show a shape completely different from the cubic form that we have seen above, an example is the Virial's equation. This equation can be derived from first principles using statistical mechanics. It is given by a power series expansion for the compressibility factor in concentration (or the reciprocal of molar volume), $1/v = 0$:

$$Z = \frac{Pv}{RT} = 1 + \frac{B}{v} + \frac{C}{v^2} + \frac{D}{v^3} + \dots \tag{3.3.19}$$

where B, C, etc. are called the second, third Virial coefficients.These parameters depend only on temperature (and composition for mixtures). An alternative expression for the Virial equation is a power series expansion in pressure:

$$Z = \frac{Pv}{RT} = 1 + B'P + C'P^2 + D'P^3 + \dots \tag{3.3.20}$$

Solving the equation 3.3.20 for P and substituting into 3.3.19, it is straightforward to show that the two sets of coefficients are related by:

$$B' = \frac{B}{RT} \tag{3.3.21}$$

$$C' = \frac{C - B^2}{(RT)^2} \tag{3.3.22}$$

The equation 3.3.20 is explicit in pressure and equation 3.3.19 is explicit in volume. An issue for this equation is the accuracy; it turns out that at pressures up to about 15 bar, when you keep only the

second Virial coefficient, the power series expansion in pressure is better:

$$Z = \frac{P\nu}{RT} = 1 + B'P = 1 + \frac{BP}{RT} \tag{3.3.23}$$

But for higher pressures, from 15 to 50 bar, the Virial equation should contain three terms, and the expansion in concentration is more accurate:

$$Z = \frac{P\nu}{RT} = 1 + \frac{B}{\nu} + \frac{C}{\nu^2} \tag{3.3.24}$$

Using the statistical mechanics, one can relate the Virial coefficients to the intermolecular potentials. The second Virial coefficient, B, is the consequence of all the "two-body" interactions in the system, that is, the interactions between two molecules; the third Virial coefficient, C, results from all the "three-body" interactions in the system; and so on. If the pressure is so low that not even two-body interactions affect the system properties, we have an ideal gas. An example about the computation of the second Virial coefficient can be found in Koretsky [49]. He illustrates that for the spherically symmetric molecules, the computation of the second Virial coefficient, B that results from all the “two-body” interactions in the system. In according to statistical mechanics, the second Virial coefficient is given by the:

$$B = 2\pi N_A \int_0^\infty \left(1 - e^{-\Gamma(r)(kT)}\right) r^2 dr \tag{3.3.25}$$

with N_A Avogadro’s number, Γ the potential energy, k Boltzmann’s constant and r the distance between the particles.

The Principle of Corresponding States (CSP), see Appendix §B, is often applied to the truncated Virial equation. We can write:

$$B_r = B^0 + \omega B^1 \tag{3.3.26}$$

where

$$B_r = \frac{BP_c}{RT_c}$$

Several correlations of parameters B^0 and B^1 to reduced temperature have been proposed.

The CSP (Appendix §B) invokes a unique generalized relation between the compressibility factor, reduced pressure and temperature and, as described after, a class of molecules. The **two parameter** compressibility factor can be written in the following form:

$$Z = Z(T_r, P_r) \tag{3.3.27}$$

From macroscopic a point of view, the relation 3.3.27 describes in the best way the **corresponding states principles** for which *all fluids at the same reduced temperature and pressure should have the same compressibility factor*. From a microscopic point of view it talks about potential energy, considering that *the dimensional potential energy is the same for all species*

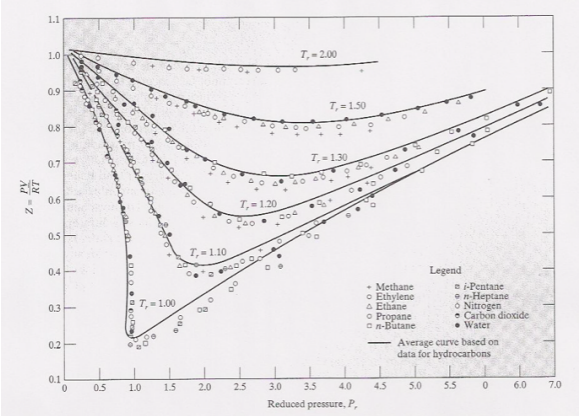

Figure 3.3.7: Compressibility factors for different fluids as a function of the reduced temperature and pressure. Z is the compressibility factor and P_r is the reduce pressure. Reprinted from Sandler [93].

Systematic deviations from the simple corresponding state are showed in figure 3.3.7. The relation 3.3.27 suggests that all fluids would have the same value of the critical compressibility but this unexpected behaviour implies a more complicate CSP. The next step is a relationship as showed in 3.3.28. This relation is the simplest generalization for the families with different values of Z_c. This mean that Z is a function of:

$$Z = Z(T_r, P_r, Z_c) \tag{3.3.28}$$

But for more substances, complex gases with molecules with strong dipolar moments or non spherical force fields, is complicate to obtain an accurate value of Z_c, and it results more convenient to use a different factor. The Pitzer factor or **acentric factor** ω can be used as the

third correlative parameter (**three parameter** compressibility factor) and the relation 3.3.28 becomes:

$$Z = Z(T_r, P_r, \omega) \tag{3.3.29}$$

where ω is function of P^{vap} P_c and T_r, see 3.3.30 or 3.3.42

$$\omega = -1.0 - \log_{10}[P^{vap}(T_r = 0.7)/P_c] \tag{3.3.30}$$

where $P^{vap}(T_r = 0.7)$ is the vapor pressure of the fluid at $T_r = 0.7$, a temperature near the boiling point.

$$Z = \mathbf{F}^0(T_r, P_r) + \omega \mathbf{F}^1(T_r, P_r) \tag{3.3.31}$$

where $\mathbf{F}^0$ and $\mathbf{F}^1$ depends only by the reduced pressure and temperature and the acentric factor is used to modulate the effect of the $\mathbf{F}^1$ term. Thus a perfectly 'spherical' molecule (such as Ar) depends only on $\mathbf{F}^0$.

3.3.4 *Compressibility factor and cubic EOS*

A generic cubic equation can be written in the compressibility factor, in this way:

$$Z^3 + \alpha Z^2 + \beta Z + \gamma = 0 \tag{3.3.32}$$

The coefficients α, β, and γ depend on several cubic EOS. In equations 3.3.33 and 3.3.40, the coefficients are written for PR's equation and SRK's equation. The trend of compressibility factor Z is illustrated in the figures 3.3.8, 3.3.9, 3.3.10 and 3.3.11: the figures 3.3.8 and 3.3.10, and 3.3.9 and 3.3.11 show the logarithmic nitrogen compressibility factor and the nitrogen compressibility factor, respectively, for PR's equation and VDW's equation. The compressibility is illustrated as variation of reduced pressure at several reduced temperatures. Comparing the behaviour of two equations, figure 3.3.12, we can note that in the PR equation the inversion point of compressibility is at P_r, bigger than VDW equation. At $P_r > 7.8$ after $P_r \approx 8.4$, the compressibility is more than one ($Z > 1$): the volume of real fluid (V_{real}) is bigger than volume of ideal fluid (V_{ideal}), the attractive forces are weaker than repulsive forces. This feature is visible in figure 3.3.12 and in figure 3.3.13 in logarithmic scale. The figures 3.3.8

and 3.3.9 show the nitrogen logarithmic compressibility factor, respectively, for PR and VDW equation.

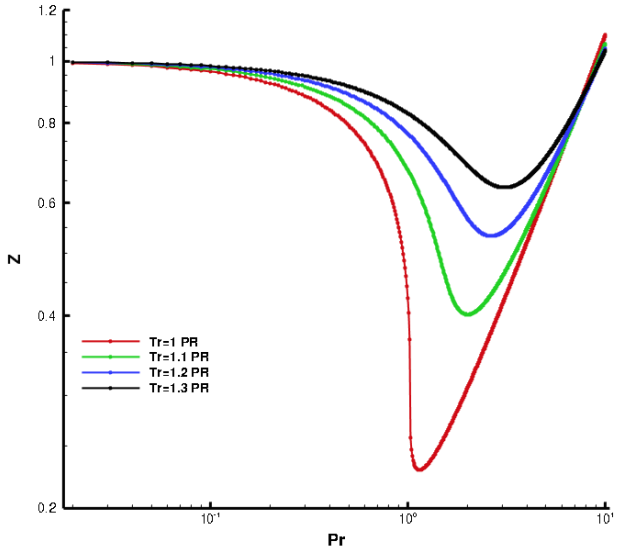

Figure 3.3.8: Peng-Robinson's compressibility factor Z with reduced pressure P_r in logarithmic scale at different reduced temperature T_r. Nitrogen case.

Remembering the previous expression of compressibility factor we can rewrite the PR and the SRK equations as done by their authors, respectively, [81] and [98]. The dimensionless scaling factor for the energy parameter as a function of acentric factor in addition to reduced temperature, in RK equation and the SRK equation, has improved the prediction of vapour pressures for pure substances and consequently the equilibrium ratios for mixtures. For equation 3.3.10 we write for PR:

$$Z^3 - (1 - B)Z^2 + (A - 3B^2 - 2B)Z - (AB - B^2 - B^3) = 0 \quad (3.3.33)$$

where

$$A = \frac{aP}{R^2T^2}$$
$$B = \frac{bP}{RT} \quad (3.3.34)$$

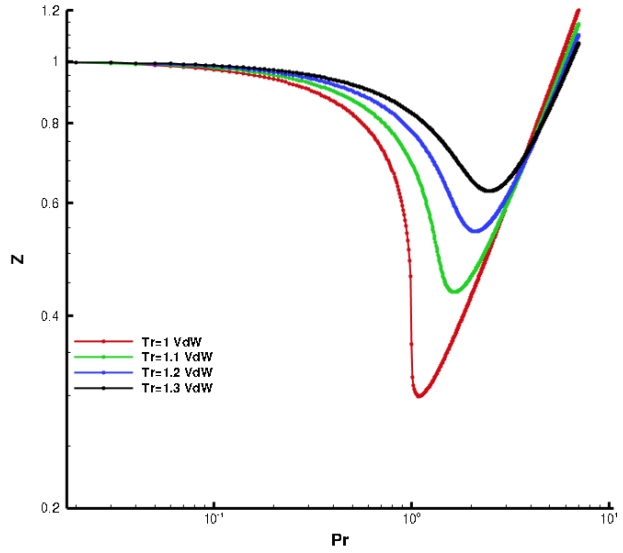

Figure 3.3.9: Van der Waals's logarithmic compressibility factor Z with reduced pressure P_r in logarithmic scale at different reduced temperature T_r. Nitrogen case.

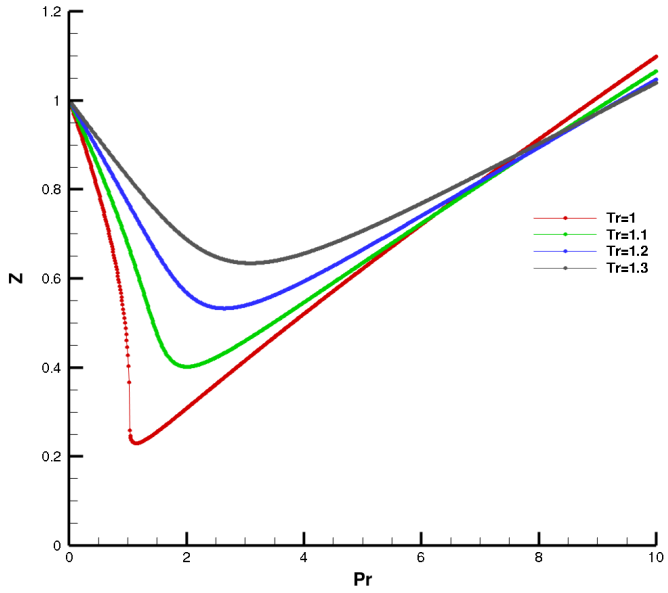

Figure 3.3.10: Peng-Robinson's compressibility factor Z with reduced pressure P_r at different reduced temperature T_r. Nitrogen case.

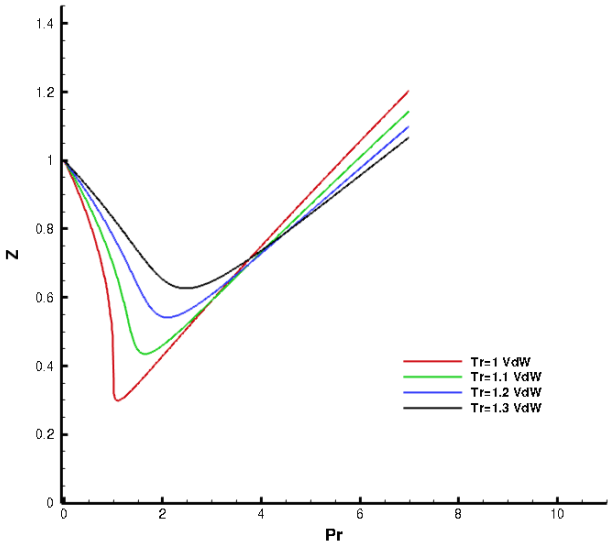

Figure 3.3.11: Van der Waals's compressibility factor Z with reduced pressure P_r at different reduced temperature T_r. Nitrogen case.

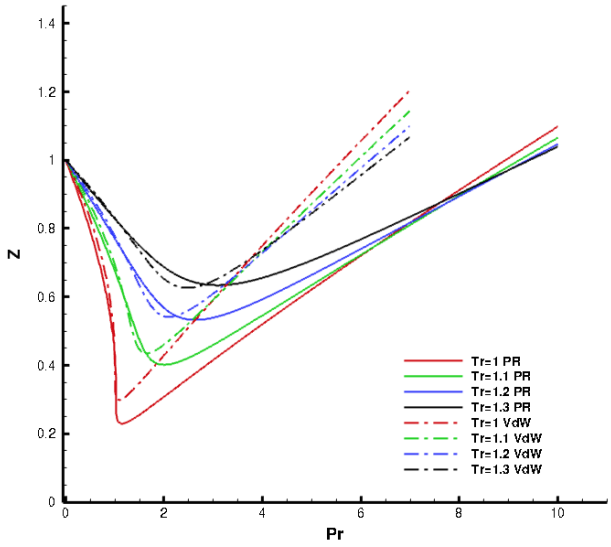

Figure 3.3.12: PR VS VDW compressibility factor Z with reduced pressure P_r at different reduced temperature T_r. —— symbols are WDV EOS and ···· symbols are the PR EOS. Nitrogen case.

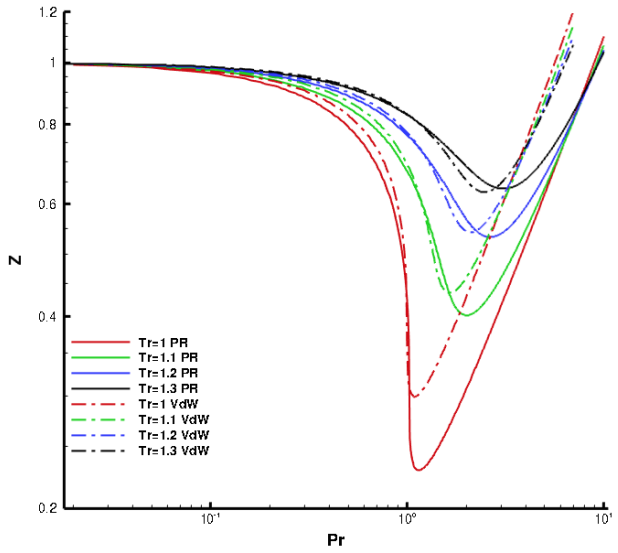

Figure 3.3.13: PR VS VDV compressibility factor Z with reduce pressure P_r in logarithmic scale at different reduced temperature T_r. —— symbols are WDV EOS and ···· symbols are the PR EOS. Nitrogen case.

The Equation 3.3.33 yields one or three roots depending on the number of phases in the system. In the two-phase region, the largest root is for the compressibility factor of the vapor while the smallest positive root corresponds to that of the liquid. Applying the thermodynamic relationship 3.3.35 to equation 3.3.10, PR obtained the expression of fugacity of a pure component and by using the compressibility factor how showed in equation 3.3.36:

$$\ln\frac{f}{p} = \int_0^P \left(\frac{v}{RT} - \frac{1}{P}\right) dP \tag{3.3.35}$$

$$\ln\frac{f}{p} = Z - 1 - \ln(Z - B) - \frac{A}{2\sqrt{2}B} 2\ln\left(\frac{Z + 2.414B}{Z - 0.414B}\right) \tag{3.3.36}$$

Moreover the ***caloric EOS*** in term of departure enthalpy of a fluid is given by:

$$H - H^\star = RT(Z - 1) + \frac{T\frac{da}{dT} - a}{2\sqrt{2}b} \ln\left(\frac{Z + 2.44B}{Z - 0.414B}\right) \tag{3.3.37}$$

$$H - H^{\star} = RT(Z-1) + \int_{\infty}^{v}\left[T\left(\frac{\partial P}{\partial T}\right)_{v} - P\right]dv \tag{3.3.38}$$

The form of $\alpha(T_r, \omega)$ was determined by means of the literature vapor pressure values and Newton's method to search for the values of α used in eq 3.3.33 and 3.3.36 such that the equilibrium condition $f^L = f^V$ is satisfied along the vapor pressure curve. The convergence criterion between f^L and f^V ($|f^L - f^V|$) was required to obtain a value for α at each temperature. PR reach relationship between α and T_r, for all the substances examined, and this relationship can be linearized by the following equation:

$$\alpha^{\frac{1}{2}} = 1 + m(1 - T_r^{\frac{1}{2}}) \tag{3.3.39}$$

with m a constant characteristic of each substance and it has been correlated against the acentric factor. The equation 3.3.39 appears similar to that obtained by Soave (1972) for the SRK equation although equation 3.3.39, for each substance, uses vapour pressure data from the normal boiling point to the critical point whereas Soave's equation uses only the critical point and the calculated vapour pressure a t T_r= 0.7 based on the value of acentric factor. Soave [98] modify the 3.3.7 replacing the term $a/T^{0.5}$ with a more general temperature-dependent term to make it possible to write the equation of state in terms of compressibility factor Z. The equation 3.3.6 can be written:

$$Z^3 - Z^2 + (A - B^2 - B)Z - AB = 0 \tag{3.3.40}$$

The RK equation can be used to calculate, with a good degree of accuracy, volumetric and thermal properties of pure compounds and mixtures. Nevertheless several authors have tried to improve the equation. They introduce empirical binary interaction constants for the purpose to obtain an improvement of mixing rules and archieve the results for the application to multicomponent in VLE.

The fugacity coefficient of a pure component can be calculated from the equation:

$$\ln\frac{f}{p} = Z - 1 - \ln(Z - B) - \frac{A}{B}\ln\left(\frac{Z+B}{Z}\right) \tag{3.3.41}$$

The compressibility factor Z used in Eq. 3.3.40 is obtained by solving Eq. 3.3.40. From this equation one or three real roots can be obtained, in particular: the smallest root will be taken for a liquid phase and the highest one for a vapor phase). For a pure substance at a

given temperature and for a given value of a(T), exists a single value of P which satisfies the saturation condition:
$f^L = f^V$

This pressure can be find by trial for each value of the pressure, solving equation 3.3.40, once for the liquid phase and once for the vapour phase, and introducing the two roots into equation fugacity SRK. In particular, the right pressure is the one where the two values of f/P calculated are equal. In equation 3.3.9 the slopes m_i can be connected with the acentric factor of the related compounds, in dirrect way. Each value of ω defines a value of the reduced vapor pressure at a reduced temperature of 0.7:

$$p_R^{sat}(T_R = 0.7) = 10^{-1-\omega} \tag{3.3.42}$$

From the pair (T_R = 0.7, $\alpha = 10^{-1-\omega}$) a value of $\alpha(0.7)$ is obtained, which depends only on the assumed ω. Considering the points (T_R, $\alpha = \alpha(0.7)$) they obtain:

$$m_i = \frac{\alpha^{0.5}(0.7) - 1}{1 - (0.7)^{0.5}} \tag{3.3.43}$$

The m_i values obtained by substitution into equation 3.3.43 of the of $\alpha(0.7)$ values are tabulated, see SRK [98], and correlated vs ω, from the equation of m in 3.3.9.

3.3.5 *EOS of gas mixtures*

In literature there are several approaches to define a optimal mixing theory that can give a good predictions of mixture properties where the classical VDW one-fluid mixing rules do not provide accurate results for complex systems.
The simplest mixing rules is the *Kay's rules*. The equations 3.3.44, 3.3.45 and 3.3.46 are the pseudo-critical temperature, pseudo-critical pressure, and pseudo-critical acentric factor which define the mixture properties. The pseudo-critical properties average the critical properties of each species in proportion to the amount of that species present in the mixture:

$$T^c{}_{mix} = T_{pc} = \sum_i x_i T_{c,i} \tag{3.3.44}$$

$$P^c{}_{mix} = P_{pc} = \sum_i x_i P_{c,i} \tag{3.3.45}$$

$$\omega_{pc} = \sum_i x_i \omega_{c,i} \tag{3.3.46}$$

An other simple rules are: *the geometric mean rule* and *VDW rule*. The geometric mean combine rule for critical temperature 3.3.47 and pressure 3.3.48, are:

$$T_{pc,ij} = \sqrt{T_{c,i} T_{c,j}}(1 - k_{ij}) \tag{3.3.47}$$

$$P_{pc,ij} = \sqrt{P_{c,i} P_{c,j}} \tag{3.3.48}$$

where k_{ij} is a binary interaction parameter that better fit the experimental data. *The Classic Mixing Rules*, the VDW rule, was used in most applications:

$$a = \sum_i \sum_j x_i x_j a_{ij}, \quad b = \sum_i \sum_j x_i x_j b_{ij}, \quad c = \sum_i \sum_j x_i x_j c_{ij} \tag{3.3.49}$$

where the geometric mean was used for the force parameter a_{ij}, and the arithmetic mean was used for the volume parameters b_{ij} and c_{ij}. To improve the correlation of phase equilibrium were included the concentration independent interaction parameters into a_{ij}, b_{ij}, and c_{ij} as in equation 3.3.55. These modifications preserve the quadratic concentration dependence of the EOS parameters and the quadratic concentration dependence of the second Virial coefficient.

$$a_{ij} = \sqrt{a_i a_j}(1 - k_{ij}), \quad b_{ij} = \frac{1}{2}(b_i + b_j(1 - \delta_{ij})) \tag{3.3.50}$$

In equation the parameter k_{ij}, δ_{ij}, or β_{ij} are calculated by regression analysis of experimental phase equilibrium data, (Valderrama [113]). If $\delta_{ij} = 0$ the b_{ij} coefficient, in equation 3.3.49, becomes 3.3.51

$$b = \sum_i x_i b_i \tag{3.3.51}$$

There are several proposals to improve the mixing rules in terms of solubility or semi empirical correlation that involve the other EOS (SRK, PR). In the PR case was developed a semi-empirical correlation for the interaction parameter as functions of the critical temperatures and critical compressibility factor of the pure components. In SRK, some workers used combining rules for molecular parameters to propose correlations for the interaction parameters as functions of the pure-component parameters (critical properties). Also combining rules for intermolecular parameters, such as the energy (ϵ) and size (σ) parameters, in the Lennard-Jones potential, was used in connection with cubic EOS. Unfortunately none of these methods proved to be of general applicability.

In *the Volume Dipendent Mixing Rules* was used the local composition concept. The PR EOS was extended to complex mixtures, and evaluated various forms of the local composition concept and in some cases for local composition model was combined with an EOS to be applied to strongly polar and asymmetric mixtures.

In *the non quadratic mixing rules*, Poiling et al. in[85], introduced a second interaction parameter making the k_{ij} parameter concentration-dependent, thus transforming the mixing rule in a nonquadratic form. Usually is sufficient for the correlation of phase equilibrium in simple systems the quadratic mixing rules.

$$a_{ij} = \sqrt{a_i a_j}[1 - k_{ij} + (k_{ij} - k_{ji})x_i], \quad b_{ij} = \frac{1}{2}(b_i b_j(1 - l_{ij})) \tag{3.3.52}$$

It is useful to summarize *the nonquadratic mixing rules* in terms of two parameters δ_i, or δ_j and to define a general form, called the "general nonquadratic mixing rule" when k_{ij} is:

$$k_{ij} = \delta_i x_i + \delta_j x_j \tag{3.3.53}$$

Among the modern approaches presented to describe phase equilibria in mixtures, methods of the type *EOS plus Gibbs free energy* seems are the most appropriate for modeling mixtures with highly asymmetric components. This type of models have been extensively used and applied to low- and high-pressure vapor-liquid mixtures, to liquid-liquid equlibria, and gas-solid equilibria. Later were proposed the models of a mixing rule based on a convenient separation of the excess Gibbs free energy:

$$g^E = g^E_{RS} + g^E_{RES} \tag{3.3.54}$$

where g^E_{RS} is the excess Gibbs free energy for a regular solution and g^E_{RES} is the residual excess Gibbs free energy. A different concept is the one developed by Mansoori. *Mansoori* based his theory of mixing rules for cubic EOS on statistical mechanical theory of the VDW, and the rules are for constants of an equation of state and not for any thermodynamic state function that might appear in an equation of state. The advantage is that an EOS includes the temperature as independent parameter. The PR EOS is reformulated as:

$$a_{ij} = \sqrt{a_i a_j}(1 - k_{ij}), \quad b_{ij} = \left(\frac{b_i^{1/3} + b_j^{1/3}}{2}\right)^3 (1 - \beta_{ij}),$$
$$d_{ij} = \left(\frac{d_i^{1/3} + d_j^{1/3}}{2}\right)^3 (1 - l_{ij}) \tag{3.3.55}$$

About the *mixture containing supercritical components*, we remember that the first efforts to model the phase behaviour in systems, containing supercritical fluids, were made using the Virial EOS, but these attempts were not successful. The best results were obtained using cubic EOS such as SRK and PR. About the mixture, for first thing, we have a glance at the PR equation [81], where is showed the computation of fugacity coefficient of component k in a mixture. The coefficient can be calculated from the following equation:

$$\ln\frac{f_k}{x_k p} = \frac{b_k}{b}(Z - 1) - \ln(Z - B) - \frac{A}{2\sqrt{2}B} \times \left(\frac{2\sum_i X_i a_{ik}}{a} - \frac{b_k}{b}\right) \ln\left(\frac{Z + 2.41B}{Z - 0.414B}\right) \tag{3.3.56}$$

and the mixture parameters are:

$$a = \sum_i \sum_j x_i x_j a_{ij} \tag{3.3.57}$$

$$b = \sum_i \sum_j x_i b_{ij} \tag{3.3.58}$$

$$a_{ij} = (1 - \delta_{ij}) a_i^{\frac{1}{2}} a_j^{\frac{1}{2}} \tag{3.3.59}$$

In equation 3.3.59 δ_{ij} is an empirically determined binary interaction coefficient that characterize the binary formed by component i and component j.

The advantages of using simple two-constant equations of state is the simplicity: equation 3.3.10 can be reduced to a cubic equation similar to equation 3.3.33 and the roots can be obtained analytically. This equation can be used to perform VLE calculations instead of multiconstant equations of state that require the use of iteration procedures to solve for the densities of the coexisting phases. The PR equation can be used to accurately predict the vapor pressures of pure substances and equilibrium ratios of mixtures and gives good agreement between predictions and experimental PVT data. For Soave [98], the mixture was chosen with original generalize mixing rules:

$$a = (\sum_i x_i a_i^{0.5})^2 \tag{3.3.60}$$

$$b = \sum_i x_i b_i \tag{3.3.61}$$

It is found that these rules could be applied with acceptable results to mixtures of nonpolar fluids, such as hydrocarbons, nitrogen, carbon monoxide but non to the carbon dioxide. By applying mixing rules 3.3.60 and 3.3.61 to Eqs. 3.3.34, 3.3.9 in a_c and b, we obtain:

$$A = 0.42747 \frac{p}{T^2} \left(\sum_k x_k \frac{\alpha^{0.5} T_{ck}}{{p_{ck}}^{0.5}} \right)^2 \tag{3.3.62}$$

$$B = 0.08664 \frac{p}{T^2} \sum_k x_k \frac{T_{ck}}{p_{ck}} \tag{3.3.63}$$

The fugacity coefficient of a component in a mixture is given by:

$$\frac{\ln f_k}{x_k p} = \frac{b_k}{b}(Z - 1) - \ln(Z - B) - \frac{A}{B} \times \left(2\frac{a_k^{0.5}}{a^{0.5}} - \frac{b_k}{b} \right) \ln \left(\frac{Z + B}{Z} \right) \tag{3.3.64}$$

with:

$$\frac{a_k^{0.5}}{a^{0.5}} = \frac{\alpha_k^{0.5} T_{ck}/p_{ck}^{0.5}}{\sum_k x_k \alpha^{0.5} T_{ck}/p_{ck}^{0.5}} \tag{3.3.65}$$

$$\frac{b_i}{b} = \frac{T_{ck}/p_{ck}}{\sum_k x_k T_{ck}/p_{ck}} \tag{3.3.66}$$

The equation 3.3.56 comes from:

$$\ln \frac{f_k}{p x_k} = \int_\infty^P \left[\frac{1}{v} - \frac{1}{RT} \left(\frac{dp}{dn_k} \right)_{T,p,n_j} \right] dv - \ln Z \tag{3.3.67}$$

Some empirical corrections are necessary for systems that containing polar compounds for which large deviations were obtained, although the vapour pressures of the single pure components were reproduced well. More generally, one could write:

$$a_{ij} = (a_i a_j)^{\frac{1}{2}}, \quad a_{ij} = (1 - K_{ij})(a_i a_j)^{\frac{1}{2}} \tag{3.3.68}$$

where K_{ij} is an empirical correction factor, to be determined from the experimental data, for each binary present in the mixture. Several authors highlight that each K_{ij} factor can be considered independent of system temperature, pressure and composition.
Another idea, to describe a mixture, is based on the Helmholtz free energy, which takes into account the real behaviour of fluids with some kind of departure functions from the perfect gas solution. In particular, the GERG EOS, Kunz et al. [50], is based on pure substances equations of state for each considered mixture component and a correlation equations for binary mixtures consisting of these components. Urbano in her analysis, [112], considered 18 components (N=18) between she include the 6 selected species, methane, in particular is he most important natural gas component. The possible combinations of binary mixtures that can be obtained with 18 components are 153. The range of validity of GERG EOS covers temperatures of $60K \leqslant T \leqslant 700K$ and pressures of $p \leqslant 70$ MPa, with an uncertainty in density lower than 0.5%. Mixing rules are applied to the reduced Helmholtz free energy "a":

$$a(\delta, \tau, \overline{x}) = \frac{A}{RT} = a^0(\delta, \tau, \overline{x}) + a^r(\delta, \tau, \overline{x}) \tag{3.3.69}$$

with ρ and T that are respectively the mixture density and temperature, R the gas constant, A the mass specific Helmholtz free energy, and $\overline{x} = (x_1, x_2, \ldots, x_N)$ the molar composition. The residual term α^r, which corrects in the real fluid regime the perfect gas term α^0, is expressed in terms of reduced mixture density δ and reduced mixture temperature τ, according to:

$$\delta = \frac{\rho}{\rho_r(\overline{x})} \quad \text{and} \quad T = \frac{T_r(\overline{x})}{T} \tag{3.3.70}$$

The equation of state describes the Helmholtz free energy as a function of temperature and density, with its derivatives and provides a complete description of the thermodynamic properties of the mixture. This EOS is equivalent to the MBWR equation of state combined with a c_p equation. It is necessary therefore to provide an empirical relationships for the terms α^0 (Section §3.2.2), α^r, ρ_r and T_r as appears in Eqs. 3.3.69 and 3.3.70.
An essential point in our problem is he determination of critical points of mixtures. This point is important especially at high pressure. Stradi et al. [99], illustrates a method for locating all the critical points of a given mixture and also to verify the nonexistence of a critical point if a mixture of a given composition does not have one.
The focal point Stradi's work is the capability to find, without know the number of mixture critical points, the mixture critical points or their approximate locations. Differently from previous models this do not lose any critical conditions and no a priori knowledge of number of critical point is necessary. The method uses a Newton generalised bisection algorithm that provides a mathematical and computational guarantee where all mixture critical points are located. The technique seems to work in several problems involving cubic equation of state models and can be applied in connection with other thermodynamic models.

3.3.6 *Residual part term*

The GERG EOS is built by two terms: a residual term and a perfect term. In particular the perfect gas mixture rule takes into account the perfect gas behaviour of the mixtures and for the Helmholtz free energy we need to consider:

$$\alpha^0(\rho, T, \overline{x}) = \sum_{i=1}^{N} x_i[{\alpha_i}^0(\rho, T) + \ln x_i] \tag{3.3.71}$$

In this equation the terms $a^0(\rho, T)$ are the Helmholtz free energy EOS for each of the considered species.
We disclose that in the range of higher temperatures the NASA polynomials, in the range of real fluid the following relationship, assumed:

$$a^0 = \frac{R^\star}{R} + \left[\ln\left(\frac{\rho}{\rho_{c,i}}\right) + {n^0}_{i,1} + {n^0}_{i,2}\frac{T_{c,i}}{T} + {n^0}_{i,3}\ln\frac{T_{c,i}}{T} + \right.$$

$$+ \sum_{k=4,6}^{N} {n^0}_{i,k} \ln\left|\sinh\left({\theta^0}_{i,k}\frac{T_{c,i}}{T}\right)\right| + \tag{3.3.72}$$

$$\left. - \sum_{k=5,7}^{N} {n^0}_{i,k} \ln\left|\cosh\left({\theta^0}_{i,k}\frac{T_{c,i}}{T}\right)\right| \right]$$

where $\rho_{c,i}$ and $T_{c,i}$ are the critical values of the pure species which can be find in tables, see Urbano [77], and ${n^0}_{i,k}$ and ${\theta^0}_{i,k}$ are the empirical coefficients also find in tables (Urbano [77])
R is the current molar gas constant, and $R^\star$ is a former gas constant for which relationships were calibrated:

$$R = 8.314472 J mol^{-1} K^{-1}, \quad R^\star = 8.314510 J mol^{-1} K^{-1} \tag{3.3.73}$$

The perfect gas terms of equation 3.3.72 are obtained combining the perfect gas law and equation for the specific heat at constant pressure give by "textitJaeschke and Schley" how cited by Urbano [77]. The GERG equation includes both the departure Helmholtz free energy of each species, linearly combined using the mole fraction x_i and the residual behaviour of the mixture (the double summation is called departure function):

$$a^r(\delta, \tau, \overline{x}) = \sum_{i=1}^{N} x_i {a^r}_i(\delta, \tau) + \sum_{i=1}^{N-1} \sum_{j=i+1}^{N} x_i x_j F_{ij} {a^r}_{ij}(\delta, \tau) \tag{3.3.74}$$

From equation 3.3.74 the residual part of the reduced Helmholtz free energy of the i-th species is given by the pure substance equation of state:

$${a^r}_i(\delta, \tau) = \sum_{k=1}^{K_{Pol,i}} n_{i,k} \delta^{d_{i,k}} \tau^{t_{i,k}} + \sum_{k=K_{Pol,i}+1}^{K_{Pol,i}+K_{Exp,i}} n_{i,k} \delta^{d_{i,k}} \tau^{t_{i,k}} e^{-\delta^{c_{i,k}}} \tag{3.3.75}$$

The coefficients $n_{i,k}$, $d_{i,k}$, $t_{i,k}$ and $c_{i,k}$ for the species of interest can be list in suitable tables (see Urbano [77]).
In the departure function (double summation in Eq. 3.3.74) F_{ij} is an adjustable factor which relates the behavior of one binary mixture to the one which can be reported in tables used for the species of interest. The remaining part of the departure term is the function $a^r{}_{ij}(\delta,\tau)$ which is given for each specific binary mixture as:

$$a^r{}_{ij}(\delta,\tau) = \sum_{k=1}^{K_{Pol,ij}} n_{ij,k}\delta^{d_{ij,k}}\tau^{t_{ij,k}} + \\ + \sum_{k=K_{Pol,ij}+1}^{K_{Pol,ij}+K_{Exp,ij}} n_{ij,k}\delta^{d_{ij,k}}\tau^{t_{ij,k}} e^{-\eta_{ij,k}(\delta-\epsilon_{ij,k})^2-\beta_{ij,k}(\delta-\gamma_{ij,k})} \tag{3.3.76}$$

The values for the coefficients $n_{ij,k}$ and the exponents $n_{ij,k}$ and the exponents $d_{ij,k}$ $t_{ij,k}$ $\eta_{ij,k}$ $\epsilon_{ij,k}$ $\beta_{ij,k}$ and $\gamma_{ij,k}$ are given in tables (see Urbano [77]).

The reduced density δ and temperature τ are calculated by means of the composition-dependent reducing functions (density is expressed in this formula in mol/dm^3):

$$\frac{1}{\rho_r(\overline{x})} = \sum_{i=1}^{N} x^2{}_i \frac{1}{\rho_{c,i}} + \\ + \sum_{i=1}^{N-1}\sum_{j=i+1}^{N} 2x_i x_j \beta_{v,ij}\gamma_{v,ij}\frac{x_i+x_j}{\beta^2{}_{v,ij}x_i+x_j}\frac{1}{8}\left(\frac{1}{\rho^{1/3}{}_{c,i}}+\frac{1}{\rho^{1/3}{}_{c,j}}\right)^3 \tag{3.3.77}$$

$$T_r(\overline{x}) = \sum_{i=1}^{N} x^2{}_i T_{c,i} + \\ + \sum_{i=1}^{N-1}\sum_{j=i+1}^{N} 2x_i x_j \beta_{T,ij}\gamma_{T,ij}\frac{x_i+x_j}{\beta^2{}_{T,ij}x_i+x_j}(T_{c,i}\cdot T_{c,j})^{0.5} \tag{3.3.78}$$

The binary parameters $\beta_{v,ij}$, $\gamma_{v,ij}$, $\beta_{T,ij}$ and $\gamma_{T,ij}$ are listed in suitable tables, Urbano [77].

In the figure 3.3.14 comparison among the density diagrams of oxygen, for several EOS is shown. The cubics EOS are compared with the GERG equation. Details of comparison are shown in figure 3.3.15 where is visible the behaviour of several equation to change of temperature.

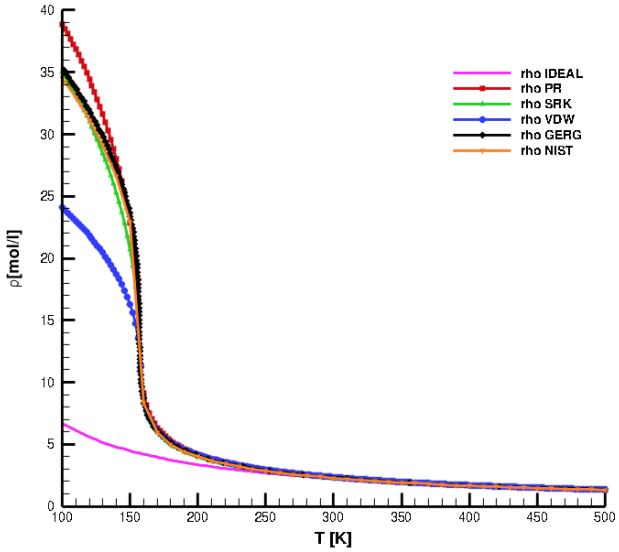

Figure 3.3.14: Comparison among oxygen's density diagrams for several EOS for pressure at 55 bar. — denotes the ideal gas EOS; ■ symbol denotes the PR equation; ▲ symbol denotes the SRK equation; ● symbol denotes the VDW equation; ♦ symbol denotes the GERG equation; ▼ symbol denotes the NIST data.

The error of several EOS is illustrated in figure 3.3.16. The SRK appears to be the best EOS in comparison with the NIST data. The GERG equation exhibits a error almost constant for every temperature of usage.

3.3.7 *Other thermodynamic variables in GERG*

Once the equation of state for the reduced Helmholtz free energy is available, the other thermodynamic properties of the mixture can be obtained from its derivatives with respect to reduced temperature and density. In particular, the compressibility factor Z can be obtained as:

$$Z(\delta, \tau, \bar{x}) = 1 + \delta \left(\frac{\partial a^r}{\partial \delta} \right)_{\tau, \bar{x}} \tag{3.3.79}$$

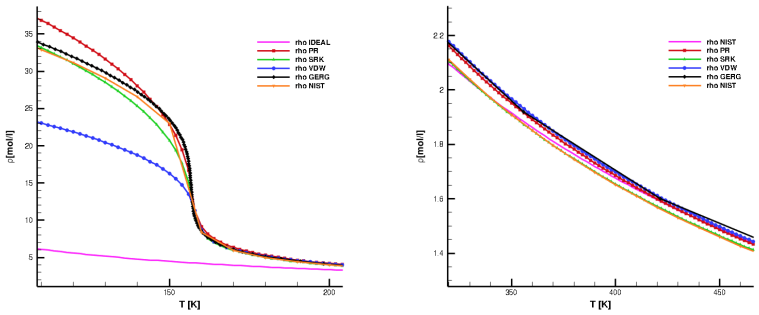

Figure 3.3.15: Details of figure 3.3.14 about the comparison among oxygen's density diagram achieved from several EOS for pressure at 55 bar. Left: detail near critical temperature. Right: detail when the temperature increases.

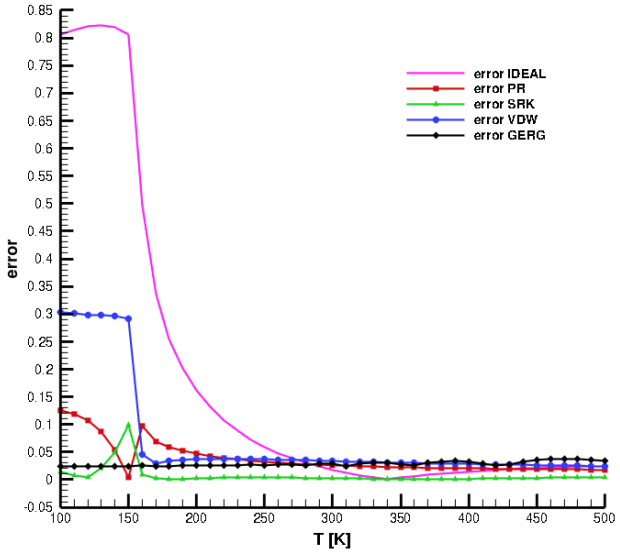

Figure 3.3.16: Comparison of oxygen's density relative errors achieved from several EOS for pressure at 55 bar. — denotes the ideal gas EOS; ■ symbol denotes the PR equation; ▲ symbol denotes the SRK equation; ● symbol denotes the VDW equation; ♦ symbol denotes the GERG equation.

pressure as:

$$p(T, \rho, \overline{x}) = Z\rho RT \tag{3.3.80}$$

enthalpy as:

$$\frac{h(\delta, \tau, \overline{x})}{RT} = 1 + \tau \left[\left(\frac{\partial a^0}{\partial \tau} \right)_{\delta, \overline{x}} + \left(\frac{\partial a^r}{\partial \tau} \right)_{\delta, \overline{x}} \right] + \delta \left(\frac{\partial a^r}{\partial \delta} \right)_{\delta, \overline{x}} \tag{3.3.81}$$

constant pressure specific heat as:

$$\begin{aligned} \frac{c_p}{R} = & -\tau^2 \left[\left(\frac{\partial^2 a^0}{\partial \tau^2} \right)_{\delta, \overline{x}} + \left(\frac{\partial^2 a^r}{\partial \tau^2} \right)_{\delta, \overline{x}} \right] + \\ & + \frac{\left[1 + \delta \left(\frac{\partial a^r}{\partial \delta} \right)_{\tau, \overline{x}} - \delta\tau \left(\frac{\partial^2 a^r}{\partial \tau \partial \delta} \right)_{\overline{x}} \right]^2}{\left[1 + 2\delta \left(\frac{\partial a^r}{\partial \delta} \right)_{\tau, \overline{x}} + \delta^2 \left(\frac{\partial^2 a^r}{\partial \delta^2} \right)_{\tau, \overline{x}} \right]} \end{aligned} \tag{3.3.82}$$

3.3.8 *Thermal expansion coefficient, and isothermal compressibility*

We introduce the definition of the *thermal expansion coefficient*, β, and the *isothermal compressibility*, k, as introduced by Koretsky [49]. Starting from the concept that the volumes of condensed phases are also much less sensitive to temperature and pressure than gases, it is possible to adjust, the measured values, for temperature or pressure changes by using a Taylor series expansion on density. We can say the same for the liquids below the critical temperature for which we can neglect all terms except the linear term of the Taylor expansion. In this way, it is possible to define a temperature and a pressure depending on the volume with the *thermal expansion coefficient*,β, and the *isothermal compressibility*, k, respectively as:

$$\beta = \frac{1}{v} \left(\frac{\partial v}{\partial T} \right)_P \tag{3.3.83}$$

$$k = -\frac{1}{v} \left(\frac{\partial v}{\partial P} \right)_T \tag{3.3.84}$$

CONCLUSIONS

In the chapter we compared, in the oxygen case, the three cubic equations of VDW, PR and RKS with the NIST data, using the density and the Andrews diagram. Comparig the PR equation with the NIST data we note that the PR equation for the temperature values lower than that critic one, has a maximum of density higher than that obtained by NIST. Near the critical temperature the relative error is lower than other equations. When the temperature decreases the RKS equation, in density term, exhibits low relative error. We can agree with the choice to use the PR. The GERG equation, how showed, presents a relative error almost constant respect of temperature. In a further analysis we showed that the dependence from the kind of equations in terms of the compressibility of fluid, in reduced temperature terms, changes respected the reduced pressure. This comparison has been done for the nitrogen, using the VDW, PR EOS.

4

GOVERNING EQUATIONS AND CHEMISTRY MODEL

Contents

OBJECTIVES OF CHAPTER

In this chapter illustrates, briefly, and in generic form, the governing equations and chemical model that CFD++ uses. In the final section we will present the Conformal Mapping Mesh Generator.

4.1 GOVERNING EQUATIONS

The general form of transport equations, such as mass conservation equation that CFD++ solves to obtain a flow field solutions, is:

$$\frac{\partial \mathbf{U}}{\partial t} + \frac{\partial(\mathbf{F_i} - \mathbf{F_v})}{\partial x} + \frac{\partial(\mathbf{G_i} - \mathbf{G_v})}{\partial y} + \frac{\partial(\mathbf{H_i} - \mathbf{H_v})}{\partial x} = \mathbf{S} \qquad (4.1.1)$$

where $\mathbf{U}$, $\mathbf{F}$, $\mathbf{G}$, $\mathbf{H}$, and $\mathbf{S}$ denote, respectively, dependent conservation variables, flux in x direction, flux in y direction, flux in z direc-

tion, source term and i, v indicate the inviscid and viscous flow terms, respectively. We can write the inviscid part for the RANS equations:

$$\mathbf{U} = \begin{pmatrix} e \\ \rho \\ \rho u \\ \rho v \\ \rho w \\ \rho\sigma_1 \\ \vdots \\ \rho\sigma_N \end{pmatrix}, \quad \mathbf{F_i} = \begin{pmatrix} (e+p)u \\ \rho u \\ \rho u^2 + p \\ \rho uv \\ \rho uw \\ \rho u\sigma_1 \\ \vdots \\ \rho u\sigma_N \end{pmatrix},$$

$$\mathbf{G_i} = \begin{pmatrix} (e+p)v \\ \rho v \\ \rho vu \\ \rho v^2 + p \\ \rho vw \\ \rho v\sigma_1 \\ \vdots \\ \rho v\sigma_N \end{pmatrix}, \quad \mathbf{H_i} = \begin{pmatrix} (e+p)w \\ \rho w \\ \rho wu \\ \rho wv \\ \rho w^2 + p \\ \rho w\sigma_1 \\ \vdots \\ \rho w\sigma_N \end{pmatrix} \tag{4.1.2}$$

In equations 4.1.2 the σ_i represents the turbulence kinetic energy and undamped eddy viscosity, in case of turbulence model and, the species in case of multi-species flow.

For a perfect gas EOS ($p = \rho RT$), the coupling among pressure, density and temperature can be written in terms of the conservation variables:

$$p = (\gamma - 1)\left(e - \frac{1}{2\rho}\left((\rho u)^2 + (\rho v)^2 + (\rho w)^2\right)\right) \tag{4.1.3}$$

In the viscous part for the RANS equations appear the viscous stress terms τ_{ij} (equations 4.1.6). The viscous part can be written as follows:

$$\mathbf{F_v} = \begin{pmatrix} K\frac{\partial T}{\partial x} + u\tau_{xx} + v\tau_{xy} + w\tau_{xz} \\ 0 \\ \tau_{xx} \\ \tau_{xy} \\ \tau_{xz} \\ \rho D \frac{\partial \sigma_1}{\partial x} \\ \vdots \\ \rho D \frac{\partial \sigma_N}{\partial x} \end{pmatrix}$$

$$\mathbf{G_v} = \begin{pmatrix} K\frac{\partial T}{\partial y} + u\tau_{xy} + v\tau_{yy} + w\tau_{yz} \\ 0 \\ \tau_{xy} \\ \tau_{yy} \\ \tau_{yz} \\ \rho D \frac{\partial \sigma_1}{\partial y} \\ \vdots \\ \rho D \frac{\partial \sigma_N}{\partial y} \end{pmatrix} \tag{4.1.4}$$

$$\mathbf{H_v} = \begin{pmatrix} K\frac{\partial T}{\partial z} + u\tau_{xz} + v\tau_{yz} + w\tau_{zz} \\ 0 \\ \tau_{xz} \\ \tau_{yz} \\ \tau_{zz} \\ \rho D \frac{\partial \sigma_1}{\partial z} \\ \vdots \\ \rho D \frac{\partial \sigma_N}{\partial z} \end{pmatrix}$$

$$\tau_{xx} = 2\mu\frac{\partial u}{\partial x} - \frac{2}{3}\mu\left(\frac{\partial u}{\partial x} + \frac{\partial v}{\partial y} + \frac{\partial w}{\partial z}\right)$$

$$\tau_{yy} = 2\mu\frac{\partial v}{\partial y} - \frac{2}{3}\mu\left(\frac{\partial u}{\partial x} + \frac{\partial v}{\partial y} + \frac{\partial w}{\partial z}\right) \tag{4.1.5}$$

$$\tau_{zz} = 2\mu\frac{\partial w}{\partial z} - \frac{2}{3}\mu\left(\frac{\partial u}{\partial x} + \frac{\partial v}{\partial y} + \frac{\partial w}{\partial z}\right)$$

For the Stokes theorem for the gases $\lambda = 2/3\mu$

$$\tau_{xy} = \mu\left(\frac{\partial u}{\partial y} + \frac{\partial v}{\partial x}\right)$$

$$\tau_{xz} = \mu\left(\frac{\partial u}{\partial z} + \frac{\partial w}{\partial x}\right) \tag{4.1.6}$$

$$\tau_{yz} = \mu\left(\frac{\partial v}{\partial z} + \frac{\partial w}{\partial y}\right)$$

$$T = \frac{p}{\rho R} = \frac{(\gamma-1)}{R}\left(\frac{e}{\rho} - \frac{1}{2\rho^2}\left((\rho u)^2 + (\rho v)^2 + (\rho w)^2\right)\right) \tag{4.1.7}$$

The source term can be write as:

$$\mathbf{S} = \begin{pmatrix} 0 & 0 & G_x & G_y & G_z & \Omega_1 & \cdots & \Omega_N \end{pmatrix}^T \tag{4.1.8}$$

4.2 CHEMISTRY MODEL

From the point of view of the chemistry model used, the CFD++ flow solver is based on the finite-rate reactions. For a general chemical reaction k:

$$\sum_i \nu'_{ik} M_i \rightleftharpoons \sum_i \nu''_{ik} M_i \tag{4.2.1}$$

where i denote the species and k the reaction step. The rate of production of species i for a generic reaction k is:

$$\omega_{ik} = \widetilde{W}_i \left(\nu''_{ik} - \nu'_{ik}\right) \left[K_{fk} \prod_l C_l^{\nu'_{ik}} - K_{bk} \prod_l C_l^{\nu''_{ik}}\right] \tag{4.2.2}$$

The forward rate constant for each reaction step k use the Arrhenius kinetics:

$$K_{fk} = \widetilde{A}_k T^{N_T} exp\left(\frac{-E_{A_k}}{R_0 T}\right) \tag{4.2.3}$$

The input for any kinetic step that including reactions with third bodies are: $\nu''_{ik}, \nu'_{ik}, \widetilde{A}_k, N_T, N_p, E_{Ak}$

The backward rate constant K_{bk} is computed from the equilibrium condition:

$$\frac{K_{fk}}{K_{bk}} = \left(\frac{P_{atm}}{R_o T}\right)^{\sum_i \nu'_{ik} \widetilde{W}_i g_i} exp\left(\frac{-\Delta\overline{G}_k}{R_0 T}\right) \tag{4.2.4}$$

the equation 4.2.5 defines the Gibbs energy for a reaction step k:

$$\Delta\overline{G}_k = \sum_{i=1}^{N} \nu'_{ik} \widetilde{W}_i g_i - \sum_{i=1}^{N} \nu'_{ik} \widetilde{W}_i g_i \tag{4.2.5}$$

4.3 SIMPLIFIED KINETIC MECHANISM

Starting from GRI-Mech 3.0,10 which consists of 53 species and 325 reversible reactions, was generated and validated (Valorani et al. [116]) a simplified kinetic mechanism for GCH4/GO2 at ambient pressure (considering the N2 initially present in the chamber as an inert), which involves only 15 species, and 57 reversible reactions (Appendix §E) All N-containing species were removed, except N2, together with all N-related reactions, to yield a detailed mechanism with 36 species and 219 reversible reactions. The basic concept to achieve the mechanism simplification is the elimination of all the reactions whose importance indices (defined as in Valorani et al. [115]), relative to a set of user-defined active species, are smaller than a chosen tolerance. Next, a new set of active species is identified by collecting all the species participating in the remaining reactions. The procedure is repeated iteratively until convergence. Errors influenced the acceptation of different reduced mechanismes. The errors are evaluated considering the igni-

tion delay time and the equilibrium temperature. For examlple: the authors considered several deposited energy and they observed that the error in the ignition delay time is low only down to 25 species or 16 species, it depends on the energy deposited. Both the ignition delay time error and the equilibrium temperature error remain small providing that the number of retained species is larger than 13. However, inspection of the trajectories in the phase space CO_2 temperature shows that the simplified mechanism with 16 species and 58 reactions offers a better approximation. The mechanism (15 species 57 reactions simplified chemical reaction) was validated. The validation was firstly conducted by computing a 1D premixed flame with both the detailed and the simplified mechanisms. Secondly, a 2D direct numerical simulation (DNS) was performed to study the kernel formation in a methane/air mixing layer with the simplified kinetic mechanism. The approach followed for the aforementioned 1D and 2D computations relies on a wavelet approach. The compressible reactive Navier-Stokes model includes detailed chemical kinetics, multi-species transport, momentum, and energy diffusion. These problems contain a wide range of spatial and temporal scales. The wavelet-based adaptive multi-resolution (WAMR) (Paolucci ed al. [87]) method allows this range of scales to be resolved (up to a user-specified accuracy) with the minimal number of collocation of points (saving in computer time). For a detailed description of the wavelet method, the interested reader could refer to Paolucci ed al. [87].

4.4 CONFORMAL MAPPING MESH GENERATOR

The main requirement of a successful mesh generator, able to cope with a multi-injector thrust chamber, is the ability to conform with the topology of the jet flame stemming from each co-axial injector, which is essentially axi-symmetric for a large portion of the large cylindrical cavity of the combustion chamber. Moreover, the mesh should account for a smooth transition of the space lying in-between adjacent injectors, which is the region where the thermo-acoustic interaction of the individual jet flames occur.

Therefore, the mesh generator should be able to cope with the singularity at the axis of any axi-symmetric discretization and with the transition from a cylindrical geometry to a rectangular box (either the whole chamber or a the fraction of it associated with a single injector).

One way to move from a rectangular box to a circle, and from a circle to a rectangular box involves using two-dimensional conformal mappings to generate the discretization in the cross-sections of injectors, combustion chamber, and nozzle. Next, the discretization of the

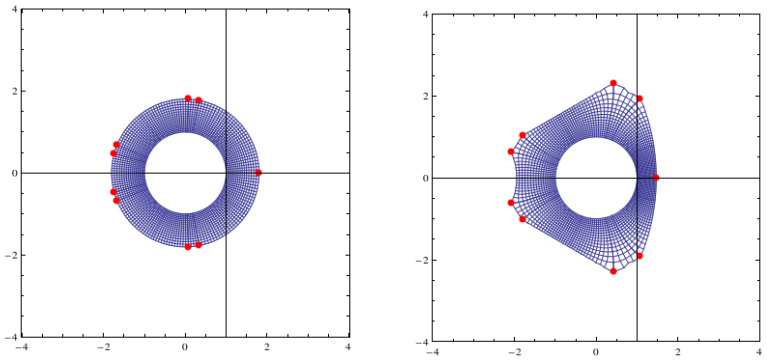

Figure 4.4.1: A polar mesh discretization a circular crown is mapped into the region comprised between a circle and a (non regular) octagon using the Theodorsen-Garrick mapping.

cross-section is extruded in the axial direction to accommodate the changes of the geometry in the meridional plane.

Two-dimensional conformal mapping is a rather old analytical technique based on the application in series of suitable mappings of the metric of the space obtained by using analytic function of complex numbers. The distinguishing feature of mappings based on analytic function is their property of generating two mutually orthogonal, and smoothly varying, families of constant curvilinear coordinates. The smooth and orthogonal changes of the metric usually determines the minimum discretization error irrespective of the particular technique used to discretize the flow model (finite elements, finite volumes, finite differences).

The critical mapping which enabled us to generate the type of curvilinear mesh that we deem the most suited to discretize a multi-injector thrust chamber is referred in the literature as Theodorsen-Garrick. Nasuti, Valorani, and Onofri [70] proposed the variant of this method which has been adopted in this work. The Theodorsen-Garrick mapping is an iterative method to find the Fourier coefficients which define the mapping from a unit circle to a closed circuit enclosing the unit circle, see figure 4.4.1

The discretization of the cross-section is extruded along the axial direction to generate the full 3D mesh in the volume of the combustion chamber (left on figure 7.5.3).

The results obtained by mesh generator are showed in figure 4.4.2.

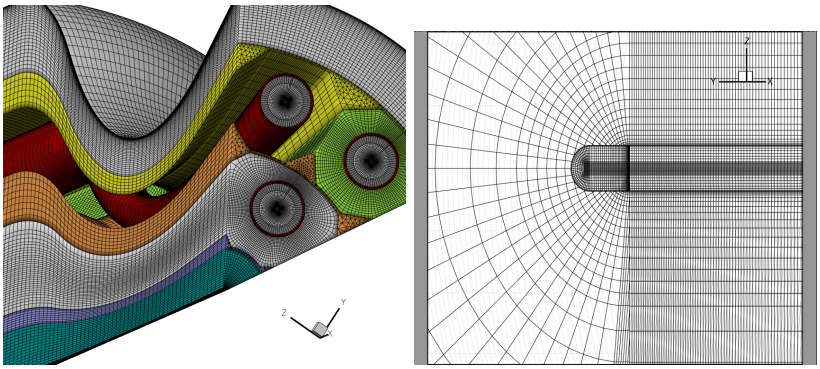

Figure 4.4.2: Detail mesh used in simulations. Left: mesh extruded along the axial direction to generate the full 3D mesh in the volume of the combustion chamber. Right: single injector mesh.

CONCLUSIONS

We have illustrated the the governing equations and the chemical model that CFD++ uses and at the end we have presented the new conformal mapping mesh generator.

5

FLAME PROPAGATION, SPREADING, AND STABILIZATION

Contents

OBJECTIVES OF CHAPTER

In this chapter we will briefly list the focal points that identify the physical processes that happen in the combustion chamber: the ignition, the flame stabilisation, the spray and atomization process. Understanding the length and position of flame is essential to evaluate the heat flux on the wall and plate. In order to highligth the importance of injector recess on the flame anchoring and influence of post-tip thickness of oxygen we show qualitatively, several flame configurations (Candel [9]). Moreover, some results about the Hyprob program, are presented in the chapter §7 but only on a quality level, with the aim to show the importance of a correct rappresentation of flame, his position and length. We illustrate the simulation of a simple 2D axisymmetric model, the SSBB model (monoinjector), and the results obtained for a geometry 3D, the DEMO geometry.

5.1 PHYSICAL PROCESSES

A better mastery of mechanisms of flame propagation, spreading flame, and flame stabilisation under supercritical and transcritical conditions can be obtained understanding totally the following physical processes:

- Ignition

- Flame propagation and spreading
- Mechanism of flame stabilization
- Factors governing the flame length
- Accurate estimation of heat transfer to the chamber walls and injector plate.
- Combustion dynamics and triggering of high frequency combustion instabilities.

One can add:

- Processes controlling liquid jet breakup
- Atomization phenomena, and mixing
- Spray vaporization and combustion
- Stabilization and flame spread near the injection backplane
- Experimental diagnostics applicable to cryogenic flames under high-pressure conditions

From engineering point of view the main problems can be identified in:

- The definition of sequence ensuring a smooth ignition transient leading to a stable nominal operation
- The sizing of injection elements and thrust chamber that provide the required efficiency
- The reduction of low frequency instabilities and the suppression of high frequency instabilities

In the following sections we are going to illustrate the influence of coaxial injector with and without recess on the flame, cone flame, wall heat flux and flame configurations.

5.2 INJECTORS WITH AND WITHOUT RECESS

The design of combustion chamber can be improved thanks to the understanding of the behaviour of the physical processes that happen in the chamber. Identification and modelling of responsible elements of the flame position is essential factor to predict the heat flux as well as the atomization and mixing.

A crucial element that involves some of these phenomena is the injector. How illustrated in Sutton [102], there are many kinds of injector:

- impinging-stream: multiple-hole injectors, self-impinging
- shower head
- coaxial injector

In figures 5.2.1 and 5.2.2 are showed the different kinds of injectors.

The *impinging-stream* (5.2.1) can be: multiple-hole injectors or self-impinging. These kinds of injection are applicable to propellants that poorly vaporize, to archieve an high combustion efficiency and combustion instabilities. The multiple-hole injectors are used with oxygen/hydrocarbon and storable propellants and the propellants are injected with unlike doublet patterns in such a manner that the fuel and oxidizer streams impinge upon each other. The self-impinging patterns are used fuel-on-fuel and oxidizer-on-oxidizer. The injectors use nonimpinging streams of propellant usually emerging normal to the face of the injector: it is the turbulence and diffusion the main process to achieve mixing.This kind of injector requires a large chamber volume for good combustion. The *coaxial* (5.2.2) injectors can be with recess or without it and the presence of recess could improve the performance of the liquid propellant rockets. The *coaxial hollow post* (5.2.2) injectors has been used for liquid oxygen and gaseous hydrogen injectors. The hydrogen flow, at high speed (typically 330 m/s), is gasified; the liquid oxygen flow is slower (usually at less than 33 m/s). The differential velocity causes a shear action, which helps to break up the oxygen stream into small droplets (Sutton [102]).

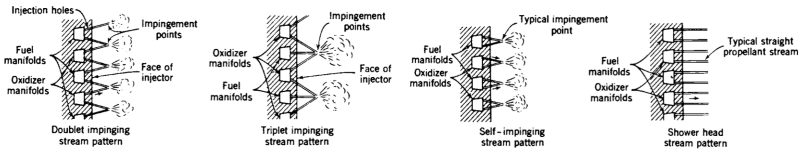

Figure 5.2.1: Several injectors type. Reprinted from Sutton[102].

Haidn et al. [55], define the recess as the axial distance of the end of the tube from the injector plate.

5.2.1 *Effects of recess*

The recess is used to improve the atomization and consequently the mixing process that in subcritical condition may lead to a flame expansion. The different recess lengths can increase the improvement of combustion efficiency and stability. For example, Haidn et al. in [55] remind that for dense fluids, the recess length can't increase for a 1.5 injector diameter, because a maximum length beyond the limit length

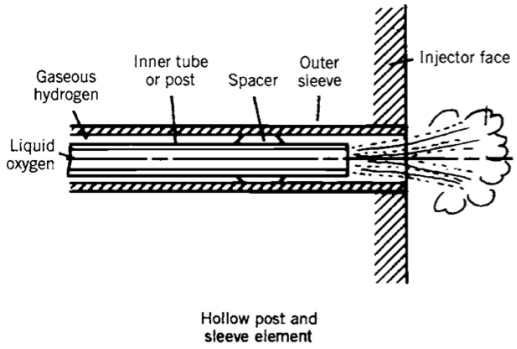

Figure 5.2.2: Coaxial injectors type. Reprinted from Sutton [102].

is not any further improvement. Furthermore, there is a different recess length between subcritical and supercritical flow caused by the different physical features. The modification of injector geometry can lead to instability phenomena. Stabilizing effects of a recessed LOX-post have been reported in LOX/ Kerosene investigations by Oefelein [20]. Mayer and Tamura [61] assumed that "*[...] the recessed region of a coaxial injector can be regarded as a small combustion chamber that is insensitive to combustion disturbances in the main chamber*". The investigators, by using numerical simulations, showed a strong high amplitude hydrodynamic instabilities in the recessed region of a coaxial injector under cold flow conditions (Kim and Kim et al. in Haidn et al. [55]). Instead, experiments conducted by Bazarov in [4] investigated about self-pulsation and the experiment results of Haidn et al. [55] in supercritical flows, when there is not recessed LOX tube figure 5.2.3, showed that the expansion angle of the jet is smaller than in the case of the recessed tube. Probably, the recess presence leads to a better initial atomization and mixing. After some diameters the flame expands and exceeds the radial dimension of the windows in the case of the recessed LOX tube and the total flame volume seems to be larger in the case of a recess. By OH emission profiles, showed in figures 5.2.3 and 5.2.4, Haidn observes that the reacting shear layer between liquid oxygen and gaseous methane is thicker and he deducts a possible zone that anchoring the flame inside the recessed region.

5.2.2 *Flame anchoring mechanisms*

From engineering point of view, the determination of anchoring and flame position is necessary to can obtain a realistic evaluation of heat flux.
The figure 5.2.5 exhibits the density field both for non reacting flow case and for reacting flow case for the LOX/H2 propellants. It is vis-

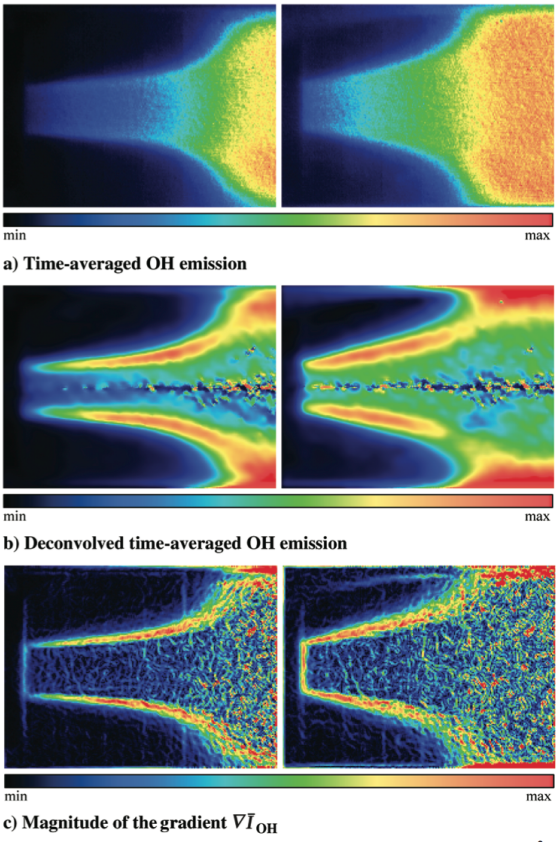

Figure 5.2.3: "OH emissions images of the near-injector zone (33.5 x 25 mm^2); injector without recess (left) and with recess (right); d_o= 7.4mm". Reprinted from Haidn et al. [55].

ible the vortex shedding and a comb-like structures typical of trans-critical state §2.3. The behaviour of oxygen stream shows that there is a oxygen movement straight forward, in hot flow case, whereas it is rolled up by the large vortices shed at the H2 corner of the lip in the cold flow case. The interactions between flame and vortices drive the turbulent mixing and reduction in the vertical extent of the mixing layer under reacting conditions how already been observed at low pressure.

In the years, several studies about the stabilization mechanism of the flame, were made by several workers. Among the researchers Candel [9], for example, focused his studies on stabilization mechanism of the flame in the wake of the oxygen injector lip and its development in the near vicinity of the oxygen flow. We can observe an alike feature also in the simulations with LOX/H2, carried by Oefelein [73]. In the years, several studies about the stabilization mechanism of the flame, were made by several workers. Among the researchers Candel [9], for example, focused his studies on stabilization mechanism of the flame in the wake of the oxygen injector lip and its development

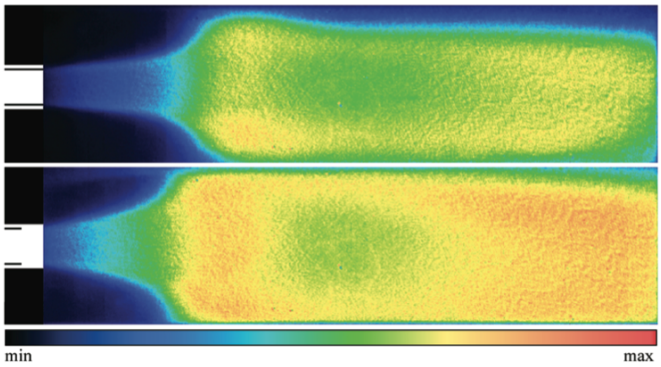

Figure 5.2.4: "Average OH emissions (100 x 25 mm^2) taken during phase 1 $P_r > 1$; injector without recess (top) and with recess (bottom); d_o= 7.4mm". Reprinted from Haidn et al. [55].

in the near vicinity of the oxygen flow. We can observe an alike feature also in the simulations with LOX/H2, carried by Oefelein [73]. Under normal operating conditions, the flame seems stable, the flame edge is close to the lip and the reaction front develops near the oxygen stream boundary but we can observe at some distance from the injection plane that it becomes highly turbulent. Moreover a critical hydrogen feed temperature (case that has been studied by Candel [9]) could causing a flame that lifts off oxygen injector and sensitise it to acoustic coupling.

It is useful, to understand the importance of the effect of injector geometries on the flame to illustrate the several types of flame geometries as in figure 5.2.6, in Candel [9], and to identify configurations corresponding to stable flames and conditions leading to the flame lift off.
Candel et al. [9] considered in annalysis about flame role two parts:

- a hot slow-moving zone just behind the oxygen injector lip in which the flow is laminar
- a thin-spreading diffusion flame which becomes turbulent within a few millimeters.

Juniper [41], recognised that three mechanisms of flame blowout are possible involving a turbulent flame: the flame extinguishes just downstream in regions of excessive strain rate and can not support itself in the recirculation zone. Oxygen evaporation does not feed the flame that quenches on the cold liquid surface. The *first*, blowout mechanism, was explored in Juniper [41], by considering a counterflow hydrogen flame above condensed oxygen. The *second* and *third* extinction mechanisms were explored in "*Juniper and Candel (2003a), and Juniper and Candel (2003c)*" ([41]) using three non dimensional

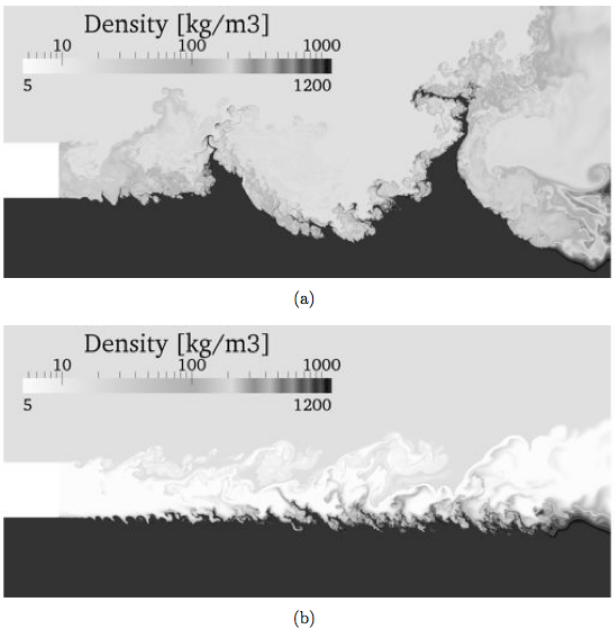

Figure 5.2.5: Non reactive and reactive flow. Reprinted from Ruiz [92].

parameters. The first parameter is the Damköhler number that affects the flame standoff distance in a cross-flow flame. Another non-dimensional parameter is the ratio of heat release due to chemical reaction to the liquid's latent heat of vaporization useful when a flame is above a liquid fuel and the last parameter is the ratio of the LOX tube thickness to the flame thickness $\psi = h_s/df$ introduced by Candel [58] In figure 5.2.6, Candel et al. [9], identified several possible flow configurations of a flame behind a step over a liquid fuel:

(a) the gaseous stream separates from the step and a flame starts in a recirculating zone

(b) the gaseous stream follows the step streamline. The flame tip is next to the liquid reactant

(c) both streams meet half way behind the step, where a flame forms

(d) the gaseous stream is separated from the step. Vaporized liquid reactant follows the streamline of the step. The flame forms at the top of the step

(e) the liquid reactant vaporizes rapidly. A corner flame forms above the step

(f) the formation of a double recirculation zone behind the step and stabilization of the flame to downstream

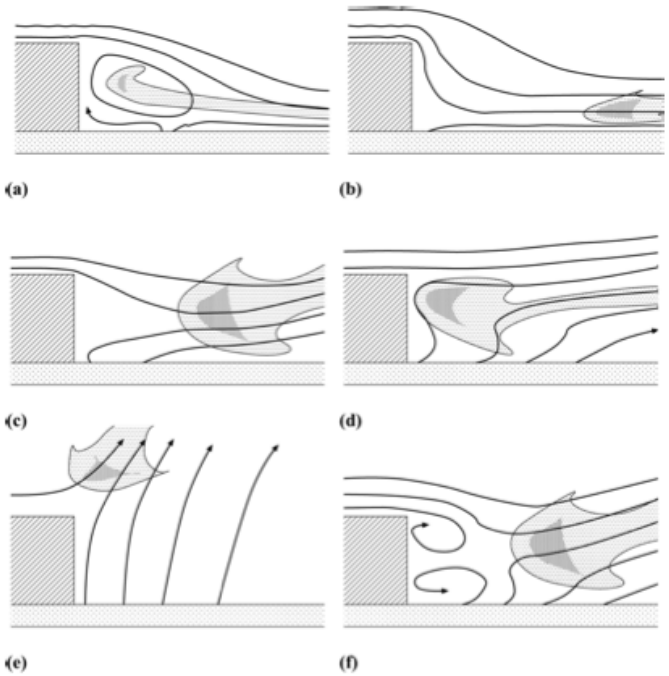

Figure 5.2.6: Various possible flow configurations of a flame. Reprinted from Candel et al. [9].

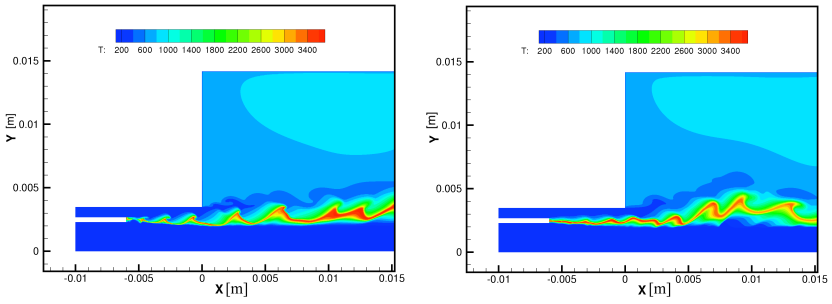

Figure 5.2.7: Left: URANS; Right: LES of supercritical LOX/methane injection at 60 bar.

In order to a process understanding we reveal in advance, in this section, the results about the anchoring flame study, figures 5.2.7 and 5.2.8. The results and figures will be debated later, in the Chapter §7 when we will show the numeric results of simulations obtained in detail. In effect, in order to investigate the impact of the numerical approach on the anchoring mechanism,both URANS and LES simulation runs of the injection zone were carried out in an axi-symmetric setting. A supercritical pressure of 60 bar was chosen as an indepen-

dent parameter and a supersonic nozzle outflow is replaced with a subsonic back pressure outflow condition.

The recirculation zone, in figure 5.2.8, is resolved with 16 cells.

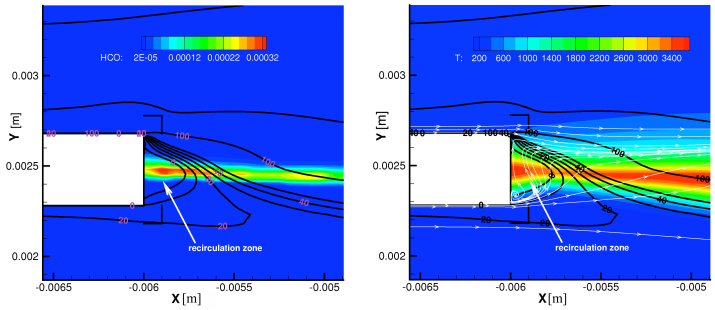

Figure 5.2.8: LES of LOX/CH_4 injection at $p_c = 60$ bar. Left, formyl (HCO) radical mass fraction, Right, temperature field. Also shown isocontours of horizontal velocity component.

5.2.3 *Effects of flame position*

In figure 5.2.9 is shown the average value of heat flux field with the heat flux value on chamber wall. We will describe in §7.4, the existence of some regions where high heat flux field, figure 5.2.10. The Figures show an area of the lateral wall adjacent to the injector plate where is possible to identify flame cones that merge and impinge on the lateral wall causing a rapid increase of heat flux.

This region exhibits a behaviour qualitatively similar to the injector footprints observed, figure 5.2.11, on the chamber wall (injector wall interactions) in a High Pressure LOX/GH2 Subscale Combustion Chamber (R. Arnold, et al., AIAA 2008-5242, 44th AIAA/ASME/SAE/ASEE Joint Propulsion Conference & Exhibit 21 - 23 July 2008, Hartford, CT).

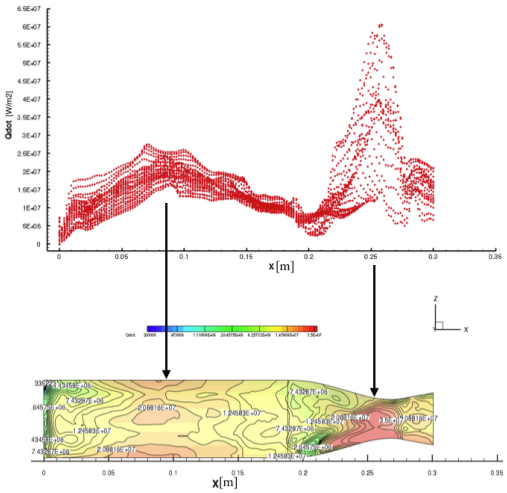

Figure 5.2.9: Average value of heat flux field and the heat flux value on chamber wall. The arrows indicate the points of relative maximum.

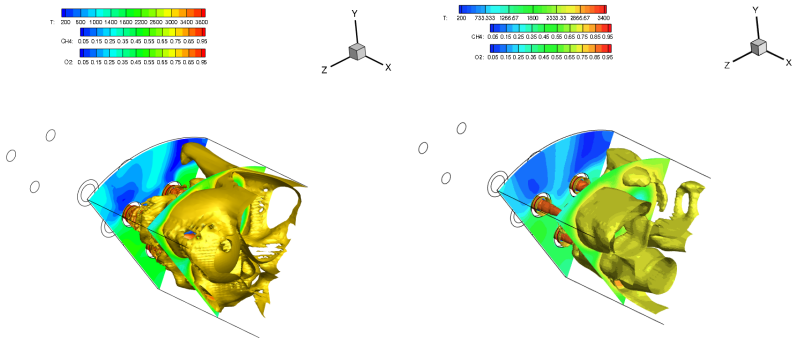

Figure 5.2.10: 3D view chamber: two instantaneous temperature and oxygen iso-surfaces with Methane slice. The flames brush the chamber wall.

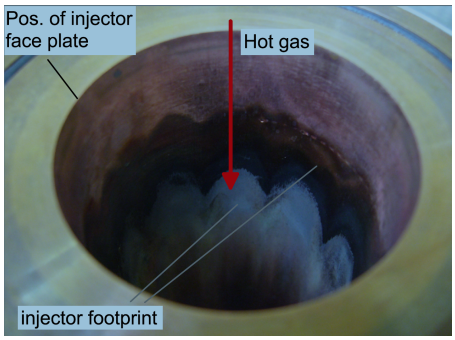

Figure 5.2.11: Injector footprints on chamber wall (injector wall interactions) in a High Pressure LOX/GH2 Subscale Combustion Chamber (reprinted from R. Arnold, et al., AIAA 2008-5242, 44th AIAA/ASME/SAE/ASEE Joint Propulsion Conference & Exhibit 21 - 23 July 2008, Hartford, CT).

CONCLUSIONS

The flame position has an important role to evaluate the thermal flux. In the case of the DEMO 3D, we have noted the existence of an impingement, on the wall. This impingement causes some tracks that have the characteristic shape like flower petals. The areas that have been touched from the flame have a heat flux higher, this effect implies a more attention on the cooling of wall and the study of injector geometry not only how an part necessary in for a correct mixing and jet atomization, if the atomization there is, but also like an important element that can determine the flame position and instability of combustion.

6

NUMERICAL ANALYSES OF COLD AND REACTIVE JETS

Contents

OBJECTIVES OF CHAPTER

In the Chapter §2, we debated the complex problematics caused by the usage of injected propellants and combustion products at high pressure. These problematics imply, for the companies interested in thrust chambers production, a marked interest in the programs that study the phenomenologies in the combustion chambers (Chapter §5). For the purpose to obtain some elements to evaluate the complex physic dynamics exhibited in the chambers, the paths aiming at the building of scale models single-injector and micro combustion multi-injectors are started. How we introduced in the Chapter §5, the aim

is that to obtain an accurate evaluation of the heat flux on the wall. This evaluation considers the interaction between the gases products by combustion on the wall and the flame, in mono-injector case or the flames in the case of multi-injectors. In this Chapter we would like:

- Finding an opportune numeric strategy. A strategy that have to be an efficient compromised between the numeric time and modeling of problem physic. The verify a correct modeling of problem and suitable numeric strategy is done with the choose of adequate variables, like density, temperature, velocity, evaluated in the case analysed, on the principale planes and on the centerline. Moreover, where possible, we have been realised a comparison between the observed variables with the experimental data. A representation of relative fields in the variable used, completed the analysis.
- Evaluating of a spatial and temporal suitable discretization, and numeric solution method have the aim to resolve the criticality caused by the modeling problem of a complex physic problem composed of different sub-problems: from injection to mixing, to combustion.
- Identifying a solution method: preconditioned density based o pressure based (only with the time integration DTS). If the DTS had not have to be converge in every internal step the method would determine the error on the conservation equations.
- comparison with numerical setup used in the Hyprob program.

We have divided the Chapter in **two parts**:

- the first part is about the ***mono-species fluids***, in particular nitrogen.
- the second part where we present the ***reactive flows*** that use the propellants LOX/methane.

The study of ***mono-species fluids*** considers the exploration, in the Diagram Phases, of two areas that are showed in figure 2.2.3 in subsection §2.2.2. The characteristics of those two areas, in terms of density and specific heat to constant pressure, are showed in figures 6.1.1. We considered:

- realising a comparison between the results obtained by CFD + + and those obtained by Schmitt ([95]) with the AVBP code by means of two simple cases: supercritical fluid injection and "trancritical" fluid injection.

- realising a comparison between the results obtained by CFD++ and those experimental obtained by Mayer (cases #3 e #4) [62]
- realising a comparison by means the literature parameters that can represent the jet: length of jet 6.1.3 or 6.1.4, spread angle, radial 2.1.10, and centerline density 2.1.13. We test and compare in both cases, identified with Mayer numeration case #3 and case #4, several solution methods and time integration (using DTS or not), to find the method that, in comparison with Mayer 's experimental data and Schmitt's numerical data, produces a relative error lower.

For ***reactive flows*** we choose to go on for grades. We considered:

- a free jet
- a combustion chamber with nozzle

The injection characteristics are: oxygen injection in transcritical conditions and methane in supercritical conditions. The addition of nozzle represents an increased of the difficulties.

6.1 INJECTION CHARACTERISTICS OF NITROGEN

In the figures 6.1.1 are specified respectively, in orange color and green, the cases #4 e #3 in density and specific heat at constant pressure terms. In the table 5, the temperature and injection velocity details are showed.
We can observe that the case #3, in density term, is near to the curve's flexed and also is very near to pseudo-boiling temperature, where we have the maximum of specific heat at constant pressure. For this raison, we have a fast variation of variables, for instance: density and specific heat at constant pressure that for a minimum temperature increase can cross the pseudo-boiling limit and can determine a unexpected variation of variables.

We identify the two different test cases we have used the Mayer's nomenclature (see [62]) in experimental test.
In table 5 there are the test conditions:

Test Cases	**T [K]**	u_{inj} [m/s]	P_{cham} **[bar]**	T_{cham} **[K]**	Re_{inj}
Case3	126.9	4.9	39.7	298	$1.7x10^5$
Case4	137	5.4	39.7	298	$1.6x10^5$

Table 5: Test cases #3 and #4.

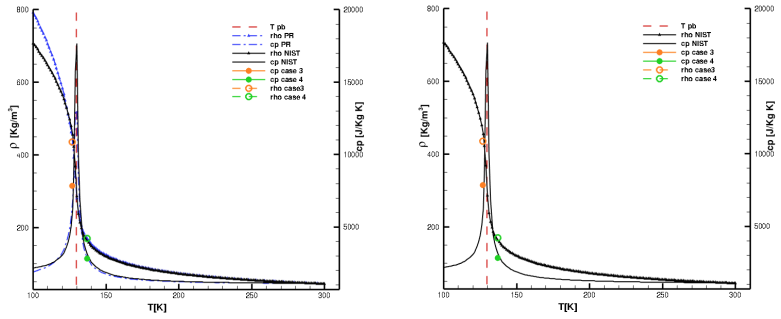

Figure 6.1.1: Density and specific heat at constant pressure for nitrogen at 37.9 bar. Left: Comparison between PR's thermodynamic properties and NIST's properties. Right: NIST's thermodynamic properties. In both figures: dashed line is T_{pb} temperature value; dashed-dot line is PR's c_p; the dashed-dot with delta symbols are the PR's density; solid line is NIST's c_p; solid line with delta symbols are NIST's density; circles are heat capacity constant pressure (c_p) for test cases #3 and #4, respectively, orange and green; circles are density for test cases #3 and #4, respectively, orange and green.

The second part (reactive flows) will use the numerical strategy chosen for non reactive flows single species.

The goal of this Chapter is the identifying an optimal strategy for the numerical integration of the set of modeling equations for the resolution of problem. We will choose among the many different model options available in CFD++ and our goal will be to maximize the numerical accuracy of the solutions and minimize the run time. This Chapter is organized in two parts as follows:

6.1.1 *Relaxation factor for transcritical flows*

In CFD++, there exists two options to carry out this calculations depending on using V_c and T_c to obtain P_c from the EOS, or T_c and P_c to obtain V_c. The two options provide different level of accuracy, and thus we carried out a preliminary assessment on the accuracy of the calculation of the critical properties.

Additionally, CFD++ provides a way to "relax" the impact of the enforcement of the real gas EoS in trans-critical flows when new products are created, as in a chemical reaction. When using cubic EOS for high-pressure applications, convergence to steady solution may deteriorate due to nonlinearities.

New species formed as product of chemical reactions may have critical properties vastly different from that of the reactants. For instance H2O formed from H2 and O2 has a critical temperature of 647.3 K.

The critical temperature of H2 is 33.2 K and that of O2 is 154.6 K, quite lower than the 647.3 K of H2O. During computational transients, the formation of products such as H2O leads to large changes to density and the velocity field. These large changes may cause the solution to diverge. To circumvent this difficulty, a new feature, "Minimum T/T_c ratio for cubic root finder", to control the changes to density has been added to CFD++, which replaces the actual reduced fluid temperature T/T_c with the prescribed $MinimumT/T_c$ value, that is if $T < (MinimumT/T_c) * T_c$ then $T = (MinimumT/T_c) * Tc$.

For simulations with a single component or a multi-component with uniform critical properties, this limit can be set low, 0.1, for example. For multi-component simulations with vastly varying critical properties, this ratio can be set closer to unity in cases where divergence occurs in severe transients that cause both the pressure and temperature of the mixture to drop below the critical values.

The effects of this "relaxation term" can be appreciated with reference to a simple test case in which we prescribed a linear variation of the temperature between 100 K to 400 K on a 1D strip illustrated in Figure 6.1.2. The density and specific heat at constant pressure for oxygen at 60 bar computed by picking two different threshold levels of the relaxation term ($MinimumT/T_c$ = 0.65 and 0.9), and by selecting either the (V_c, T_c) option or the (P_c, T_c) option are shown in Figure 6.1.3. It is apparent that the action of the relaxation term is to prevent the attainment of the (actual) high values of density and the (actual) low values of the specific heat at constant pressure in the low temperature region below the critical temperature. Therefore, the calculation should be advanced during the transients involving transcritical flows while using a high value of the "relaxation term" (say of order unity), which can be later brought to small values (say of order 0.1) when the computational transient is over.

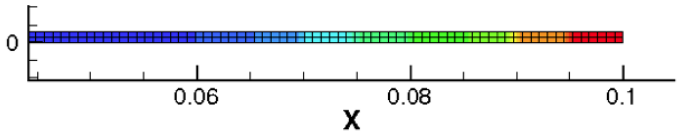

Figure 6.1.2: Simple geometry test.

6.1.2 *Mixing rules*

Among the different mixing rules available in CFD++, Kay's (Eq. (6.1.1)) and Van der Waals (Eq. (6.1.2)) mixing rules, we adopted the Kay rule

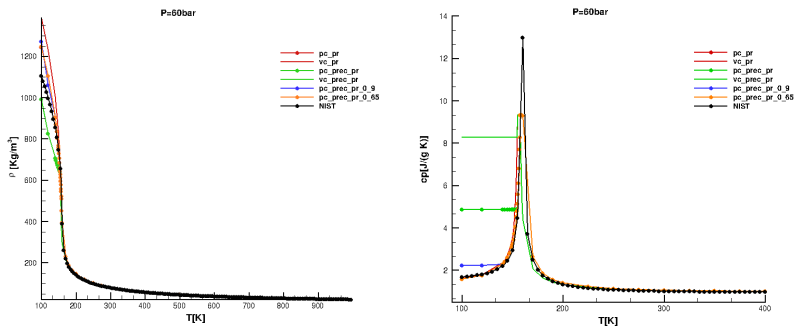

Figure 6.1.3: Density (left) and specific heat at constant pressure (right) for oxygen at 60 bar for two different threshold levels of the relaxation term ($MinimumT/T_c$ = 0.65 and 0.9), and by selecting either the (V_c, T_c) option (vc) or the (P_c, T_c) option (pc).

(see section §3.3.5). In Kay's mixing rule the critical pressure, temperature and the value of the 'a' constant of the mixture are computed by using a molar weighted averaging. We invite to look back at the equations 3.3.45, 3.3.44 and 3.3.46 .

$$P^c{}_{mix} = \sum_i x_i P^c, \qquad T^c{}_{mix} = \sum_i x_i T^c \tag{6.1.1}$$

In section 3.3.5 the VDW's mixing rule was introduced. Now, we illustrate the VDW's mixing rule, in the CFD++ software, to calculate the temperature and pressure. The equations 6.1.2 is used in the CFD++ software:

$$T_c{}^{mix} = \sum_j \frac{x_j T_c}{P_c{}^{1/2}} \frac{\sum_j \frac{x_j T_c}{P_c{}^{1/2}}}{\sum_i \frac{x_i T_c}{P_c}}, \qquad P_c{}^{mix} = \frac{T_c{}^{mix}}{\sum_i \frac{x_i T_c}{P_c}} \tag{6.1.2}$$

6.1.3 *Non dimensional parameters in jet flows*

In this section, we introduce the non dimensional parameters used to characterize a jet flow.

We will first consider the "dense core length" and and the "jet spread angle" as introduced by Chehroudi [13] and Mayer [62].

Three different regions of jet can be identified in a jet mixing flow field; with reference to Fig. 6.1.4, we can define:

- The "potential core" as the distance measured along the jet centerline where the fluid properties remain relatively constant. Mayer and al. suggested two different empirical methods to

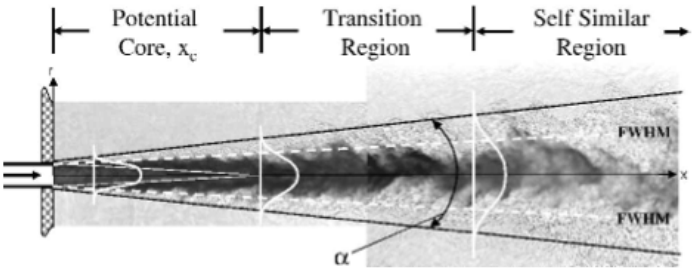

Figure 6.1.4: Jet mixing flow field. Reprinted from Schmitt [95].

measure the potential core: Chehroudi method (eq. 6.1.3) and Harsha method (eq. 6.1.4):

$$\frac{x_c}{d} = C\left(\frac{\rho_0}{\rho_\infty}\right)^{\frac{1}{2}} \qquad 3.3 < C < 11 \tag{6.1.3}$$

$$\frac{x_c}{d} = 2.13 Re_d^{0.097} \tag{6.1.4}$$

- The transition region is considered the region of turbulent mixing for a jet. This area shows the influence on jet development of velocity ratio between (initial jet velocity and the surrounding environment) and the density ratio (initial jet density and the surrounding environment). The parameters, velocity ratio and density ratio, illustrate how the momentum and thermal energy dissipates from the jet into the flow field.
- The self similar region is situated at certain distance from the injection plane. In this area, the flow field profiles no vary in the axial direction and they become a function of only one variable.

To compare the flow properties in the radial direction, we will adopt $\rho^\star$ and ρ^+ as defined in Eq. (2.1.10) and (2.1.13).

Also we will consider the iso-surface value of density $\rho_{0.5}$ for the curvature analysis of intermediate density between the oxygen and methane streams (how evaluated by Ruiz [92]). The following relation shows in 6.1.5 the $\rho_{0.5}$:

$$\rho_{0.5} = (\rho_{inj} - \rho_\infty)/2 \tag{6.1.5}$$

6.1.4 *Validation*

The validation of our numerical results is carried out with reference to two among test cases presented by Mayer [62], namely test case #3 (Fig. 6.1.5) and #4 (Fig. 6.1.6) according with the Mayer's labelling. Mayer's experiments involve a jet of nitrogen into a cavity filled with quiescent nitrogen under supercritical and transcritical condition of pressure.

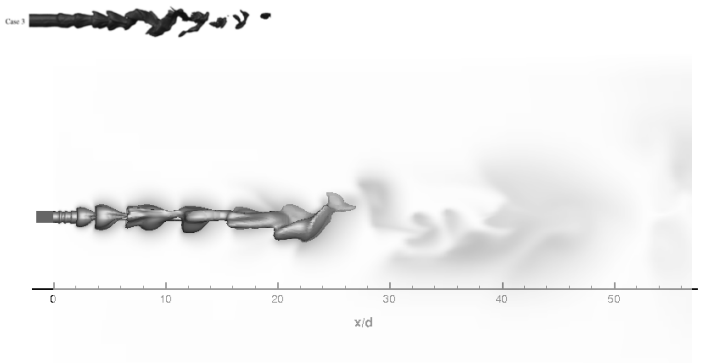

Figure 6.1.5: Mayer's Case #3: Density isosurface at 50%; (top) Schmitt's results ; (bottom) this work's results.

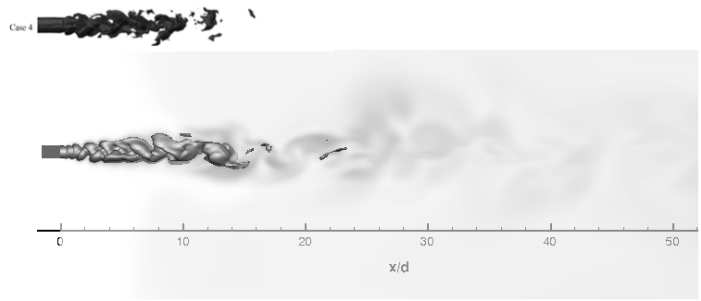

Figure 6.1.6: Mayer's Case #4: Density isosurface at 50%; (top) Schmitt's results ; (bottom) this work's results.

We compare our numerical results both with respect to Mayer's data, and to the numerically predicted data generated by Schmitt's et al. (see [95]) for the same test conditions. The Schmitt's numerical analyses are carried out using the AVBP Real Gas flow solver, which solves the compressible Navier-Stokes equation for multicomponent mixture of fluids on unstructured meshes under the Large-Eddy Simulation (LES) framework for turbulent combustion modeling. A typical output of Schmitt's analyses which illustrates the jet morphology in terms of density iso-surface evaluated for $\rho_{0.5}$ using the relation (6.1.5) is shown in Fig. 6.1.5 and Fig. 6.1.6 for the test case #3 and #4,

respectively. In these figures, we also anticipate what is the outcome of our simulation for the same test cases.

Observing the figures 6.1.5 and 6.1.6 we note that the density iso-contour in the case #3 is longer than case #4. This is correct due to injection conditions that are illustrated in table 5 and showed in the figures 6.1.1 how follows in the section §6.3.1.3 in figure 6.3.26 .

6.2 COLD FLOWS: NUMERICAL SETUP AND RESULTS

We presented the results obtained by CFD ++ and compared them to Mayer's experiment data and Schmitt's numerical results obtained by AVBP code.In subsection §6.1.3 are introduced some variables to compare the jet flows properties taking in account the spread angle, density core length , density and radial profiles. After are illustrated the numerical setup §6.2.2 and the test case used in simulations §6.3.1.3.

6.2.1 *Geometry and mesh*

The chamber geometry is shown in figure 6.2.1 and in table 6 are shown the geometry dimentions. The geometrical chamber dimensions adopted in CFD++ simulations are similar to the Schmitt one. To reduce computational cost, the radius is 1/2 one employed in Schmitt simulations but the boundary conditions chosen for the simulations have been the same one Schmitt.

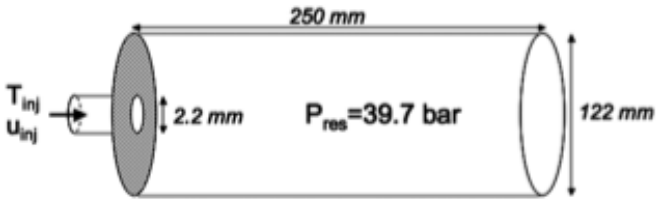

Figure 6.2.1: Sketch of geometry chamber. Reprinted from Schmitt [95].

Geometry	Injector diameter [mm]	Chamber diameter [mm]	Length chamber [mm]
Schmitt	2.2	120	250
Simulation	2.2	60	125

Table 6: Geometry sizes.

The mesh visible in figure 6.2.2 is generated by a house-mesh generator, see section §7.5, and it is made by 600000 hexahedral elements, coarse mesh. The max cell volume is $1.4E-08$ and the min volume is $3.6E-14$.

6.2.2 *Numerical setup*

The numerical results are presented in the following subsections, we showed the test-case in supercritical condition with a temperature af-

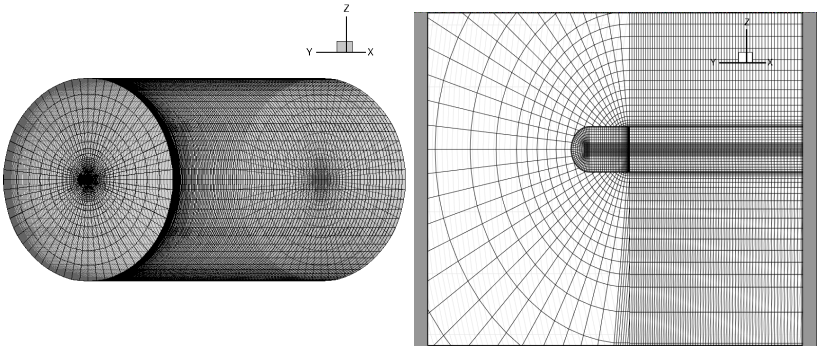

Figure 6.2.2: Left: mesh used in simulations performed by CFD++. Right: detail mesh used in simulations.

ter the pseudo-boiling temperature and the test-case in supercritical condition but with a temperature before the pseudo-boiling temperature, we have named this case "transcritical". The latter case is the nearest to the transcritical region.

After we will define three elements that are the bases of numerical setup **density based** solver, **pressure based**, solver DTS. In the subsection following the BC we select among the possible options of CFD $+ +$ software. The simulations that reproduce the Mayer's jet flow and the Schmitt have been realised taking in account the following choice given by CFD $+ +$ software:

- A comparison between a **density based** solver and a **pressure based** solver.
  A **density based** solver (Coupled Solvers) with a preconditioning scheme was compared with a **pressure based** (Segregate Solver, although coupled pressure based scheme exist) approach in terms of accuracy of results and computational time. In the past the density based scheme evolves from algorithms devised for the compressible Navier-Stokes (or Euler) equations instead the pressure based scheme evolves from algorithms devised for the incompressible Navier-Stokes in which the divergence ($\nabla \cdot \vec{v}$) is imposed to zero using a pressure Poisson solver. Nowadays this division is not true: the pressure based algorithms have been extended to the compressible flow equations (with the the density term used as a source term in the$\nabla \cdot \overrightarrow{v}$ equation and the density based approaches have been extended to the incompressible flow or low speed compressible flow by means of preconditioning algorithms. The usage of preconditioning scheme in combustion problems solution with presence of flow at low Mach number (transcritical flow) is mandatory and very useful with thrust chambers where there are a high differences of

velocity. An equations set with density based scheme and a preconditioning method has been compared to an equations set with pressure based solver only for the test case #3 and #4. Usually for the other simulations, chamber and thrust chamber, we used the preconditioned method. The **preconditioned** involves premultiplying the time-derivative term in the governing differential equations by a matrix which alters the rate of evolution of the physical problem.
The preconditioned is applied to reduce the spread of the eigenvalues, this makes the problem less stiff and helps to improve convergence rates. Reducing the magnitude of the largest modulus eigenvalues, preconditioning also has an interesting side effect, which is to reduce the levels of artificial dissipation present in the numerical flux at low speeds.

- The usage of **Dual Time Stepping** (DTS). The DTS schemes are constructed appending a pseudo time derivative term, through a "false" time step (see CFD + + User Guide [65]). At the beginning of the physical time step, $U^{\star}$ is set to time n and is updated, iteratively, to $U^{\star\star}$ reached at the end of the inner (local) time step and at convergence of the inner iterations. At this point, the inner iterations are halted and the state $n+1$ is set equal to $U^{\star\star}$. At convergence, the pseudo time derivative vanishes and the solution represents an advance through the physical time step. The result is that the path chosen to drive the pseudo-time derivative to zero has no effect on the physical transient solution and any convergence-acceleration mechanism can be employed on these inner iterations (local time-stepping, time-derivative preconditioning and multi-grid). In CFD + + this integration time method is mandatory in pressure based solver and optional in other cases.

- In the **fluid properties** the T/T_c ratio controls the density change. This ratio is more important in multi species flows and defines the limit of compressibility: the compressibility value can not fall below the parameter value. Since this parameter underestimates density of transcritical flows, it is desirable to set is as low as possible unless there is difficulty with converging the solution.This parameter could be change from expected value only temporarily. This happen with transcritical flows when new products are created, as in a chemical reaction.

6.2.3 *Boundary Conditions*

The **boundary conditions** used in CFD ++ are alike to those used by Schmitt et al.. The boundary conditions are presented in figure 6.2.3: the walls near the injector are treated as adiabatic, whereas the reservoir walls are kept at a constant temperature of 298 K.
Velocity and temperature are imposed at the inlet.In particular, in *inflow* has been used the **Temperature-Velocity Inflow/Pressure Outflow**. This boundary condition uses the knowledge of the free stream velocity that is far away from the region of interest. This BC does not use solution data to determine inflow or outflow. It compares the normal boundary with the user-specified velocity vector. For subsonic inflow, the temperature and velocity are prescribed and the pressure is taken from the interior. For subsonic outflow, the pressure is prescribed, and the temperature and velocity are taken from the interior. The normal velocity to the boundary is computed from the interior and it's possible to determine where there is inflow or outflow. For inflow, this BC imposes specified pressure and temperature as stagnation conditions. For outflow, the BC imposes the input pressure as a static back pressure. This boundary condition should be used when the reservoir conditions are known. In *outflow* we adopted **back pressure** in which pressure is prescribed and all other quantities extrapolated from the interior. The pressure at the outlet is computed as the local Riemann problem is solved. One Riemann invariant and the entropy are taken from the interior. The *walls* are **isothermal** in chamber with the usage of **wall function**, and **adiabatic** for the injector

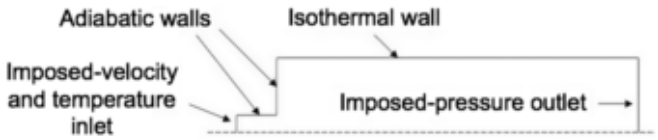

Figure 6.2.3: Sketch of boundary conditions. Reprinted from Schmitt [95].

6.3 SUPERCRITICAL AND TRANSCRITICAL TEST CASES

In the section we summarized the main elements (EOS model, governing equations, space and time discretization) used by Schmitt, in AVBP code.

The numerical setup prefered by Schmitt is:

- EOS: Peng-Robinson (PR) is chosen
- AVBP code: for this study it solves the compressible Navier-Stokes equation for multicomponent mixture of fluids on unstructured meshes
- AVBP is in third order in time and space
- The boundary conditions are treated with the characteristic wave decomposition method

For high quality LES Schmitt et al. have used a high order low dissipation centered schemes at third-order in time and space. In order to reduce spurious oscillations caused by steep density gradient, the numerical chosen by investigators has been the Jamenson's strategy [38] with addiction of the artificial viscosity. A second-order derivative is used to add viscosity and smoothes largest gradients, whereas a fourth-order derivative is added to avoid node-to-node oscillations outside the gradients [18].
The computational domain made by hexahedral cells is finest near the injector, with a constant characteristic cell size of 0.1 mm in a cylinder length 1.8 times the jet diameter and length almost 10 diameters. This zone is followed by a smoothly coarsening region. The mesh contains $5x10^6$ hexahedral cells. Our configuration is alike to that of Schmitt [95] but the geometry change: it is similar but not equal. The geometry consists of a single round jet injected in a cylindrical chamber at a pressure 39.7 bar at a temperature of 298 K. The injector diameter is 2.2 mm, the chamber diameter is 60 mm and the chamber length 125mm. The numerical setup used for both case (case #3 and case #4) has been:

- The equations set used is the preconditioned for real fluid;
- The EOS used is PR;
- We used an option to return, for $P < P_c$, to liquid density. The minimum $T/T_{critical}$ is limit at 1.0;
- The simulations use an **One Equation LES Subgrid-Scale Model**;
- The turbulence model is one equation variable: k;

- The turbulence level i s: 2.5%;
- The spatial discretization is at second order with base polynomial nodal;
- In second step the time discretization is at second order and a time step is imposed;

In the *One Equation LES Subgrid-Scale Model*, the Leonard stresses and the subgrid-scale Reynolds, and cross stresses are modeled using the linear Boussinesq relationship. We suggest how reference the User Guide of CFD $++$, [65] pages $546 - 550$.

The boundaries conditions are:

- Outflow: back pressure;
- Inflow: temperature-Velocity Inflow/Pressure Outflow;
- Wall: are isothermal in chamber with the usage of wall function, the injector wall and the injector plate are adiabatic;

The initial conditions are:

- chamber: filled with nitrogen;
- $T_{chamber}$: 298 K;
- $P_{chamber}$: 39.7 bar;

6.3.1 *Comparison of integration methods*

In the newt step we look for the best compromise between solution accuracy and computational time. We used the compressible Navier-Stokes equations, and we chose two among numerical methods provided:

1. preconditioning
2. pressure based

and at the end we chose the time discretization. In tables 7 and 8 are summarized the results of several numeric methods.

The tables 9 and 10 indicate, for cases #3 e #4, the total calculus time.

Test case #3	Method	Time discretization	Time step	CPU Time
1	pressure based	only implicit with Dual Time Stepping (dts)	-	-
2	preconditioning	implicit	$1.82E-05$	13h $\rightarrow$ 0.5sec/step
3	preconditioning	implicit plus dts	$1.82E-05$	38h $\rightarrow$ 1.3sec/step

Table 7: Test case #3: methods, time discretisation, time steps, CPU's time

Test case #4	Method	Time discretization	Time step	CPU Time
1	pressure based	only implicit with Dual Time Stepping (dts)	$1.83E-05$	55h $\rightarrow$ 2sec/step
2	preconditioning	implicit	$1.83E-05$	13h $\rightarrow$ 0.5sec/step
3	preconditioning	implicit plus dts	$1.83E-05$	38h $\rightarrow$ 1.3sec/step

Table 8: Test case #4: methods, time discretisation, time steps, CPU's time

Test case #3	Method	Time discretization	Total simulation time
1	pressure based	only implicit with Dual Time Stepping (dts)	-
2	preconditioning	implicit	1.62 sec
3	preconditioning	implicit plus dts	1.82 sec

Table 9: Test case #3: methods, time discretisation, total time

Test case #4	Method	Time discretization	Total simulation time
1	pressure based	only implicit with Dual Time Stepping (dts)	4 sec
2	preconditioning	implicit	1.83 sec
3	preconditioning	implicit plus dts	1.83 sec

Table 10: Test case #4: methods, time discretisation, total time

6.3.1.1 *Comparisons: numerical result Test Case #3*

In this subsection we analyse the results obtained from the simulations of case #3 using a preconditioned density based method, but with two different time integrations: implicit with DTS or not. We note that in the transcritical case, the time integration that uses the DTS, gives us the best results. In effect, these results are deduced from the density profile extracted on centerline (figure 6.3.1) and from the relative error (figure 6.3.9) that was obtained comparing the experimental data of Mayer and the numerical results obtained by CFD++.

In the figure 6.3.3 are showed the average density fields for two different solution methods. In figure 6.3.3 we have at the left side a preconditioned implicit density based and at the right side a preconditioned implicit density based with time integration with DTS. We underline that times in the legend of figure 6.3.3 indicate the several densities taken at an overall sampling interval. We compare the cores length: one calculated with a implicit preconditioned method with DTS and the another calculated only with implicit preconditioned method. We show in figures 6.3.2 and 6.3.3 that the core length obteined using a preconditioned equations with DTS, with density

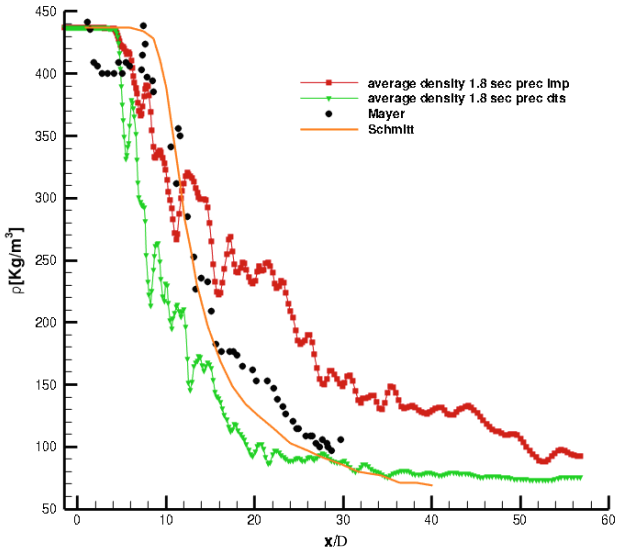

Figure 6.3.1: Comparison among the centerline average density profiles with several numerical methods: case #3. ■ symbols are implicit preconditioned method; ▼ symbols denote the implicit preconditioned method with DTS; • symbols are the Mayer's experimental data; — is Schmitt numerical data.

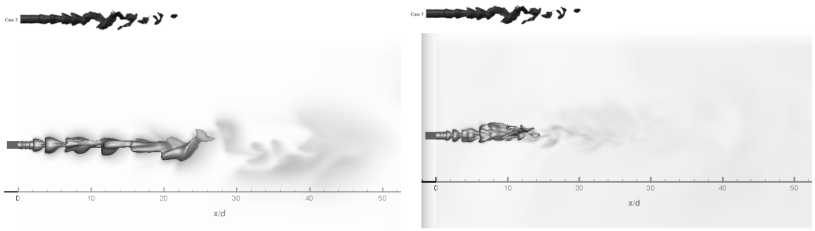

Figure 6.3.2: Comparison of dense core length in cases #3 using relation 6.1.5: preconditioned implicit density based method VS preconditioned implicit density based method with DTS.

isosurfaces evaluated with the relation 6.1.5, is shorter than a core length obtained using only a preconditioned method. In figure are shown the average density field extract on one slice.

This behaviour, in addition, results visible also in the figure 6.3.4 where we compared the radial density profile, extracted on the centerline at several x stations. This profile is extracted from the results obtained using two methods: implicit preconditioned or implicit preconditioned with DTS. From the figure we note that the density profile, obtained from the implicit preconditioned method, shows a higher value for $x/D > 1$ (when the jet distances himself from the plate). When the radius varies, that is when it distances himself from center-

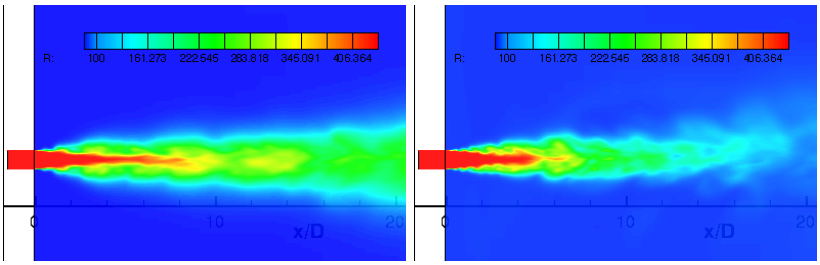

Figure 6.3.3: Average field in case #3: slice of density field. Left: implicit method density based , precoditioned. Right: implicit method density based, precoditioned and time integration with DTS.

line in radial direction, the density profile, obtained with the implicit preconditioned, exhibits a lower density, that is the jet spreads near the plate, while the jet exhibits a constant behaviour when it distances himself from the plate. In figure 6.3.5 are exhibited the spread angles of jets (preconditioned with DTS, preconditioned) and the jet with a longer core has an narrow angle.

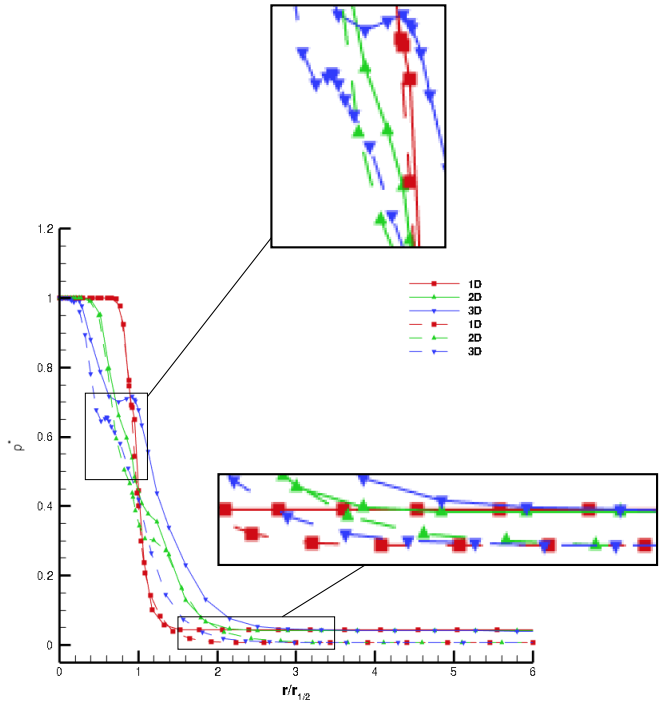

Figure 6.3.4: The comparison between radial profiles of density half in test case #3: implicit preconditioned density based method (····) VS implicit preconditioned density based method with DTS (——)

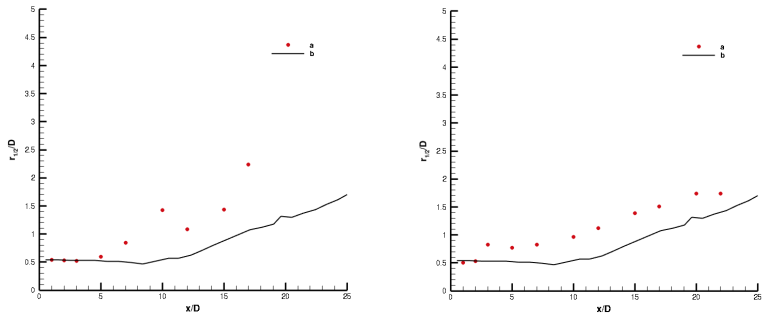

Figure 6.3.5: Half-width L_ρ of the jet in LES case #3: implicit preconditioned density based method VS implicit preconditioned density based method with DTS. • have been calculated with our numerical simulations; —— is the Schmitt's results.

The figures below 6.3.6 and 6.3.8 illustre the vorticity magnitude lines on the field, respectively, of density and pressure; the figure 6.3.7 exhibits a field of velocity magnitude with the pressure lines.

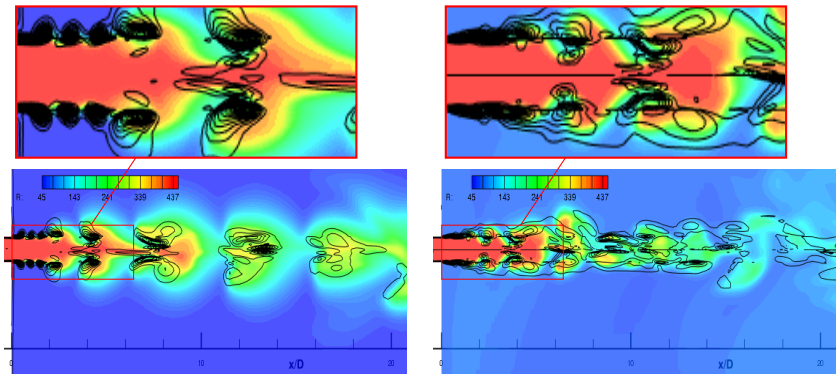

Figure 6.3.6: Instantaneous field case #3: slice of vorticity magnitude line and density field. Left: solution method density based implicit, preconditioned. Right: solution method density based implicit, preconditioned and time integration with DTS.

These figures give us a qualitative behaviour of the jet. The figures 6.3.8 and 6.3.7 highlight the superficial jet behaviour and wavy surfaces are visible in the areas at low pressure (figure 6.3.8) together with vortices that are convected in the field. We will identify a similar behaviour in the case #4. It is evident the presence of velocity variation that origins a shear layer and at the end the jet breakup.

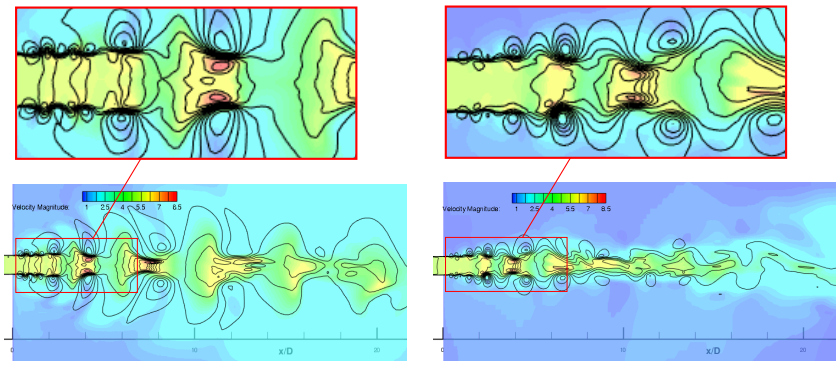

Figure 6.3.7: Instantaneous field case #3: slice of pressure line and velocity magnitude field. Left: solution method density based implicit, preconditioned. Right: solution method density based implicit, preconditioned and time integration with DTS.

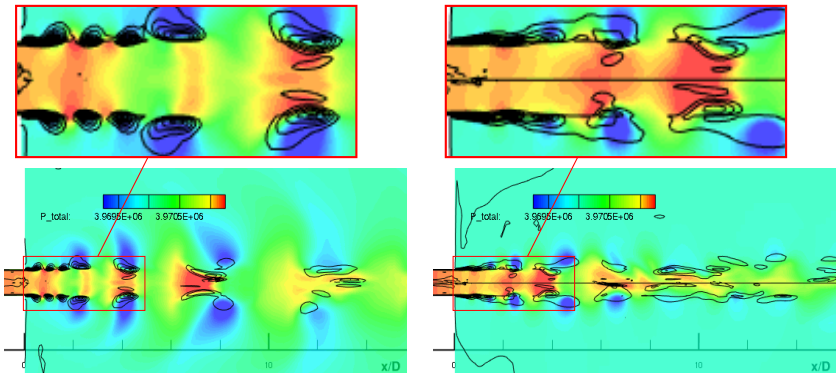

Figure 6.3.8: Instantaneous field case #3: slice of vorticity magnitude line and pressure field. Left: solution method density based implicit, precoditioned. Right: solution method density based implicit, preconditioned and time integration with DTS.

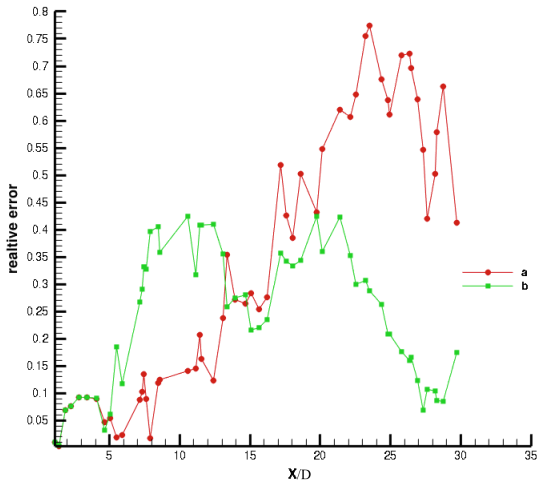

Figure 6.3.9: Case #3: relative errors among values taken on centerline density of several equations set and numerical methods. ● (a) is a preconditioned scheme without DTS. ■ (b) is a preconditioned scheme with DTS.

6.3.1.2 *Comparisons: numerical results Test Case #4*

The figure 6.3.10 shows the average density centerline for three different solver methods: a density based solver with a preconditioned scheme, a density based solver with a preconditioned scheme and time integration with DTS, and a pressure based solver with time integration with DTS. We have used two different methods, for the time integration:a time integration method without the dual time stepping method (DTS) and an other time integration method with the usage of DTS. We underline that times in the legend of figure 6.3.10 indicate the several densities taken at an overall sampling interval.

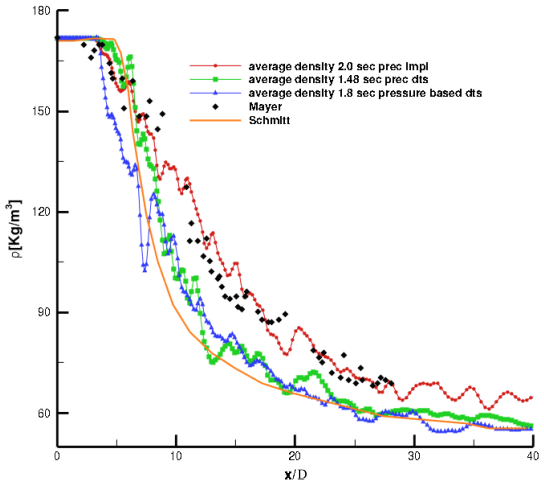

Figure 6.3.10: Comparison among the average density centerline for several numerical methods: case #4. ● symbols denote implicit preconditioned method; ■ symbols denote implicit preconditioned method with DTS; ▲ symbols denote pressure based method with DTS; ♦ symbols denote Mayer's experimental data; — is Schmitt's numerical data.

In detail, when we use a density based solver with a preconditioned scheme we can choose to use the DTS for the time discretization when we use a pressure based solver DTS is a method of time integration mandatory. Summarizing: if we use the the pressure based solver the DTS is required but it is facultative for a preconditonated compressible real gas Navier-Stokes method. From the figure 6.3.10 only density based preconditioned set equation produces the best result and in table 8 we can observe that this method results more efficient that the other. The numerical results seem to fit the experimental results in case of prenconditional scheme with a time discretizaiton method without the DTS. In fact, the relative error analysis, showed in figure 6.3.23, illustrate three trend of relative errors for three kinds of

schemes: the prenconditional scheme without the DTS exhibits a relative error lower than other two solution. Also for the prenconditional scheme at $8 < x < 20$ the error increases but after $x > 20$ it decreases. From the figure 6.3.22 and 6.3.24 we can see that the area of maximum error is where there is the change of slope of density.

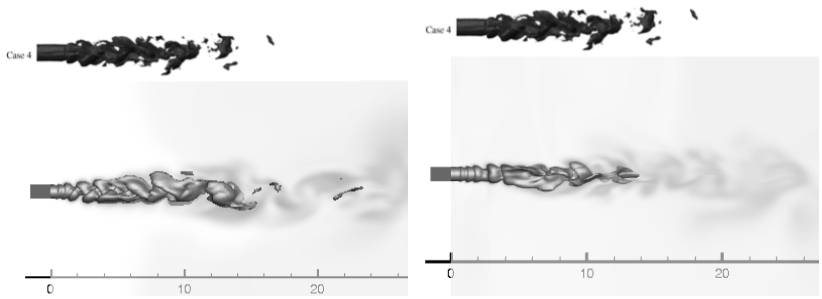

Figure 6.3.11: Comparison of dense core length in cases #4 using relation 6.1.5: implicit preconditioned density based method VS implicit preconditioned density based method with DTS.

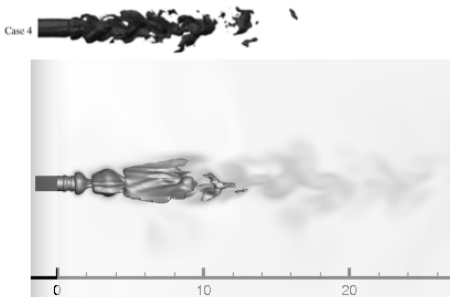

Figure 6.3.12: Comparison of dense core length in case #4 using relation 6.1.5: pressure based method with DTS.

In the figures 6.3.13 and 6.3.14 are shown the density fields for the three different methods used: implicit preconditioned density based , implicit preconditioned density based with DTS and pressure based method with DTS. In figure 6.3.13 we have on the left a implicit density based preconditioned and on the right a implicit density preconditioned with a time integration that uses a DTS. In the figure 6.3.14 we showed a field obtained with a pressure based method with a time integration with DTS. We note that in the supercritical case the implicit preconditioned method gives us the best results, how we can see from density profile extracted from centerline, figure 6.3.10, that was compared with figure 6.3.13, and from graphic of the relative error, figure 6.3.23, evaluates with the experimental data of Mayer with the numerical results obtained by CFD++.

The core, obtained using the implicit preconditioned method, in comparison with those obtained using the DTS (implicit precondi-

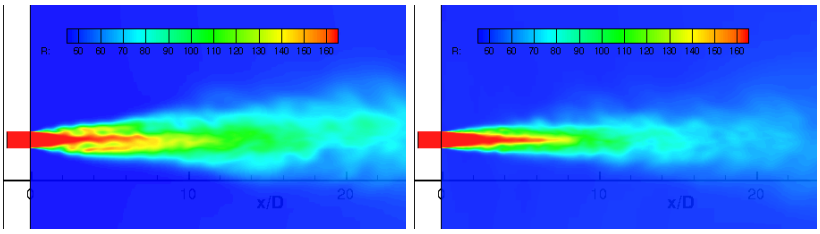

Figure 6.3.13: Average field in case #4: slice of density field. Left: implicit preconditioned solution method density based. Right: implicit preconditioned solution method density based with DTS time integration.

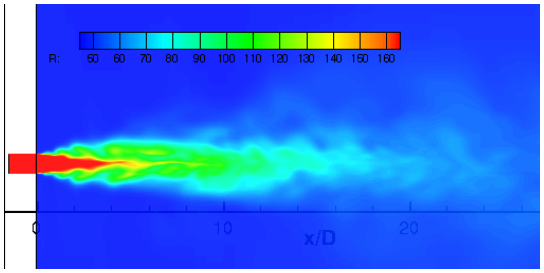

Figure 6.3.14: Average field in case #4: slice of density field. Solution method pressure based implicit and time integration with DTS.

tioned method with DTS and pressure based), is longer, how visible in the figures 6.3.11 and 6.3.12, in the figures 6.3.13 and 6.3.14, where are showed the average density fields. This behaviour is also visible in figure6.3.15 where we compared the radial density profile, taken on the centerline at different x stations, and evaluated with three different methods: implicit preconditioned, implicit preconditioned with usage of DTS and pressure based with DTS. In the figure we note that the density profile, calculated with the implicit preconditioned method, exhibits the density values higher when $x/D > 1$ (when the jet distances himself from the plate). When the radius varies, and the jet distances himself in radius direction from the plate, the density profile, in the case of implicit preconditioned, exhibits a lower density, this is the jet spread near the plate, while, when the jet distances himself from the plate, the density value remains high and constant. We note that the density profile obtained with the pressure base method has lower values than those obtained from the density based methods. This behaviour decreases when the jet distances himself, in radius direction, from the centerline. We can see, in the figures 6.3.16 and 6.3.17, that the spread angle is narrow when the jet core is longer.

The figures below 6.3.18 and 6.3.20 illustre the vorticity magnitude lines on the field, respectively, of density and pressure, only for the

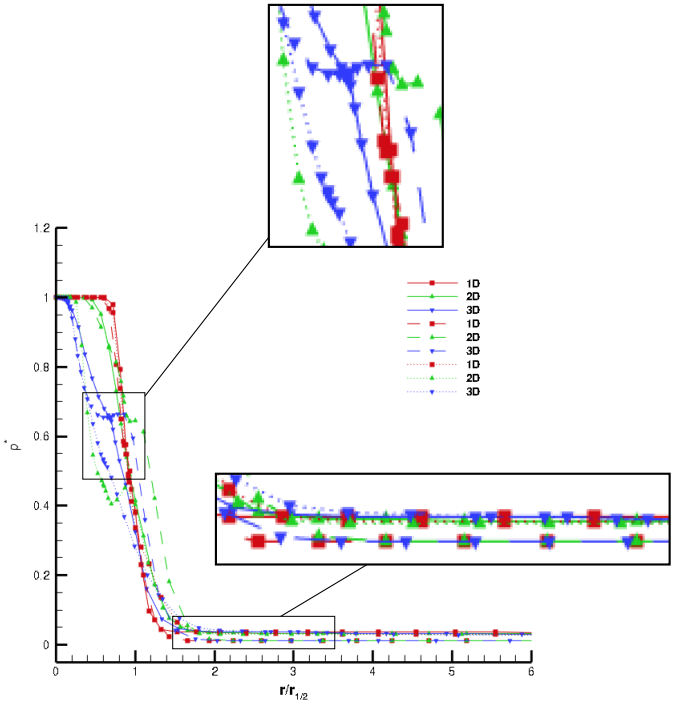

Figure 6.3.15: The comparison between radial profiles of density half for test case #4: implicit preconditioned density based method (——) VS implicit preconditioned density based method with DTS (- - - -) VS pressure based method with DTS (·····).

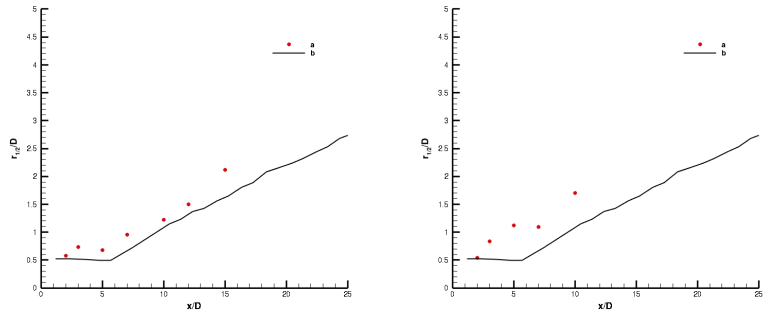

Figure 6.3.16: Half-width L_ρ of jet in LES case #4: density-based preconditioned implicit method VS pressure-based method with DTS. • have been calculated with our numerical simulations. —— is Schmitt's results.

implicit preconditioned solution method density based with DTS and implicit preconditioned solution method density based. The figure 6.3.19 exhibits a field of velocity magnitude and the pressure lines with areas, within the jet, where it is evident the presence of velocity variation that causes a shear layer and at the end the jet breakup.

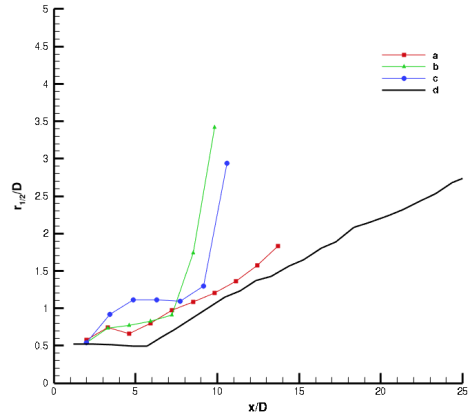

Figure 6.3.17: Half-width L_ρ of jet in LES case #4. ■ (a): implicit preconditioned density based method; ▲ (b): implicit preconditioned density based method with DTS; ● (c): pressure based method with DTS; — (d): Schmitt's results.

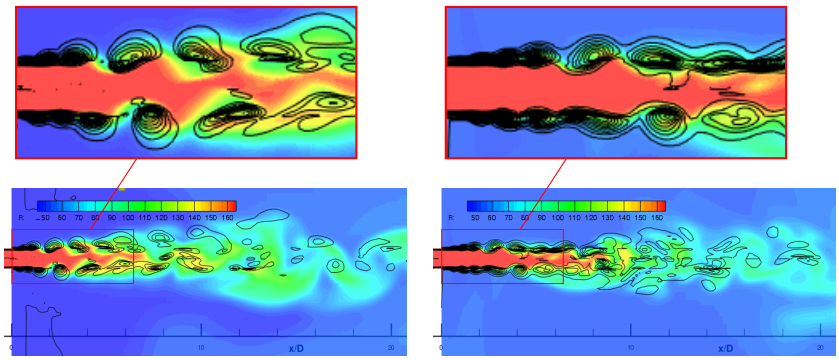

Figure 6.3.18: Instantaneous field for case #4: slice of vorticity magnitude line and density field. Left: implicit preconditioned solution method density based. Right: implicit preconditioned solution method density based with time discretisation with DTS.

In particular, the figures 6.3.18 and 6.3.19 highlight the jet surface behaviour: it is shown a wavy surface with maximum and minimum of velocity field where are visible the areas with low pressure figure 6.3.18 and the convection of vortices in the field.

Two other point are debated, the first about a sensibility analysis of mesh and the second about a gradient density sensibility at several average times. In figure 6.3.21 is shown the average density center line for two different mesh refinements: a coarse mesh with number of elements 600000 and a fine mesh with number of elements 2.5million. The results of mesh coarse, compared with Mayer's results, shows a better agreement than the mesh fine. The meshes that are compared

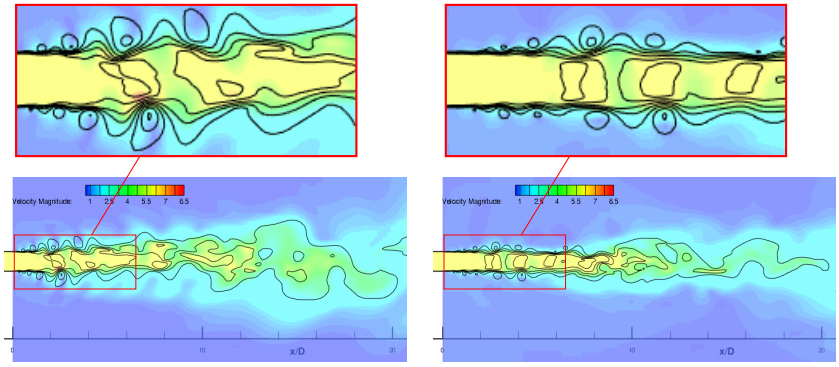

Figure 6.3.19: Instantaneous field for case #4: slice of pressure line and velocity magnitude field. Left: implicit preconditioned solution method density based. Right: implicit preconditioned solution method density based, and time discretisation with DTS.

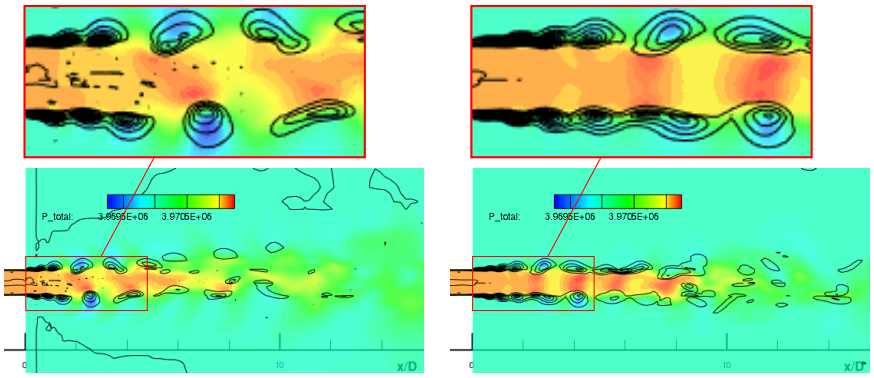

Figure 6.3.20: Instantaneous field for case #4: slice of vorticity magnitude line and pressure field. Left: implicit preconditioned solution method density based. Right: implicit preconditioned solution method density based and time discretisation with DTS.

have been obtained redoubling the points in **all directions**: there is not significant variations.

In figure 6.3.22 are shown three trends of the density take on the centerline density profile at three several times. When the time increases we observe an appreciable growth of density value above all after the change of density slope, where there is the inflection point: in the course of time. After the broken of jet flow in the chamber, the temperature in the chamber tends to level out and the density values increase.

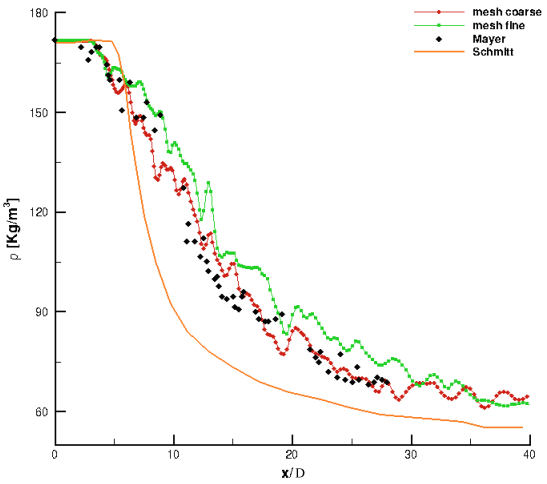

Figure 6.3.21: Comparison among the centerline average density profiles for several mesh resolutions: case #4. ● symbols denote the mesh coarse; ■ symbols denote the mesh fine; ♦ symbols denote Mayer's experimental data; — is Schmitt's numerical data.

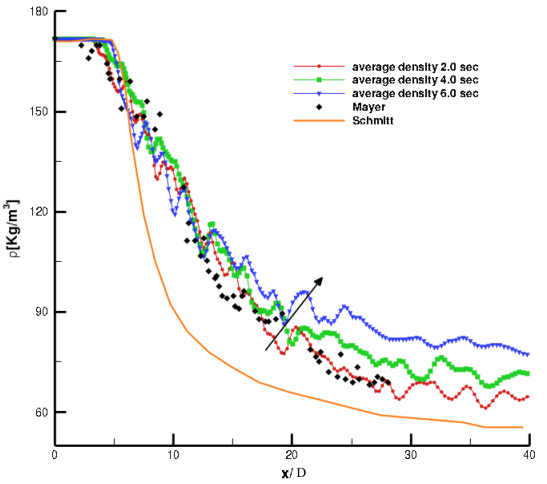

Figure 6.3.22: Comparison among the centerline average density profiles to several average times: case #4. ● symbols denote the average density after 2 sec; ■ symbols denote the average of density after 4 sec; ▼ symbols denote the average of density after 6 sec; ♦ symbols denote Mayer's experimental data; — is Schmitt's numerical data.

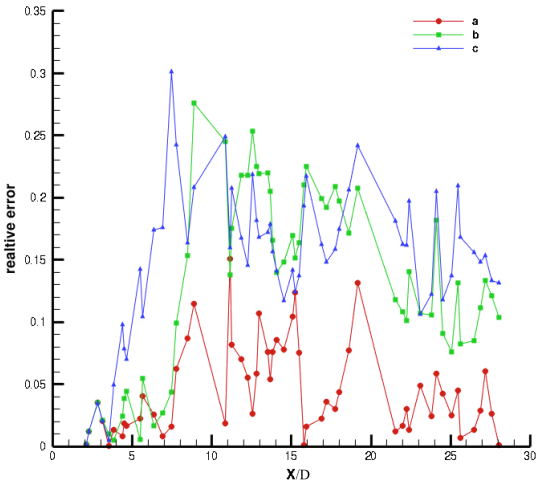

Figure 6.3.23: Case #4: relative errors among values taken on centerline density profile with several equations set and numerical methods. ● (a) is a preconditioned scheme without DTS; ■ (b) is a preconditioned scheme with DTS; ▲ (c) is the pressure based scheme with DTS.

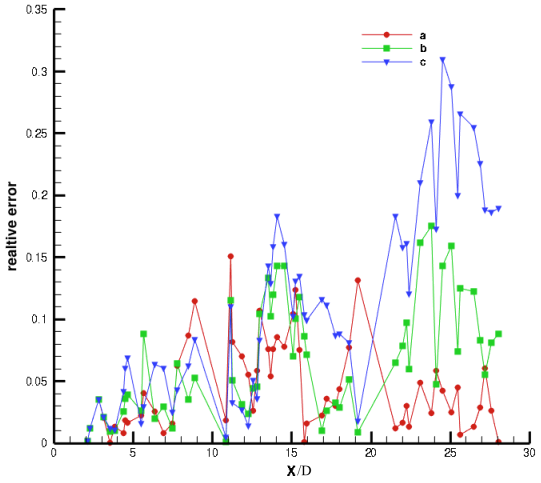

Figure 6.3.24: Case #4: relative errors among values taken on centerline density profile at several time using a preconditioning method. ● (a) the density profiles after 6 sec; ■ (b) is a preconditioning method after 4 sec; ▼ (c) is a preconditioning scheme after 2 sec.

6.3.1.3 *Numerical results: Test Case #3 & Test Case #4*

The injection condition of test case #3 shows a density values higher than test case #4. In this condition the jet flow exhibits similar characteristics of a jet injected in transcritical conditions and the dense core is longer than the one in supercritical case (test case #4) as showed in figure 6.3.25.

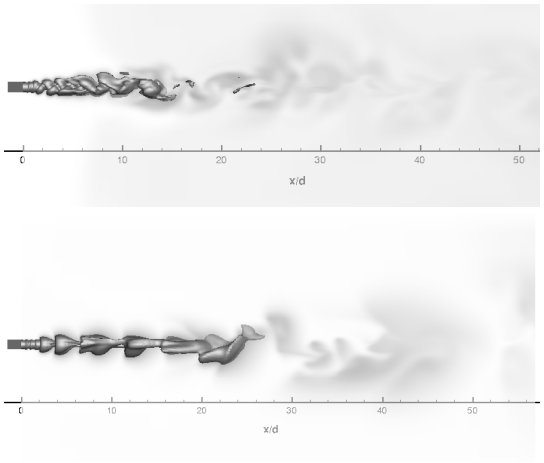

Figure 6.3.25: Comparison of the dense core length in case #3 and #4 using the relation 6.1.5.

In the figure 6.3.26 are showed the results in logarithmic scale. The length cores are showed in test cases #3 and #4 for the two best cases obtained from the previous comparisons . The results have been achieved from extraction of mean values of the density on the centerline.

- **Test Case #3**
  In figure 6.3.27 are compared the Mayer's experimental results (results extracted from Schmitt [95]) to Schmitt's numerical results, and numerical results obtained by CFD++, in test case #3, the injection conditions consider a higher density gradient than case #4. A sharp change of thermodynamic variables. The centerline density calculated by CFD++ does not accord with the other result In case we use a solution method density based with DTS, the results show (figure 6.3.9) a relative error lower and the density on the centerline with a slope greater. In figure 6.3.27 are reported the graphics obtained from the experimental results of Mayer (results extracted from Schmitt [95]), the Schmitt simulations and those deduced by CFD + +. The density trend, that we chose between the two possible trends that we have evaluated, is that that shows the lower error, that is that is obtained with a method that use the preconditioned and DTS.

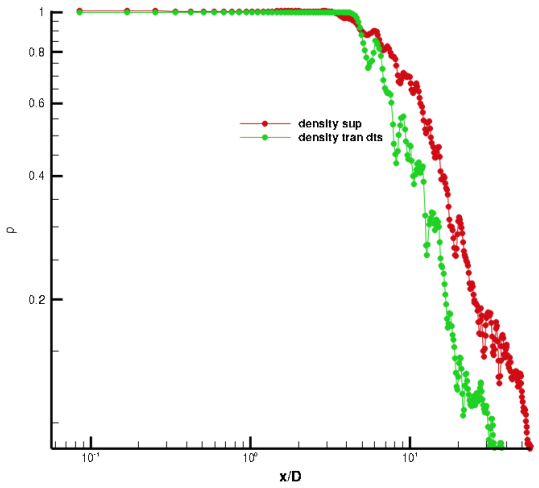

Figure 6.3.26: Comparison of the centerline density in case #3 and #4 in logarithmic scale for average values.

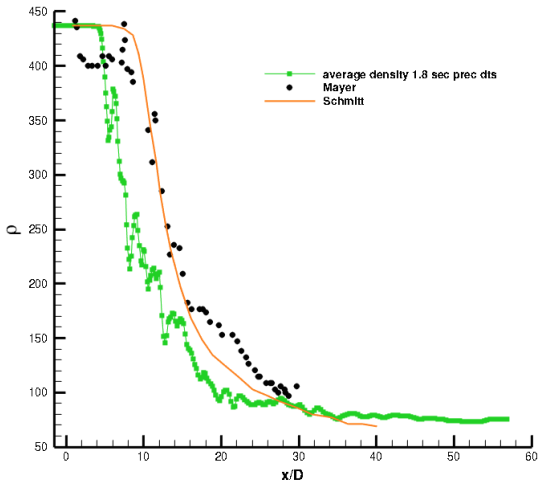

Figure 6.3.27: Centerline density profiles: case #3. ■ symbols denote the preconditioning implicit N-S with DTS method; ● symbols denote Mayer's experimental data; — is Schmitt's numerical data.

In figures 6.3.28 and 6.3.29 are reported the density and radial velocity trends. In figure 6.3.30 we observe on jet surface the presence of crests and troughs of density. This trend causes, on the velocity curve, some peaks when the jet separates from plate just 2 diameters. The figure 6.3.30 represents an instantaneous density field of test case #3 in a LES simulation obtained using CFD++.

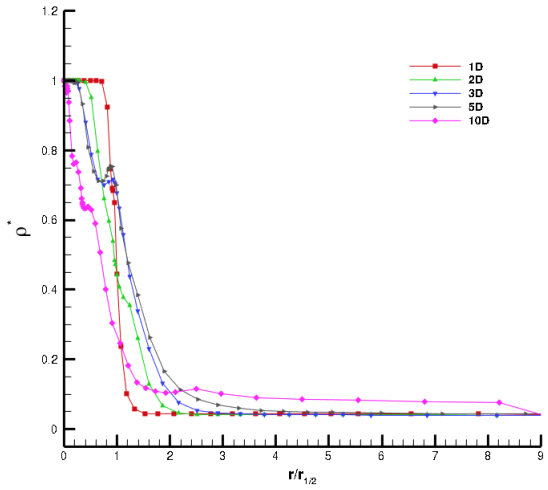

Figure 6.3.28: Radial profiles of density obtained using a preconditioning implicit N-S with DTS: case #3. Different symbols denote different distances (in diameter "*D*") from injector plate. ■ symbols denote 1D; ▲ symbols denote 2D; ▼ symbols denote 3D; ► symbols denote 5D; ♦ symbols denote 10D

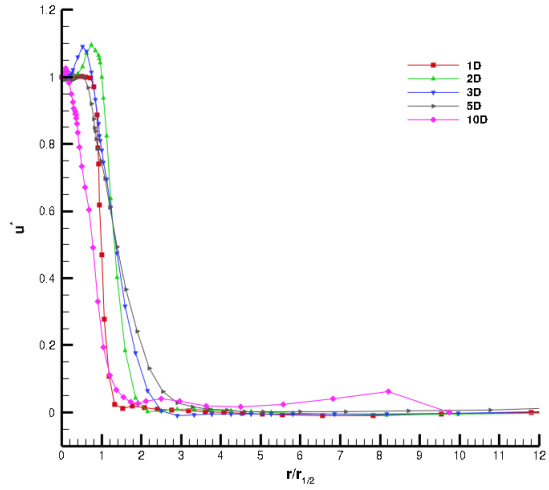

Figure 6.3.29: Radial profiles of axial velocity, u, obtained using a preconditioning implicit N-S with DTS: case #3. Different symbols denote different distances (in diameter "*D*") from injector plate. ■ symbols denote 1D; ▲ symbols denote 2D; ▼ symbols denote 3D; ► symbols denote 5D; ♦ symbols denote 10D

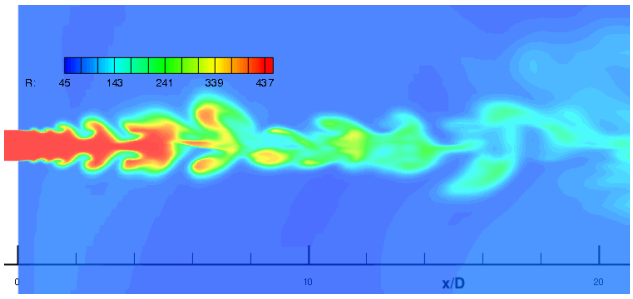

Figure 6.3.30: Instantaneous field for case #3 at 1.6 sec: slice of density.

- **Test Case #4**

  In figure 6.3.31, Mayer's experimental data, Schmitt's results [95] are compared with the results obtained by a CFD++ simulation. In addition we included in figure the Mayer's experimental results taken from Schmitt's [95].

  In figure 6.3.31 are showed the results obtained from experimental results of Mayer, from Schmitt's simulations and those obtained by CFD++. The density tendency chosen among the three possible is that with lower error, that is obtained with only implicit preconditioned method density based.

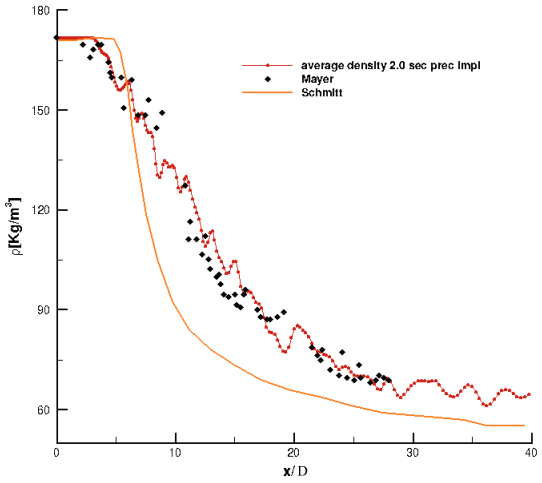

Figure 6.3.31: Centerline density profiles for case #4. ● symbols denote the preconditioning implicit N-S method; ♦ symbols denote Mayer's experimental data; — is Schmitt's numerical data.

In the figures 6.3.32 and 6.3.33, are illustrated the density and radial velocity tendencies. How in the previous case, we observe that in figure 6.3.34 on jet surface the are presence of on jet surface of wave with crests and troughs of density. This trend

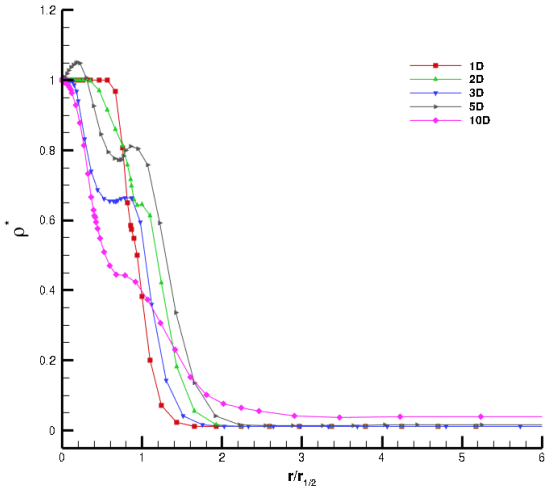

Figure 6.3.32: Radial profiles of density obtained using a preconditioning implicit N-S: case #4. Different symbols denote different distances (in diameter "*D*") from injector plate. ■ symbols denote 1D; ▲ symbols denote 2D; ▼ symbols denote 3D; ► symbols denote 5D; ♦ symbols denote 10D

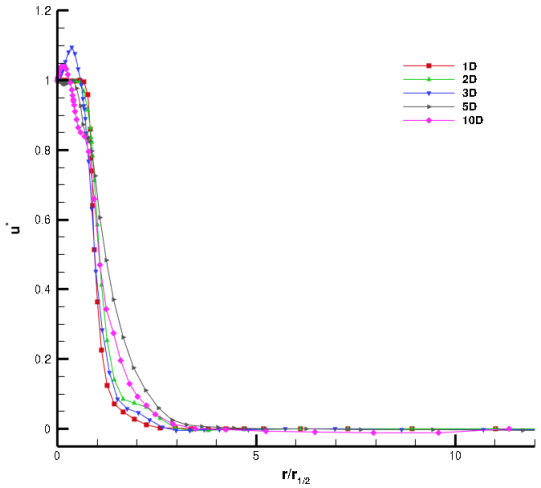

Figure 6.3.33: Radial profiles of axial velocity, u, obtained using a preconditioning implicit N-S: case #4. Different symbols denote different distances (in diameter "*D*") from injector plate. ■ symbols denote 1D; ▲ symbols denote 2D; ▼ symbols denote 3D; ► symbols denote 5D; ♦ symbols denote 10D

causes, on the density and velocity trends, some peaks when the jet divides himself from the plate on 10 diameters. The figure

6.3.34 represents an instantaneous density field of test case #4 in a LES simulation with the usage of CFD++.

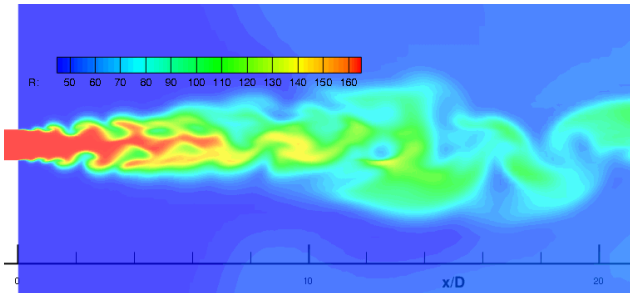

Figure 6.3.34: Instantaneous field for case #4 at 2 sec: slice of density.

The figures 6.3.36, in case #3, the figures 6.3.38 and 6.3.39, in case #4, show, in the time, the difference between the entry and exit mass flux. The difference does not zero, how we expect us, but the variations are minimal except for the cases that use the implicit preconditioned method, figure 6.3.35, case #3, and figure6.3.37, case #4 , where the oscillations are more evident. Moreover in the figures are reported the normalised errors, obtained by CFD++ software, of energy, mass flux and momentum x,y,z. The energy error is higher than those evaluated for other parameters.

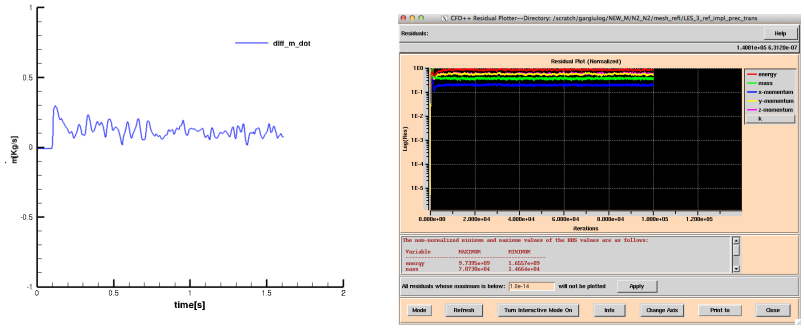

Figure 6.3.35: Case #3. Left: Massflow time evolution using implicit preconditioned method; right: energy, mass and momentum conservation normalised error evaluate with CFD + +

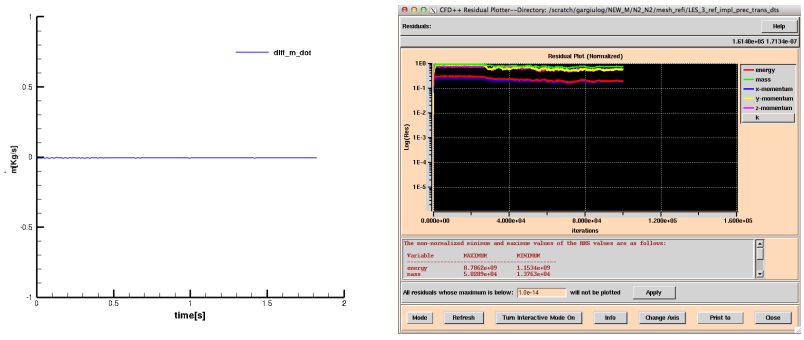

Figure 6.3.36: Case #3. Left: Massflow time evolution using implicit preconditioned method with DTS; right: energy, mass and momentum conservation normalised error evaluate with CFD++.

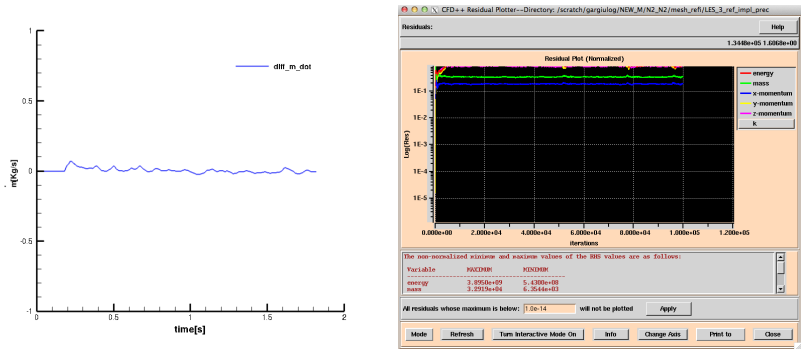

Figure 6.3.37: Case #4. Left: Massflow time evolution using implicit preconditioned method; right: energy, mass and momentum conservation normalised error evaluate with CFD++

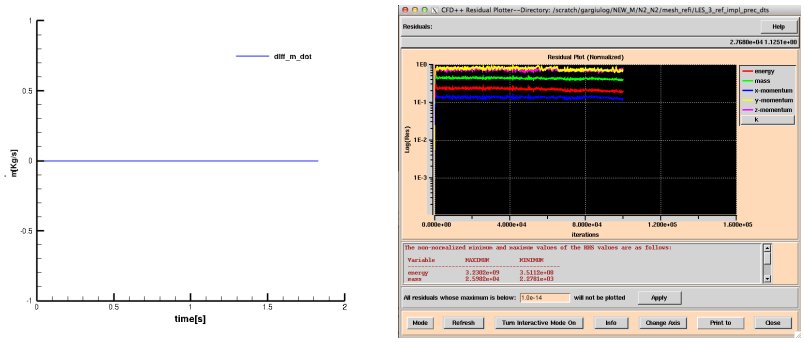

Figure 6.3.38: Case #4. Left: Massflow time evolution using implicit preconditioned method with DTS; right: time.

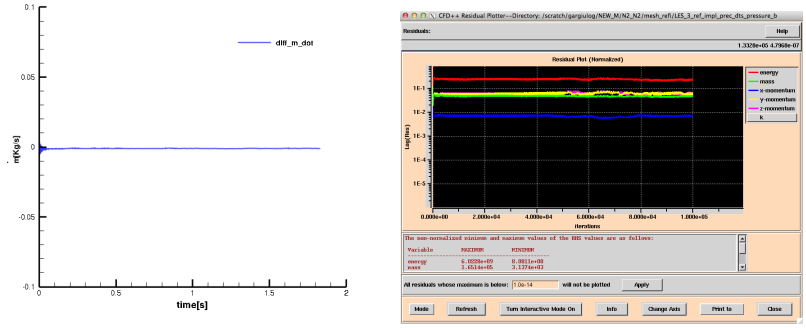

Figure 6.3.39: Case #4. Left: Massflow time evolution using pressure based method with DTS; right: time.

6.4 REACTIVE FLOWS: NUMERICAL SETUP AND RESULTS

We have divide into two main parts this section: in the first part we illustrated the injection of propellants in a condition similar to free jet for a reactive flow, and in the second part we illustrated a injection of propellants in a thrust chamber for a reactive flow with. We define the geometry, the initial condition and the boundary conditions.

6.4.1 *Single injector chamber and thrust chamber*

In this subsections two simulations with reactive flow are illustrated. The first simulation analyses a cylindrical chamber with the same geometrical size of the chamber used in test case #4 and #3, the only difference is the injection of two propellants: in this case in chamber are injected oxygen and methane. The chamber is filled with nitrogen.

species,	**T [K]**	$\dot{m}$ [Kg/s]	P_{cham} **[bar]**	Re_{inj}
Oxygen	110	0.036	60	$1.4x10^4$
Methane	300	0.0168	60	$5.6x10^3$

Table 11: Test chamber oxygen-methane.

The second simulation analyses a thrust chamber with a radius 1/3 smaller than the previous. In table 11 are reported the characteristic of propellant injection. The simulations consider the injection of methane and oxygen. Methane is injected into chamber at 131 m/s, oxygen is injected into chamber at 10.7 m/s. Their momentum flux ratio is $J \approx 4$

6.4.2 *Geometry and mesh chamber*

The computational domain is presented in figure 6.4.1 made by 450000 hexahedral elements. The max cell volume is $2.29E-08$ and the min volume is $3.0E-14$.

6.4.3 *Numerical Setup*

This case is only a preliminary test to simulate a thrust chamber. The numerical setup of simulation considers:

- The equations set used is the preconditioned for real fluid
- The EOS used is the PR and the kinetically mechanism is made by 15 species and 57 reactions

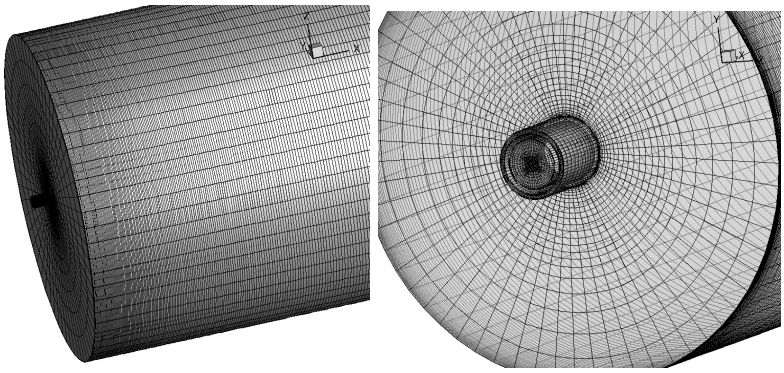

Figure 6.4.1: Left: mesh detail chamber. Right: injector detail.

- We used an option to return, for $P < P_c$, to liquid density. The minimum $T/T_{critical}$ is limit at 1.0
- At the beginning the simulations use a RANS model
- The turbulence model is an k-ϵ model
- The spatial discretisation is at second order with base polynomial nodal
- In second step the time discretisation is at second order and a time step is imposed

6.4.4 *Boundary Conditions*

The boundaries conditions used in this case are:

- Outflow: back pressure;
- Inflow: mass flow and static temperature whit direction of flow normal to face;
- Walls: are isothermal with the usage of a wall function and only the injector wall are adiabatic;

The initial conditions are written below:

- chamber: filled with nitrogen;
- $T_{chamber}$: 298 K;
- $P_{chamber}$: 60 bar;

At the beginning, for the turbulence simulation, we considered a URANS and a turbulence closure with 2 equations (k-ϵ), in a second step we have to move toward a different kind of turbulence simulation and we chose a LES where, the turbulence model, is an equation

model (k). The turbulence level was been 3%

6.4.4.1 *Numerical results: Chamber*

The figure 6.4.2 shows the density field of oxygen liquid core. This surface does not exhibit the characteristic behaviour of wrinkly surface, like cases #3 and #4 (nitrogen-nitrogen), probably due to an initial start where the turbulence has been modeled with an URANS with a turbulent closure that uses two equations k-ϵ and in a second moment, after the ignition,we used a LES model.

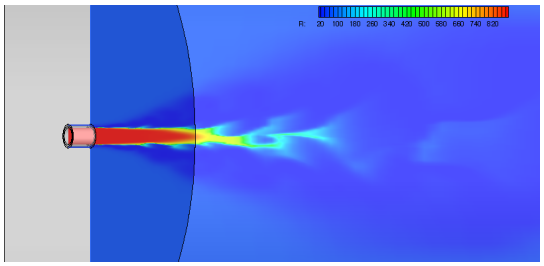

Figure 6.4.2: LOX density field in chamber.

Observing the instantaneous oxygen and methane fields, in left figure 6.4.3, is visible small area between the two propellants where we can see, in right figure 6.4.3, the formation of combustion products and the oxygen limitation. This behaviour is exhibited also in figure 6.4.4 to left.

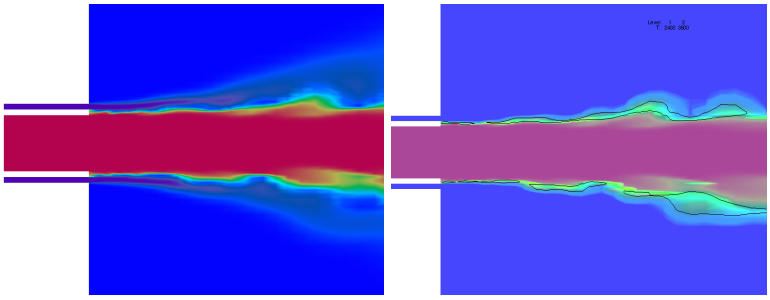

Figure 6.4.3: Left: slice of oxygen and methane field. Right: slice of oxygen and HCO fields with temperature contourlines for 2000K $<$ T $<$ 3000K.

In figure 6.4.4 is illustrated to right a narrow zone, which consists of hot combustion products. This zone separates the Methane and LOX streams that has a liquid-like behaviour. This behaviour produces a steep density gradient between the flame and the oxygen stream, and vortex structures emerging from the outer post of the LOX how we

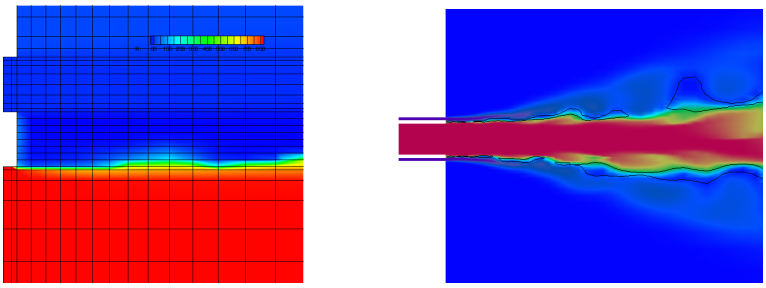

Figure 6.4.4: Left: density detail with mesh slice. Right: slice of oxygen and methane fields with temperature contourlines.

can see in figure 6.4.5. The evolution of those vortices enhance the mixing of methane and hot products.

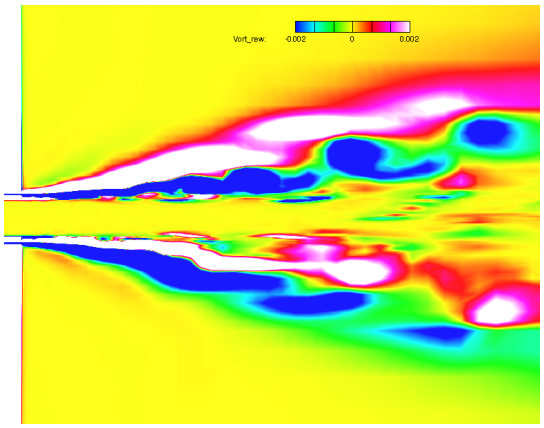

Figure 6.4.5: Slice of magnitude of Z vorticity component.

In the following figures 6.4.6 and 6.4.7 are showed a slice of temperature field with the stream lines in the chamber and the velocity field.

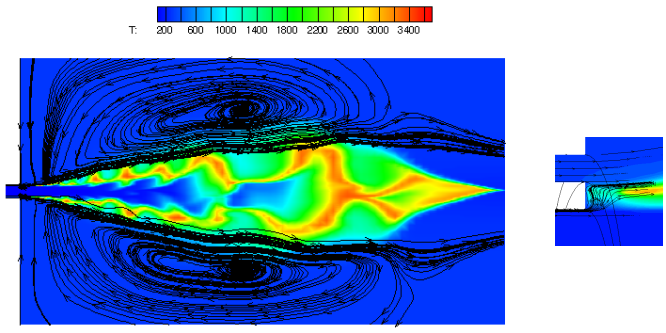

Figure 6.4.6: Left: temperature field and streamlines in chamber. Right: streamlines detail near the LOX post and temperature field.

In the figure 6.4.8, is showed the 3D chamber with the temperature isosurfaces, 2500K $<$ T $<$ 3000K, and the streamlines.

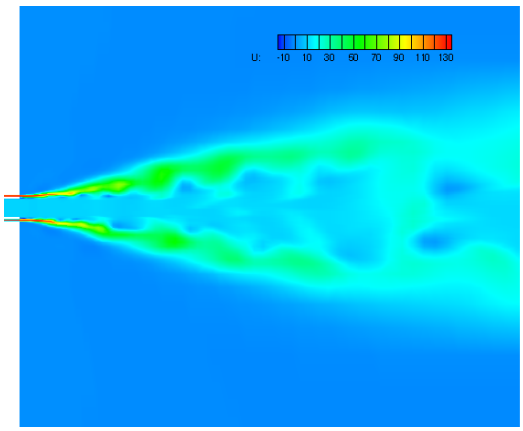

Figure 6.4.7: Axial velocity, u, field in chamber.

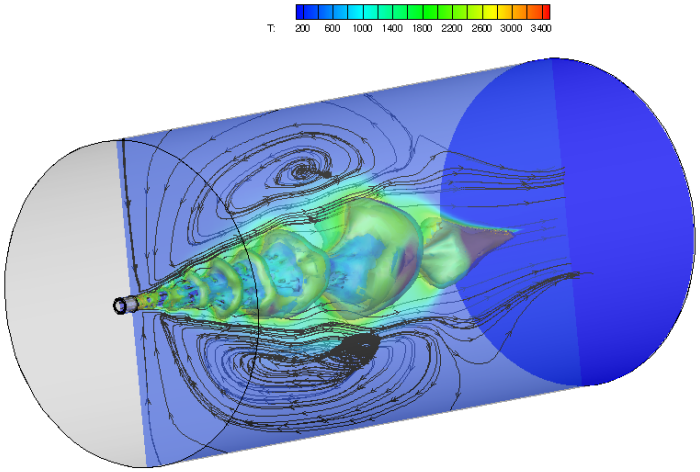

Figure 6.4.8: 3D chamber streamlines with temperature field and temperature isosurface (2500K $<$ T $<$ 3000K)

We note, in the zoom figures 6.4.9 and 6.4.10, some recircle areas that promote the mixing between the combustion products at high temperature also some not burned products. Probably, the wide chamber dimension and a not consistent time, $t = 0.022sec.$, deaden the effects caused by mixing. The high temperature in the flame cone does not warm up the environment. We note also the presences, in these recircle areas, of some combustion products: CO_2 in 0.1% , CO in 0.3%, H_2O plus CH_4, N_2 and small quantity of oxygen.

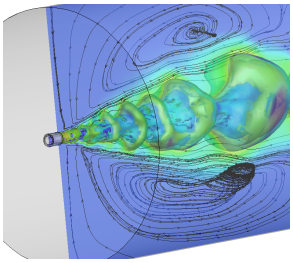

Figure 6.4.9: 3D chamber with detail of streamline: detail.

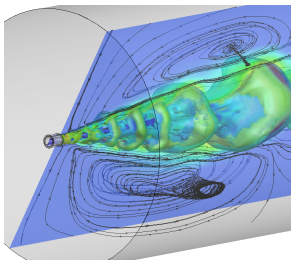

Figure 6.4.10: 3D chamber with detail of streamline. Detail with rotation of plane.

6.4.5 *Geometry and mesh thrust chamber*

In this case the **geometric dimensions** are smaller than in the previous cases and was added the nozzle.
The **boundary conditions** are equals to the test case chamber also at **initial conditions** which had been modified in a second step.

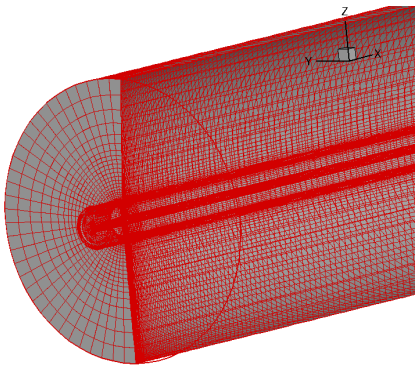

Figure 6.4.11: Combustion chamber mesh longitudinal section.

6.4.5.1 *Numerical results: Thrust Chamber*

An other simulation has been performed: a thrust chamber.

The first step uses as boundary conditions the outflow type **back pressure** with a value equals to the chamber: the flow is rest and only the activation of heat source at the outflow boundary condition can be changed it and the pressure value decreases. This simulation is carried out to obtain an efficient standard procedure for the following simulations. The mesh is shown in figure 6.4.11 and the thrust chamber geometry is shown in figure 6.4.12. The injector dimensions are the seems than last reactive case but the chamber radius is 1/3.

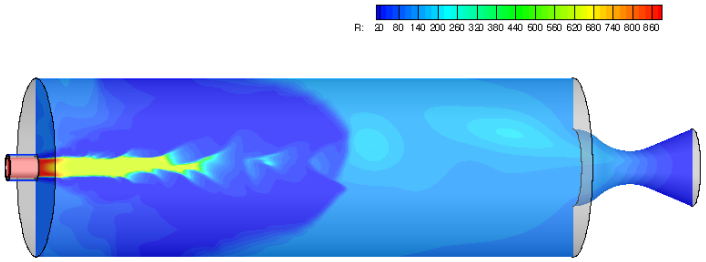

Figure 6.4.12: Density field of combustion chamber.

The simulation is compromised by a wrong restart condition: we start with a steady state condition and later becomes a unsteady condition. The consequences are visible in the density fields. In addition we suppose also an relevant influence on results due to mesh . The other figures illustrate a temperature field figure 6.4.13, and a velocity field, figure 6.4.14, where is evident that the nozzle is correctly started.

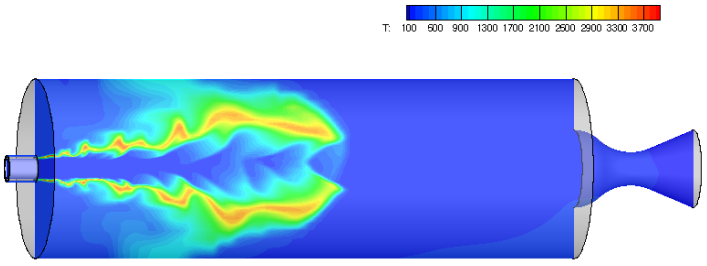

Figure 6.4.13: Temperature field in combustion chamber.

The figure 6.4.15 highlight the recirculation zone near the oxygen post. The little area with its combustion products permit the flame

anchoring.
The figure 6.4.16 illustrates a local density peak which is the cause of crashing of simulation.
Therefore, we thought that an not adapts mesh resolution could be the cause the unexpected density behaviour, and we tried to refine it.

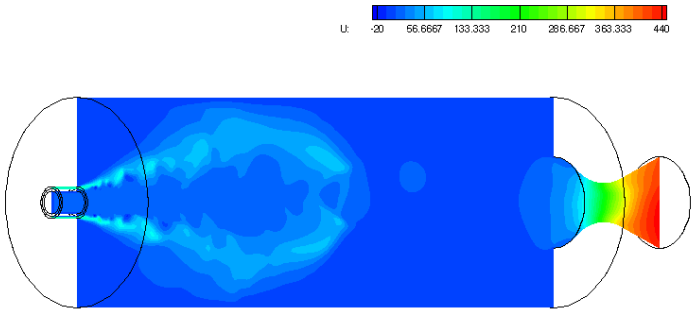

Figure 6.4.14: Axial velocity, u, field in combustion chamber.

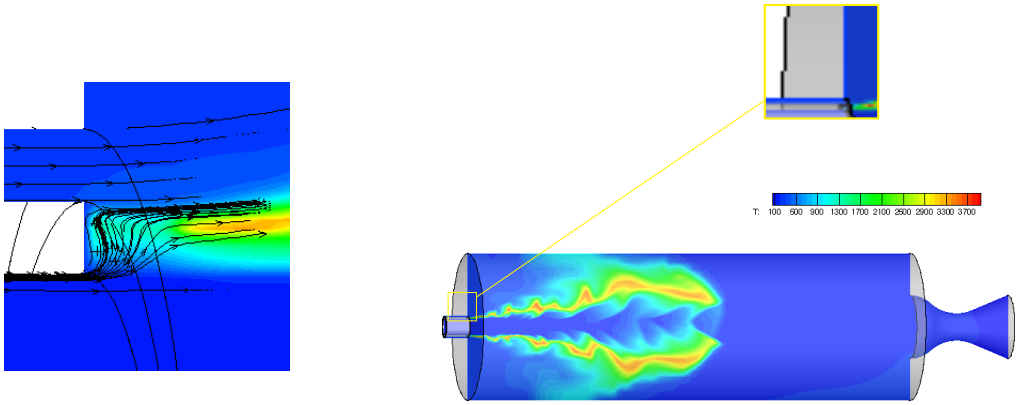

Figure 6.4.15: Combustion chamber with temperature field. Left: post-tip detail in combustion chamber with temperature field and streamlines. Right: combustion chamber with temperature field.

The refinement, in figure 6.4.17, in axial and radial direction was used to try resolve the problem of the highest density values. This strategy does not gave us the expected result. This strategy has only postponed the problem of peak, reducing the temporal step of one order and shifting the the problem in further times.

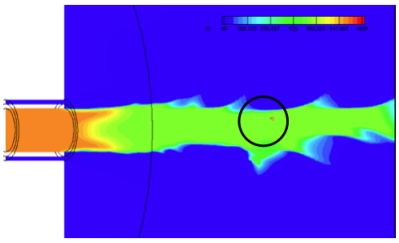

Figure 6.4.16: Peak of density in jet flow.

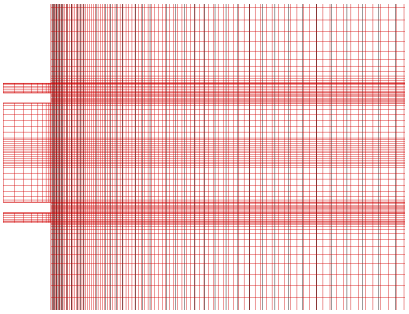

Figure 6.4.17: Coarse mesh (black) and fine mesh (red).

CONCLUSIONS

In this Chapter we debated on two test cases (case #3 e case #4) of Mayer. We realised a comparison, among the experimental data of Mayer, the numerical results of Schmitt, and our numerical results using the centerline density , the jet spread angle, and the core length. We observed that the usage of implicit preconditioned density-based method, in the case #3, gave us a relative error lower than a implicit preconditioned method with a DTS time integration. In the case #4 the implicit preconditioned method gave us the results with a relative error lower than a implicit preconditioned method with a DTS time integration. We look for a strategy for the reactive case but the results obtained are not good. A simple implicit preconditioned method for the free jet gave us the sufficient results but when we tried to simulate a combustion chamber with nozzle and a reduced geometry, we met multiple convergence problems: the interruption of simulations has been the result. We observed that a mesh refinement on the axis and radius direction determined some benefit but the simulation time is increased.

7

NUMERICAL RESULTS HYPROB PROJECT

Contents

OBJECTIVES OF CHAPTER

The chapter will show the results of numerical simulations obtained during the Hyprob program. An important element is estimate of heat flux on the wall and on plate. The numerical simulations realised for the SSBB, are showed. The simulations have been realised using two different EOS, moreover we had compared two different

approaches to evaluate the heat flux: the solve to wall and the wall function. Another part will show the analysis of DEMO and will exhibit a slice of it 60^0 with 3 injectors: the first belongs of internal crown and the other two belong to external crown. In last analysis we will present the second part of the mesh generator.

7.1 HYPROB PROGRAM

Within the framework of the HYPROB-BREAD program, CIRA is conducting system design studies on both the Sub-Scale single injector Calorimetric setup (SSBB) and the multiple-injector demonstrator setup, both taken as stepping stones for the establishment of technological expertise in LOX/CH_4 Liquid Rocket Engines (LRE). The general context of section is the CFD simulation of SSBB and the 3-dimensional demonstrator assembly (DEMO) in a 60 degree sector configuration comprising 3 injectors. The use of structured and unstructured grids, for the DEMO, will be illustrated in an effort to extract wall heat flux data both on chamber wall and on injector plate. Such studies adopt engineering methodologies used as design tools on one hand, and Computational Fluid Dynamics (CFD) techniques on the other, employed as verification and as a means to establish phenomenological trends.

7.2 SUB SCALE BREAD BOARD ASSEMBLY

All the URANS simulation runs for the Sub Scale Bread Board Assembly (SSBB) adopt an axi-symmetric steady (or unsteady) RANS approach, variable real gas equations of state (EOS) and a 15 species, 57 reactions finite-rate chemical mechanism.

Table 12 is a summary of the main simulation runs performed.

Particular attention was devoted to the application of PR real gas equation of state EOS as opposed to VDW EOS. In addition, a validation campaign of the wall heat-flux estimation technique was also addressed.

Run #	EOS	Grid type Δy	Wall treat.	LOX IN T[K]	LOX ρ [Kg/m^3]	Peak Wall $\dot{q}$ [MW/m^2]	Eq.Chamb. Pressure [bar]	c^* [m/s]	T_{max} [K]	Comb. Eff. c^*/c^*_{eq} $c^*_{eq} = 1847$
#1	VDW	C 200µm	WF	110	953	60	43.7	1437	3762	0.78
#2	VDW	R/WR 5µm	STW $y^+ \sim 3-7$	110	953	15	44.0			
#3	PR	C/WR 10µm	STW $y^+ \sim 10-20$	140	1013	10	44.0	1590	3747	0.86
#4	PR	R/WR 5µm	STW $y^+ \sim 5-10$	140	1013	15	44.0			
#5	PR	R/WR 0.4µm	STW $y^+ \sim 0.2-2.5$	140	1013	22.5				

Table 12: C: Coarse; R: Refined; WR : Wall-Refined; WF: Wall Function; STW: Solve to wall . Where absent, the particular data was not extracted.

7.2.1 *Run #1*

Details of simulation are given in Table 13. The temperature field relative to Run #1. is displayed in Fig.7.2.1. The Run revealed a rather low combustion efficiency, essentially due to a severe stratification of the temperature field.

EOS	VDW	
grid	coarse	$\Delta_{wall} \approx 200\mu m$
wall treatment	wall function	$y^+ = 200 \sim 2000$
LOX inlet T, ρ	110K	950 Kg/m^3
peak wall heat-flux	$60MW/m^2$	
equilibrium chamber p_c	43.7bar	

Table 13: Run #1

This results in a low characteristic velocity ($c^* \approx 1430$ m/s) with respect to the theoretical value emerging from thermodynamic equilibrium considerations ($(c^*)_{eq.} \approx 1840$ m/s), the ratio of such values being ~ 0.8, which can be taken as a representative value of combustion efficiency. Such low efficiency is the ultimate cause of a lower than nominal (nominal pressure 55bar) equilibrium chamber pressure, at the given throat area and mass inflow. We also note that p_c is lower than the critical pressure of oxygen, hinting at the possibility of a two-phase flow.

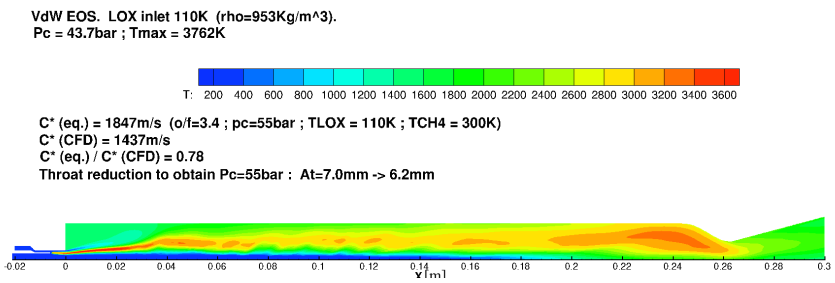

Figure 7.2.1: Temperature field, Run #1

It should be mentioned, however, that the axi-symmetric assumption effectively acts as a constraint of the flow which limits the degree of mixedness of the propellants, produces a longer flame length by suppressing the flow instabilities of the cold oxygen core, and, ultimately, underestimating the combustion efficiency. It is therefore possible that a three-dimensional simulation of the single injector configuration could yield a higher combustion efficiency and thus a higher chamber pressure.

We also note that the wall grid spacing for Run #1 exceeds the requirements of the wall function methodology implemented in CFD++ ($y^+ < 300$). To acquire confidence on the reliability of the wall heat flux levels obtained with the application of wall functions, a validation campaign was carried out, which will be illustrated in Sec.7.2.4. We anticipate that the peak value of $60MW/m^2$ of Run #1, occurring at the throat, is a rather large overestimation of the expected peak heat flux value, which should lie between $20MW/m^2$ and $60MW/m^2$.

7.2.2 *Run #2*

Run #2 represents an improvement over Run #1 as the level of grid refinement is overall higher with a local refinement at the wall boundaries. Details are given in Table 14. Wall functions are now dropped in favor of a direct resolution of the boundary layer up to the wall.
While the chamber pressure and combustion efficiency levels were not observed to vary significantly, the wall heat flux experienced a dramatic drop from the peak level of Run #1. The left panel of Fig.7.2.2 displays such wall heat flux for Run #2. Although the values of y^+ are far closer to unity, as they should for a direct estimation of the flux, uncertainty on the heat flux level estimation persists, making the validation procedure all the more necessary.

EOS	VDW	
grid	refined/wall-refined	$\Delta_{wall} \approx 5\mu m$
wall treatment	solve to wall	$y^+ = 3 \sim 7$
LOX inlet T, ρ	110K	$950\ Kg/m^3$
peak wall heat-flux	$15MW/m^2$	
equilibrium chamber p_c	44.0bar	

Table 14: Run #2.

Run #2 was also used as a benchmark for the flame anchoring mechanisms. The flame anchoring is achieved artificially by placing a persistent heat source downstream the recess. The size of such hot spot was reduced in order to assess whether anchoring was still possible. However the diffusive flame was observed to detach from its anchoring point and move downstream. During this motion, the flame progressively acquires a premixed nature. This can be assessed by inspection of the 'flame index' scalar field (Westbrook et al. [119] and Mizobuchi et al. [67]), shown on Fig.7.2.3, which is a measure of the angle between fuel and oxidizer concentration gradients. If such gradients are opposed (red zone in Fig.7.2.3), the flame is diffusive in nature, otherwise, if aligned, the flame tends to acquire a premixed character (blue zone in Fig.7.2.3). Interestingly, as the flame detaches, the premixed zone, albeit not stationary, seems to be larger that the

diffusive flame, exhibiting a higher mean temperature, which, in turn, causes an increase in chamber pressure. Although only a qualitative phenomenon, the detachment of the flame and subsequent rise in pressure may to some degree be realistic and be of some concern in the operation of the SSBB.

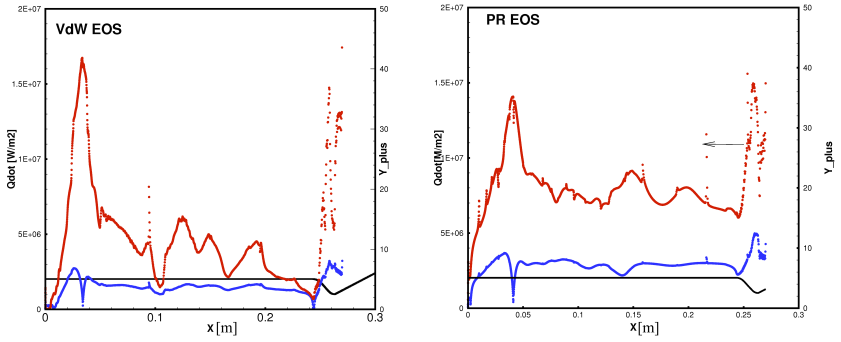

Figure 7.2.2: Left: wall heat flux for Run #2. Right: wall heat flux for Run #4.

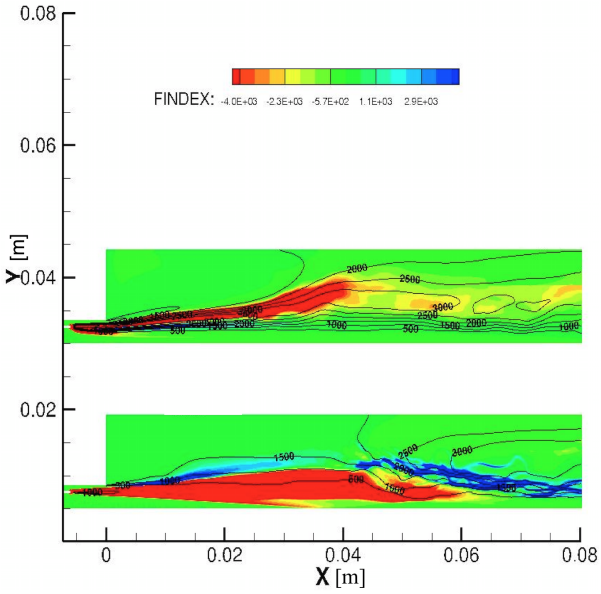

Figure 7.2.3: Run #2. Flame Index. Top: anchored flame; Bottom: detached flame.

Run	#3		#4	
EOS	Peng-Robinson		Peng-Robinson	
grid	coarse/wall-refined	$\Delta_{wall} \approx 10\mu m$	refined/wall-refined	$\Delta_{wall} \approx 5\mu m$
wall treatment	solve to wall	$y^+ = 10 \sim 20$	solve to wall	$y^+ = 5 \sim 10$
LOX inlet T, ρ	140K	$1013\ Kg/m^3$	140K	$1013\ Kg/m^3$
peak wall heat-flux	$10MW/m^2$		$15MW/m^2$	
equilibrium chamber p_c	44.0bar		44.0bar	

Table 15: Runs #3 and #4.

7.2.3 *Runs #3 and #4*

These simulations are summarized in Table 16. A number of measures were adopted to allow for the Peng-Robinson (PR) EOS to be implemented without causing instabilities during integration. Among such measures, the nozzle divergent was reduced in length in order to limit the range of Mach numbers and pressures spanned by the simulation. The LOX inlet temperature was also raised to 140K to reduce the density gradients at the LOX core periphery. Such measures were successful in allowing for the P-R EOS to be implemented.

An initial comparison between Run #1, utilizing VDW EOS and Run #3, using PR EOS, is displayed in Fig. 7.2.4. A general conclusion is that the application of PR EOS yields similar scalar fields and in general similar flame conformation as the VDW case. Equilibrium pressures and c^* estimates are also very similar. Comparable values of wall heat flux are observed for similar grids, as shown in Fig. 7.2.2. The LOX core length and conformation, visible in Fig. 7.2.5, is also very similar in both cases, setting aside the small change in inflow density.

Analysis of species concentrations fields, Fig. 7.2.6, reveals that gaseous oxygen is present at high concentration well past the end of LOX core. Fuel is basically confined to the recirculation zone and fully consumed and dissociated at the chamber exit, this in spite of the overall inlet conditions being fuel-rich ($(f/o)/(f/o)_{st} = (1/3.4)/(1/4) \approx 1.18$). The latter is due to the complete dissociation of excess methane at the exhibited chamber temperatures.

A close examination of the present and past simulations yields the scheme displayed on Fig. 7.2.7, representing the main features of the reactive flow field conformation and flame morphology. In particular we can conclude that the LOX core typically extends to 0.5L, where L is the chamber length, preserving the high density and low temperature of a cryogenic liquid. High oxygen concentrations extent even further to 0.7L. Assuming the flame anchored at the recess zone, between the fuel and oxidizer injection zones, it exhibits the typical diffusive nature with a semi-aperture of $\sim$ 5 to 7 degrees and peak temperature of $\sim$ 3650K. The recirculation zone exhibits temperatures

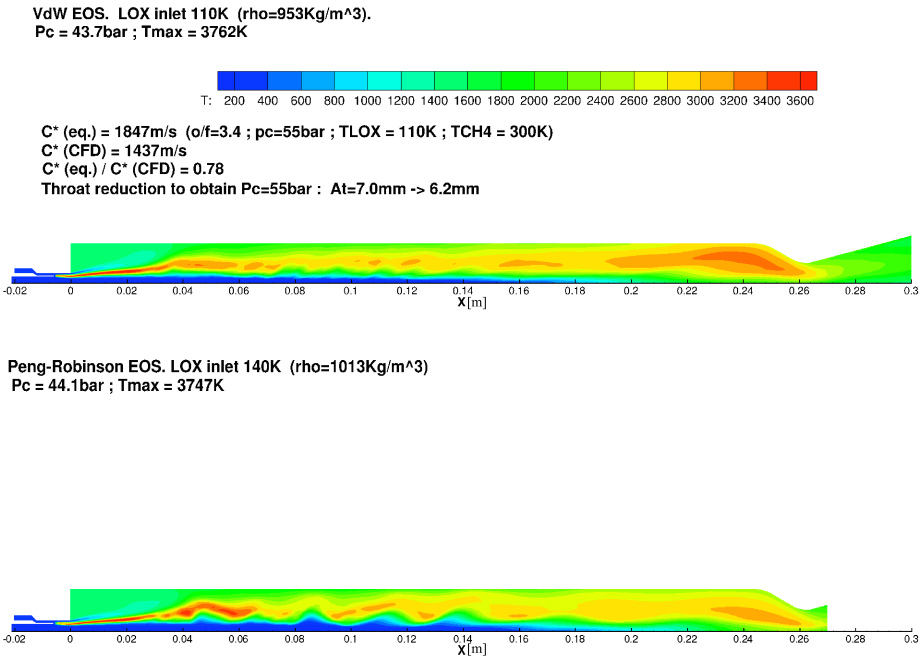

Figure 7.2.4: Temperature field: comparison between Run #1 and Run #3.

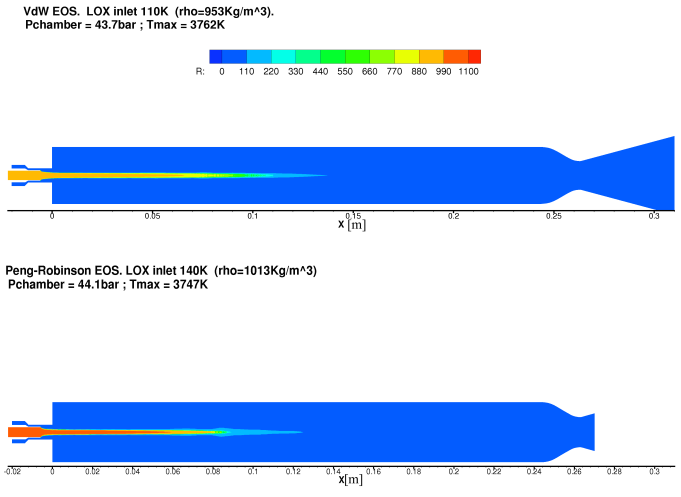

Figure 7.2.5: Density field: comparison between Run #1 and Run #3.

of 1500K, is characterized by a high methane concentration, and typically extends up to a stagnation point placed at 0.15L. An important aspect is that peak values of wall heat flux are observed roughly at the mid point of the recirculation zone. Such values are comparable to those observed in the vicinity of the throat area (see e.g. Fig. 7.2.2).

The high wall heat flux at the recirculation point has a different genesis to the throat peak. At the throat, the peak is a result of a peak in the convective heat flux coefficient (proportional to $(\rho u)^{0.8}$). At the recirculation zone the heat flux peaks when the tangential velocity is greatest, corresponding to a point of maximum wall shear stress (τ_w) and therefore of y^+. This is better illustrated in Sec.7.2.6. The relative intensity of the two peaks is comparable, although a clearer picture will only be possible with a solution exhibiting a satisfying grid convergence, and for which $y^+ \sim 1$ (see Run #5 and Sec.7.2.6).

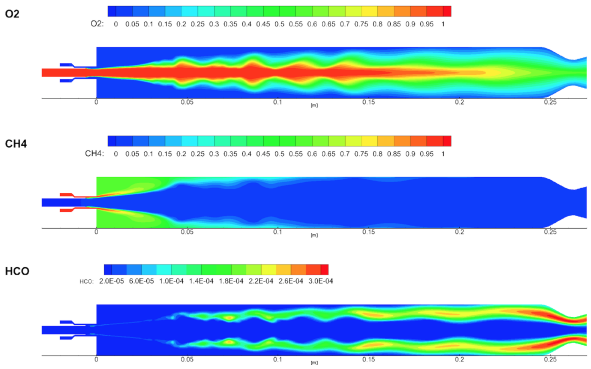

Figure 7.2.6: Species concentrations in Run #3.

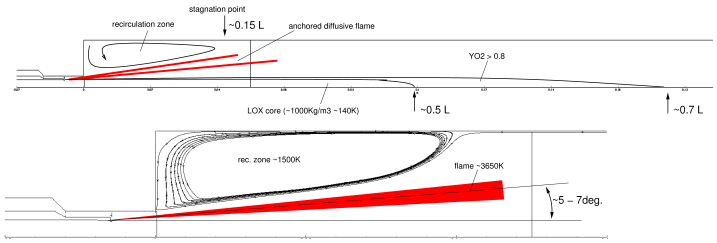

Figure 7.2.7: Schematic representation of reactive flow conformation and morphology.

7.2.4 *Validation of wall heat flux estimation*

Given the foregoing arguments, a rather dramatic discrepancy was observed between heat flux values estimated using wall functions on coarse grids on one side, and values estimated directly, solving

the boundary layer to the wall, with wall-refined grids on the other. The need for a validation of the wall function approach has therefore arisen, in order to establish a confidence level for y^+ above which heat flux estimates become unrealistic. We have taken advantage an approach used to establish wall fluxes on the Demonstrator geometry. This approach validated (Betti et al. [7], Suslov et al. [100], Pizzarelli et al.[83]) by CRAS in-house CFD code was used with a mesh that guarantees $y^+ \sim 1$ along the entire wall chamber and where wall fluxes were established by solving the boundary layer field up to the wall. Such results were taken as a reference, and heat flux calculations were repeated on the CFD++ platform using the wall function approach with grids at various levels of refinement.

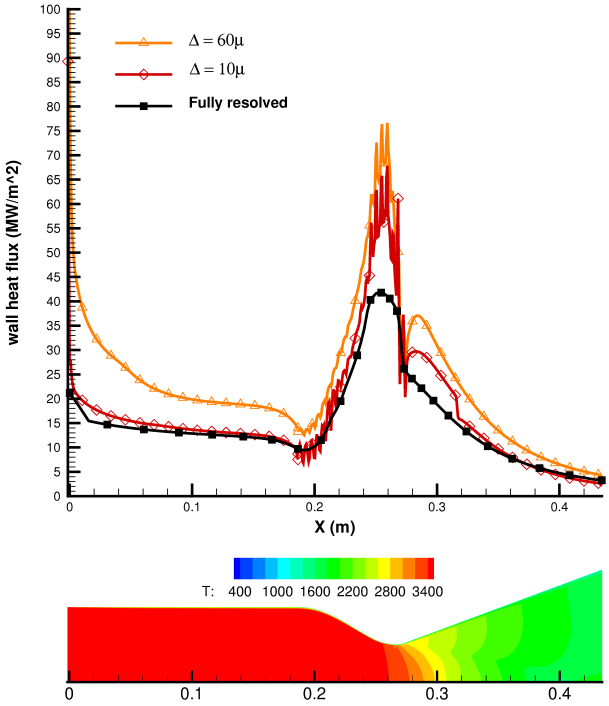

Figure 7.2.8: Heat flux validation on Demonstrator geometry. Wall heat flux for two different grid wall resolutions (△ and ◇ symbols) at $\Delta_{wall} = 60\mu m$, $10\mu m$ obtained with CFD++ using the wall function approach. Shown in ■ symbols is the reference heat flux profile obtained independently using the in-house CRAS code, by directly resolving the boundary layer up to the wall with a wall resolution of $\Delta_{wall} \approx 1\mu m$.

As a reference simulation we chose the full-flow case where a mixture of gases at equilibrium temperature ($T = 3587K$) and composition (at $p \approx 54bar$) is fed uniformly through the whole injection plate area with a mass flow $\dot{m} = 8.45Kg/s$. The composition, in this

validation phase, is kept frozen by disabling the chemical reactions. Figure 7.2.8 shows the results of such a validation campaign in terms of wall heat flux. Two CFD++ grid wall resolutions were used, namely $\Delta_{wall} = 60\mu m$ and $\Delta_{wall} = 10\mu m$. The corresponding y^+ profiles are displayed on Fig.7.2.9 where it appears evident that for the reference solution $y^+ \sim 1$. Note that a certain degree of high frequency effects is present in the results, due essentially to grid effects in areas of maximum wall curvature.
Analysis of such results reveals that the $\Delta_{wall} = 60\mu m$ grid is too coarse, yielding peak values of $y^+ > 400$. In this case, the wall function approach clearly overestimates the heat flux. On the other hand the $\Delta_{wall} = 10\mu m$ is fully adequate, yielding $y^+ < 50$. In this case, the heat flux estimate obtained through the wall function is accurately estimated as the comparison with the reference solution shows. Discrepancies are essentially due to differences in the boundary profile reconstruction which, in the case of CFD++ grids, was not sufficiently smooth, thus giving rise to local jumps in heat flux caused by local unphysical peaks in curvature.
From the above validation procedure we can draw the general conclusion that the wall function approach can be considered reliable for $y^+ < 20 \sim 30$, i.e. for $\Delta_{wall} \approx 10\mu m$. This indicates that the heat flux estimated in Run #1 is clearly overestimated and can safely be regarded as an upper bound. On the other hand, it is equally important, when trying to fully resolve the boundary layer in order to attempt a direct estimate of the heat flux, to obtain $y^+ \sim 1$. As was shown with Runs #3 and 4, a convergence study on grid resolution reveals that an insufficient resolution underestimates wall heat fluxes (contrary to the wall function case). We can therefore conclude, as we did at the end of Sec.7.2.1, that for the SSBB geometry, the expected peak heat flux value, located at the throat and at the recirculation zone, should lie between $20MW/m^2$ and $60MW/m^2$. On the other hand, the uniform heat flux value at the chamber walls (away from the recirculation and nozzle areas), due to the far lower values of y^+, has a lower degree of uncertainty and should be in the order of $10 \sim 20MW/m^2$.

7.2.5 *Effect of wall recombination*

The thermal layer at the wall clearly exhibits lower temperatures than the bulk of the chamber flow. This will generally cause radical species to recombine into products through exothermic processes which will generally modify the temperature profile in the layer with respect to a frozen scenario in which the composition is though to be constant. As a result of this additional heat release, we expect the temperature gradient at the wall to be higher and consequently the wall heat flux

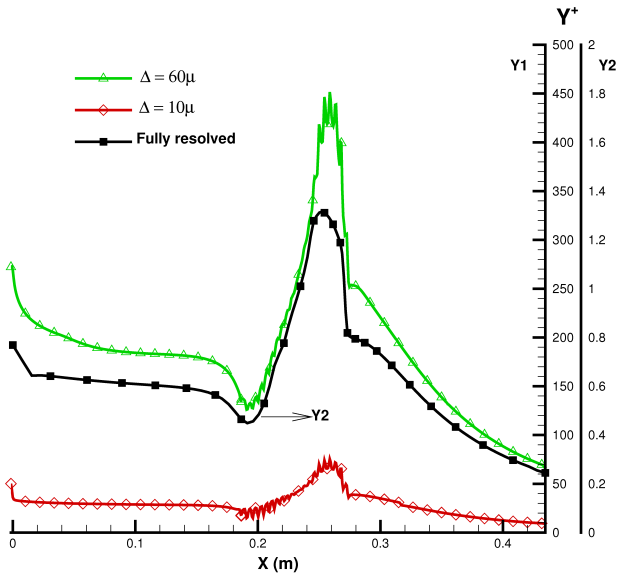

Figure 7.2.9: Y^+ profiles along the Demonstrator chamber. ◇ and △ symbols denote, respectively, a $\Delta_{wall} = 10\mu m$ and a $\Delta_{wall} = 60\mu m$; Shown in ■ symbols is the reference heat flux profile obtained independently using the in-house CRAS code (full resolved)

larger than any estimate carried out using a frozen composition assumption. Note that this scenario would additionally change in the presence of a catalytic wall assumption. Figure 7.2.10 displays the temperature profiles in the frozen and reactive cases, as well as, in this latter case, the composition profiles of the major radicals and products.

We can observe a steeper temperature profile in the reactive case which causes higher fluxes, visible in Fig. 7.2.11. The increase in heat flux due to radical recombination, in this case, is of the order of up to 50%, taking the frozen estimate of $\sim 10 MW/m^2$ on the chamber side wall to $\sim 15 MW/m^2$ in the reactive case.

7.2.6 *Run #5*

At the time of this writing a simulation (Run #5) is under way for the SSBB geometry with a low wall-cell size $\Delta_{wall} \approx 0.4\mu m$ which guarantees $y^+ \approx 1$ while directly resolving the boundary layer up to the wall. The simulation was initiated by mapping the Run #3 field onto the new grid. A new steady state has not yet been established although it can be argued that a new, better resolved boundary layer has indeed developed, allowing for more reliable estimates of wall heat fluxes. Fig.7.2.12 is a preliminary result showing a comparison

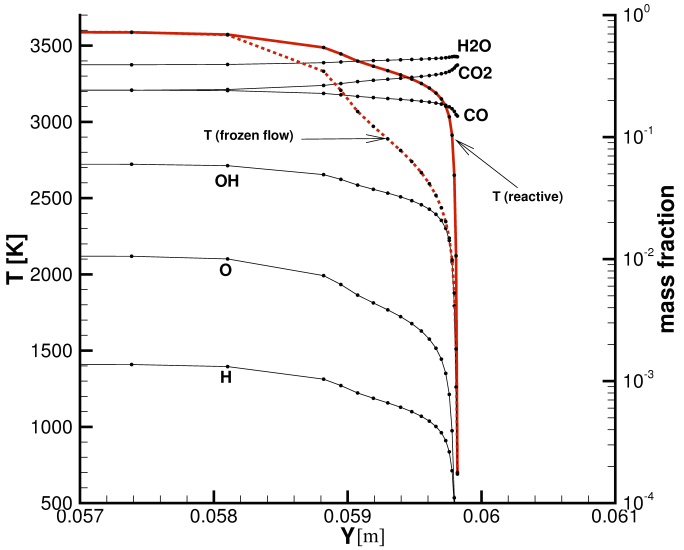

Figure 7.2.10: Demonstrator geometry. Temperature and composition profiles at X = 0.18m station. Wall temperature T = 700K

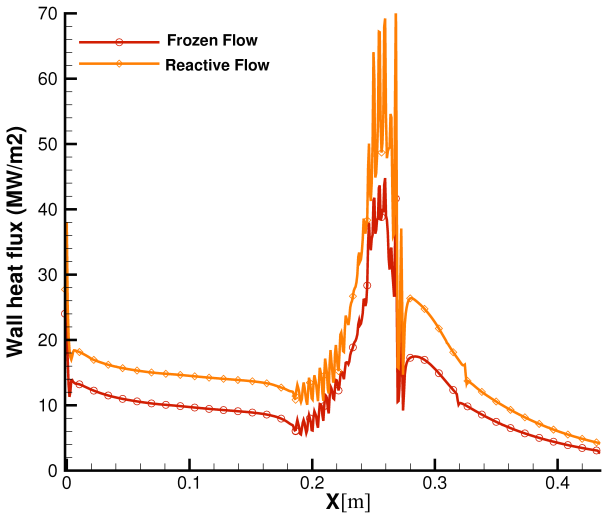

Figure 7.2.11: Demonstrator geometry. Wall heat flux. Wall temperature T = 700K. ◇ Symbol denotes the reactive flow and ○ symbol denotes the frozen flow

between throat heat fluxes for Runs #3,#4,#5. Note that Simulation 5 now guarantees $y^+ \approx 1$ with an upper bound $y^+ < 2.5$ which is better than all of the previous simulations. As expected the peak flux has grown compared to the other simulations. We record, for the particular set of data shown in Fig.7.2.12, a peak flux of $22.5 MW/m^2$ at the throat.

Fig.7.2.13 shows the heat flux characteristics and the flowfield at the recirculation zone. It is again worth pointing out that the results shown are not steady state results although they indeed carry valuable information on the conformation of the boundary and thermal layers at the new resolution. The figure clarifies the genesis of the wall heat flux peaks at the recirculation zone. Such peaks are generally located in correspondence of the center of any recirculation vortex where the wall shear stress and thus y^+ is expected to be a maximum. We conclude that the recirculation vortex will be responsible for a substantial convective wall heat flux, with the peak to be expected in correspondence of the vortex center where boundaries are thinner and wall shear stresses and gradients generally higher.

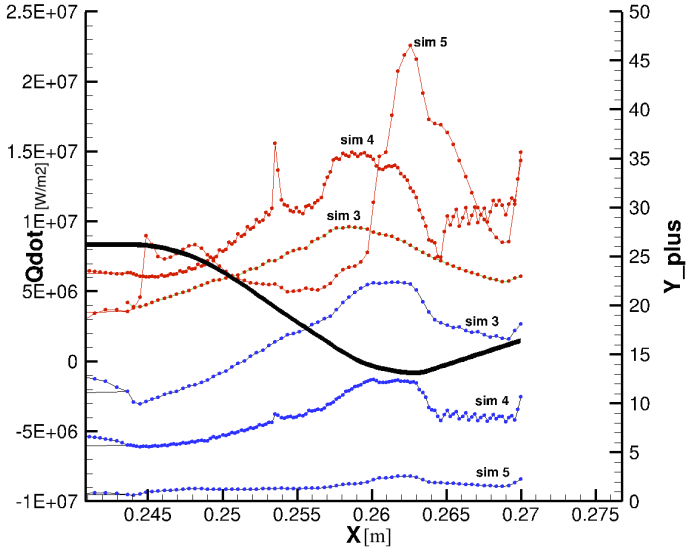

Figure 7.2.12: Wall heat flux (⊖) and y^+ (⊖) at nozzle throat for SSBB geometry for Runs #3, #4, #5.

7.2.7 *Injector Assembly: Axi-symmetric LES Analysis*

All URANS simulations conducted thus far, whether Axi-symmetric or 3-dimensional, have shown a systematic failure to capture the flame anchoring mechanism in the framework of LOX/methane su-

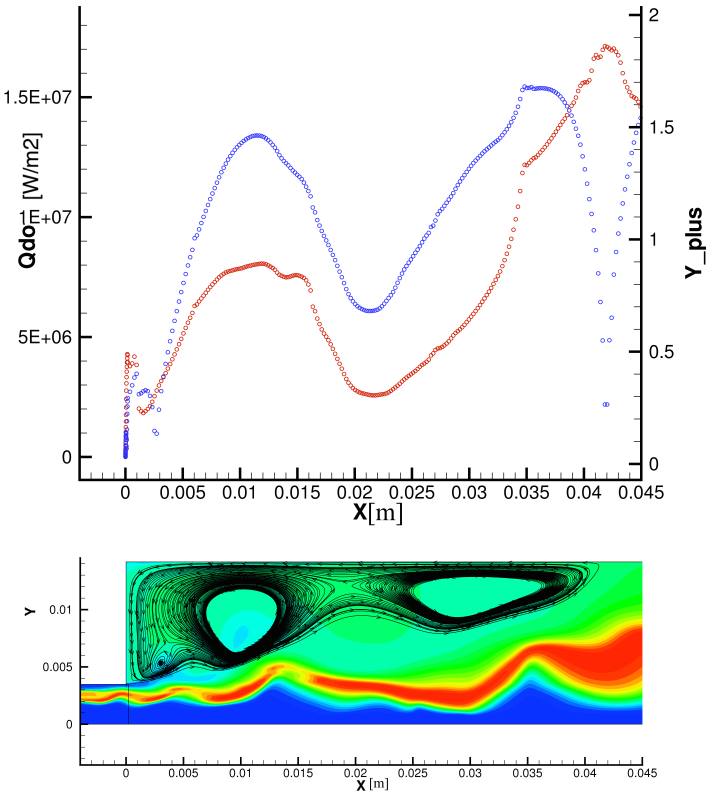

Figure 7.2.13: Wall heat flux (⊖) and y^+ (⊖) at recirculation zone for Run #5.

percritical injection, mostly because of inadequate resolution of the post tip region. The current literature Zong et al. [127] states that flame stabilization for a shear coaxial injector with cryogenic propellants is achieved by the recirculation flow downstream of the LOX post, which acts as a hot-product pool providing the energy to ignite incoming propellants. In this respect a URANS approach may be insufficient to capture such a small recirculation zone and a Large Eddy Simulation (LES) may be a far more suited approach to resolve the anchoring mechanism.
In order to investigate the impact of the numerical approach on the anchoring mechanism, both URANS and LES simulations of the injection zone were carried out in an axi-symmetric setting. In order to avoid the drawbacks related to the use of the Peng-Robinson equation of state in trans–critical (or even subcritical) conditions, a supercritical pressure of 60 bar was chosen as an independent parameter. To achieve this the supersonic nozzle outflow was replaced with a subsonic back pressure outflow condition.

Figure 7.2.14 is a comparison of a typical URANS simulation (with $k-\varepsilon$ closure) and a LES simulation (with one equation for the sub

grid-scale turbulent kinetic energy k). In addition to turbulence closure, a *thickened flame model* (Legier et al. [54]) for turbulent diffusive combustion was also used in this case. Such model tracks the flame surface and artificially thickens it by acting on diffusivity and reaction rate.

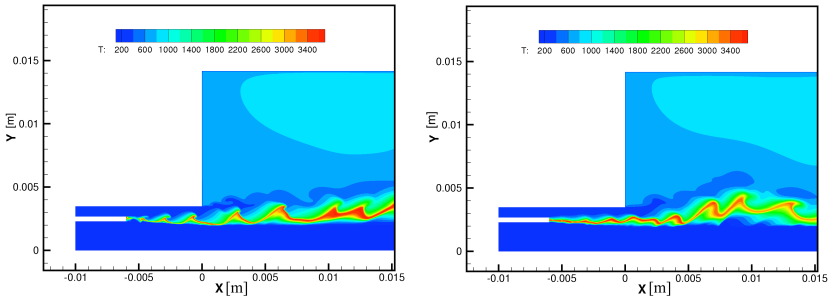

Figure 7.2.14: Left: URANS; Right: LES simulations of supercritical LOX/methane injection at 60 bar.

The recirculation zone is resolved with 16 cells while a 1µm cell is used to resolve wall gradients. Although URANS does capture some form of hot product recirculation, it is still not capable of maintaining an anchored flame in spite of the thickened flame model. On the other hand the LES approach succeeds in maintaining an anchored flame without any flame breakup. Figure 7.2.15 is a closeup of the recirculation zone in the LES simulation.

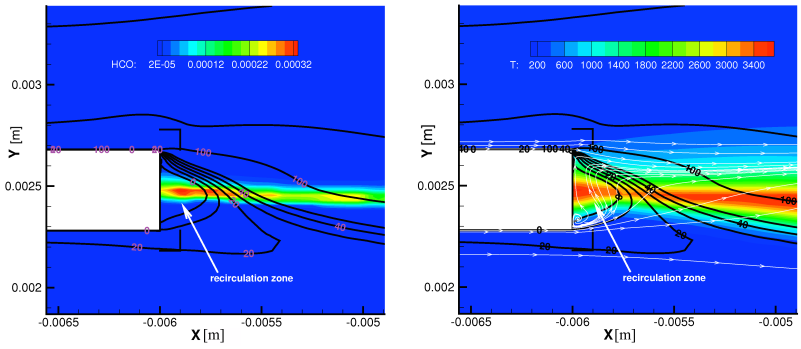

Figure 7.2.15: LES simulation of LOX/CH_4 injection at $p_c = 60$ bar. Left: HCO radical mass fraction; Right: temperature field. Also shown iso-contours of horizontal velocity component.

Such zone may be defined as the locus of negative horizontal velocity component $u < 0$. In this zone a radical pool is formed with enough residence time to form hot products and thus maintain an anchored flame. See also Figure 7.2.16 displaying various instantaneous

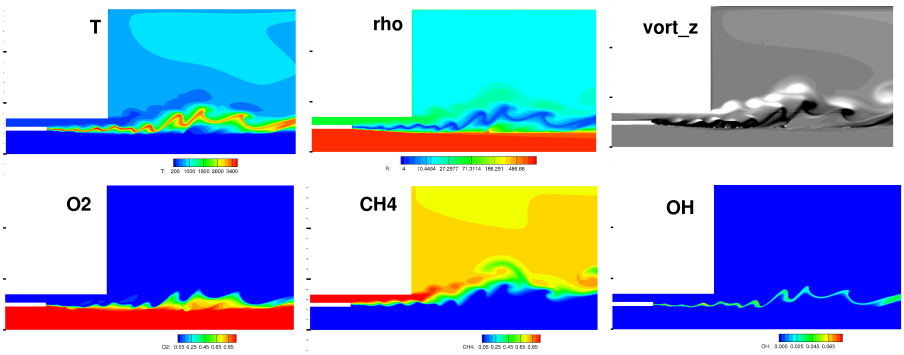

Figure 7.2.16: Various instantaneous fields for LES simulation. Shear layer instability causes vortex shedding which deforms and folds the flame. LES grid spacing is a uniform 25 µm with wall refinement at ~ 1µm.

scalar fields for the LES simulation. Future developments include the extension of the LES approach to a 3-dimensional setting so that the injector near-field may be studied with reference to the local flame conformation and aperture and to local heat flux on the injector plate or recess zone.

7.3 DEMONSTRATOR ASSEMBLY

Three-dimensional simulations of the DEMO assembly were the subject of this section. Two computational grids were adopted in the framework of URANS simulations: (i) a structured grid with block overlay which lacked refinement at the injector plate and (ii) an unstructured grid with a structured refined structure at the walls which included refinement at injector plate.

7.3.1 *Structured grid*

The 3-dimensional DEMO configuration was simulated using a URANS approach on a 1.5 M cells structured mesh representing a 60 degree slice comprising 3 of the 18-injector overall assembly shown in Fig 7.3.1. In order to adequately capture the flame system issuing from the injectors, refined cylindrical mesh blocks were overlaid on the cylindrical sector where the main chamber mesh is constructed.
Initial simulations were carried out using a steady state approach with finite rate methane/oxygen chemistry (15 species / 57 reactions) and an artificial anchoring hot-spot placed in a position equidistant from the injectors and approximately 1 cm from the injector plate. Upon ignition the hot spot was deactivated and a flame system was observed to be autonomously sustained without artificial anchoring.

The RANS simulation was then continued in unsteady mode (URANS) with no significant change in flow and flame conformation. Results shown in this section are all extracted from the unsteady simulation.

Equilibrium pressure	67 bar
Peak Temperature	3574 K
LOX inlet density	1027 Kg/m^3
Peak wall heat flux	40MW/m^2 (before nozzle throat)
Chamber Mach	0.1 ~ 0.15

Table 16: Main parameters for 3D DEMO simulation on structured grid.

Observation of Fig. 7.3.2 clearly reveals that the self sustained flame system does not exhibit the classical diffusive conformation of coaxially injected propellants, nor does it exhibit anchoring at or near the LOX post recirculation zone. Indeed the structured mesh used for this simulation does not account for enough resolution at the post tip for any recirculation to be resolved. On the other hand the flame system is self sustained at a finite steady standoff distance of approximately 2 cm from the injector plate. A closer examination reveals the presence of a narrow recirculation zone, visible in Fig 7.3.3. The recirculation zone length is approximately equal to flame standoff distance. This may indicate that the flame system standoff mechanism is related to the recirculation.
Some of the 3D simulation parameters are summarized in table 16.

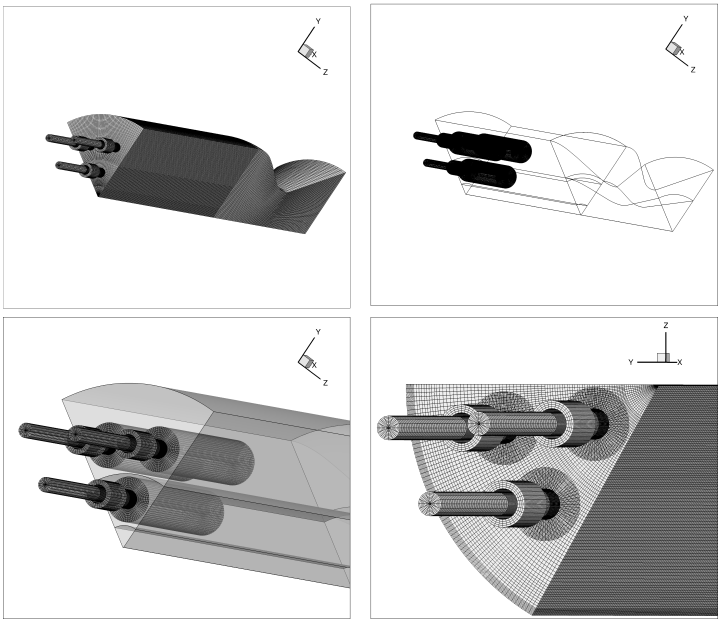

Figure 7.3.1: 3D DEMO geometry: structured grid

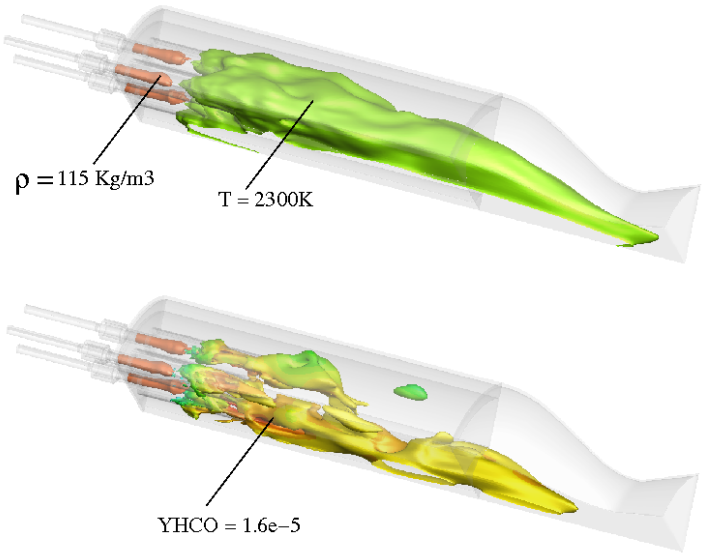

Figure 7.3.2: Temperature and HCO iso-contours showing the flame system stabilised at a standoff distance from injector plate.

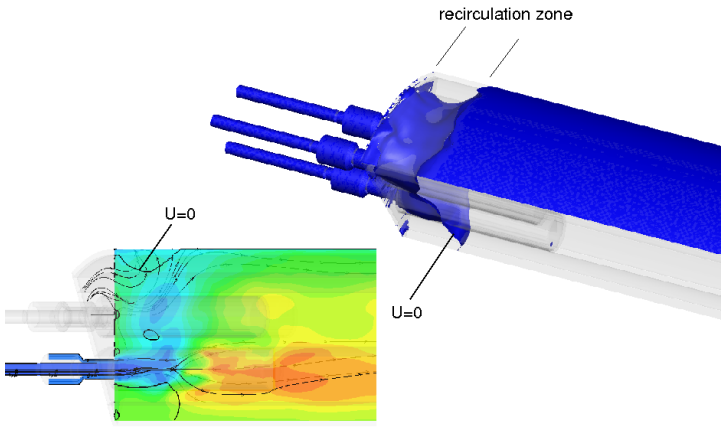

Figure 7.3.3: Recirculation zone.

The relatively high chamber pressure level of $P_c = 67$bar - with respect to previous 2-dimensional simulations - may be explained by a higher combustion efficiency. In turn, the latter is justified by a more uniform and far less stratified temperature field than in 2D simulations.

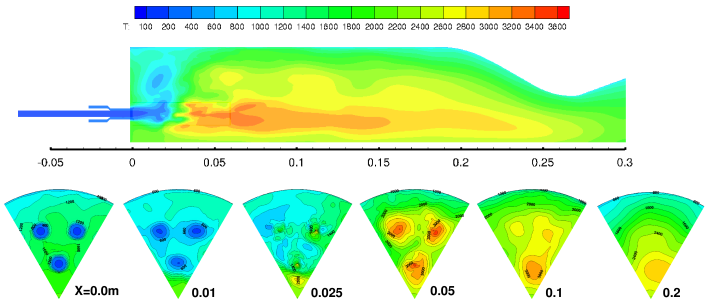

Figure 7.3.4: 3D DEMO simulation: temperature field on axial section (top) and transverse sections (below).

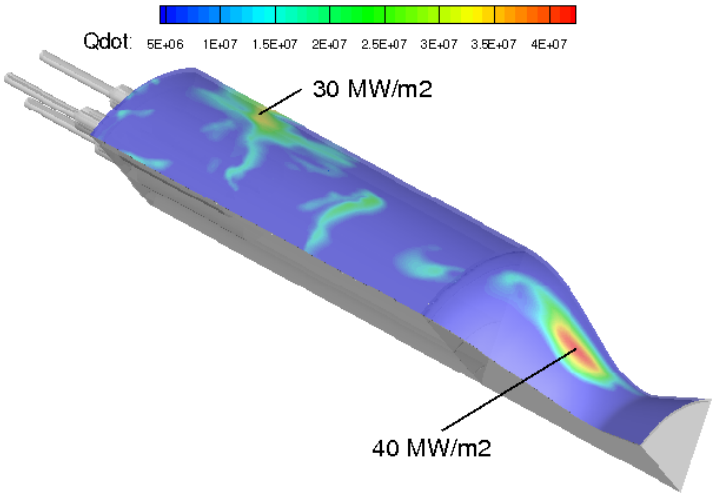

Figure 7.3.5: Wall heat flux on DEMO chamber wall.

The additional degree of freedom of 3D simulations allows for the presence of vortex stretching mechanism[1], absent in two dimensions, which greatly enhances turbulent mixing in unsteady flows. Figure 7.3.4 clearly shows the temperature field conformation and the lack of stratification leading to higher temperatures at the nozzle inlet compared to previous 2-dimensional simulations.
The structured grid was refined at the chamber lateral wall but not at the injector plate. Thus, wall heat flux measurements were performed only at the lateral wall by directly solving the boundary layer, without

1 This mechanism represents a source of vorticity and is represented, in the vorticity transport equation, by the term $(\boldsymbol{\omega} \cdot \nabla)\mathbf{v}$ which is identically zero in two dimensions.

the use of wall functions. Owing to the unsteady character of the solution, wall heat flux field is found to be extremely non-uniform (spotty) as can be observed in Fig. 7.3.5. In spite of this, we can nonetheless conclude that nozzle throat peaks in heat flux are $\sim 40 MW/m^2$ while recirculation zone peaks are $\sim 30 MW/m^2$.

7.3.2 *Unstructured grid*

An unstructured grid was constructed in order to test grid sensitivity and, in particular, to establish a wall heat flux field at the injector plate which was missing in the structured grid. Figues 7.3.6 shows such unstructured grid, comprising 2.5 M cells and 1 M points, highlighting the wall refinements at both injector plate and lateral wall, and a general refinement in the injection zone. Note, also, that the unstructured grid possesses some degree of resolution at the LOX post recirculation zone which was previously absent.

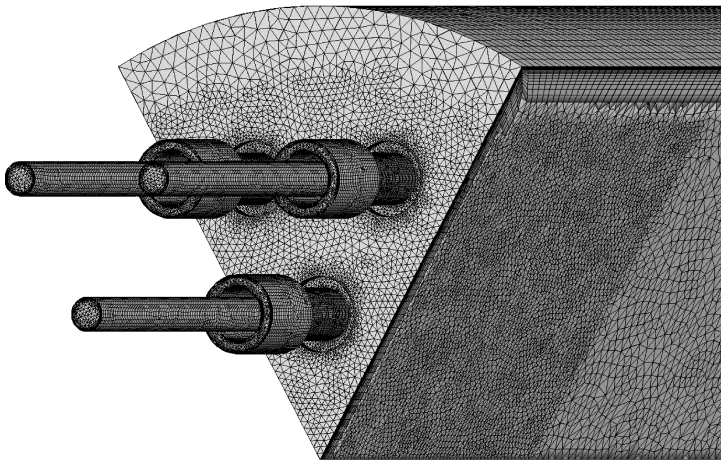

Figure 7.3.6: Unstructured chamber grid.

The simulation used a steady state, pressure based URANS scheme with $k-\varepsilon$ turbulence modeling. The main objective, in this context, was to establish the heat flux field on the injector plate, a quantity that could not be established on the structured grid. The heat flux on the injector plate is drastically influenced by the conformation of the flame structure issuing from the injectors.

If the established flame structure is stabilised at some standoff distance from the plate, as in the structured grid simulation, then the plate heat flux will be unrealistically low as most of the injector plate will be in contact with cold and unburned propellants. On the other hand URANS simulations have shown repeated failure in establishing an anchored flame without some artificial means such as the positioning of a hot spot. On the contrary, flame anchoring at the small

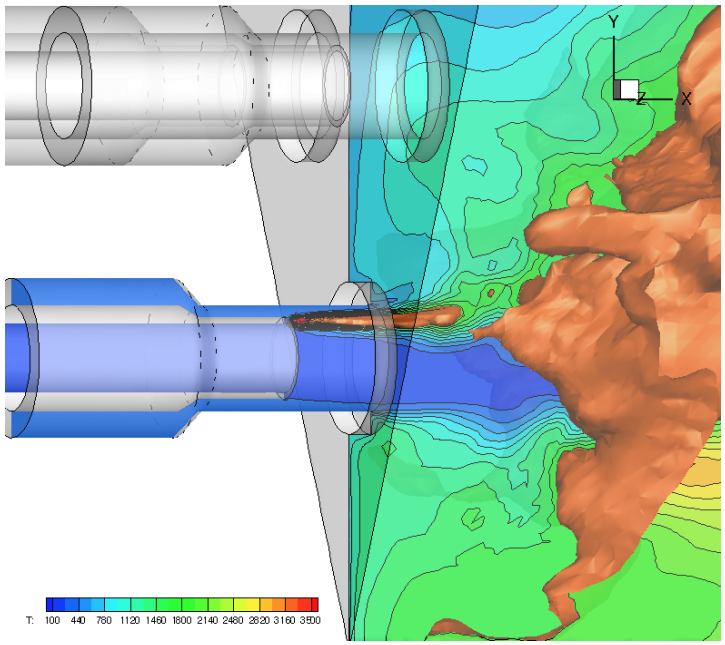

Figure 7.3.7: Artificial flame anchoring at post tip. Shown is the T = 1800 K isosurface and the temperature field on an axial bisecting plane.

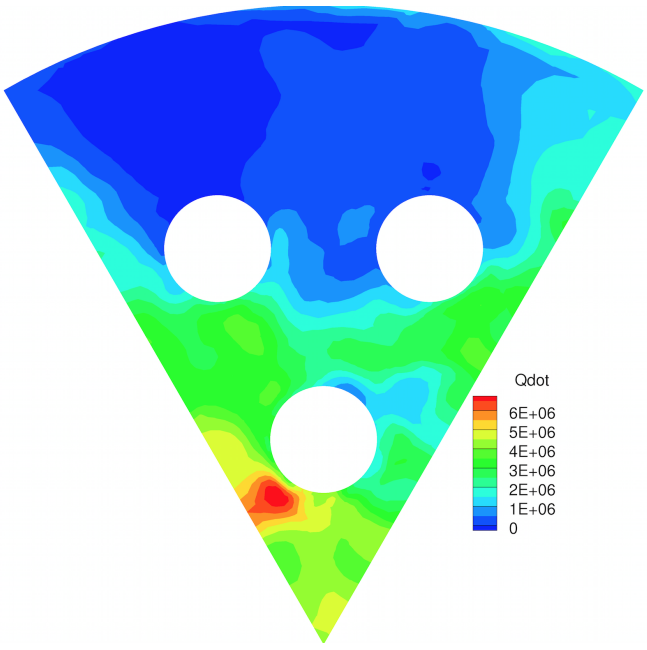

Figure 7.3.8: Heat flux on injector plate as a result of artificial flame anchoring on central injector.

LOX post recirculation zone is definitely to be expected as most of the current literature shows Lux et al. [56] and Yang et al. [130] In order to achieve reasonable heat flux readings, as they would develop from an anchored flame system, the diffusive flame at the LOX post tip was artificially anchored using a hot spot source. The ensuing 3-dimensional temperature field is visible in Fig. 7.3.7 where the hot source was placed near the recirculation zone of the central injector closest to the chamber axis. In CFD++ , it is possible to activate only one point-like hot spot at the time. With a single point-like hot spot, we obtained the partial diffusive flame shown in Fig. 7.3.7. The resulting heat flux at the injector plate is shown in Fig. 7.3.8 and exhibits a peak of ~ 7 MW/m^2.

7.3.3 *3D URANS Analyses*

As mentioned in sec. 7.3.2, in order to achieve a realistic injector plate heat flux field, artificial anchoring was achieved by implementing a small heat source near the recirculation zone of the central injector closest to the chamber axis. The other two injectors, however, were left without post-tip anchoring, this leading to a lower plate heat flux in their vicinity. To further improve heat flux readings, a complete flame anchoring was achieved for the three injectors, as it would be expected, around the full perimeter of the post-tip zones. This was achieved by implementing three toroidal heat sources in the post-tip zones.

7.3.4 *Using the steady state solver option*

This 3-dimensional DEMO simulations has been carried out using a steady state approach.

Figure 7.3.9 displays temperature fields showing three attached diffusive flames issuing from the three injectors. Note that flames are not continuous and tend to break and re-form as they enter the chamber. This is possibly due to lack of local resolution just downstream of the ignition source and to a greater extent to the steady state nature of the simulation.

The injector plate heat flux in visible in Fig. 7.3.10. A higher heat flux is now visible around each injector with a peak of about 20MW/m^2 in the mean field. With all of the three flames artificially anchored, the recirculation zone is now far more realistic in terms of the temperature field that is established in front of the plate. Thus, heat flux obtained is now to be considered with a higher level of confidence.

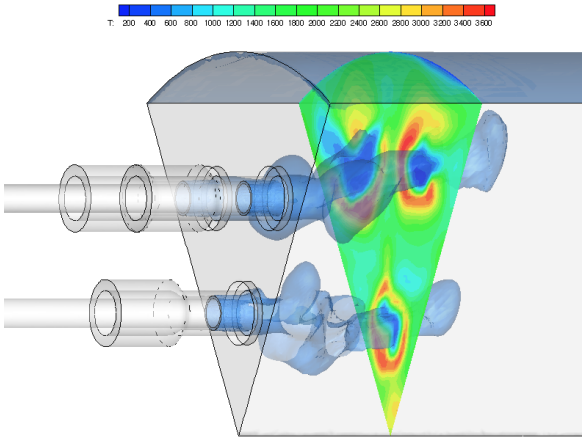

Figure 7.3.9: Full flame anchoring for the DEMO assembly by means of toroidal ignition zones.

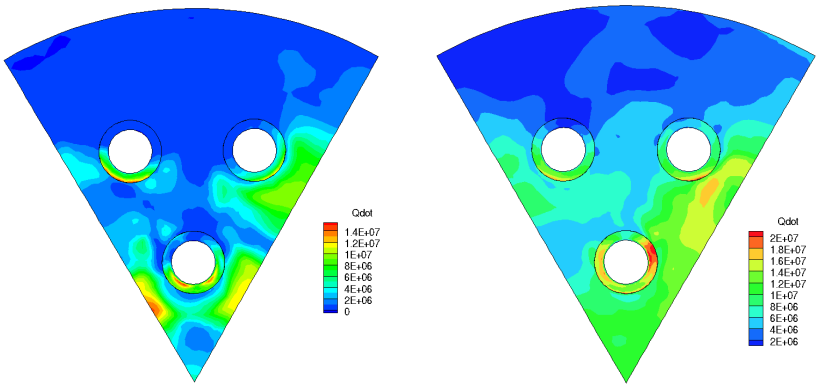

Figure 7.3.10: Injector plate heat flux. Left: instantaneous; right: averaged

7.3.5 *Using the time accurate option*

The 3-dimensional DEMO simulations seen thus far were carried out using a steady state approach. In this section, we transitioned to a time accurate URANS simulation using a dual time stepping scheme (with outer $\Delta t = 10^{-7}$ s) in order to achieve a time accurate reactive flowfield. The three toroidal hot sources were maintained in order to enforce flame anchoring on the three injectors.
The calculation was started at time 0.125 s and terminated at about time 0.147 s, that is for about 22 msec. With a time step of the order of 10^{-7} s, we completed about 84,000 integration time step. Note that 22 msec is roughly corresponding to one transit time. The unstructured mesh consisted of 2.9M cells.The run utilised 128 cores for about 3 months of wall clock computing time. The transition to a different anchoring mechanism forces the overall flow towards a very different topology involving jet diffusion flames anchored at the Lox post, clearly visible in Fig. 7.3.11, which is expected to reach some form of statistical steady state, at least near the injector plate, in a time which is smaller albeit of the order of the overall transit time across the chamber (roughly estimated as 10^{-2} s). During this transient, it can happen that the bulk temperature inside the chamber might decrease, this leading to a decrease of the chamber pressure.

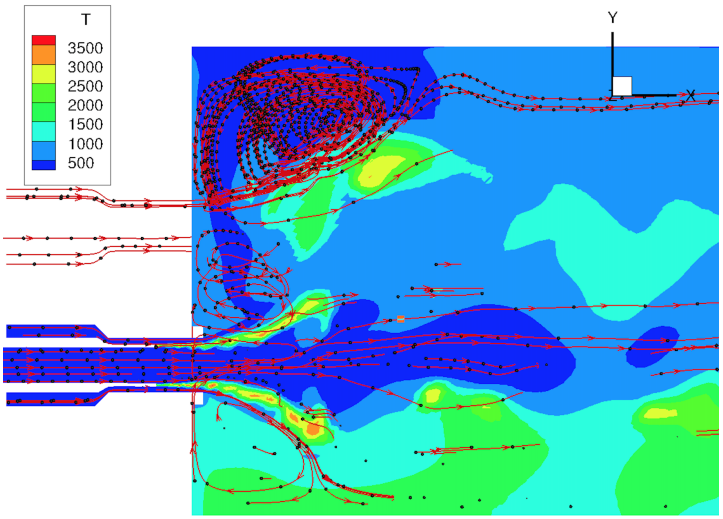

Figure 7.3.11: Temperature field and recirculation zones.

Figures 7.3.11 and 7.3.12 reveal the formation of of a system of recirculating zones adjacent to the injector plate. The lower zone, developing around the chamber axis, has a higher average temperature

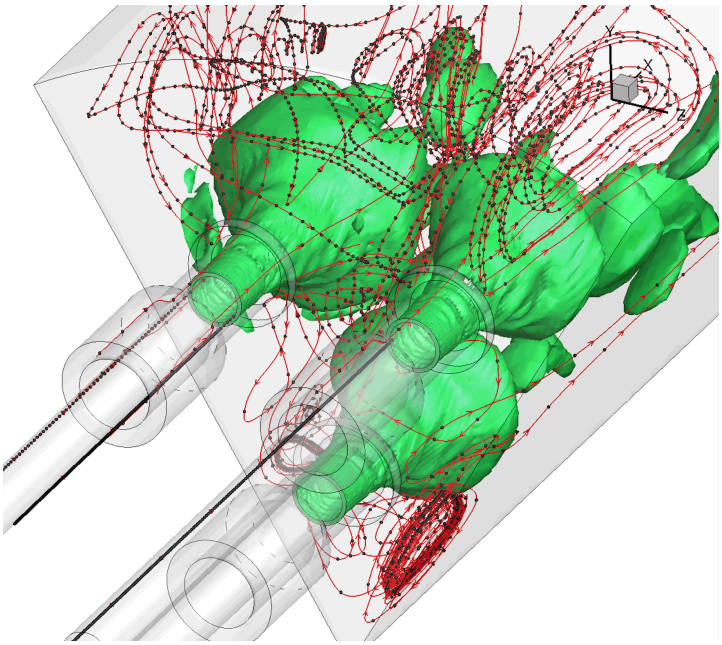

Figure 7.3.12: Velocity streamlines and temperature iso-surface, T=2000K.

and is responsible for a wall heat flux on the corresponding injector plate zone of ~ 14.5 MW/m^2, visible in Fig. 7.3.13. Because this recirculating zone seems to be rather well established (in a statistical sense), the corresponding plate heat flux value is to be considered realistic.

The recirculating zone developing close to the chamber lateral walls, on the other hand, has a far lower average temperature, indicating that in these early stages hot gases have not formed in sufficient amounts and the zone is therefore not sufficiently established. A peak wall heat flux of ~ 8.5 MW/m^2, at the lateral wall of the combustion chamber is found about the nozzle throat (Fig. 7.3.14). One has to expect, at later times, longer diffusive flames and a higher temperature in this upper recirculating zone.

A similar reasoning may apply to the central recirculating zone between the injectors which exhibits a similar low temperature. As a result, the corresponding plate heat flux values are by all means to be considered greatly underestimated.

From Fig. 7.3.15, it is possible to estimate the width of the jet cone angle as of being about 21-22 degrees with respect to the axial direction. Moreover, one can note that the Mach number inside the cryogenic oxygen stream is of the order of 0.1, whereas in the gaseous methane stream is of the order of 0.3. Thus, the Mach number inside the two streams differs by a factor 3, which on one hand is a relatively large gap, but not as large as it can occur if the oxygen stream would be a strictly incompressible fluid. A possible consequence of

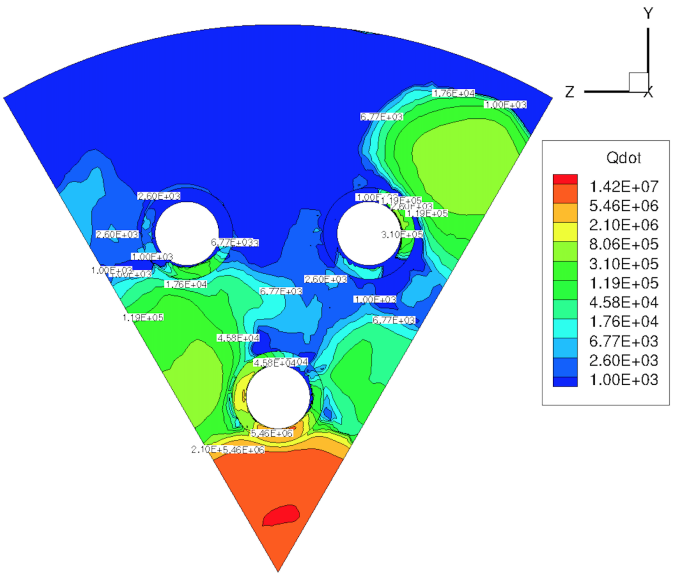

Figure 7.3.13: Thermal loads at injector plate

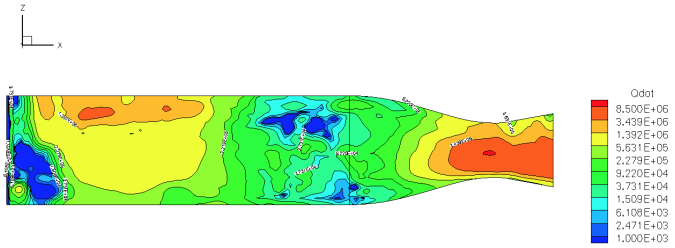

Figure 7.3.14: Thermal loads at lateral walls

this finding is the possibility of avoiding the adoption of pressure-based or density-based solvers, and/or of preconditioning or dual time stepping procedures to circumvent the stiffness associated with the different speed of sounds in the two streams.

From Fig. 7.3.16, one can note how the cryogenic oxygen stream dissolves after entering the chamber because of the combined action of the exchange of momentum and mass with the co-axial methane stream and of the vaporization. Note also that the frictional effects along the constant cross section area oxygen pipe (Fanno problem) cause a slight increase of the oxygen temperature and a decrease of the oxygen pressure, whose combined effect is to drop the (prescribed) density of the cryogenic oxygen stream at the entrance of the pipe from about 1032 Kg/m^3 (since the oxygen temperature is 110K, see Table 12), to about 760 Kg/m^3 at the pipe exit, while the density of the methane stream from the value of 55 Kg/m^3 at the methane

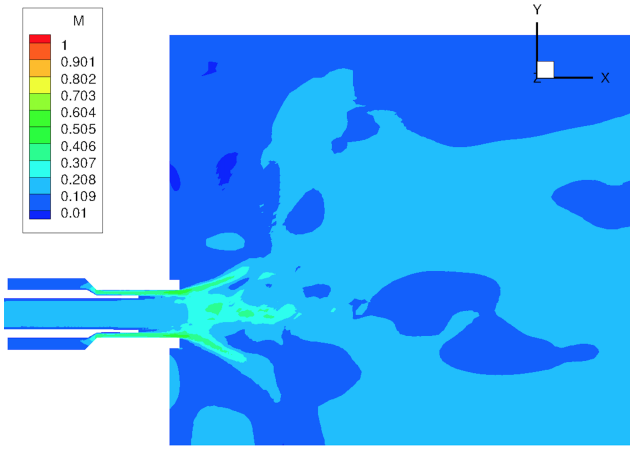

Figure 7.3.15: Mach number contour field.

pipe inlet drops to 50 Kg/m^3, (see Fig. 7.3.17); as a consequence, the density ratio between oxygen and methane at the exit of the coaxial injector is about 760/50=15.2, while the one computed at the inflow conditions of the two stream amounts at 1032/55=18.7.

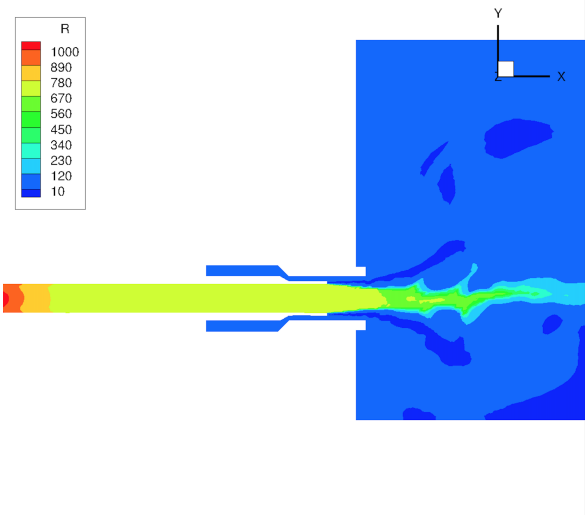

Figure 7.3.16: Density contour field.

From Fig. 7.3.17, we obtain also that at the exit of the coaxial injector the oxygen stream velocity and temperature are u_l=30 m/s and T_l=145 K, respectively, while the methane stream velocity and temperature are u_g=135 m/s and T_g=295 K.

With these data, the parameter J is evaluated as $J=\dot{m}_g u^2_g/\dot{m}_l u^2_l$ =1.55, the velocity ratio in-between the flow velocity of the gaseous

methane stream and the cryogenic oxygen stream is $v_r = u_g/u_l \sim 4.5$, the ratio of the chamber pressure with the critical pressure of oxygen is $P_r = P_{cc}/P_{crit,O_2} = 1.12$.

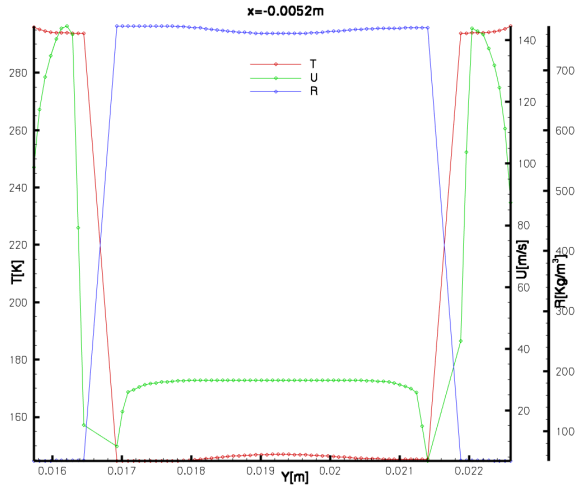

Figure 7.3.17: Flow conditions at the exit of the coaxial injector. ⟠ symbol denotes the temperature; ⟠ symbol denotes the velocity and ⟠ symbol denotes the density

7.3.6 *Time evolution of flow observables*

We report in Figs. 7.3.18 and 7.3.19 the time evolution of the average chamber pressure and temperatures, as well as the pressure and temperatures at selected locations in the chamber as detailed in Table 17. One can note that the average chamber pressure varies in the range 5.4 and 6.3 MPa. Note also that the average chamber pressure

	x [m]	y [m]	z [m]
Probe1	0.0	0.27	0.0
Probe2	0.085	0.27	0.0
Probe3	0.178	0.27	0.0

Table 17: Location of Flow Probes

is approaching quite closely the nominal value of 5.5MPa at about time 0.147 s. The local readings of the pressure levels are somewhat higher than the average pressure because the average is computed by considering the nozzle region which is obviously characterized by pressure values lower than that in the chamber. The local readings of the temperature levels indicates that the temperature of the combustion products varies in the range 2200-3400K. The green line in

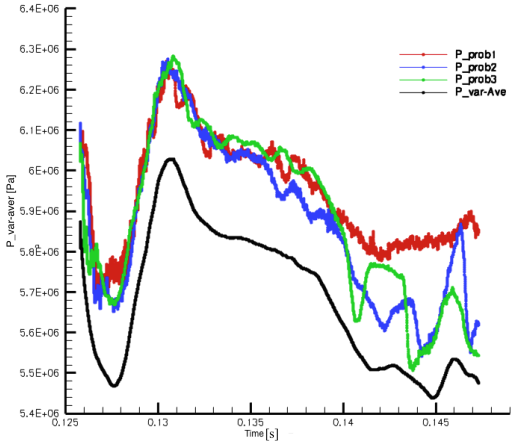

Figure 7.3.18: Pressure time evolution at selected locations: • symbol denotes the pressure in Probe1; • symbol denotes the pressure in Probe2; • symbol denotes the pressure in Probe3 and • symbol denotes the pressure average in chamber

Fig. 7.3.19 exhibits a sharp rise at about time 0.143 s: this is the time instant at which the contact discontinuity separating the hot products ($\approx$ 3500K) from the cold gas ($\approx$ 1300K) initially filling the chamber reaches the probe located at x=0.178m. The time evolutions in both

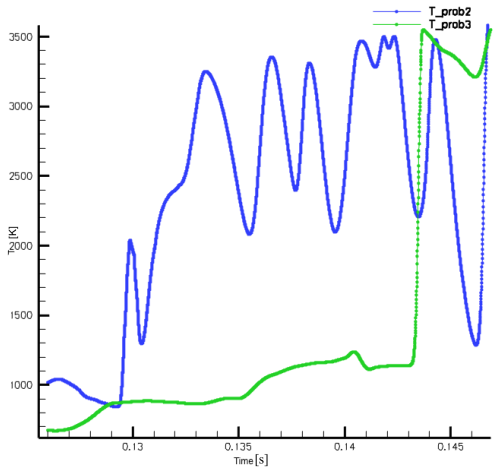

Figure 7.3.19: Temperature time evolution at selected locations: • symbol denotes the temperature in Probe2 and • symbol denotes the temperature in Probe3

Figs. 7.3.18 and 7.3.19 point out that the flow simulation covers a time period characterized by marked wave phenomena (compression and expansion waves, contact discontinuities), which are strongly multi-

dimensional in nature (mostly longitudinal convective waves and longitudinal and transversal pressure waves). In particular, in Fig. 7.3.20, we plot at the top the XY-slice passing through the center of the inner injector, and at the bottom the XZ-slice passing through the center of the two outer injector. The temperature field obtained at the XY-slice passing through the center of the inner injector, Fig. 7.3.20, indicates that a jet flame of diffusive nature is anchored at the post tip region of the co-axial injector. The temperature field presents three main thermal levels (blue, green and red colors). The blue region corresponds to the cryogenic oxygen stream which is dissolved by the mechanical action of the exchange of momentum with the co-flowing methane stream and by vaporization. The red region corresponds to very hot combustion products (mostly CO_2 and H_2O). The green region has a varied composition. It is either formed by a mixture of hot products and cold unburnt methane, or by pockets of unburnt oxygen. It is apparent, at the middle of the convergent region of the nozzle,

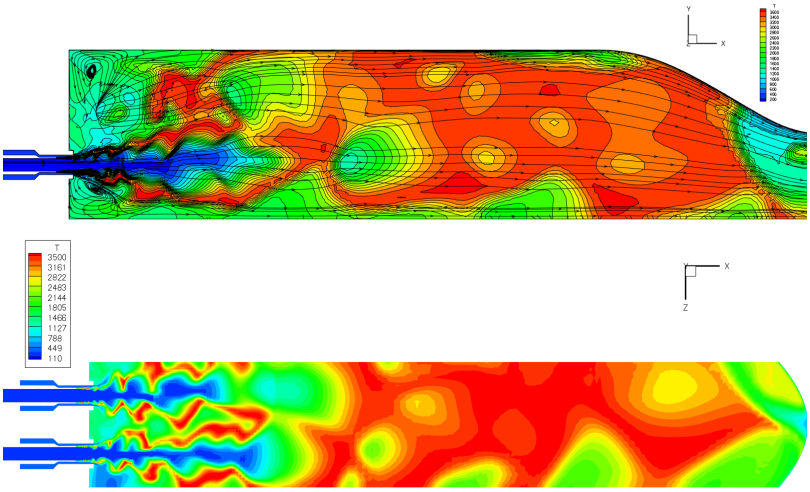

Figure 7.3.20: Temperature field sliced at selected planes; top: XY-slice passing through the center of the inner injector; bottom: XZ-slice passing through the center of the two outer injectors.

the presence of a strong contact discontinuity which separates the hot products proceeding towards the nozzle and the cold gas initially present in the combustion chamber. The passage of this contact discontinuity causes the formation of pockets of supersonic flow in the convergent which eventually bring the calculation to a stop. It is not clear if the emergence of these supersonic bubbles are due to an erroneous implementation of the PR equation of state or to other unidentified causes. From Fig. 7.3.20, it is possible to estimate the size of the

recirculation regions at the lateral wall and at the symmetry axis, the first being of about 0.022 m, the latter of about 0.017m.

7.4 THERMAL LOADS AT WALLS

Fig. 7.4.1 shows the heat flux field at the lateral wall at three successive time instants, t=0.129 s, t=0.136 s, and t=0.147 s. It is apparent that only at t = 0.147 s, the heat flux field attained a relatively stationary configuration, where one can identify three main regions according with the prevailing levels of thermal loads.

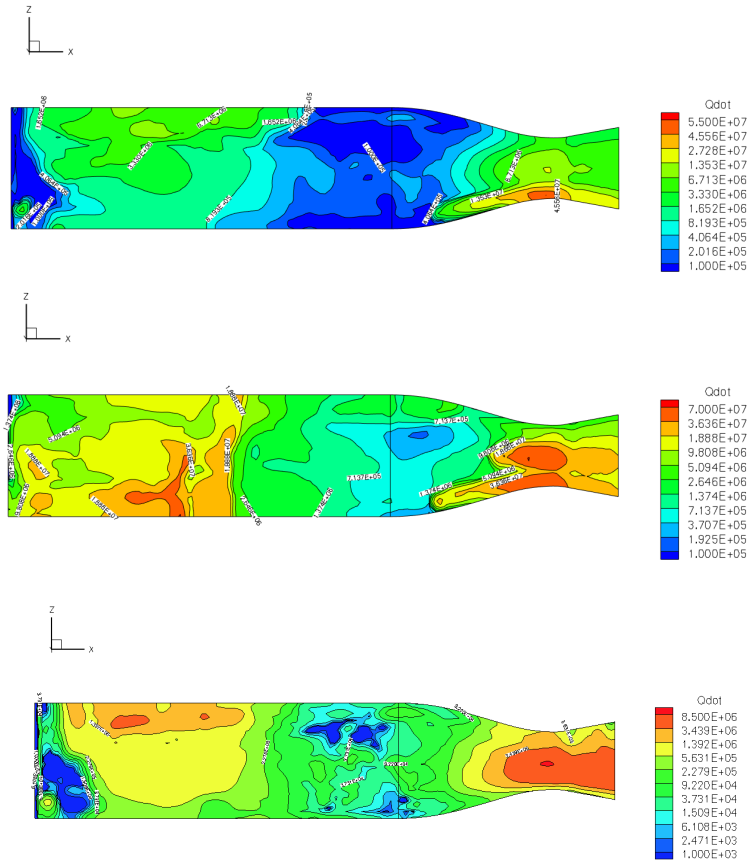

Figure 7.4.1: Thermal loads at lateral walls at three different time instants; left: t=0.129 s; center: t= 0.136 s; right: t=0.147 s

The green, yellow, orange regions correspond to an heat flux of the order of ~ 10, 20, and 60 MW/m^2, respectively. The red regions in the throat attain peak values as high as 90 MW/m^2.

These data can be extracted also from Fig. 7.4.2, where one can easily tell that there exists a region of the lateral wall adjacent to the injector plate (and terminating at about x=0.06m) of relatively low heat

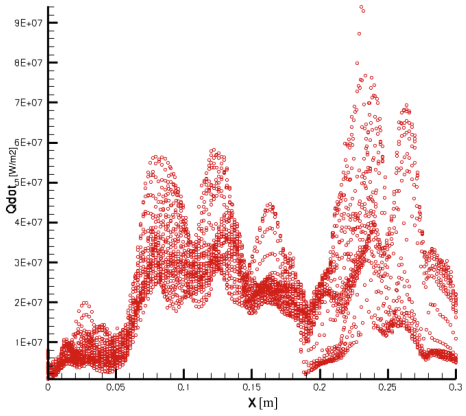

Figure 7.4.2: Heat flux at wall chamber and nozzle

flux (10-20 MW/m^2). At x=0.06m, the jet flame cones merge and impinge on the lateral wall causing a rapid increase of heat flux (20-60 MW/m^2). The orange regions of high heat flux field at t = 0.147 s clearly noticeable in Fig. 7.4.1 resemble qualitatively the injector footprints observed, Fig. 5.2.11, on the chamber wall (injector wall interactions) in a High Pressure LOX/GH2 Subscale Combustion Chamber (R. Arnold, et al., AIAA 2008-5242, 44th AIAA/ASME/SAE/ASEE Joint Propulsion Conference & Exhibit 21 - 23 July 2008, Hartford, CT).

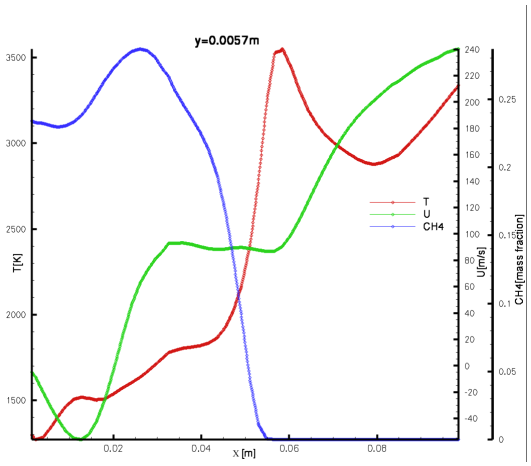

Figure 7.4.3: Flow variables extracted along lines at constant $y = 0.057$ in the XY-symmetry plane

Fig. 7.4.3 helps understanding why the heat flux upstream x=0.06m is relatively low. Indeed, in this portion of the chamber the temperature is rather low (1800K) because of the dilution of unburnt methane ($y_{CH4} \sim 0.25$) and the peak negative U velocity component is

-50m/s at x=0.12m, while the largest positive U velocity component is +100m/s in-between x=0.035m and x=0.06m.

Past x=0.06m, the temperature rises quite abruptly up to 3600K because the jet flame cones merge and impinge on the lateral wall, and at the same time the U velocity component increases from 100 to 240 m/s. Both the larger flow velocity and the larger flow temperature combine to yield a larger heat flux.

Note that the extent of the recirculation region at the lateral wall ends at about x=0.022m (the location at which the U component of the flow velocity (green line) crosses the zero in Fig. 7.4.3), where a local peak of heat flux (20 MW/m^2) forms. This means that there is no connection between the extent of the recirculation region with the location of peak heat flux at the lateral wall, being this location controlled by the spread angle of the jet diffusion flame emanating from the two outer injectors.

How has been written in Chapter §5.2.3, is evident that there are some regions where high heat flux field, figure 7.4.1, is present and it seems qualitatively the injector footprints observed, we showed here, the figure 5.2.11 which we showed in Chapter §5.2.3 how figure 7.4.4.

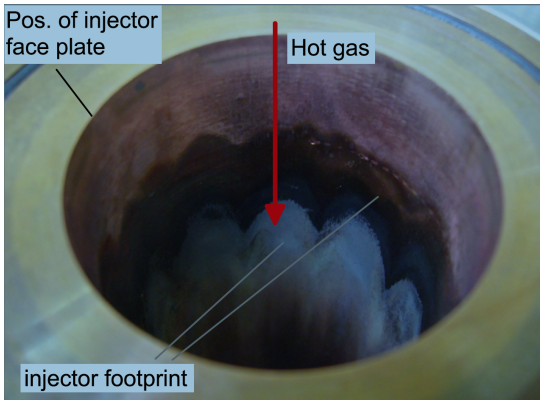

Figure 7.4.4: Injector footprints on chamber wall (injector wall interactions) in a High Pressure LOX/GH2 Subscale Combustion Chamber

We show here, also the figure 5.2.9 which we showed in Chapter §5.2.3 and that exhibits, in figure 7.4.5, the peak of heat flux where the flame impinges on the lateral wall.

In figures 7.4.6, 7.4.7 the heat flux is shown. Also in this case we can observe that the heat flux exhibits peaks that appear in correspondence where the flames touch the wall.

In following figure, 7.4.8, is showed the heat flux iso-contour on the chamber wall. In figure are evidenti the areas where there are the peak of flux heat.

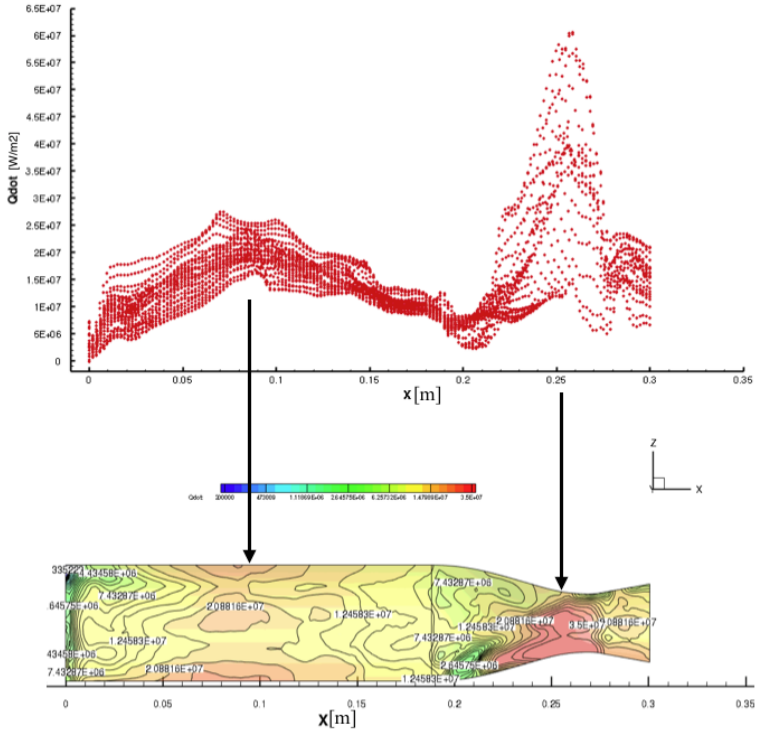

Figure 7.4.5: Average value of heat flux field with heat flux value on wall chamber

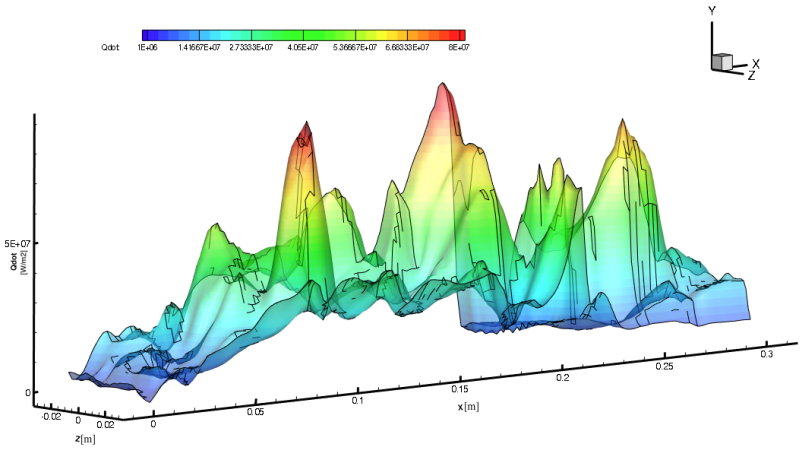

Figure 7.4.6: Instantaneous heat flux at time= 0.1453 s. Several heat flux peaks in a 3D graphic on y axis there is the heat flux.

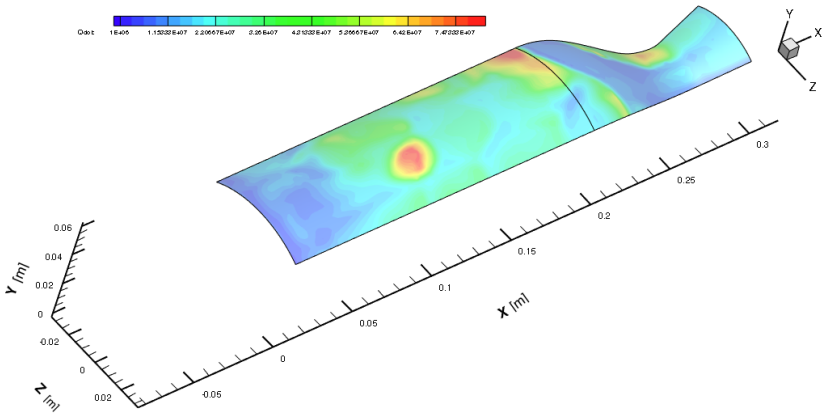

Figure 7.4.7: Instantaneous heat flux the time= 0.1453 s. Heat flux on wall chamber

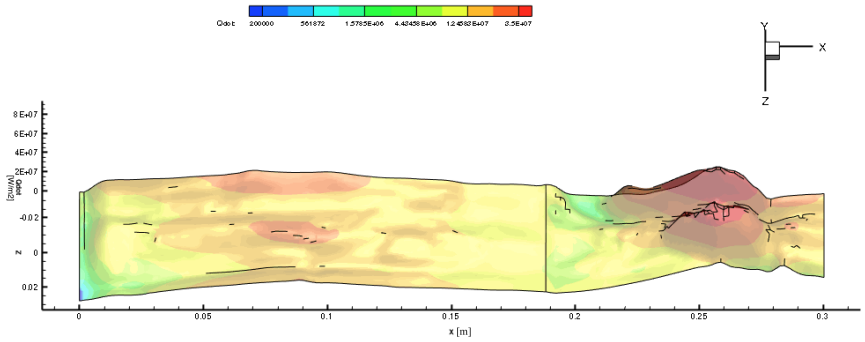

Figure 7.4.8: Average heat flux iso-contour

7.4.1 *Thermal loads at injector plate*

Fig. 7.4.9 shows the heat flux field at the injector plate at three successive time instants, t=0.1453 s, t=0.1463 s, and 0.1473 s. Inspection of the figure reveals that: (i) the region close to the chamber axis appears to have reached a relatively stationary configuration; (ii) the region close to the chamber wall shows strong unsteady flow motion, (iii) the triangular region comprised in-between the three injectors also shows strong unsteady flow motion.

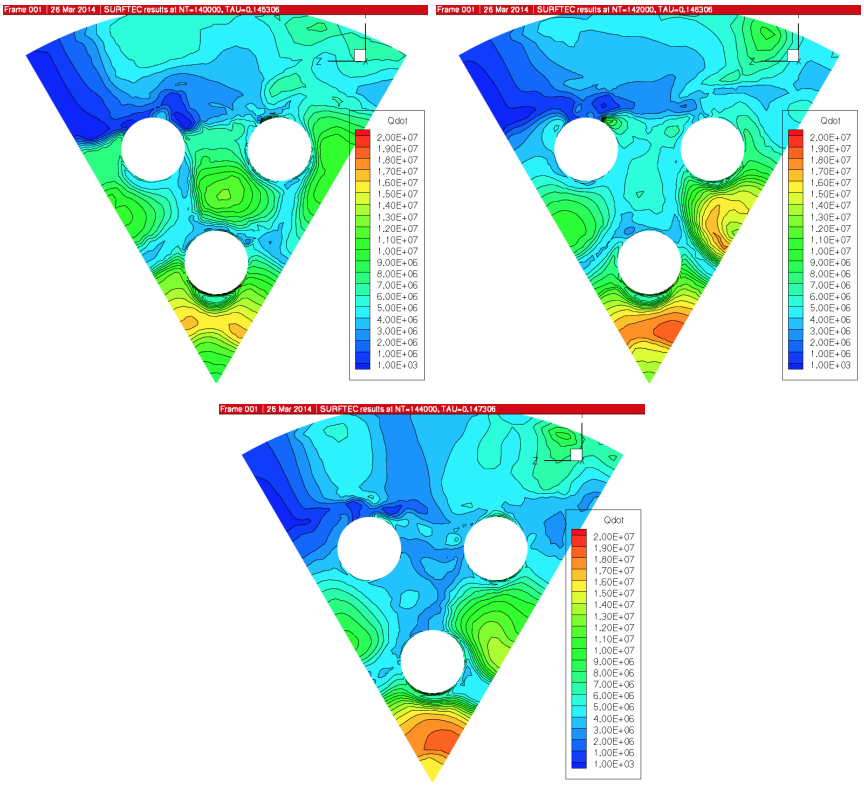

Figure 7.4.9: Thermal loads at injector plate at three successive time instants (t=0.1453 s, t=0.1463 s, and t=0.1473 s).

In Fig. 7.4.10, we note that, in the range (y=0-0.013m) close to the chamber axis, the V component of velocity is about V=20-40 m/s, the hot gas are at the temperature of 1200-1500 K, and methane mass fraction is about 0.35-0.50; this flow region is associated with the occurrence of the recirculation region visible in Fig. 7.3.20. These flow data yield a thermal load of about $\sim 14 - 19$ MW/m^2.

Again in Fig. 7.4.10, we note that the V component of velocity is about V=-10 m/s, the hot gas are at the temperature of 1300-1500 K, and methane mass fraction is about 0.20-0.45 in the range (y>0.025 m). These flow data yield a rather fluctuating thermal load in the range between $2 - 10$ MW/m^2.

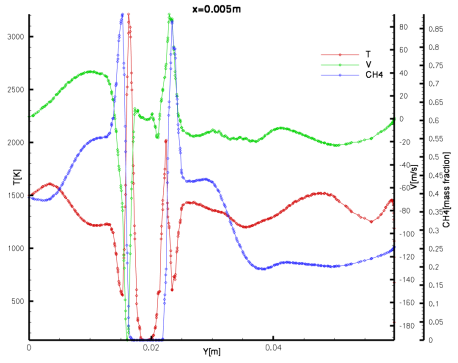

Figure 7.4.10: Flow variables extracted along lines at constant $x = 0.005$ (top) in the XY-symmetry plane

7.4.2 *Flow topology near injector plate*

In this section, we attempt at investigating the flow structure at the injector plate. In a three-dimensional flow, skin friction is a two-dimensional vector, $\mathbf{fi_n} = \{\tau_{nx}, \tau_{ny}\} = -\mu \left\{ \frac{\partial u_x}{\partial n}, \frac{\partial u_y}{\partial n} \right\}$, where n is the direction normal to the viscous wall. A skin friction line is defined as a line tangent at each of its points to the local skin friction vector. The skin friction lines can be visualized by means of a viscous film deposited of the model surface. The set of skin friction lines will be called the skin friction line surface pattern, or, more shortly, skin friction line pattern or surface pattern.

In general, by one point on the body goes one and only one such trajectory called a skin friction line. This is not true at a point P_0 where the skin friction vector vanishes. There, the skin friction dynamics is singular. Such a point is called singular or critical, the solution of the skin friction dynamics at a critical point leads to an eigenvalue problem. In the vicinity of a critical point, the solution lines behavior depends of the nature (real or complex) and sign of the eigenvalues.

There exists different types of critical points according with the nature (real or complex) and sign of the two eigenvalues λ_1 and λ_2:

- λ_1 , λ_2 real and of same sign: node
- λ_1 , λ_2 real and such that $\lambda_1 = \lambda_2$: isotropic node
- λ_1 , λ_2 real with opposite signs: saddle point
- λ_1 , λ_2 complex conjugate: focus
- λ_1 , λ_2 imaginary: degenerate focus or centre

The sense of displacement along the trajectories gives a physical meaning to the solution behavior in the vicinity of the critical points.

Sometimes the concept of limit streamline is used: it is defined as the limit of a streamline when the distance normal to the wall, ε_n, tends to zero. It can be shown that the limit direction of the velocity vector when ε_n tends to zero is co-linear with the skin friction vector (if the fluid is Newtonian), so that skin friction lines and limit streamlines coincide ($\tau_{nx} \sim \frac{\Delta u_x}{\varepsilon_n} \sim \frac{u_x(\varepsilon_n) - u_x(0}{\varepsilon_n} \sim u_x(\varepsilon_n)$). We will discuss the flow topology near the injector plate by resorting to the limit streamline concept as a good approximation of the skin friction lines.

In Fig. 7.4.11, we have identified the blue, yellow, and red circle symbols as sources, saddles, and sinks, respectively, of the skin dynamics. The black lines with an arrow indicates the direction of the skin friction lines as they originate from the sources, flow through the saddles and terminate at the sinks. The large black circles stand for the injector ports. Inspection of Figs. 7.4.12, suggests that, if the flow were stationary, the sources, saddles, and sinks should arrange themselves as indicated in Fig. 7.4.11. Departures from this typical configuration indicate the presence of unsteady skin flow motion.

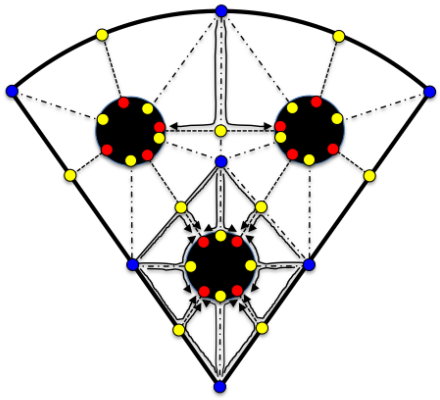

Figure 7.4.11: Skin friction dynamics at the injector plate.

Comparing the maps computed at the three time instants t=0.1453 s, t=0.1463 s, and t=0.1473 s and reported in Figs. 7.4.12 suggests that the region closer to the symmetry axis has attained a relatively stationary state, whereas both the triangular region across the three injectors and the circular crown region in-between the two outer most injectors and the lateral chamber wall undergo significant unsteady motion. These comments are also supported by the visual inspection of Fig. 7.4.13, which portraits the instantaneous locations of the significant points of the skin dynamics at the three time instantst=0.1453 s, t=0.1463 s, and t=0.1473 s.

It is conjectured that the circular crown region might eventually attain relatively stable flow conditions whereas the triangular region

is most likely prone to exhibit persistent flow instabilities, given the interaction of three 3-dimensional recirculations.

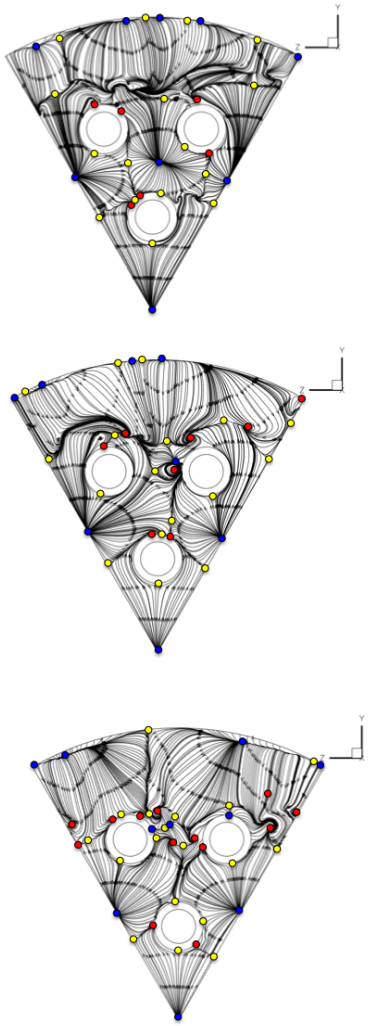

Figure 7.4.12: Limit streamlines at a plane parallel and close (10^{-5}m) to the injector plate at three different times (t=0.1453 s, t=0.1463 s, and t=0.1473 s).

7.5 CONFORMAL MAPPING MESH

The 3D analyses have been carried out by adopting two different mesh generation techniques, one resorting to multi-block structured meshes with overset regions of intersections, the other generated by means of a fully unstructured single-block generator. However, both approaches manifested flaws: the overset approach introduces severe approximations when accommodating the hanging nodes with interpolations, while the unstructured mesh is never able to provide reg-

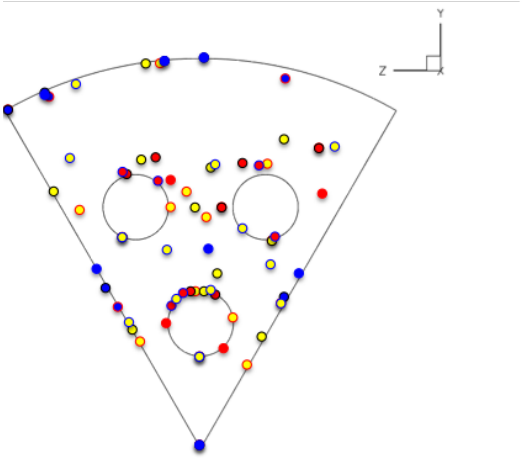

Figure 7.4.13: Sources, sinks, and saddles at the injector plate as found at the three time instants t=0.1453, 0.1463, and 0.1473 s.

ular (symmetric) discretization even when it is useful and easy to achieve this goal.
How we showed in the chapter §4, section §4.4, the mesh generator can help us for the axis singularity problem using the conformal mesh. The new mesh generator has been used to build a section of combustion chamber, multi-injectors. We decided to adopt a closed circuit having eight straight sides (see the detail the right of Fig. 7.5.1) so that the volume of the chamber is easily filled by the juxtaposition (tessellation) of the 8-side boxes (the "tiles" of the tessellation, see the left side of Fig. 7.5.2)

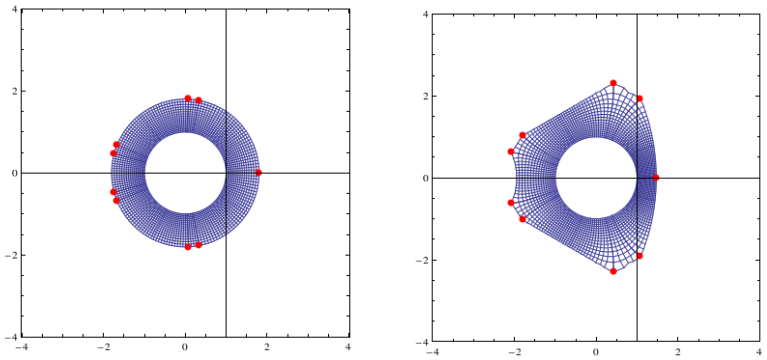

Figure 7.5.1: A polar mesh discretization of a circular crown is mapped into the region comprised between a circle and a (non regular) octagon using the Theodorsen-Garrick mapping.

The same mapping is also used to map a square circuit into a circle (both entities having their centers coincident with the symmetry axis). This way, the region about the symmetry axis can be discretized

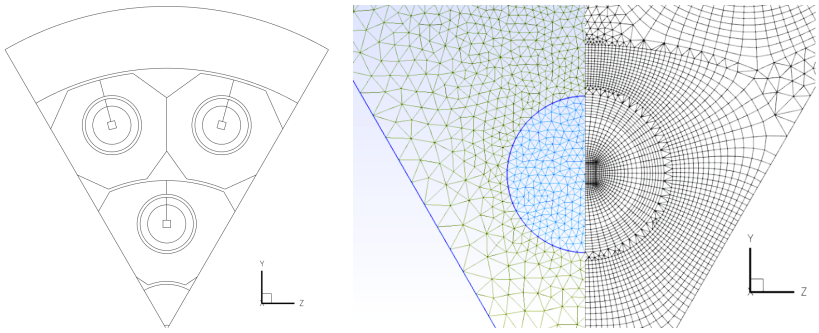

Figure 7.5.2: Left: the "tiles" of the tessellation used to fill cross-section of the combustion chamber. Right: comparison of a fully unstructured mesh with our proposed mesh

using a cartesian metric, which, differently from a polar metric, is not singular at the axis.

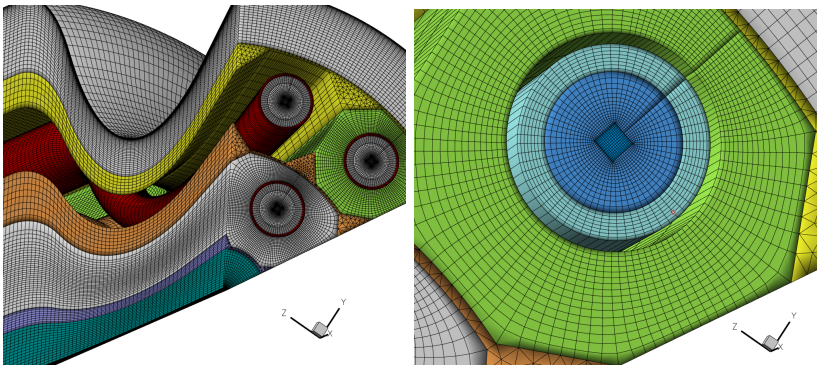

Figure 7.5.3: The discretization of the cross-section is extruded along the axial direction to generate the full 3D mesh in the volume of the combustion chamber.

A comparison of a fully unstructured mesh with our proposed mesh is shown in the right of Fig. 7.5.2. Note that, a simple juxtaposition of the conformal injector meshes would produce a matching frontier still featuring hanging nodes. To prevent this development, we decided to leave a small region separating each conformal injector mesh and to discretize (using the open source package Gmsh[2]) this buffer region using an unstructured (triangular) mesh. Thus, the overall cross-section discretization consists of several (one per each injector) conformal injector structured blocks which are "glued" one to another using unstructured triangles so as to wholly eliminate the presence of hanging nodes (right on Fig. 7.5.2). This way we constructed the conformal meshes emanating from each injector. The dis-

2 C. Geuzaine and J.-F. Remacle. Gmsh: a three-dimensional finite element mesh generator with built-in pre- and post-processing facilities. International Journal for Numerical Methods in Engineering 79(11), pp. 1309-1331, 2009.

cretization of the cross-section is extruded along the axial direction to generate the full 3D mesh in the volume of the combustion chamber (left on Fig. 7.5.3); an enlargement shows the mapping from the square at the axis to the circles of the injectors to the octagon of the injector "tile" in the chamber (right on Fig. 7.5.3). The tool is currently able to dump the information in a TECPLOT compatible format, and produces all the binary and ascii files required by CFD++.

7.6 Computational Requirements and Performance

In this project we adopted CFD++ as flow solver. We tested the strong scaling performance of the code on the CIRA facility. The size of the 3D mesh is of about 3M of cells, with about 20 unknowns per cell. The strong scaling parameter we used is defined as:

$$S_s = t_{ref}/(t * n_{core}/n_{ref})$$

The strong scaling performance is reported in Table 18. The excellent scaling performance advocates the use of as many core as possible in the limit of the available hardware resources.

Table 18: Strong scaling assessment on CFD++

# of cores	CPU time per step [s]	Scaling
16 (n_{ref})	202 (t_{ref})	1.
32	104	0.97
64	54	0.93
128	29	0.87

Conclusions

The outcome of the analyses reported earlier in this chapter is summarized in this section; the section numbering adopted in this section is the same adopted in the chapter to establish an easy link between the analytic illustration of the results and their synthetic summary.

- Sub Scale Bread Board (SSBB) Assembly: Axi-symmetric URANS Analysis
  - Run #1 The simulation revealed a rather low combustion efficiency, essentially due to a severe stratification of the temperature field. Such low efficiency is the ultimate cause

of a lower than nominal (not larger that 44bar vs. a nominal pressure of 55bar) equilibrium chamber pressure, at the given throat area and mass inflow, hinting at the need of accounting for the modeling of subcritical two-phase flow. The axi-symmetric assumption effectively acts as a constraint of the flow, since it prevents mixing of the propellants to occur in three dimensions, which produces a longer flame length by suppressing the flow instabilities of the cold oxygen core; ultimately, the poor axi-symmetric mixing yields a lower-than-actual combustion efficiency. Indeed, a full three-dimensional simulation of the single injector configuration yields a higher combustion efficiency and thus a higher chamber pressure.

- Run #2 Run #2 represents an improvement over Run. #1 because of an overall higher mesh resolution with a local refinement at the wall boundaries. While the chamber pressure and combustion efficiency levels were not observed to vary significantly with respect to Run. #1, the wall heat flux experienced a significant drop from the peak level of Run #1. Run #2 was also used as a benchmark for the flame anchoring mechanisms. As the flame detaches, the premixed zone, albeit not stationary, seems to be larger that the diffusive flame, exhibiting a higher mean temperature, which, in turn, causes an increase in chamber pressure.
- Runs #3 and #4 A number of measures were adopted to allow for the Peng-Robinson EOS to be implemented without causing instabilities during the numerical integration: (i) the nozzle divergent was reduced in length in order to limit the range of Mach numbers and pressures spanned by the simulation; (ii) the LOX inlet temperature was also raised to 140K to reduce the density gradients at the LOX core periphery. A comparison between Run #1, utilizing the VDW EOS and Run #3, using the P-R EOS, indicates that the application of the P-R EOS yields similar scalar fields and in general similar flame conformation observed in the VDW case. Comparable values of wall heat flux are also observed for similar meshes. The LOX core length and conformation is also very similar in both cases, setting aside for a small change in inflow density.
- Wall heat flux: mesh sensitivity Run #4 was performed with a mesh having a resolution exactly twice as large as that adopted in Run #2. Both Runs do not adopt a wall function approach and the heat flux is estimated by di-

rectly resolving the boundary layer through a wall-refined mesh. Doubling the resolution has virtually the effect of doubling the wall heat flux and concurrently halving the y^+ level.

- Issues associated with subcritical pressures The low combustion efficiency causes a lower than nominal equilibrium chamber pressure. However, no multiphase modeling was envisioned, and this clearly affects the fidelity of the simulation since the subcritical oxygen is expected to undergo a phase change when injected into the chamber. Instead, it was decided to artificially increase the equilibrium pressure to a supercritical value by increasing the overall injection massflow. This prevented any phase change and avoided pathologies in treating a subcritical flow with a single phase model.
- Validation of wall heat flux estimation A significant discrepancy was observed between heat flux values estimated using wall functions on coarse meshes on one side, and values estimated directly, by solving the boundary layer to the wall, with wall-refined meshes on the other. To acquire confidence on the reliability of the wall heat flux levels obtained with the application of wall functions, a validation campaign was carried out where the prediction obtained with CFD++ were compared with those of an in-house code. From the above validation procedure, we draw the general conclusion that the wall function approach can be considered reliable for $y^+ < 20 \sim 30$, i.e. for $\Delta_{\text{wall}} \approx 10\mu\text{m}$. This indicates that the heat flux estimated in Run #1 is clearly overestimated and can safely be regarded as an upper bound. It is equally important, when trying to fully resolve the boundary layer in order to attempt a direct estimate of the heat flux, to obtain $y^+ \sim 1$; note that an insufficient resolution underestimates wall heat fluxes (contrary to the wall function case).
- Run #5 Run #5 has a low wall-cell size $\Delta_{\text{wall}} \approx 0.4\mu\text{m}$ which guarantees $y^+ \approx 1$ while directly resolving the boundary layer up to the wall. The peak flux has increased in comparison with all other simulation runs (a peak flux of 22.5MW/m^2 at the throat).

- DEMOnstrator (DEMO) assembly: 3D URANS Analysis Two computational meshes were adopted in the framework of the URANS simulation Runs: (i) a structured mesh with block overlay which lacked refinement at the injector plate and (ii) an un-

structured mesh with a structured refined structure at the walls which included refinement at injector plate.

  - Structured Mesh The 3-dimensional DEMO configuration was simulated using a URANS approach on a 1.5 M cells structured mesh representing a 60 degree slice comprising 3 of the 18-injector overall assembly. During the initial transient, an artificial anchoring hot-spot is active, this yielding a diffusion jet flame emanating from the coaxially injected propellants. However, the structured mesh used for this simulation does not provide enough resolution at the post tip to capture the anchoring at or near the LOX post recirculation zone. Thus when, after ignition, the hot spot is deactivated, the flame system detaches from the post-tip. However, a stable configuration involving a detached pre-mixed flame is attained at a finite standoff distance of approximately 2 cm from the injector plate. The flame system standoff mechanism could be related to a recirculation zone. A chamber pressure level of $P_c = 67$bar is attained possibly due to a high combustion efficiency. The additional degrees of freedom inherent of a 3D simulation runs allows for the presence of vortex stretching mechanism, which greatly enhances turbulent mixing in unsteady flows, and produces a faster disintegration of the core of the cold oxygen jet. The average heat flux value peaks at the nozzle ($\sim 40\text{MW/m}^2$) while at the recirculation zone peaks at $\sim 30\text{MW/m}^2$. The lack of a adequate resolution at the injector plate wall prevented the evaluation of a reliable heat flux field when using the structured mesh.
  - Unstructured Mesh An unstructured mesh comprising 2.5 M cells and 1 M points was constructed to test mesh sensitivity and to provide adequate resolution to estimate the heat flux field at the injector plate wall. The heat flux on the injector plate is very different when the flame system is attached to the rim of the injector or is detached from them. However, under-resolved URANS simulation runs cannot capture the anchoring mechanism without some artificial means such as the addition of a hot spot. To assess the resolution requirements to describe the anchoring mechanism, we considered a slightly different configuration assembly, described below.

- Injector Assembly: Axi-symmetric LES Analysis A new configuration assembly has been studied which involves: (i) a subsonic

back pressure outflow condition set at a supercritical pressure of 60 bar to avoid using the P-R EOS in transcritical (or even subcritical) conditions, (ii) a single injector, (iii) a chamber length of about one third of the nominal. Both URANS and LES simulation runs were carried out in a 2-dimensional axis-symmetric setting. In addition to turbulence closure, a Thickened Flame model (see Appendix D) for turbulent diffusive combustion was also used. The recirculation zone is resolved with 16 cells while a 1µm cell is used to resolve wall gradients. URANS does capture some form of hot product recirculation, but it is not capable of maintaining an anchored flame in spite of the thickened flame model. On the other hand the LES approach succeeds in maintaining an anchored flame without any flame breakup.

- DEMO assembly: 3D URANS Analysis with enforced flame anchoring The main findings of this section are the following:
  - The artificial anchoring procedure was successfully able to anchor the flame even if the local mesh resolution at the post-tip region of the injectors was inadequate to describe the actual details of the anchoring mechanism;
  - The main injection flow parameter relevant of this run, where
    - At the exit of the coaxial injector the oxygen stream velocity and temperature are u_l=30 m/s and T_l=145 K, respectively, while the methane stream velocity and temperature are u_g=135 m/s and T_g=295 K;
    - the parameter J =1.55;
    - the velocity ratio in-between the flow velocity of the gaseous methane stream and the cryogenic oxygen stream is v_r=$u_g/u_l \sim 4.5$;
    - the Mach number inside the cryogenic oxygen stream is of the order of 0.1, whereas in the gaseous methane stream is of the order of 0.3;
    - the ratio of the chamber pressure with the critical pressure of oxygen is P_r=$P_{cc}/P_{crit,O_2}$=1.12;
    - the density ratio between oxygen and methane at the exit of the coaxial injector is about 15.
  - The anchoring at at the post-tip region of the injectors leads to the formation of jet diffusion flames between the cryogenic oxygen stream and the gaseous methane stream; the aperture angle of these jet flame is about 22 degree;

  - The three dimensional jet flames produced a flow of hot gases that completely filled the cross section of the chamber; this way the characteristic velocity c^* attains a value close to the theoretical value emerging from thermodynamic equilibrium considerations and as a consequence the calculated average chamber pressure is close to the design value;
  - There exists a region at the injector plate and close to the chamber axis where the heat flux is about $14 - 19$ MW/m^2
  - There exists a region at the injector plate and close to the chamber wall where the heat flux is about $2 - 10$ MW/m^2.
  - There exists a region of the lateral wall adjacent to the injector plate (and terminating at about x=0.06m) of relatively low heat flux (10-20 MW/m^2). At x=0.06m, the jet flame cones merge and impinge on the lateral wall causing a rapid increase of heat flux (20-60 MW/m^2).
  - The rapid rise in heat flux moving downstream the chamber is associated with the impingement of the jet flames, it is not associated with the stagnation point of the recirculation region which forms between the injector plate and the lateral wall;
  - At the throat, the heat flux peak attain values as high as 90 MW/m^2;
  - The flow at the injector plate is relatively stationary close to the chamber axis, it manifests strong unsteadiness in the triangular region comprised in-between the three injector ports.
  - At the injector plate, the regions of high heat flux are associate with source points of the skin friction dynamics, the region of low heat flux are associated with heteroclinic lines connecting sources to saddles.
  - The recognition of the existence of a characteristic pattern of the skin friction dynamics can offer useful insight to draw design guidelines for the location of the injectors.

- DEMO assembly: Conformal Mapping Mesh Generator A new tool to generate multi-block structured/unstructured meshes especially tailored for multi-injector combustion chambers has been designed, tested, and is ready to be applied in a possible extension of the research program. The overall cross-section discretization consists of several (one per each injector) conformal injector structured blocks which are "glued" one to another

using unstructured triangles so as to wholly eliminate the presence of hanging nodes. The tool is currently able to dump the information in a TECPLOT compatible format, and produces all the binary and ascii files required by CFD++.

8

CONCLUSIONS

Contents

8.1 INTENTIONS

The goal of Thesis has been the evaluation of heat loads on the plate and wall of thrust chamber in case of the reactive transcritical and supercritical fluids. The understanding of features reactive and non reactive flows at trascritical and supercritical conditions and the understanding of the best way to modeling these flows, helped us to reach our goal. We obtained useful informations about the level of criticality for the numerical modelling. In addition to this we accomplished a study about a pure nitrogen jet which was followed by the study of a reactive flow, in a first case, using a free jet and later using a combustion chamber with nozzle. The case of the combustion chamber highlighted some critical elements that determined the interruption of simulations. The numerical setup chosen that has been used in the case of pure fluid, where has not been useful probably because between a reactive and non reactive fluid there are of the properties variations. The compressibility variation between the injected propellants and the produced species by means of combustion, that participate in the chamber, can be resolved with the usage of a convergence strategy. This strategy was not used in simple study cases of Mayer's jet. Moreover in this case, how we observed in precedence in the cases of SSBB and DEMO, an attentive spatial discretisation of the domain is fundamental.

8.2 ACCOMPLISHMENTS

The work has been divided in **four parts** or **steps** and every parts is preparatory to the one which coming after. The key points of the analysis, show physic and numerical complex features (i.e: two-phase flow, high density gradients, wall refinement). The key points are shown below:

- Comparison among several EOSs (*Chapter 3 and Chapter 7.1 - second part*)
- High density gradients and two-phase flow (*Chapter 6 - first part; Chapter 7.1 section §7.2 - second part; Chapter 7.1 section §7.2.7 - third part and Chapter 7.1 section §7.3 - fourth part*)
- Evaluation of flame length and evaluation of combustion efficiency (*Chapter 7.1section §7.2 - second part and Chapter 7.1 section §7.3 - fourth part*)
- Flame anchoring, analysis post tip refinement and spread angle (*Chapter 7.1 section §7.2 - second part; Chapter 7.1 section §7.2.7 - third part and Chapter 7.1 section §7.3 - fourth part*)
- Heat flux ($\dot{Q}$) evaluation and wall mesh refinement (*Chapter 7.1 section §7.2 - second part and Chapter 7.1 section §7.3 - fourth part*)

In every part of work we underlined what the we learnt and things that could be useful to solve the part which follows after. In the last section §8.3 we underlined the open issue for every parts and its possible solutions. The four parts of work can be schematize in:

- mono-specie nitrogen simulations (3D case) and reactive flows simulations (3D case): comparison among several solution methods and different temporal discretisations for two Mayer's test cases (mono-specie nitrogen simulations). Simulation of reactive flow in a combustion chamber mono-injector.
- SSBB simulations (2D axi-symmetric case): heat flux evaluation on the plate and wall. Preliminary study about the mesh resolution: an essential point to modeling the flame anchoring.
- LES simulations (2D axi-symmetric case): study about the flame resolution for the representation of the flame anchoring.
- DEMO simulations (3D case): heat flux evaluation on the plate and wall. Preliminary study about the mesh resolution, an essential point to modeling the flame anchoring. Study of intersection areas of flames that touch on the wall. Identification of recircle area of the combustion products that exhibits in the volume

between the axis and the injector of internal crown of DEMO and determines an evident local increase of plate temperature.

An essential element has been the possibility to use a chemical kinetic mechanism that is a simplification of the GRI − mech3.0. The simplified mechanism is constituted by 15 species (included nitrogen) and 57 reactions. By the use of this mechanism has been possible to mark the flame by means the HCO combustion product instead of the temperature. Due the HCO specie is among the first combustion products, it has the advantage to indicate with more precision the reaction area. If we used only the temperature, the area would been less accurate and more wide because of the reaction area goes with an increase of temperature but this area is wide if we compared it with just the flame zone.
The ***first part*** made up of 3D simulations: one by a nitrogen pure fluid and the other one by a study about the reactive flows. The goals of these simulations has been to test the strong and weak points of our discrete model and the limits of software used. We compared different numerical strategies to find the best and the efficient ones. Pursuing our aim, two experimetal cases of Mayer [62] (cases #3 and #4) have been reproduced and compared with the numerical results of Schmitt. The simulations have been realized also with the aim to obtain the useful informations about the future DEMO simulations and add a contribution to understand the numerical analysis of "transcritical" and "supercritical" jets. Although the existence of this contribution, we did not find an unique appropriate solution method to simulate "transcritical" and "supercritical" fluids. The *main results* that we obtained in this phase have been:

- in case of fluids injected in "transcritical" conditions we deducted that an efficient numeric strategy is the usage of a preconditioned method with DTS for the time integration, thing that gives us some good results for a non reactive jet.
- in case of fluids injected in "supercritical" conditions a good numeric strategy seems to be the usage of a preconditioned method without DTS for the time integration.

In addition, we observed that the usage of an implicit preconditioned compressible density based method gives us a good compromise in terms of time and computational cost, with the exception of supercritical cases. About the reactive flow the addition of nozzle highlighted:

- the importance of a mesh refined with the volumes with a good aspect ratio.

We note that when we use a time integration with DTS, the cores of jets in both "transcritical" conditions and in "supercritical" conditions

are shorter than other methods, in particular: we observe that the core obtained from centerline density with a DTS time integration, in "transcritical" case (case #3) is a little long than the core observed in the "supercritical" case (case #4). This fact is in contradictions with the experimental data and physic behaviour of problem. The qualitative goodness of PR's EOS to represent the thermodynamic properties of real fluids is confirmed. In the ***second part*** the *main results* obtained have been:

- higher density gradients are evident in the area where there is the contact between the transicritical oxygen and the supercritical methane. This area appears as though a contact discontinuities (figure 6.4.4 in the section §6.4.5.1). Methane, injected to an higher temperature than the oxygen one, determines an increase of the oxygen temperature in the contact area. When the reaction is triggered, a "buffers" zone of elements resulting from reaction, is originated. This zone has an higher temperature and should assure, thanks to recircle of hot gases, the flame anchoring.

and we considered also:

- the differences we have when we use two different EOS: VDW and PR. In a first moment, we used the VDW's EOS (chapter §7 and section §7.2) and in this way in project conditions, we avoided the numerical problem of convergence. The problem of modelisation was resolved just in part because of the VDW's EOS, how showed in the chapter §7, and this determines a density with lower values than the PR's EOS and this fact cause, for the momentum flux ratio and equivalence ratio, a leaving from the project conditions. In effect, the relative velocities between the oxidising and fuel are different from the ones established. This occurrence for reactive flows (the different velocity ratio) could influence the recircle to downstream of post-tip.

In addition, we analysed and studied a problem that comes up in the chamber:

- pressure in the chamber is lower than that project. This highlighted some level of criticality revealed with the presence of a bi-phase state of flow and this state is not considered in our simulations. In addition, we determined a more efficient lower combustion that implies an overvalue of flame length and a temperature stratification.

The ***third part*** is about the study on the flame anchoring. For this reason we realised an axisymmetric model, approximately 1/3 of the

SSBB length without any nozzle, on which we studied the anchoring study. In the several tests we observed the influence of mesh resolution on the post-tip: an inadequate resolution, with a limited number of points in both directions (minimum value find to discretize the circular crown was 16 points, 1 order smaller than post-tip height: in this case it is $\Delta y \approx 6.25\%$ of post-tip height) that implies a flame detachment. This choice causes a less accurate evaluation of heat flux on the plate but also to the wall when the flame detaches is convected to the throat. This event provokes an increase of the heat flux value and a more downstream flame touch on the SSBB walls. The *main result* has been:

- to understand the importance to choose an efficient mesh resolution to identify the flame and its anchorage.

The ***fourth part*** is composed of 3D numeric simulations. These simulations have been accomplished in a second moment, with a new version of software, and do not show the same criticality in the physical-mathematic modelling of EOS (i.e: PR) as we saw in the SSBB case.The *results* show that:

- when we have a non reactive flow, oxygen and methane, are represented correctly. We can see, distinctly an oxygen jet and later a methane jet. Also the reactive flow did not give complications in the simulations and the software simulated with a good approximation a flux in the combustion chamber.

In addition, the combustion efficiency valuation is improved and we obtain also a better evaluation of length flame. We highlighted a flame impingement. We also observed it, in the first study phase, when we made a geometry without post-tip:

- in a starting phase, we built a geometry without post-tip and we observed the importance of this elements of geometry. The choice to remove the post-tip implied, on the plate, an evaluation of heat flux lower because of the flame position is incorrect and the flame appears like a stand-off.

Summarizing, we deducted from the ***first part*** the optimal numeric strategy for us to resolve the transcritical flow in reactive and non reactive conditions: we obtained a preconditioned method with and without DTS, respectively. The ***second part*** treated about the useful informations about the existence of higher density gradients where there is the contact between the different injection conditions of propellants: this area appears like a contact discontinuities. A comparison between two different EOS (VDW vs PR) was realized and we understood the importance the EOS (PR) usage for the reproduction

of density features for the evaluation of heat fluxes: a wrong density value implies a wrong velocity ratio, momentum flux ratio and equivalence ratio. The presence of nozzle when it started provokes a decrease in the combustion chamber and the possibility of a bi-phase flow. In the ***third part*** we observed the importance of an efficient mesh resolution at the post tip to identify the flame and its anchorage: the mesh resolution captured the thin thickness of flame. The ***fourth part*** we reproduced a simulation of DEMO a thrust chamber evaluating by combustion process simulation the heat fluxes at the chamber and nozzle walls. We obtained also a better evaluation of length flame and we observed the importance of post-tip element in load evaluation evaluation.

8.3 OPEN ISSUES

The results satisfied the objectives of Thesis about the valuation of thermic loads and the behaviour of flames. We can note that the usage of CFD $++$ software has been a valid support to understand the difficulties in which it is possible to bump for the problems solution with a complex features that are difficult to modelling, and to obtain a qualitative valuation of thermic flux. We can not define a unique numeric strategy to use when we have the "transcritical" and "supercritical" fluids both of non reactive flows and reactive flows, and some problems remain opened.
For example, in the *first part* additional simulations could to verify if the number of internal interactions of method DTS had been in a number sufficient to permit the convergence because this could have consequences in terms of errors on the conservation equations. In the case of reactive flows, when the nozzle is added, we had not sufficient indications to obtain the conclusion about the usage of an implicit preconditioned method how the best one.
In the *second part*, we would have had to accomplish additional (study of the SSBB) simulations for a more reliable evaluation of heat flux value on the wall.
In the *third part*, we note the need to accomplish additional simulations to verify the contribution given from the usage of DTF to determine the flame and its anchorage.
In the *fourth part* a mesh refinement and consequently a results sensibility analysis would have been necessary. The lack of a high resolution of mesh, provokes an inaccuracy of the heat flux evaluation on the wall both of the plate and of the post-tip. In addition, the lack of resolution caused by a coarse mesh prevented the extinguishing of the source. In this way we could not verify the possibility of flame anchoring artificially anchored to post-tip

APPENDIX

A

PSEUDO-BOILING

A definition of *'pseudo-boiling'* among the several, has been produced by Kafengauz and Federov in [42] and [43], who described a phenomenon in cooling pipes which resembled subcritical boiling but at supercritical pressures. Oschwald et al. in [79] use this term to define a supercritical liquid-like to gas-like transition and to denote, in this way, the extension of the saturated pressure curve into supercritical states in according with Banuti and Hannemann in [2]. This phenomenology results singular and Hall in [31] wrote that it is " irrational and unnecessary because, clearly, two distinct phases do not exist at supercritical pressures". In particular, in [2], Banuti explains that at subcritical pressures, the heat of vaporization needs to be added for a substance to change its state through the saturated pressure curve. Near the critical point, the heat of vaporization vanishes. When isobarically heating a substance above the critical point, a distinct peak in specific heat can be found: this peak coincides with the region of maximum density variation respect to temperature ($\partial\rho/\partial T$) and with a maximum of the thermal expansion coefficient. The general effect illustrates that a process which passes through this temperature upon heat addition originates just a moderate temperature rising during a substantial increase in specific volume: the fluid will expand. This behaviour appears like a liquid one at its boiling point, how illustrated by Oschwald et al. [79]. This behavior has permitted to perceive the 'pseudo-boiling' like a subcritical phenomenon, [79]. Thermal phenomena at supercritical pressures are related to the thermodynamic fluid state. Oschwald and al. explained that, at a given supercritical pressure, a peak in specific heat capacity can be found at a certain supercritical temperature (look at Banuti and Hannemann [3]). The energy required to heat the fluid, passing the peak in specific heat, is supposed to have influence on the dense core structure.

B

CSP AND ECSP

Leland [107] underlines the importance of CSP method to predict the mixture properties and the pure components. In general, there are two principal approaches in applying the CSP to mixtures. The first approach uses the CSP for pure components in describing ideal solution behavior and the deviations from it. The second approach uses the CSP to find conditions at which the known properties of a pure component will be identical to the unknown properties of a given mixture. The latter method in many cases, is referred to as the development of a ***one-fluid*** model for a mixture. It may be extended to the development of ***multifluid*** models, in which the known properties of two or more pure fluids at different conditions can be combined to predict the unknown properties of a mixture.
The simple corresponding states principle predicts the properties of pure fluids and mixtures that are conformal with a reference. For slightly non conformal substances is required an extended CSP for satisfactory representation. In their paper Leland and Fisher [23] consider an extension of the simple CSP. They involve an additional parameter ***shape factors*** to modify the critical properties of non conformal fluids so that they conform to the reference. They found that the prediction of partial thermodynamic properties is limited to reduced temperatures above 0.6 and mixtures having no large differences in molecular properties. Two features of components are considered by Leland:

- the mixture components and the reference are conform to the same intermolecular potential function. In this case the mixture can be represented with a simple two-parameter corresponding states theory.
- the components are not conformal with respect to the reference because of non central force fields, small differences in polarizability, or weak dipole moments. In this case the mixture can be represented with sufficient accuracy by an extended corresponding states theory.

The total thermodynamic properties of the mixture, such as enthalpy, entropy, and compressibility can be predict by the Leland's theory. The prediction of mixture thermodynamic properties which requires differentiation with respect to composition, such as partial volumes or fugacity coefficients, is not enough accurate without incorporating empirically fitted parameters from binary data. But Leland's CSP theory exhibits some limits for the mixtures of components which have a strong polarity or hydrogen bonding. The approximations occur in the following:

- The defining equation for the pseudo force parameters for the mixture.
- The combining rules for the intermolecular potential parameters for unlike pair interactions.
- Corrections to account for deviations for each component in the mixture from the simple intermolecular potential.

The range of applicability of corresponding states can be broadened considerably by introducing the extended corresponding states model (ECSP), Leland [107] and *Rowlinson and Watson, 1969* (see Ely [21]). The of two-parameter corresponding states formalism is maintained but the equivalent substance reducing parameters became, for example in pure fluid, a function of shape factors that are functions of Pitzer's acentric factor ω, critical values of variables and reduced variables $T_r^\star$ and $V_r^\star$ (variable reduction by the critical point value). The shape factors (energy and size) were determined exactly for any pure fluid with respect to a reference fluid by solution of the conformal solution equations and compressibility equation in terms of reduced variables. It's more convenient for Ely ([21]) to generalize the relationship for shape factors.

C

TRANSPORT PROPERTIES

C.1 TRANSPORT PROPERTIES FOR PURE FLUIDS

The real-gas effects have a significant impact on the flame structure in high-pressure combustion therefore, a suitable equation of state, together with adequate constitutive equations for the transport properties must be employed. Transport properties include μ, λ, D_{nm} and $D_{T,m}$. The study of transport properties presents several difficulties. The transport properties are based on empirical correlations and on theoretical treatments. The theories followed depending on if one considers a dilute gas or a density gas, a polar fluid or a non polar fluid. In the case of a dilute gas it is possible to use a distribution function approach, a generalized Boltzmann equation method, as wrote by Chung [15] (Chapman and Cowling, 1952) or a time-correlation function (Steele and Hanley, 1969). In the case of a density gas it is possible to use the Enskog dense gas theory for the hard-sphere-potential model, Chung [15] cited Chapman (*Chapman and Cowling, 1952*). The model considers the correlations for the viscosity ratio $(\frac{\mu}{\mu_0})$ as a function of reduced density and reduced temperature as used Reid [85] the one that gave us a complete review about the different methods. Unfortunately none of the methods available are particularly reliable, especially for polar fluids. Gubbins et al. [105], used a method of correspondent states, predict the transport properties of simple dense fluids and later Gubbins developed a conformal solution theory for mixtures. Later Tham [106] try to use the method of correspondent states for complicate molecules but the liquid viscosity do not obey this simple method. After Chung et al. in [16] observed a discrepancies for thermal conductivity since polyatomic fluids do not obey the principle also at dilute gases. In fact, this could be caused by the argument which points out that the corresponding states do not correctly take into account the effect of internal degrees of freedom on especially for the thermal conductivity.

The applicability of corresponding states for thermodynamic properties has been considerable by the introduction of state-dependent shape factors "*Leland et al., 1968; Rowlinson and Watson, 1969*". This in-

cludes substances of more complicated molecules, Haile et al., 1976 in [21] and [22]. Unfortunately, this method is easily applicable not for polar fluids, by mean of complicated procedures. The correlation of low-pressure gas viscosity and thermal conductivity based on the kinetic gas theory has been published by Chung et al. [16]. In their theory accurate models were presented for dilute gas viscosity and thermal conductivity of non polar and polar. The low-pressure gas viscosity and thermal conductivity models are extended to fluids at high densities by introducing empirically correlated, density-dependent functions. As fluid density approaches zero, these correlations will reduce to the low-pressure gas expressions. These correlations use Pitzer's acentric factor (ω), the dimensionless dipole moment (μ_r), and an empirically determined association parameter (κ) to characterise the molecular structure effect of polyatomic molecules, the polar effect, and the hydrogen-bonding effect, respectively.
Chung et al. [15], developed the correlations for viscosity and thermal conductivity starting from the Chapman-Enskong theory (*Chapman and Cowling, 1952*) for the dilute gas and use the same approach both for viscosity and thermal conductivity. Considering a simple molecular gases, for the dilute gas one can be used a collision integral that is bound to some empirical coefficient and at Boltzmann constant (k) and energy potential parameter (ϵ) by a dimensionless temperature. To extend it to polyatomic molecular gases (polar and non polar), Chung multiplied by a factor F_c, to account for molecular structure and polar effects and reached simplifying the relation between distance potential parameter (σ) and V_c and between the Boltzmann constant, the energy potential parameter and T_c. At the end by F_c Chung obtained the new relation for i.e the viscosity containing the V_c and F_c where F_c is the shape factor. The shape factor is obtained from the Pitzer's acentric factor ω, κ and μ_r. The κ is a correction factor for hydrogen-bonding. The thermal conductivity for dilute gases can be deducted in similar way using also the relationship between viscosity, density and internal self-diffusion coefficient $\beta = \mu/\rho D$. Chung et al. deducted in this way, a relationships for dense fluids in case of non polar and polar substances. They account for the effects of temperature and pressure develop an empirically correlated function of density and temperature. Both the viscosity and the thermal conductivity are composed with two addend:

$$\eta = \eta_\kappa + \eta_P \tag{C.1.1}$$

For viscosity, the two addends are definitively made from the constants and are linear functions of the acentric factor (ω), the reduced dipole moment (μ_r), and the association factor (κ), fitted as follows:

$$A_i = a_0(i) + a_1(i)\omega + a_2(i)\mu_r^4 + a_3(i)\kappa \quad i = 1, ..., 10 \qquad (C.1.2)$$

Constants $a_0 and a_1$, were determined by regression of the viscosity data for non polar fluids, and a_2 and a_3 were determined from the data of polar and associating fluids. For non polar substances considered only the first two terms. The third term is included for polar substances and the last term for hydrogen-bonding substances. From their studies Chung et al. concluded that viscosity increase drastically with density. For the thermal conductivities of pure fluids at high pressures (or densities) was adopted the same approach as for viscosity. The low-pressure-gas thermal conducivity was modified introducing an empirically correlated function obtained from two addend:

$$\lambda = \lambda_\kappa + \lambda_P \qquad (C.1.3)$$

The constants are functions of the acentric factor (ω), the reduced dipole moment (μ_r), and the association factor (κ) as shown below:

$$B_i = b_0(i) + b_1(i)\omega + b_2(i)\mu_r^4 + b_3(i)\kappa \quad i = 1, ..., 7 \qquad (C.1.4)$$

Constants $b_0, b_1, b_2 and b_3$, are obtained from the regression analysis of thermal conductivity data for polar, nonpolar, and associating fluids. Summarizing Chung et al., can define a calculation procedure when the density is known, the viscosity and thermal conductivity calculations are straightforward. Input parameters are the critical temperature, volume, acentric factor, and molecular weight for non polar substances, and dipole moment for polar substances. In addition to these parameters, an empirically determined κ. For pure fluids, the potential constants, σ and ϵ, are calculated using the critical temperature and volume, respectively.

C.2 TRANSPORT PROPERTIES FOR MIXTURES

C.2.1 *Perfect gas*

On empirical mixture rules provide the values of the mixture transport properties, viscosity and thermal conductivity of a mixture of perfect gases, as a weighted average of those of the species in the mixture. Viscosity and thermal conductivity expressions for each of the

species are taken from Gordon [27] and [28] , according to the empirical relations provided in *Boushehri et al.* as cited in Urbano [77]. The dependence of transport properties on temperature has the following form:

$$\mu_i^0(T) = 10^{-7} exp[a_{\mu,1,i} log(T) + a_{\mu,2,i} T^{-1} + a_{\mu,3,i} T^{-2} + a_{\mu,4,i}] \quad \text{(C.2.1)}$$

$$k_i^0(T) = 10^{-7} exp[a_{k,1,i} log(T) + a_{k,2,i} T^{-1} + a_{k,3,i} T^{-2} + a_{k,4,i}] \quad \text{(C.2.2)}$$

The coefficients necessary to get values in the S.I for each species considered are listed in tables for viscosity and for thermal conductivity. Once data for the species are available, perfect gas mixture viscosity μ_0 and thermal conductivity k_0 are computed according to Gordon [27] and [28] as:

$$\mu^0(T, \overline{x}) = \sum_{i=1}^{N} x_i \mu_i^0 \left(x_i + \sum_{\substack{i=1 \\ j \neq i}}^{N} x_j \phi_{ij} \right)^{-1} \quad \text{(C.2.3)}$$

$$k^0(T, \overline{x}) = \sum_{i=1}^{N} x_i k_i^0 \left(x_i + \sum_{\substack{i=1 \\ j \neq i}}^{N} x_j \psi_{ij} \right)^{-1} \quad \text{(C.2.4)}$$

where the coefficients ϕ_{ij} depends on the values of μ_i, μ_j and on the molar weights of the species:

$$\phi_{ij} = \frac{1}{2\sqrt{2}} \left[1 + \left(\frac{\mu_i}{\mu_j} \right)^{1/2} \left(\frac{W_j}{W_i} \right)^{1/4} \right]^2 \left(1 + \frac{W_i}{W_j} \right)^{-1/2} \quad \text{(C.2.5)}$$

and the coefficients ψ_{ij}, necessary to evaluate the thermal conductivity, are computed by a suitable correction of ϕ_{ij}:

$$\psi_{ij} = \phi_{ij} \left[1 + \frac{2.41(W_i - W_j)(W_i - 0.142W_j)}{(W_i + W_j)^2} \right] \quad \text{(C.2.6)}$$

We recall another import term, the mass diffusion velocity that can be expressed in Fick's Law form by assigning a mixture diffusivity, $D_{n,mix}$, to each species, so that:

$$V_n = -D_{n,mix}\frac{\nabla Y_n}{Y_n} \tag{C.2.7}$$

A simple formula to obtain the approximate mixture diffusivities from the binary diffusivity matrix was proposed by Bird [8]:

$$D_{n,mix} = \frac{1-\chi_n}{\sum\limits_{n\neq m}\frac{\chi_n}{D_{nm}}} \tag{C.2.8}$$

C.2.2 *Real fluid*

The purpose of article of Ely and Hanley [21] has been to present a reliable self-consistent method for predicting the viscosity of non polar fluids and their mixtures over a wide range of thermodynamic states from the dilute gas to the dense liquid. Ely and Hanley [21] refer themselfs to a procedure presented by *(Mo and Gubbins, 1974; Hanley, 1976)*, to estimate the transport properties of natural gas and similar mixtures which basing itself on the corresponding states principle and the conformal solution, the predictive concept ***one-fluid concept***. The ***one-fluid*** requires only the critical parameters and Pitzer's acentric factor of each mixture component as input and does not require any mixture properties or transport data of the components of the mixture. The idea assumes that the configurational properties of a single-phase mixture can be make equal to an hypothetical pure fluid. The properties of this hypothetical pure fluid are then evaluated with the corresponding states respecting with a given reference fluid. This approach is defined for a conformal system in equilibrium but it is not immediate to understand in different systems and the ***one-fluid*** concept appears weak for transport because of the transport properties can contain contributions, an example is the diffusion coefficient, unique to the mixture. There is also the difficulty in formulating a consistent mass mixing rule which is unnecessary for equilibrium properties.
Ely and Hanley [21] by means of ECSP theory can assume:

- A pure fluid and a reference fluid obey to two parameter classical corresponding states formalism and, for a mixture, that all interactions in the mixture follow this principle.

- The mixture can be represented by an hypothetical pure fluid which implies mixing rules exist to evaluate the reducing ratios. Ely [21] has been assumed that the introduction of extended corresponding states allows these assumptions to be upheld.

From previously studies about the usage of mixing rules, Ely et al. [21] deducted that for the purpose of their work, the VDW mixing rules are satisfactory if then components of a mixture are not too dissimilar. The procedure made from Ely and Hanley [21] to evaluate a viscosity is: the input parameters are at the critical temperature, density or volume, pressure, acentric factor, and molecular weight of each component of the mixture of interest. These parameters for the reference fluid are required by an equation of state and some functional form of the viscosity for this fluid. Typical experimental input are be the pressure, temperature, and mixture composition. The density of the fluid or mixture is obtained finding the equivalent pressure of the reference substance from the corresponding pressure in the mixture. Initially the shape factors are set to unity and given the pressure, it is possible obtain the density by an iterative process.
In a further article [22], Ely extend the model descriptor from the calculus of viscosity to thermal conductivity. How in the viscosity calculus the thermal conductivity requires only the critical parameters and Pitzer's acentric factor of each mixture component. The method was applied to non polar fluid and over a large range of state from the dilute gases to dense liquids and differently from (*Mo and Gubbins 1976; Hanley 1976, 1977*: Ely [22]) the theory of Ely and Hanley does not required in input any transport data. The idea is that the properties of a single-phase mixture can be equated to those of a hypothetical pure fluid. The properties of this fluid are then evaluated via corresponding states with respect to a given reference fluid (in this case methane) at the appropriate corresponding pressure and temperature, or density and temperature. Urbano in her study about the GERG EOS [77], illustrated an application of ECSP theory presented in *Huber et al.* applied to the transport properties and that sorts the equations of state given and the prefect gas contribution to viscosity and thermal conductivity. In general the viscosity of the fluid mixture is:

$$\mu = \mu^0(T, \overline{x}) + \mu^r(T, \rho, \overline{x}) + \mu^m(T, \rho, \overline{x}) \tag{C.2.9}$$

where μ_0 is the diluted gas term (that is taken as equal to the perfect gas mixture viscosity given in Eq. C.2.3), μ_r is the residual viscos-

ity, and μ^m is a correction term for mixtures. The latter term can be neglected. The basic assumption of the ECSP model is:

$$\mu^r(T, \rho, \overline{x}) = \mu_0^r(T_0, \rho_0) F_\mu^r \tag{C.2.10}$$

namely, the residual viscosity of the mixture is equal to the residual viscosity of the reference fluid μ_0^r evaluated at the conformal temperature T_0 and density ρ_0 and modified for a correction factor F_μ^r. Assuming that the residual viscosity of the reference fluid as a function of temperature and density is known, it is only necessary to evaluate conformal temperature and density and the reducing factor F_μ^r. The conformal temperature and density are defined as such that:

$$\begin{cases} a^r(T, \rho, \overline{x}) = a_0^r(T_0, \rho_0) \\ Z(T, \rho, \overline{x}) = Z_0(T_0, \rho_0) \end{cases} \tag{C.2.11}$$

where a^r is the residual part of the reduced Helmholtz free energy ($a = A/RT$) and Z is the compressibility factor of the mixture, whereas a_0^r and Z_0 are the corresponding functions for the reference fluid. The mixture values are obtained by Eq. 3.3.74 and Eq. 3.3.79 whereas the reference fluid values can be write linked to EOS and transport properties of R134a. The system of equations C.2.11 is then solved for T_0 and ρ_0. Following equivalent reducing ratios are defined:

$$f_x = T/T_0; \quad h_x = \rho_0/\rho \tag{C.2.12}$$

Once the conformal values are available, only lacks the reducing factor F_μ^r to get the value of viscosity. The reducing factor is then expressed as:

$$F_\mu^r = f_x^{1/2} h_x^{-2/3} g_{x,\mu}^{1/2} \tag{C.2.13}$$

where f_x and h_x are the reducing factors for the mixture and $g_{x,\mu}$ an equivalent mass for the mixture:

$$g_{x,\mu}^{1/2} = \frac{\sum_{i=1}^{N} \sum_{j=1}^{N} x_i x_j f_{ij}^{1/2} h_{ij}^{4/3} W_{ij}^{1/2}}{f_x^{1/2} h_x^{4/3} W_0^{1/2}} \tag{C.2.14}$$

The latter expression for $g_{\chi,\mu}$ requires the introduction of the three terms W_{ij}, f_{ij} and h_{ij}. The first term is easily computed as the mean molar weight of the two species i and j:

$$W_{ij} = \frac{2W_i W_j}{W_i + W_j} \tag{C.2.15}$$

The second and third terms require more computations as they rely on the species values f_i, f_j h_i and h_j:

$$f_{ij} = \sqrt{f_i f_j} \tag{C.2.16}$$

$$h_{ij} = \frac{1}{8}\left(h_i^{1/3} + h_j^{1/3}\right)^3 \tag{C.2.17}$$

where f_i and h_i are the ratio of conformal values of temperature and density of the species to the conformal temperature and density of the reference fluid:

$$f_i = T_i/T_0 \tag{C.2.18}$$

$$h_i = \rho_0/\rho_i \tag{C.2.19}$$

Conformal temperature and density of the species are computed as for the reference fluid:

$$\begin{cases} a^r(T,\rho,\overline{x}) = a_i^r(T_i,\rho_i) \\ Z(T,\rho,\overline{x}) = Z_i(T_i,\rho_i) \end{cases} \tag{C.2.20}$$

The evaluation of thermal conductivity follows the same procedure as for viscosity. In general the thermal conductivity of the fluid mixture can be (in according to *Huber and al.* Urbano [77]):

$$k = k^0(T,\overline{x}) + k^r(T,\rho,\overline{x}) + k^c(T,\rho,\overline{x}) \tag{C.2.21}$$

where k_0 is the diluted gas term (that is taken as equal to the perfect gas mixture viscosity given in Eq. C.2.4), k_r is the residual viscosity, and k_c is the so-called critical enhancement which allows to predict the thermal conductivity peak in the vicinity of the critical

point. This latter term could be neglected. The basic assumption of the ECSP model is as in case of viscosity:

$$k^r(T,\rho,\bar{x}) = k_0^r(T_0,\rho_0)F_k^r \tag{C.2.22}$$

namely, the residual thermal conductivity of the mixture is equal to the residual thermal conductivity of the reference fluid ${k_0}^r$ evaluated at the conformal temperature T_0 and density ρ_0, and modified for a correction factor ${F_k}^r$. Because the reference fluid is the same as for viscosity conformal temperature and density these are given by Eqs. C.2.11 and already available from the computation of viscosity. Therefore, it is only necessary to evaluate the reducing factor ${F_k}^r$. The reducing factor has the same expression as Eq. C.2.13, except for the value of $g_{x,k}$ instead of $g_{\mu,k}$:

$$F_k^r = f_x^{1/2} h_x^{-2/3} g_{x,k}^{1/2} \tag{C.2.23}$$

The reducing ratios f_x and h_x are those computed for viscosity in Eq. C.2.12, whereas $g_{x,k}$ can be computed after evaluating f_{ij} and h_{ij} on the basis of species conformal temperatures and densities according to Eqs. C.2.15 - C.2.20:

$$g_{x,k}^{1/2} = \frac{\sum_{i=1}^{N}\sum_{j=1}^{N} x_i x_j f_{ij}^{1/2} h_{ij}^{4/3} W_{ij}^{-1/2}}{f_x^{1/2} h_x^{4/3} W_0^{-1/2}} \tag{C.2.24}$$

which slightly differs with respect to Eq. C.2.14.
The theoretical basis of these mixing rules is the conformal solution theory of *Mo and Gubbins (1976)*, see Chung et al. [15] . According to their model, the properties of mixtures are calculated from the same correlations as for a pure fluid, except that the characterization parameters $\sigma, \epsilon, \omega, \mu, \kappa$ (respectively: distance potential parameter, energy potential parameter, Pitzer's acentric factor, dipole moment, empirically determined association parameter) and molecular weight M that are substituted with corresponded mixture parameters. The Chung's mixing rules for $\sigma_m, \epsilon_m, \omega_m$, where 'm' indicate the mixture, are compatible with the three-parameter corresponding state of thermodynamic properties *Lee et al. 1977* (Chung et al. [15]). The binary interaction parameters are important for the viscosity and thermal conductivity predictions, and their numerical values could differ for viscosity and thermal conductivity, for systems which contain polar substances, or components with large differences in molecular structure. About the **textitdiffusion coefficients** of gases at high pressures,

in Takahashi [103], we can find a generalized chart analogous to that Slattery and Bird (SB chart). The Takahashi's chart has been prepared from the observed values of the self-diffusion and binary-diffusion coefficients of gases at high pressures. The diffusion coefficients and pressure are correlated to T_r and P_r and the new chart is built by correlating the observed values to T_r and P_r.

D

THICKENED FLAME MODEL

The Dynamically Thickened Flame model (DTF) is achieved modifying the thickened flame model derived for premixed flames. The crucial point of model, Poinsot et al. [53], is that does not require any a priori assumption on the flame structure and is able to compute flows where both premixed and non-premixed flamelets coexist. The DTF is a LES subgrid scale turbulent combustion model and can compute mixing, diffusion, and premixed flames simultaneously without using a constant thickening factor but a local thickening factor F. The F factor is active only in the vicinity of the flame front ($F > 1$) and relaxes to $F = 1$ (no effect) far away from the flame. The advantage of the model is that outside of the flame zones, thickening is suppressed and mixing can be predicted correctly. In the equation of the fuel consumption rate D.0.25:

$$\dot{\omega}_F = A\nu_F W_F \left(\frac{\rho Y_F}{W_F}\right)^{\nu F} \left(\frac{\rho Y_O}{W_O}\right)^{\nu O} exp\left(-\frac{T_a}{T}\right) \tag{D.0.25}$$

where W_O, W_F are respectively the atomic weight of oxydizer and fuel, T_a is the activation temperature and the pre-exponential constant A is fitted to provide correct flame speeds for lean premixed flames when compared to full chemistry results. The heart of the ***Thickened Flame*** is a multiply factor F. The F factor multiplies the heat diffusion molecular coefficient decreasing the constant A (A/F) in equation D.0.25, one can note that the flame propagates at the same laminar flame speed s_l^0 than the non-thickened flame. Instead a change visible is in the thickness that increases by a factor F and becomes $\delta_L^1 = F\delta_L^0$. Adjusting F to sufficiently large values (for example between 10 and 100) allows the resolution of flame on an LES grid
The model presented above had been integrated by Poinsot [53] considering the dynamic thickening, depending on time and spatial location, recognizing that a premixed flame where the thickening factor F changes spatially still propagates at the laminar flame speed s_l^0. The thickening factor F may then be adjust from large values inside the reaction zone (where the reaction rate, inducing large gradients) to

unity away from the flame front (to avoid a modification of mixing description by changing molecular diffusion coefficients), retaining the right propagation speed of a laminar premixed flame.
The modulation of thickened uses a sensor *'Arrhenius-like'* and determines whether the flame should be thickened or not. The expression which is:

$$\Omega = Y_F^{\nu F} Y_O^{\nu O} \exp\left(-\Gamma \frac{T_a}{T}\right) \tag{D.0.26}$$

The sensor Ω controls the value of the thickening coefficient F through:

$$F = 1 + (F_{max} - 1)\tanh\left(\beta \frac{\Omega}{\Omega_{max}}\right) \tag{D.0.27}$$

The sensor detects the presence of the reaction zone but is active in a broader zone and it's necessary that Γ parameter artificially decreases the activation temperature ($\Gamma < 1$).
To account for the unresolved flame wrinkling linked to problems among the flame and the smallest turbulent motions, was been added an efficiency function E. This function E depends on the thickening factor F, the length scale and the velocity ratios consider the combustion LES the filter size and the subgrid scale rms velocity. In the practical implementation of the thickened flame model, the molecular diffusion coefficient D is replaced by EFD and the pre-exponential constant A of the Arrhenius law in equation D.0.25 by EA/F.

E

CHEMICAL KINETIC MECHANISM

```
SIMPLIFIED KINETIC MODEL
PRODUCED BY GEN1D GRI-Mech Version 3.0 7/30/99 CHEMKIN-II format
See README30 file at anonymous FTP site unix.sri.com, directory gri;
WorldWideWeb home page http://www.me.berkeley.edu/gri_mech/ or
through http://www.gri.org , under 'Basic  Research',
for additional information, contacts, and disclaimer

ELEMENTS
O H C N AR

SPECIES
H2 H O O2 OH H2O HO2 CH3 CH4 CO CO2 HCO CH2O CH3O C2H3 N2

REACTIONS
2O+M<=>O2+M                               1.200E+17   -1.000        .00
 H2/2.40/ H2O/15.40/ CH4/2.00/ CO/1.75/ CO2/3.60/
O+H+M<=>OH+M                              5.000E+17   -1.000        .00
 H2/2.00/ H2O/6.00/ CH4/2.00/ CO/1.50/ CO2/2.00/
O+H2<=>H+OH                               3.870E+04    2.700    6260.00
O+HO2<=>OH+O2                             2.000E+13     .000        .00
O+CH3<=>H+CH2O                            5.060E+13     .000        .00
O+CH4<=>OH+CH3                            1.020E+09    1.500    8600.00
O+CO(+M)<=>CO2(+M)                        1.800E+10     .000    2385.00
   LOW/ 6.020E+14     .000    3000.00/
 H2/2.00/ O2/6.00/ H2O/6.00/ CH4/2.00/ CO/1.50/ CO2/3.50/
O+HCO<=>OH+CO                             3.000E+13     .000        .00
O+HCO<=>H+CO2                             3.000E+13     .000        .00
O+CH2O<=>OH+HCO                           3.900E+13     .000    3540.00
O+CH3O<=>OH+CH2O                          1.000E+13     .000        .00
O2+CO<=>O+CO2                             2.500E+12     .000   47800.00
O2+CH2O<=>HO2+HCO                         1.000E+14     .000   40000.00
H+O2+M<=>HO2+M                            2.800E+18    -.860        .00
 O2/.00/ H2O/.00/ CO/.75/ CO2/1.50/ N2/.00/
H+2O2<=>HO2+O2                            2.080E+19   -1.240        .00
H+O2+H2O<=>HO2+H2O                        11.26E+18    -.760        .00
H+O2+N2<=>HO2+N2                          2.600E+19   -1.240        .00
H+O2<=>O+OH                               2.650E+16    -.6707  17041.00
2H+M<=>H2+M                               1.000E+18   -1.000        .00
 H2/.00/ H2O/.00/ CH4/2.00/ CO2/.00/
2H+H2<=>2H2                               9.000E+16    -.600        .00
2H+H2O<=>H2+H2O                           6.000E+19   -1.250        .00
2H+CO2<=>H2+CO2                           5.500E+20   -2.000        .00
```

```
H+OH+M<=>H2O+M                            2.200E+22   -2.000        .00
 H2/.73/ H2O/3.65/ CH4/2.00/
H+HO2<=>O+H2O                             3.970E+12     .000     671.00
H+HO2<=>O2+H2                             4.480E+13     .000    1068.00
H+HO2<=>2OH                               0.840E+14     .000     635.00
H+CH3(+M)<=>CH4(+M)                       13.90E+15    -.534     536.00
     LOW  /  2.620E+33   -4.760   2440.00/
     TROE/   .7830   74.00  2941.00  6964.00 /
 H2/2.00/ H2O/6.00/ CH4/3.00/ CO/1.50/ CO2/2.00/
H+CH4<=>CH3+H2                            6.600E+08    1.620   10840.00
H+HCO(+M)<=>CH2O(+M)                      1.090E+12     .480    -260.00
     LOW  /  2.470E+24   -2.570    425.00/
     TROE/   .7824  271.00  2755.00  6570.00 /
 H2/2.00/ H2O/6.00/ CH4/2.00/ CO/1.50/ CO2/2.00/
H+HCO<=>H2+CO                             7.340E+13     .000        .00
H+CH2O(+M)<=>CH3O(+M)                     5.400E+11     .454    2600.00
     LOW  /  2.200E+30   -4.800   5560.00/
     TROE/   .7580   94.00  1555.00  4200.00 /
 H2/2.00/ H2O/6.00/ CH4/2.00/ CO/1.50/ CO2/2.00/
H+CH2O<=>HCO+H2                           5.740E+07    1.900    2742.00
H+CH3O<=>H2+CH2O                          2.000E+13     .000        .00
H+CH3O<=>OH+CH3                           1.500E+12     .500    -110.00
H2+CO(+M)<=>CH2O(+M)                      4.300E+07    1.500   79600.00
     LOW  /  5.070E+27   -3.420  84350.00/
     TROE/   .9320  197.00  1540.00 10300.00 /
 H2/2.00/ H2O/6.00/ CH4/2.00/ CO/1.50/ CO2/2.00/
OH+H2<=>H+H2O                             2.160E+08    1.510    3430.00
2OH<=>O+H2O                               3.570E+04    2.400   -2110.00
OH+HO2<=>O2+H2O                           1.450E+13     .000    -500.00
 DUPLICATE
OH+HO2<=>O2+H2O                           0.500E+16     .000   17330.00
 DUPLICATE
OH+CH4<=>CH3+H2O                          1.000E+08    1.600    3120.00
OH+CO<=>H+CO2                             4.760E+07    1.228      70.00
OH+HCO<=>H2O+CO                           5.000E+13     .000        .00
OH+CH2O<=>HCO+H2O                         3.430E+09    1.180    -447.00
OH+CH3O<=>H2O+CH2O                        5.000E+12     .000        .00
HO2+CH3<=>O2+CH4                          1.000E+12     .000        .00
HO2+CH3<=>OH+CH3O                         3.780E+13     .000        .00
HO2+CO<=>OH+CO2                           1.500E+14     .000   23600.00
CH3+O2<=>O+CH3O                           3.560E+13     .000   30480.00
CH3+O2<=>OH+CH2O                          2.310E+12     .000   20315.00
CH3+HCO<=>CH4+CO                          2.648E+13     .000        .00
CH3+CH2O<=>HCO+CH4                        3.320E+03    2.810    5860.00
HCO+H2O<=>H+CO+H2O                        1.500E+18   -1.000   17000.00
HCO+M<=>H+CO+M                            1.870E+17   -1.000   17000.00
 H2/2.00/ H2O/ .00/ CH4/2.00/ CO/1.50/ CO2/2.00/
HCO+O2<=>HO2+CO                           13.45E+12     .000     400.00
CH3O+O2<=>HO2+CH2O                        4.280E-13    7.600   -3530.00
C2H3+O2<=>HCO+CH2O                        4.580E+16   -1.390    1015.00
O+CH3=>H+H2+CO                            3.370E+13     .000        .00
OH+CH3=>H2+CH2O                           8.000E+09     .500   -1755.00
```

F

LIST OF MOVIES

DEMOnstrator

- Temperature field (0.1368 s) click here
- Temperature field (0.1272 s) click here
- Density field (0.1272 s) click here
- CH_4 field (0.1272 s) click here
- O_2 field (0.1272 s) click here
- HCO field (0.1272 s) click here

BIBLIOGRAPHY

[1] M.J. Assael, M.J.P. Trusler, and T.F. Tsolakis. *Thermophysical Properties of Fluids: An Introduction to Their Prediction*. 1996.

[2] D.T. Banuti and K. Hannemann. Thermodynamic interpretation of cryogenic injection experiments. 2011. (pag 195(2)b).

[3] D.T. Banuti and K. Hannemann. Supercritical pseudo-boiling and its relevance for transcritical injection. 2014. (pag 195).

[4] V.G. Bazarov and V. Yang. Liquid-propellant rocket engine injector dynamics. *Journal of Propulsion and Power*, 14(5):797–806, 1998. (pag 85).

[5] J. Bellan. Supercritical (and subcritical) fluid behavior and modeling: drops, streams, shear and mixing layers, jets and sprays. *Progress in Energy and Combustion Science*, 26(4):329–366, 2000. (pag 13).

[6] B. Betti. *Flow Field and Heat Transfer Analysis of Oxygen / Methane Liquid Rocket Engine Thrust Chambers*. PhD thesis, La Sapienza University, La Sapienza, Roma, 2012.

[7] B. Betti, E. Martelli, and F. Nasuti. Heat flux evaluation in oxygen/methane thrust chambers by rans approach. *Conference Proceeding Series Published by AIAA*, 15(8):835–842, 2010. (pag 148).

[8] R.B. Bird, W.E. Stewart, and E.N. Lightfoot. *Transport Phenomena*. New York, 1960. (pag 202).

[9] S. Candel, M. Juniper, G. Singla, P. Scouflaire, and C. Rolon. Structure and dynamics of cryogenic flames at supercritical pressure. *Combustion Science and Technology*, 178(1-3):161–192, 2006. (pag xiii, xv, 10, 33, 34, 82, 86(2)b , 87(3)b , 88, and 89).

[10] B. Chehroudi, R. Cohn, and D. Talley. Cryogenic shear layers: Experiments and phenomenological modeling of the initial growth rate under subcritical and supercritical conditions. *International Journal of Heat and Fluid Flow*, 23(5):554–563, 2002. (pag 8).

[11] B. Chehroudi and D. Talley. Understanding injection into high pressure supercritical environments. *Journal of Propulsion and Power*, 19(3):332–341, 2000.

[12] B. Chehroudi and D. Talley. Interaction of acoustic waves with a cryogenic nitrogen jet at sub- and supercritical pressures. 2002. (pag 9).

[13] B. Chehroudi, D. Talley, and E. Coy. Initial growth rate and visual characteristics of a round jet into a sub- to supercritical environment of relevance to rocket, gas turbine, and diesel engines. 1999. (pag 8, 29(2)b , 31, 33, and 98).

[14] B. Chehroudi, D. Talley, and E. Coy. Visual characteristics and initial growth rates of round cryogenic jets at subcritical and supercritical pressures. *Physics of Fluids*, 14(2):850–861, 2002.

[15] T.H. Chung, M. Ajlan, L.L. Lee, and K.E. Starling. Generalized multiparameter correlation for nonpolar and polar fluid transport properties. *Industrial and Engineering Chemistry Research*, 27(4):671–679, 1988. (pag 198(2)b , 199, and 206(2)b).

[16] T.H. Chung, L.L. Lee, and K.E. Starling. Applications of kinetic gas theories and multiparameter correlation for prediction of dilute gas viscosity and thermal conductivity. *Industrial and Engineering Chemistry Fundamentals*, 23(1):8–13, 1984. (pag 198 and 199).

[17] M. Cismondi and J. Mollerup. Development and application of a three-parameter rk-pr equation of state. *Fluid Phase Equilibria*, 232(1-2):74–89, 2005. (pag 51).

[18] O. Colin and M. Rudgyard. Development of high-order taylor-galerkin schemes for les. *Journal of Computational Physics*, 162(2):338–371, 2000. (pag 106).

[19] L. Cutrone. *Predicting reactive flows for propulsion applications using a Flamelet/Progress-Variable approach*. PhD thesis, Politecnico di Bari University, Politecnico di Bari, Bari, 2001. (pag 1(2)b , 7, 8, and 15).

[20] R.N. Dahms and J.C. Oefelein. On the transition between two-phase and single-phase interface dynamics in multicomponent fluids at supercritical pressures. *Physics of Fluids*, 25(9), 2013. (pag xiii, 28, 31, 32, and 85).

[21] J.F. Ely and H.J.M. Hanley. Prediction of transport properties. 1. viscosity of fluids and mixtures. *Industrial and Engineering Chemistry Fundamentals*, 20(4):323–332, 1981. (pag 197(2)b , 199, 202(3)b , and 203(3)b).

[22] J.F. Ely and H.J.M. Hanley. Prediction of transport properties. 2. thermal conductivity of pure fluids and mixtures. *Industrial*

and Engineering Chemistry Fundamentals, 22(1):90–97, 1983. (pag 199 and 203(2)b).

[23] G.D. Fisher and T.W. Leland Jr. Corresponding states principle using shape factors. *Industrial and Engineering Chemistry Fundamentals*, 9(4):537–544, 1970. (pag 196).

[24] A. Ghafourian, S. Mahalingam, H. Dindi, and J.W. Daily. A review of atomization in liquid rocket engines. 1991. (pag 9, 24, 29(2)b , and 30).

[25] V. Giovangigli, L. Matuszewski, and F. Dupoirieux. Detailed modeling of planar transcritical h2-02-n2 flames. *École Polytechnique Centrede Mathématiques Appliquées*, 2010. (pag 17).

[26] V. Giovangigli, L. Matuszewski, and F. Dupoirieux. Numerical simulation of transcritical strained laminar flames. *École Polytechnique Centrede Mathématiques Appliquées*, 2011. (pag 17).

[27] S. Gordon and B.J. McBride. Computer program for calculation of complex chemical equilibrium compositions and applications: I analysis. Technical report, 1994. (pag 40 and 201(2)b).

[28] S. Gordon and B.J. McBride. Computer program for calculation of complex chemical equilibrium compositions and applications: Ii users manual and program description. Technical report, 1994. (pag 40 and 201(2)b).

[29] D. Haeseler, C. Mäding, A. Götz, V. Roubinski, S. Khrissanfov, and V. Berejnoy. Recent developments for future launch vehicle lox/hc rocket engines. In *Proc. 6th International Symposium Propulsion for Space Transportation of the XXIst Century,13-17 May 2002, Versailles, France.*, 2002.

[30] O.J. Haidn. Advanced rocket engines. in advances on propulsion technology for high-speed aircraft. *Educational Notes RTO-EN-AVT-150*, 2008. (pag xiii and 5).

[31] W.B. Hall and J.D. Jackson. Heat transfer near the critical point. (pag 195).

[32] K. Harstad and J. Bellan. The lewis number under supercritical conditions. *International Journal of Heat and Mass Transfer*, 42(6):961–970, 1999.

[33] K.G. Harstad, R.S. Miller, and J. Bellan. Efficient high-pressure state equations. *AIChE Journal*, 43(6):1605–1609, 1997. (pag 16).

[34] C. Hirsch. *Numerical Computation of Internal and External Flows: The Fundamentals of Computational Fluid Dynamics volume 2*. 1990.

[35] H. Huang and D.K Huzel. *Modern Engineering for Design of Liquid-Propellant Rocket Engines*. Oxford, 1 edition, 1992. (pag 3).

[36] N. Ierardo. *Supercritical Combustion Modelling for LOX/HC Propulsion*. PhD thesis, La Sapienza University, La Sapienza, Roma, 2001. (pag 31(2)b).

[37] B. Ivancic and W. Mayer. Time-and length scales of combustion in liquid rocket thrust chambers. *Journal of Propulsion and Power*, 18(2):247–253, 2002. (pag 10).

[38] A. Jameson, W. Schmidt, D. Gmbh, E. Turkel, and T. Aviv. Numerical solution of the euler equations by finite volume methods using runge-kutta time-stepping schemes. *AIAA Paper*, M:1–19, 1981. (pag 106).

[39] M. Juniper and S. Candel. The effect of damköhler number on the stand-off distance of cross-flow flames. *Combustion Theory and Modelling*, 7(3):563–577, 2003.

[40] M. Juniper, A. Tripathi, P. Scouflaire, J.-C. Rolon, and S. Candel. Structure of cryogenic flames at elevated pressures. *Proceedings of the Combustion Institute*, 28(1):1103–1109, 2000. (pag 8 and 18).

[41] M.P. Juniper and S.M. Candel. The stability of ducted compound flows and consequences for the geometry of coaxial injectors. *Journal of Fluid Mechanics*, (482):257–269, 2003. (pag 87(3)b).

[42] N.L. Kafengauz and M.I. Fedorov. Excitation of high-frequency pressure oscillations during heat exchange with diisopropylcyclohexane. *Journal of Engineering Physics*, 11(1):63–67, 1969. (pag 195).

[43] N.L. Kafengauz and M.I. Fedorov. Pseudoboiling and heat transfer in a turbulent flow. *Journal of Engineering Physics*, 14(5):489–490, 1972. (pag 195).

[44] D. Kendrick, G. Herding, P. Scouflaire, C. Rolon, and S. Candel. Effects of a recess on cryogenic flame stabilization. *Combustion and Flame*, 118(3):327–339, 1999. (pag 10).

[45] S.K. Kim, H.-S. Choi, and Y. Kim. Thermodynamic modeling based on a generalized cubic equation of state for kerosene/lox

rocket combustion. *Combustion and Flame*, 159(3):1351–1365, 2012. (pag 15 and 51).

[46] T. Kim, Y. Kim, and S. Kim. Numerical study of cryogenic liquid nitrogen jets at supercritical pressures. *The Journal of Supercritical Fluids*, 56(2):152 – 163, 2011. (pag 15).

[47] T. Kim, Y. Kim, and S. Kim. Real-fluid flamelet modeling for gaseous hydrogen/cryogenic liquid oxygen jet flames at supercritical pressure. *The Journal of Supercritical Fluids*, 58(2):254–262, September 2011. (pag 15).

[48] T. Kim, Y. Kim, and S.K. Kim. Effects of pressure and inlet temperature on coaxial gaseous methane/liquid oxygen turbulent jet flame under transcritical conditions. *J. of Supercritical Fluids*, 81:164–174, 2013. (pag 13).

[49] M.D Koretsky. *Engineering and Chemical Thermodynamics 2nd edition*. 2013. (pag 53 and 72).

[50] O. Kunz, R. Klimeck, W. Wagner, and M. Jaeschke. *The GERG-2004 Wide-Range Equation of State for Natural Gases and Other Mixtures*. Published for GERG and printed in Germany by Publishing House of the Association of German Engineers, Reihe 6 Nr. 557, 2007. (pag 66).

[51] T.Y. Kwak, E.H. Benmekki, and G.A. Mansoori. Van der waals mixing rules for cubic equations of state(applications for supercritical fluid extraction modeling and phase equilibrium calculations). volume 30, pages 119–129, 1985.

[52] J.C. Lasheras, E. Villermaux, and E.J. Hopfinger. Break-up and atomization of a round water jet by a high-speed annular air jet. *Journal of Fluid Mechanics*, 357:351–379, 1998.

[53] J.P. Légier, T. Poinsot, B. Varoquié, F. Lacas, and D. Veynante. Large eddy simulation of a non-premixed turbulent burner using a dynamically thickened flame model. *Fluid Mechanics and its Applications*, 70:315–326, 2002. (pag 21 and 208(2)b).

[54] J.P. Legier, T. Poinsot, and D. Veynante. Dynamically thickened flame les model for premixed and non-premixed turbulent combustion. In *Center for Turbulence Research - Proceedings of the Summer Program 2000*, pages 157–168, 2000. (pag 154).

[55] J. Lux and O. Haidn. Effect of recess in high-pressure liquid oxygen/methane coaxial injection and combustion. *Journal of Propulsion and Power*, 25(1):24–32, 2009. (pag xv(2)b , 84(2)b , 85(2)b , 86, and 87).

[56] J. Lux and O. Haidn. Flame stabilization in high-pressure liquid oxygen/methane rocket engine combustion. *Journal of Propulsion and Power*, 25(1):15–23, 2009. (pag 11 and 161).

[57] J. Lux, D. Suslov, M. Bechle, M. Oschwald, and O. Haidn. *Investigation of Sub- and Supercritical LOX/Methane Injection Using Optical Diagnostics*. American Institute of Aeronautics and Astronautics, 2006. (pag 11).

[58] J. Matthew and C. Sébastien. Edge diffusion flame stabilization behind a step over a liquid reactant. *Journal of Propulsion and Power*, 19(3):332–341, 2003. (pag 88).

[59] W. Mayer, A. Schik, M. Schäffler, and H. Tamura. Injection and mixing processes in high-pressure liquid oxygen/gaseous hydrogen rocket combustors. *Journal of Propulsion and Power*, 16(5):823–828, 2000. (pag 9 and 17).

[60] W. Mayer and J. Smith. *Liquid Rocket Thrust Chambers: Aspect of Modeling, Analysis , and Design*. AIAA, 2004. (pag 11 and 29(2)b).

[61] W. Mayer and H. Tamura. Propellant injection in a liquid oxygen/gaseous hydrogen rocket engine. *Journal of Propulsion and Power*, 12(6):1137–1147, 1996. (pag 9 and 85).

[62] W. Mayer, J. Telaar, R. Branam, G. Schneider, and J. Hussong. Characterization of cryogenic injection at supercritical pressure. 2001. (pag xiii, 9, 24, 25(2)b , 30, 31, 95(2)b , 98, 100, and 190).

[63] W.O.H. Mayer, B. Ivancic, A. Schik, and U. Hornung. Propellant atomization and ignition phenomena in liquid oxygen/gaseous hydrogen rocket combustors. *Journal of Propulsion and Power*, 17(4):794–799, 2001. (pag 10 and 29).

[64] H. Meng, O, and V. Yang. A unified treatment of general fluid thermodynamics and its application to a preconditioning scheme. *Journal of Computational Physics*, 189(1):277 – 304, 2003. (pag 14 and 17).

[65] Inc. Metacomp Technologies. *CFD++ user manual*. Metacomp Technologies, Inc., 28632 Roadside Drive, #255 Agoura Hills, CA 91301, USA., 2013. (pag 104 and 107).

[66] Richard S. Miller, Kenneth G. Harstad, and J. Bellan. Direct numerical simulations of supercritical fluid mixing layers applied to heptane-nitrogen. *Journal of Fluid Mechanics*, 436:1–39, 6 2001. (pag 13 and 14).

[67] Y. Mizobuchi, S. Tachibana, J. Shinio, S. Ogawa, and T. Takeno. A numerical analysis of the structure of a turbulent hydrogen jet lifted flame. In *Proc. of Combustion Institute (DISC 2002)*, volume 29, pages 2009–2015, 2002. (pag 143).

[68] K. Mohamed and M. Paraschivoiu. Real gas simulation of hydrogen release from a high-pressure chamber. *International Journal of Hydrogen Energy*, 30(8):903–912, 2005.

[69] M.J Moran and H.N Shapiro. *Fundamentals of Engineering Thermodynamics*. Wiley, 5 edition, 2006. (pag 42).

[70] F. Nasuti, M. Onofri, and M. Valorani. Orthogonal grid generation for internal flows by conformal mapping. *Proc. 8th Int. Conf. on Num. Meth. in Laminar and Turbulent Flow, part.2*, pages 1359–1370, 1993. (pag 80).

[71] J. C. Oefelein. Mixing and combustion of cryogenic oxygen-hydrogen shear-coaxial jet flame at supercritical pressure. *Combust. Sci. and Tech.*, 178:229–252, 2006. (pag 13 and 15(2)b).

[72] J.C. Oefelein. Thermophysical characteristics of shear-coaxial lox-h2 flames at supercritical pressure. volume 30 II, pages 2929–2937, 2005. (pag 48).

[73] J.C. Oefelein and V. Yang. Modeling high-pressure mixing and combustion processes in liquid rocket engines. *Journal of Propulsion and Power*, 14(5):843–857, 1998. (pag xiii(2)b , 13, 18, 32, 34(2)b , 86, and 87).

[74] N. Okong'o and J. Bellan. Consistent boundary conditions for multicomponent real gas mixtures based on characteristic waves. *Journal of Computational Physics*, 176(2):330 – 344, 2002. (pag 17).

[75] N. Okong'o, O, and J. Bellan. Real-gas effects on mean flow and temporal stability of binary-species mixing layers, 2003. (pag 15 and 17).

[76] N. Okong'o, O, J. Bellan, and K. Harstad. Direct numerical simulations of lox/h2 temporal mixing layers under supercritical conditions, 2001. (pag 14).

[77] M. Onofri, F. Nasuti, and A. Urbano. Deliverable d2.2.2: Physical and chemical characterization of lox/methane system equation of state of binary and ternary system. Technical report, Sept 2012. (pag 68(3)b , 69(3)b , 201, 203, and 205).

[78] M. Oschwald, F. Cuoco, M. De Rosa, and O. Haidn. Combustion of lox/h2-and lox/ch4-spray. (pag 8).

[79] M. Oschwald, J.J. Smith, R. Branam, J. Hussong, A. Schik, B. Chehroudi, and D. Talley. Injection of fluids into supercritical environments. *Combustion Science and Technology*, 178(1-3):49–100, 2006. (pag 28 and 195(3)b).

[80] D. Papamoschou and A. Roshko. Compressible turbulent shear layer: An experimental study. *Journal of Fluid Mechanics*, 197:453–477, 1988.

[81] D. Peng and D.B. Robinson. New two-constant equation of state. *Ind Eng Chem Fundam*, 15(1):59–64, 1976. (pag 46, 56, and 64).

[82] X. Petit, G. Ribert, G. Lartigue, and P. Domingo. Large-eddy simulation of supercritical fluid injection. *Journal of Supercritical Fluids*, 84:61–73, 2013. (pag 1, 18(2)b , 48, and 52).

[83] M. Pizzarelli, B. Betti, and F. Nasuti. Coupled analysis of hot-gas and coolant flows in lox/methane thrust chambers. *4th European Conference on Aerospace Sciences*, 2011. (pag 148).

[84] T.J. Poinsot and S.K. Lelef. Boundary conditions for direct simulations of compressible viscous flows. *Journal of Computational Physics*, 101(1):104–129, 1992.

[85] B. Poling, J.M. Prausnitz, J.P. Ó Connel, and Reid. *The Properties of Gases and Liquids*. 2000. (pag 42, 43(2)b , 63, and 198).

[86] L. Pons, N. Darabiha, and S. Candel. Pressure effects on non-premixed strained flames. *Combustion and Flame*, 152:218 – 229, 2008. (pag 16(2)b).

[87] Y. A. Rastigejev and S. Paolucci. Wavelet-based adaptive multiresolution computation of viscous reactive flows. *International Journal for Numerical Methods in Fluids*, 52(7):749–784, 2006. (pag 79(2)b).

[88] R.D. Reitz and F.V. Bracco. Mechanism of atomization of a liquid jet. *Physics of Fluids*, 25(10):1730–1742, 1982. (pag 29 and 30).

[89] P.H. Renard, D. Thévenin, J.C. Rolon, and S. Candel. Dynamics of flame/vortex interactions. *Progress in Energy and Combustion Science*, 26(3):225–282, 2000.

[90] G. Ribert, D. Taieb, X. Petit, G. Lartigue, and P. Domingo. Simulation of supercritical flows in rocket-motor engines: application to cooling channel and injection system. In *Proc. in Propulsion Physics*, volume 4, pages 205 – 226, 2013. (pag 47 and 48).

[91] G. Ribert, N. Zong, V. Yang, L. Pons, N. Darabiha, and S. Candel. Counterflow diffusion flames of general fluids: Oxygen/hydrogen mixtures. *Combustion and Flame*, 154(3):319 – 330, 2008. (pag 16(2)b).

[92] A. Ruiz. *Unsteady Numerical Simulations of Transcritical Turbulent Combustion in Liquid Rocket Engines*. PhD thesis, Politécnique University, Politécnique, Touluse, 2012. (pag xiii(2)b , xv, 7, 8, 17, 28, 32(2)b , 33, 88, and 99).

[93] I. Sandler, S. *Chemical, Biochemical, and Engineering Thermodynamics, 4th Edition*. 2006. (pag xiv and 54).

[94] T. Schmitt, Y. Méry, M. Boileau, and S. Candel. Large-eddy simulation of oxygen/methane flames under transcritical conditions. *Proceedings of the Comb. Inst.*, 33:1383–1390, 2011. (pag 12 and 16).

[95] T. Schmitt, L. Selle, A. Ruiz, and Bénédicte Cuenot. Large-eddy simulation of supercritical-pressure round jets. *AIAA Journal*, 48(9):2133–2144, sep 2010. (pag xvi, xvii(2)b , 17, 20, 94, 99, 100, 102, 105, 106, 122(2)b , and 125(2)b).

[96] G. Singla, P. Scouflaire, C. Rolon, and S. Candel. Transcritical oxygen/transcritical or supercritical methane combustion. *Proceedings of the Combustion Institute*, 30(2):2921 – 2928, 2005. (pag xiii(2)b , 8, 10, 34(4)b , and 35).

[97] R. Smith, H. Inomata, and C. Peter. *Introduction to Supercritical Fluids. A Spreadsheet-based Approach*. Elsevier Science, 1 edition, 2013. (pag xiii, 42, and 43).

[98] G. Soave. Equilibrium constants from a modified redlich-kwong equation of state. *Chemical Engineering Science*, 27(6):1197–1203, 1972. (pag 56, 60, 61, and 65).

[99] B.A. Stradi, J.F. Brennecke, P. Kohn, and M.A. Stadtherr. Reliable computation of mixture critical points. *AIChE Journal*, 47(1):212–221, 2001. (pag 67).

[100] D. Suslov, B. Betti, T. Aichner, S. Soller, F. Nasuti, and O. Haidn. Experimental investigation and cfd simulation of the film cooling in a o2/ch4 subscale combustor chamber. *Space Propulsion 2012*, 2012. (pag 148).

[101] G.P. Sutton. History of liquid propellant rocket engines in the united states. *Journal of Propulsion and Power*, 19(6):978–1007, 2003. (pag xiii, 2, and 3).

[102] G.P Sutton and O. Biblarz. *Rocket Propulsion Elements*. Wiley, 8 edition, 2010. (pag xv(2)b , 83, 84(2)b , and 85).

[103] S. Takahashi. Preparation of a generalized chart for the diffusion coefficients of gases at high pressures. *Journal of Chemical Engineering of Japan*, 7(6):417–420, 1975. (pag 207).

[104] H. Terashima and M. Koshi. Strategy for simulating supercritical cryogenic jets using high-order schemes. *Computers & Fluids*, 85:39 – 46, 2013. (pag 17).

[105] M.J Tham and K.E. Gubbins. Correspondence principle for transport properties of dense fluids. pure monatomic fluids. *Ind Eng Chem Fundam*, 8(4):791–795, 1969. (pag 198).

[106] M.J. Tham and K.E. Gubbins. Correspondence principle for transport properties of dense fluids. nonpolar polyatomic fluids. *Industrial and Engineering Chemistry Fundamentals*, 9(1):63–70, 1970. (pag 198).

[107] JR.T.W. Thomas, W. Leland and P.S Chappelear. The corresponding state principle: a review of current theory and practice. In *Proc. in Propulsion Physics*, volume 60, pages 15–43, 1968. (pag 196 and 197).

[108] K.W. Thompson. Time dependent boundary conditions for hyperbolic systems. *Journal of Computational Physics*, 68(1):1–24, 1987.

[109] E.F. Toro. *Riemann Solvers and Numerical Methods for Fluid Dynamics*. Springer-Verlag, Berlin, Germany, 1999.

[110] M.E Tuckerman. *Statistical Mechanics - Theory and Molecular Simulation*. Oxford, 2 edition, 2000. (pag xiii(2)b , 27(2)b , and 28).

[111] A. Urbano. *Analysis of Heat Transfer Characteristics of Supercritical Fuels in Rocket Cooling Systems by a Space Marching Numerical Technique*. PhD thesis, La Sapienza University, La Sapienza, Roma, 2012.

[112] A. Urbano and F. Nasuti. Numerical analysis of heated channel flows by a space-marching finite-volume technique. 2010. (pag 66).

[113] J.O. Valderrama. The state of the cubic equations of state. *Industrial and Engineering Chemistry Research*, 42(8):1603–1618, 2003. (pag xiv, 44, 45, 51(2)b , and 62).

[114] M. Valorani, F. Creta, G. Gargiulo, and P.P. Ciottoli. Cfd analyses on combustion for lre. Technical report, Jan 2014.

[115] M. Valorani, F. Creta, D.A. Goussis, J.C. Lee, and H.N. Najm. An automatic procedure for the simplification of chemical kinetic mechanisms based on CSP. *Combustion and flame*, 146(1):29–51, 2006. (pag 78).

[116] M. Valorani, E. Martelli, G. Gargiulo, P. Ciottoli, P. Grenard, and J. Sender. Cfd analysis of laser-pulse ignition of gch4/go2 in m3-dlr test bench. 2012. (pag 78).

[117] H.C. Van Ness and M. M. Abbott. *Classical Thermodynamics of non-electrolyte Solutions*. McGraw-Hill, 1982. (pag 43).

[118] H. Vernin and P. Pempie. Lox/ch4 and lox/lh2 heavy launch vehicle comparison. 2009.

[119] C.K. Westbrook, Y. Mizobuchi, T.J. Poinsot, P.J. Smith, and J. Warnatz. Computational combustion. *Proceedings of the Combustion Institute*, 30(1):125–157, 2005. (pag 143).

[120] O. Wolfgang and H. Mayer. Fundamentals of supercritical mixing and combustion of cryogenic propellants. *Journal of Propulsion and Power*, 19(3):332–341, 200.

[121] B. Yang, F. Cuoco, and M. Oschwald. Atomization and flames in lox/h2-and lox/ch4-spray combustion. *Journal of Propulsion and Power*, 23(4):763–771, 2007. (pag 11).

[122] B.-E. Yang, F. Cuoco, L. Wang, and M. Oschwald. Experimental investigation of liquid oxygen/ch4 coaxial spray and flame stabilization. *Tuijin Jishu/Journal of Propulsion Technology*, 29(3):262–268, 2008. (pag 11).

[123] V. Yang. Modeling of supercritical vaporization, mixing, and combustion processes in liquid-fueled propulsion systems. *Symposium (International) on Combustion*, 28(1):925–941, 2000. (pag 13).

[124] B. A. Younglove and J. F. Ely. Thermophysical properties of fluids. ii. methane, ethane, propane, isobutane, and normal butane. *Journal of Physical and Chemical Reference Data*, 16(4):577–798, 1987. (pag 38).

[125] N. Zong, H. Meng, S.-Y. Hsieh, and V. Yang. A numerical study of cryogenic fluid injection and mixing under supercritical conditions. *Physics of Fluids*, 16(12):4248–4261, 2004.

[126] N. Zong, G. Riber, and V. Yang. A flamelet approach for modeling of (lox)/methane flames at supercritical pressures. 2008. (pag 14 and 15).

[127] N. Zong and V. Yang. Cryogenic fluid injection and mixing at supercritical condition. 2003. (pag 31 and 153).

[128] N. Zong and V. Yang. Cryogenic fluid jets and mixing layers in transcritical and supercritical environments. *Combustion Science and Technology*, 178(1-3):193–227, 2006.

[129] N. Zong and V. Yang. An efficient preconditioning scheme for real-fluid mixtures using primitive pressure-temperature variables. *Int. J. Comput. Fluid Dyn.*, 21(5-6):217–230, 2007. (pag 14).

[130] N. Zong and V. Yang. Near-field flow and flame dynamics of lox/methane shear-coaxial injector under supercritical conditions. *Proceedings of the Comb. Inst.*, 31:2309–2317, 2007. (pag 13, 14, 15, 16, 18(2)b , and 161).